CORONARY ARTERIAL DYNAMICS AND ATHEROGENESIS

by

J. Scott VanEpps

B.S., University of Pittsburgh, 2001

Submitted to the Graduate Faculty of

School of Engineering in partial fulfillment

of the requirements for the degree of

Doctor of Philosophy

University of Pittsburgh

2007

UNIVERSITY OF PITTSBURGH

SCHOOL OF ENGINEERING

This dissertation was presented

by

J. Scott VanEpps

It was defended on

August 1, 2007

and approved by

Sanjeev G. Shroff, Professor, Department of Bioengineering

William R. Wagner, Professor, Departments of Surgery and Bioengineering

Suresh Mulukutla, Assistant Professor, Department of Medicine

Dissertation Director: David A. Vorp, Associate Professor, Departments of Surgery and Bioengineering

CORONARY ARTERIAL DYNAMICS AND ATHEROGENESIS

J. Scott VanEpps, Ph.D.

University of Pittsburgh, 2007

While documented risk factors (e.g., hypertension, diabetes, etc.) for atherosclerosis are systemic in nature, atherosclerotic plaques appear in a heterogeneous distribution in the vasculature. This heterogeneity is thought to be related in part to the fact that the plaques tend to develop in areas of disturbed blood flow such as bifurcations and curvatures. Moreover, the coronary arteries, which also experience the added mechanical deformations of cyclic flexing, stretching, and twisting due to their tethering to a beating heart, are particularly susceptible to atherogenesis. This suggests that both fluid-induced (shear) and deformation-induced (mural) stress contribute to location specific susceptibility or protection from disease. We hypothesized that local variations in shear and mural stress associated with dynamic motion of arterial segments influence the distribution of early markers of atherogenesis.

To test this hypothesis, we utilized our unique, well-established, and validated ex vivo vascular perfusion system in a combined experimental / computational study. Pairs of freshly-harvested porcine arterial segments were perfused ex vivo under normal hemodynamic conditions. One of the paired segments was exposed to coronary levels of either cyclic axial stretching, flexure, or twist. Post-perfusion tissue processing provided the extent and spatial distribution of early markers of atherogenesis, including endothelial permeability, apoptosis, and proliferation. Finite element analysis and computational fluid dynamics techniques were used to estimate the mural and shear stress distributions, respectively, for reconstructed models of each

experimentally perfused segment. Quantitative correlations between biological marker and mechanical stress distributions were determined using multiple linear regression analysis.

Vessel segments exposed to cyclic axial stretch and flexure showed significant increases in both permeability and apoptosis. In addition, we demonstrated that all three deformations generated complex, non-uniform distributions of both biologic endpoints and mechanical stresses. These distributions displayed a high degree of specimen-to-specimen variability which was attributed to the highly variable vessel geometries. Several specific mechanical stress measures, both mural and shear, were shown to be associated with cellular atherogenic marker distribution. Future work should be aimed at more fully elucidating the molecular mechanism linking mechanical stress in the tissue to these cellular based responses.

TABLE OF CONTENTS

LIST OF TABLES

LIST OF FIGURES

PREFACE

Obtaining a doctorate in Bioengineering has been one of the most challenging endeavors I have ever faced. It challenged me as an engineer and scientist as well as a son, friend, and husband. I am pleased to say that in putting all these facets of my being to the test, I have bent but not broken and managed to come out a better engineer, scientist, son, friend, and husband. This document is the physical manifestation of that challenge and my answer to it. While my name appears as the sole author, the work described here would not have been possible without the love, help, support, and mentorship of several people that I would like to acknowledge. In the words of Sir Isaac Newton, "If I have seen further, it is by standing on the shoulders of giants".

I would first like to thank my dissertation advisor David Vorp, Ph.D. His guidance and mentorship helped mold me into the scientist that I am today. In working with him I have gained many pearls of wisdom I plan to employ in building my career as an independent investigator and teacher.

Douglas Chew has played a major role in my career and personal development for over eight years. During that time he has been my teacher, advisor, advocate, mentor, and most importantly, friend. I am so thankful he decided to take a position in our lab so we could work together again. I would not be here without him.

There is no doubt that Harvey Borovetz, Ph.D. was my inspiration for pursuing a Ph.D. in bioengineering. I took his course in Artificial Organs my senior year as a professional elective

and was hooked. His love for his students and the field of bioengineering is what convinced me to stay at the University of Pittsburgh for my doctoral training.

My parents Tim and Diane VanEpps are my constant inspiration. They are an eternal flame that drives me to excel in whatever I set my mind to. Their unwavering support, love, and faith have propelled me to heights that even my "overactive imagination" could not grasp. Their zest for life and learning is unparalleled and will continue to be a driving force in all that I do.

A common phenomenon in science, known as synergy, is best described as the whole is greater than the sum of its parts. This is a perfect description of the relationship my wife, Jamie VanEpps, and I have. My accomplishments are made possible through the synergy created between us. I alone am not as great as I am with her. She allows me to stretch my mind, body, and spirit beyond what I though was possible. She is my extra pair of wings, my shelter, my cushion, and most all, my giving tree.

1.0 INTRODUCTION

In the United States cardiovascular disease (CVD) currently afflicts over 70 million people and claims almost a million lives each year [1]. The most prominent cardiovascular diseases, heart disease and stroke, account for almost 40% of all deaths and an estimated economic burden of $394 billion dollars in 2005 [2]. Atherosclerosis, the primary etiology of CVD, is characterized by intimal plaques that form as a time-dependent response to chronic arterial injury [3]. The mechanism of the vessel response to this insult is not well characterized but it is clear that the result is an atherosclerotic plaque with the potential to rupture, thrombose, and occlude the injured artery leading to the loss of blood flow to vital organs such as the heart and brain [4]. Current therapies for CVD are directed at the revascularization of occluded blood supplies or the reduction of risk factors associated with atherogenesis (e.g., dyslipidemia, hypertension, diabetes, and smoking). These approaches have led to modest reductions in mortality for coronary heart disease [5]. Unfortunately this trend is leveling off, demonstrating a lack of understanding of the true pathogenic mechanisms of the disease [6]. That is, known risk factors do not completely determine the probability of disease and revascularization merely slows the inevitable. Similar therapies have not been as successful in the management of stroke, as indicated by the little change in mortality rate over the same time period, further demonstrating the need to better understand the pathogenesis of atherosclerosis [6]. With the aging population, the prevalence of CVD will continue to increase unless a more basic understanding of the primary causes and pathogenesis of atherosclerosis is reached. Such an understanding would

certainly lead to new therapies directed at prevention of those primary causes and halting the pathogenic process.

Possible contributors to the development of atherosclerosis can be categorized as biochemical (e.g., lipids) or biomechanical (e.g., hypertension). The most noteworthy biochemical agent associated with atherosclerosis is low-density lipoprotein (LDL) [7, 8]. However, LDL, like other documented risk factors provides a systemic type stimulus while atherosclerosis is a highly localized, heterogeneous disease predominately affecting the coronary arteries, infrarenal abdominal aorta, and carotid bifurcation while sparing the thoracic aorta and arteries of the upper extremities [7]. On the other hand, biomechanical forces are not necessarily systemic and vary greatly with anatomical location. The complex biomechanical milieu of the vasculature is an area of intense research. There is a preponderance of data to suggest that these complex biomechanical stimuli play a pivotal role in the location specific development of atherosclerosis. In other words, biomechanical forces (depending on their magnitude, frequency, direction, etc.) either facilitate or protect against the systemic insults provided by the above mentioned risk factors. This introductory section reviews the mechanopathobiology of atherosclerosis by highlighting the observational correlations between local hemodynamics and atherosclerotic lesion localization and articulating how vasculature-specific mechanical stimuli can affect known atherogenic processes. In doing so, it will demonstrate the need for rigorous mechanistic studies that provide a framework for mapping a biomechanical stimulus to a well-defined spectrum of biological endpoints delineating atheroprotective versus atherogenic phenotypes. First, it is prudent to summarize the relevant, known pathobiological features of atherosclerosis.

1.1 RELEVANT PATHOLOGICAL FEATURES OF ATHEROGENESIS

The development of atherosclerotic plaques has been hypothesized to be a "response to injury" to the vessel wall [8]. This injury is usually a chronic low level insult to the endothelial or smooth muscle cells of the arterial wall manifesting itself in endothelial dysfunction [9]. This leads to, among other things, lipid accumulation [10] and leukocyte adhesion and infiltration [13-17] (Figure 1.1). Therefore, any investigation of the potential mitigating effects of biomechanics in atherogenesis should be made with respect to these pathobiologic mechanisms.

1.1.1 Endothelial Dysfunction

The endothelium has three important functions that are particularly relevant to atherogenesis: (1) maintenance of a selectively permeable barrier between the intravascular space and the tissue space, (2) ability to modify and transport lipoproteins into the vessel wall, and (3) provision of a nonadherent surface for leukocytes [11]. In accordance with the response to injury hypothesis, loss of these functions can be the most preliminary event in atherogenesis [9]. Injurious agents lead to inflammatory responses that ultimately cause endothelial cell (EC) death through apoptosis [12]. Russell Ross postulated that, if the injury is chronic the remaining viable ECs in the vessel wall will proliferate (to heal the wound) until they reach senescence at which time the wound will not heal properly resulting in increased convection of macromolecules (e.g., LDL) from the circulation to the vessel wall [9] (Figure 1.1).

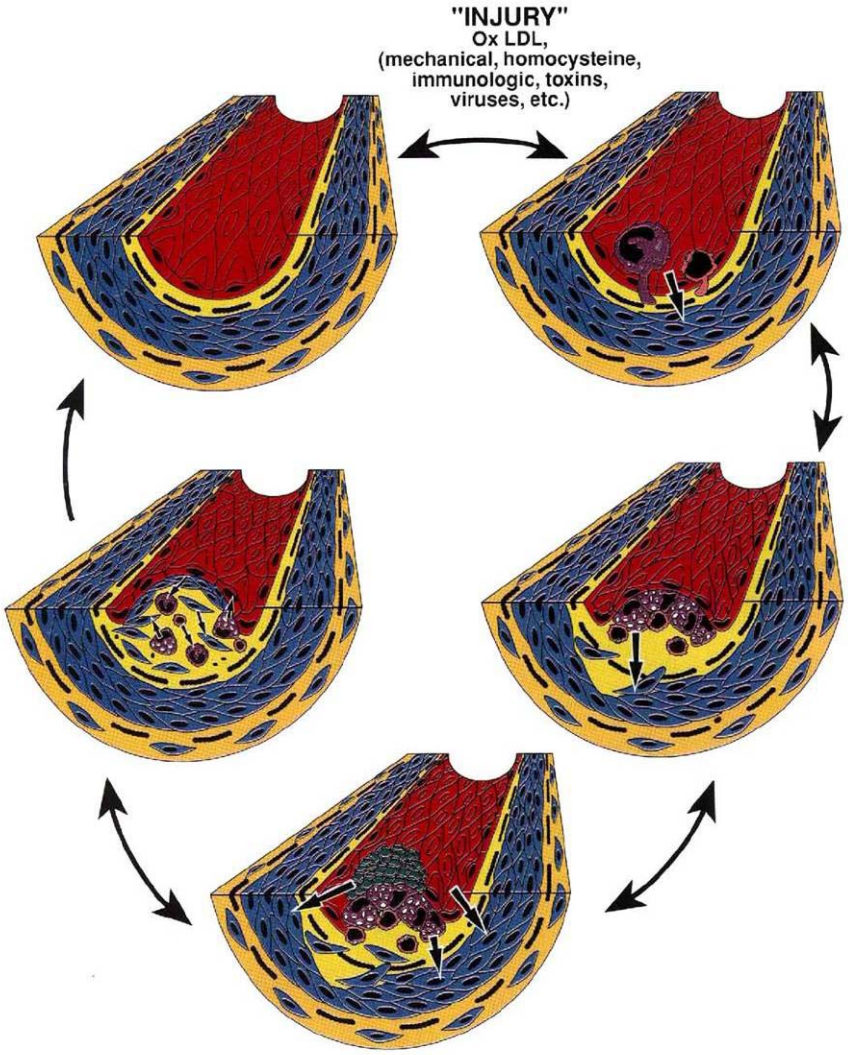

Figure 1.1 The response-to-injury hypothesis of atherosclerosis. Several different sources of injury to the endothelium (e.g., oxLDL, mechanical, homocysteine, immunologic, toxins, virus, etc.) can lead to endothelial cell dysfunction. One of the parameters associated with endothelial cell dysfunction is increased adherence of monocytes/macrophages and T lymphocytes (top right). These cells then migrate between the endothelium and localize subendothelially. The macrophages become large foam cells because of lipid accumulation and, with the T cells and smooth muscle, form a fatty streak (middle right). As the lesions accumulate more cells, and the macrophages scavenge the lipid, some of the lipid-laden macrophages may emigrate back into the bloodstream by pushing apart the endothelial cells. On doing so, those sites where blood flow is irregular (e.g., branches and bifurcations) with eddy currents and back currents, may become thrombogenic sites that lead to formation of platelet mural thrombi (bottom). Ultimately, the formation and release of numerous growth-regulatory molecules and cytokines from a network established between cells in the lesion consisting of activated macrophages, smooth muscle, T cells, platelets, and endothelium, lead to progression to a fibrous plaque or advanced, complicated lesion (middle left). Each of the stages of lesion formation is potentially reversible if the injurious agents are removed or when protective factors intervene to reverse the inflammatory and fibroproliferative processes. Cell color coding: smooth muscle (blue), endothelium (red), macrophage (violet), T cell (pink), and platelet (green). Image from Ross [9].

Indeed, endothelial cells of vascular lesions have been shown to have shortened telomeres indicating a senescent phenotype [13]. Therefore, increased permeability with comcomitant changes in proliferation and apoptosis signify EC dysfunction, the most preliminary event in the pathogenesis of atherosclerosis.

1.1.2 Lipid Accumulation

Lipid accumulation is a major manifestation of the vascular response to injury, and there are three means by which this occurs. First, dysfunctional ECs lose their selective barrier function. Illustrating this is the observation that convection of horseradish peroxidase from the plasma to the intima is increased in rats with spontaneous hypertension (a well-known chronic arterial insult and risk factor for atherosclerosis) [14]. Since the permeability of the internal elastic lamina remains relatively unchanged with hypertension, macromolecules accumulate in the intima [14]. An intact endothelium minimizes this effect, while a chronically injured endothelium amplifies it [14]. In addition, confluent monolayers of endothelial cells exposed to atherogenic levels of LDL show a dose-dependent increase in macromolecular permeability [15]. The effect is even more pronounced when the lipids are oxidized as demonstrated by Rong et al., [16]. They showed that injection of cholesterol oxidation products in rabbits resulted in accumulation of those products in the aortic wall and increased vascular permeability and accumulation of lipids and macromolecules even under normocholesterolemic conditions [16]. Similar results have been seen for endothelial dysfunction induced by nicotine and streptozotocin induced diabetes [17, 18].

Second, EC dysfunction leads to altered expression of lipoprotein receptors used to internalize and modify various lipoproteins. Certain lipoproteins, specifically oxidized LDL,

perpetuate the insult by activating ECs and trigging the inflammatory cascade [19]. Sawamura et al. identified the lectin-like low-density lipoprotein receptor-1 (LOX-1) specific for oxidized LDL (ox-LDL) [20]. The modification of native LDL to ox-LDL is a result of oxidative stress (a common manifestation of chronic insult) on ECs and macrophages [21]. Binding and internalization of ox-LDL by LOX-1 on ECs can stimulate the production of monocyte chemotactic protein-1 (MCP-1) and increase monocyte adhesion [22] as well as trigger the apoptotic cascade[23]. LOX-1 mRNA is positively regulated by its injurious ligand ox-LDL in a concentration dependent manner [24, 25] illustrating the role of EC dysfunction in the binding and internalization of ox-LDL. The results of several other studies also support this notion. For example, lysophosphotidylcholine, a major component of ox-LDL which has been implicated in atherogenesis [26-28], induces mRNA and protein expression of LOX-1 in cultured ECs [24]. Similarly, tumor necrosis factor-alpha (TNF-α), which has been shown to be increased in atherosclerosis [29, 30], induces a concentration dependent increase in LOX-1 expression[31]. There is also a complicated crosstalk between angiotensin II, which is known to cause EC dysfunction [30, 39], and LOX-1. That is, angiotensin II induces LOX-1 mRNA and protein expression [23] and ox-LDL upregulates angiotensin II receptors [32]. Although originally discovered as an endothelial scavenger receptor, LOX-1 has also been shown to be expressed by macrophages and SMCs where it contributes to foam cell formation [33]. *In vivo* studies demonstrating LOX-1 expression in balloon injury [34] and vein graft [35] models of atherosclerosis lend even greater validity to its role in ox-LDL accumulation in atherogenesis. Figure 1.2 illustrates the multi-faceted role of LOX-1 in atherosclerosis [36].

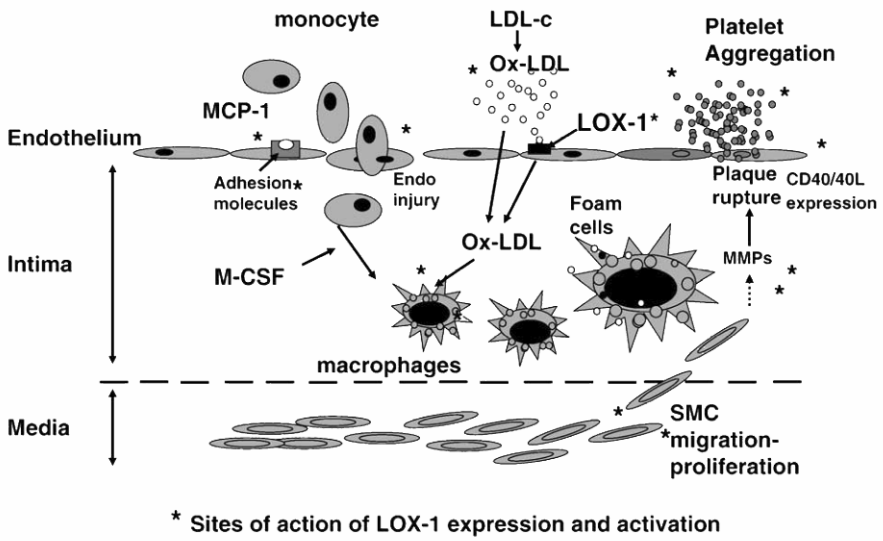

Figure 1.2 LOX-1 expression and activation has been demonstrated from the beginning of atherosclerosis (such as endothelial activation and apoptosis) to the culmination into an acute event (such as plaque rupture). Image from Mehta et al., [19].

A third means by which lipid accumulation may occur in response to vessel injury is that, once lipids have been transported into the subintimal space they are retained there by smooth muscle cells (SMCs) and macrophages which ingest lipoproteins (e.g., ox-LDL) via scavenger receptors [37, 38]. Since these receptors are not downregulated by increasing intracellular concentrations of cholesterol, these cells continue to accumulate lipid and become foam cells [39, 40]. In addition, SMCs in atherosclerotic lesions undergo a phenotypic modulation from a contractile to a synthetic phenotype [41, 42]. Synthetic SMCs have a decreased cholesteryl esterase activity as compared to contractile SMCs and therefore cannot metabolize cholesterol which leads to even more lipid accumulation [43]. Accumulation of lipids via increases in EC permeability, changes in lipoprotein receptor expression, and modulation of SMC phenotype represents a second set of early atherogenic markers.

1.1.3 Inflammatory Cell Infiltrate

Atherosclerosis has been described as an inflammatory process [3] in that a major manifestation of the "response to injury" is leukocyte adhesion and infiltration. Mononuclear leukocytes have been identified in lesions in various stages of atherosclerosis [8, 44, 45]. Davies et al. demonstrated this infiltration process in human coronary arteries with known atherosclerosis via scanning electron microscopy [46]. Monocytes and T lymphocytes adhere to the luminal surface of an artery where the endothelial layer is altered. Once there, they spread, migrate along the surface, and then extravasate through the endothelium into the subendothelial intimal space. This process is mediated through a variety of chemokines that allow these inflammatory cells to "home" to regions of insult or injury [47] and adhesion molecules that provide the necessary contacts for the cells to attach and migrate from the vascular lumen into the vessel wall [48].

1.1.3.1 Chemokines

The role of chemokines in inflammatory reactions is to become immobilized to the endoluminal surface of arteries, where they are presumed to enhance integrin adhesiveness and mediate leukocyte arrest and firm adhesion [49, 50]. In addition, they have been shown to promote transendothelial migration of leukocytes [51, 52]. The inflammatory component of atherosclerosis is demonstrated by the observation that MCP-1 is expressed on the luminal surface of human atherosclerotic lesions [53], and by ECs and SMCs in early and advanced atherosclerotic lesions [53-56]. Also, atherogenic agents such as minimally modified LDL [57], and lysophosphotidylcholine[58] can induce the transcription of MCP-1 mRNA in ECs. IL-8 is another chemokine with an established role in atherosclerosis [59]. It has been shown to arrest

monocyte rolling and induce firm adhesion in a dose-dependent manner on EC monolayers under flow conditions [60, 61].

1.1.3.2 Adhesion Molecules

Adhesion molecules related to the inflammatory process of atherosclerosis can be grouped into two categories, namely the selectins and the immunoglobulin adhesion molecules. Selectins are adhesion molecules that provide a loose attachment for leukocytes that allow them to roll along the luminal surface [62] (Figure 1.3), and include P-selectin, E-selectin, and L-selectin. L-selectin is constitutively expressed in leukocytes [48]. E-selectin is expressed in activated ECs but its role in atherosclerosis has not been well established [48]. P-selectin is not constitutively expressed by ECs but is expressed in ECs overlying active atherosclerotic plaques [63]. In addition, P-selectin is focally expressed in lesion prone areas of rabbit aortas after one week of an atherogenic diet [71, 72]. This expression preceded macrophage infiltration indicating P-selectin's role in monocyte recruitment [55, 71, 73].

Immunoglobulin adhesion molecules allow leukocytes to firmly adhere to the endothelium and extravasate into the vessel wall (Figure 1.3) and include intracellular adhesion molecule-1 (ICAM-1) and vascular cell adhesion molecule-1 (VCAM-1). ICAM-1 is detected on ECs of atherosclerotic lesions and is increased by injury [64], whereas normal ECs show little expression [70, 75]. VCAM-1 is expressed in ECs overlying lipid containing human atherosclerotic lesions [65]. Like P-selectin, VCAM-1's involvement in monocyte recruitment has been demonstrated by the fact that its expression was seen in lesion prone areas, one week after the onset of atherogenic diet in rabbits and prior to macrophage appearance [48, 66, 67]. Furthermore, expression of VCAM-1 is modulated by lipid-based injury; LDL can induce its expression in human coronary artery ECs [68]. The more atherogenic lipoprotein, ox-LDL,

upregulates ICAM-1 [69], and enhances TNF-α induced expression of VCAM-1 and ICAM-1 in human arterial ECs [70]. Increased expression of chemokines (IL-8 and MCP-1) and adhesion molecules (P-Selectin, ICAM, and VCAM) indicate an inflammatory state marking a third important event in atherogenesis.

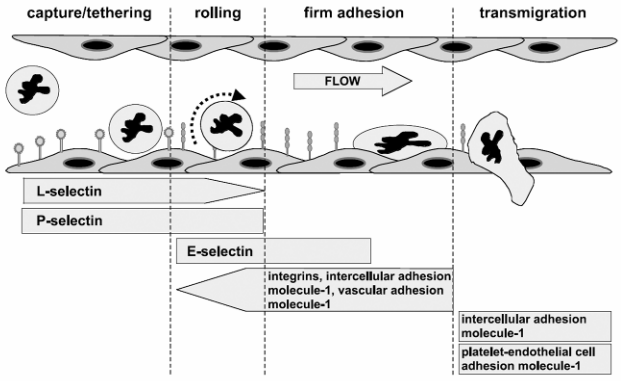

Figure 1.3 Schematic representation of leucocyte rolling, adhesion and transmigration across the endothelium and the cellular adhesion molecules involved in these processes. Image from Hope and Meredith, [71].

1.2 ROLE OF BIOMECHANICS IN ATHEROSCLEROSIS

Established risk factors for atherogenesis (e.g., hypertension and dyslipidemia) are systemic in nature and therefore cannot account for the fact that certain arteries such as the coronary arteries, carotid bifurcation, and infrarenal abdominal aorta are more susceptible to atherosclerosis than others [7]. Furthermore, the spatial distribution of atherosclerosis within the highly susceptible coronary arterial tree is heterogenous [74-78]. Evidence suggests that biomechanical forces

could account for this heterogeneity [72-75] by providing a facilitating or protective effect for the various systemic risk factors. This section will examine the current understanding of the relationship between biomechanical stimuli and atherogenesis with respect to the pathobiological processes discussed above. First, a brief description of the vascular biomechanical environment is provided.

1.2.1 Biomechanical Environment of the Vasculature

The cells (i.e., EC and SMC) of the vasculature live in a dynamic mechanical environment due the hemodynamics of blood flow as well as the movement of the surrounding tissue beds. Mechanical stimuli seen by cells of a blood vessel include, shear force due to contact with blood flow, strain due to pressure distension of the diameter of the vessel, and strain due to mural deformation of a vessel by its tethering to a surrounding tissue bed. Physiologic arterial shear stress magnitude ranges from 0-30 dyne/cm^2 during a cardiac cycle [89, 90]. In addition the direction of the shear changes due to blood flow reversal leading to oscillatory shear stress. The time average mean shear stress and amplitude of the oscillation are dependent upon anatomical location. Circumferential strain due to pressure distention ranges from 5-20% depending on arterial size and location [76]. While every major artery in the body experiences these two mechanical stimuli, several other arteries also experience extraneous mechanical deformations due to their tethering to surrounding tissue beds. The coronary arteries are the most well-known example of this as described in the following section. Although less well studied there are other examples of arteries that undergo tissue bed-induced deformations. The renal arteries have been shown to have cyclic changes in curvature due to kidney movement caused by respiration [77]. Flexure of the femoral arteries has been shown to induce spiral secondary flows indicating the

interrelated nature of the solid and fluid mechanics [78]. Just recently Cinthio et al. quantified the degree of longitudinal motion of several arteries (i.e., aorta, carotid, popliteal, and brachial arteries). They showed significant variation in the pattern of longitudinal motion over the cardiac cycle among different anatomical locations as well as subjects. Furthermore, they demonstrated that the intimal/medial portion of the arteries had a different longitudinal motion pattern than the adventitial portion suggesting massive shear strains between the media and adventitia. This work provides another anatomically heterogeneous mechanical stimulus that could mitigate the development of atherosclerosis.

1.2.2 Coronary Biomechanical Environment

The mechanical environment of a coronary artery is complex and spatially variable. Using flow visualization and high-speed cinemicrographic techniques, Asakura et al showed that the flow patterns in the left and right coronary circulation are complicated with distinct regions of disturbed flow, recirculation and secondary flows [79]. Velocity and wall shear stress can vary greatly with both longitudinal and circumferential position in the coronary arteries [79-83]. In general, arterial geometry has been shown to be a key component in the distribution of shear stress in the coronary vasculature (Figure 1.4) [84].

The effect of geometry on arterial biomechanics is further complicated by the fact that it is dynamic. That is, the geometry of a given coronary artery changes in time due to its firm attachment to the epicardial surface of a beating heart (Table 1.1) [99-102]. Gross et al showed that curvature (inverse of the radius of curvature) in coronary arteries ranged from 0.25 to 1.8 cm^{-1} [85].

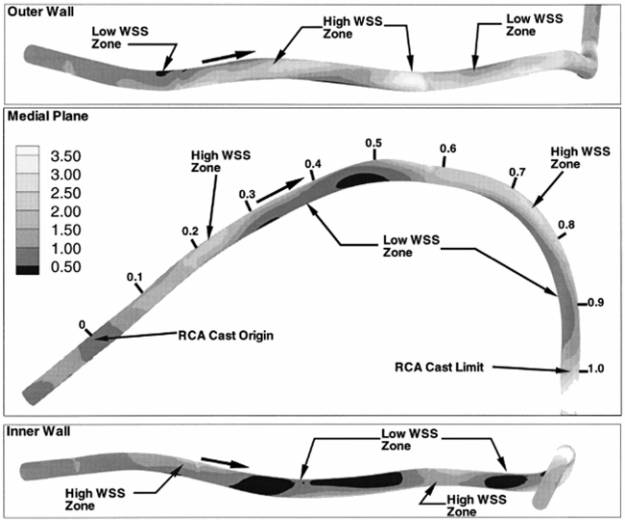

Figure 1.4 Contour plot of normalized wall shear stress (WSS) magnitude in a right coronary artery model for steady flow with a Poiseuille inlet velocity profile. Note the alternating regions of high and low WSS on the model walls. WSS values are normalized by the inlet Poiseuille value. Image from Myres et al., [84].

Table 1.1 Dynamic coronary artery geometry adapted from Ding et al., [91]. *Mean values for 4 patients' right coronary arteries (RCA) **Mean values for 8 patients' left anterior descending arteries (LAD) ^Values for Flexure and Twisting represent total flexure and twisting rather than instantaneous rates of change which would have units of ($cm^{-1}s^{-1}$).

Motion parameter	Explanation	Mean value for RCA**	Mean value for LAD^
Displacement (cm)	3D displacement of a material point	6.00±2.59	2.91±0.74
Strain	Relative length change of a point	0.054±0.020	0.040±0.018
Curvature (C) (cm^{-1})	Inverse of the radius of curvature	0.39±0.10	0.48±0.17
Flexure (cm^{-1})	Rate of change of curvature	0.95±0.35^^	1.16±0.44
Pulse curvature (cm^{-1})	C_{max}-C_{min} over cardiac cycle	0.33±0.14	0.39±0.12
Torsion (T) (cm^{-1})	Shear strain caused by a torque	1.50±0.60	2.69±0.79
Twisting (cm^{-1})	Rate of change of torsion	12.13±5.50^^	26.35±14.60
Pulse torsion (cm^{-1})	T_{max}-T_{min} over cardiac cycle	4.45±2.59	8.65±5.08

The degree of twisting and the rate of change of curvature were also shown to be highly position-specific [86]. In addition, coronary vessels undergo 4-6% cyclic longitudinal stretch during each cardiac cycle [87, 88]. These cyclic motions of flexure, stretching, and twisting as well as translational displacement can alter blood flow and therefore shear stress [89, 90]. Those dynamic motions can also lead to complex mural deformations and stress patterns in the arterial wall. These studies demonstrate the highly variable and complex biomechanical environment of the coronary arteries, which is depicted schematically in Figure 1.5. This environment is sufficiently complex to provide both atherogenic and atheroprotective stimuli which could account for the heterogeneous distribution of atherosclerotic lesion in the coronary vasculature despite systemic risk factors. The next section will summarize some key studies that suggest that biomechanical stimuli play a role in the location-specific pathogenic processes of atherogenesis.

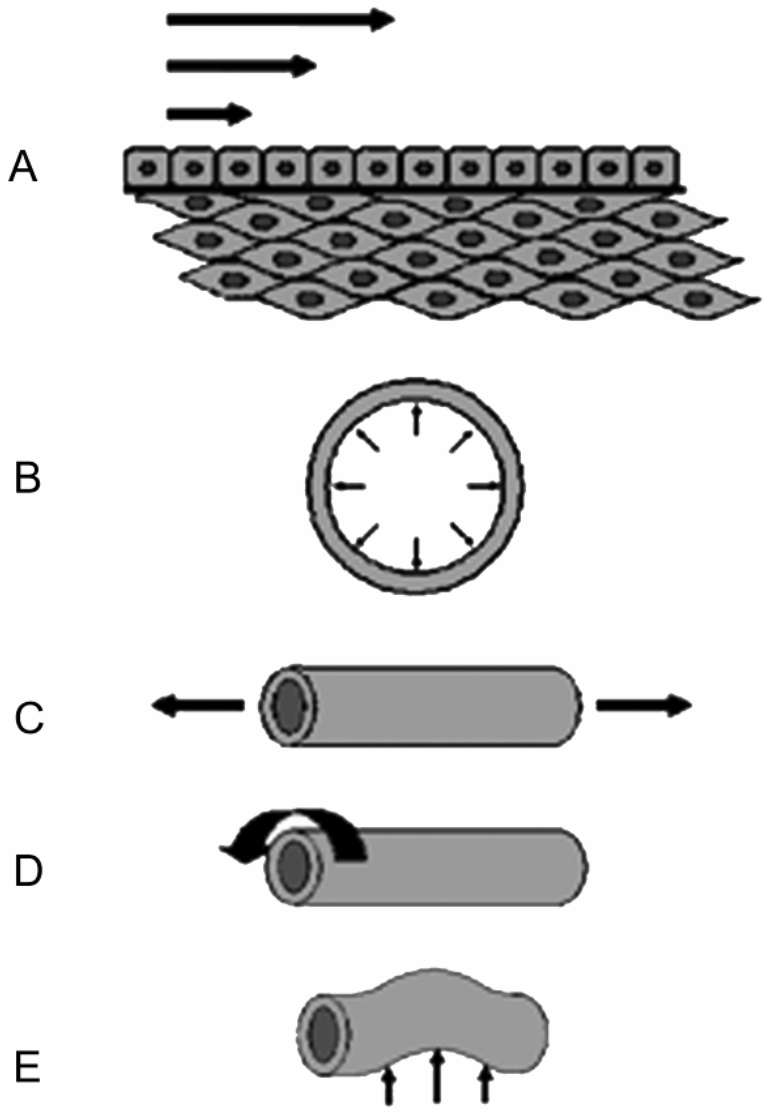

Figure 1.5 Schematic of vascular mechanical stimuli including: (a) flow-induced shear stress, (b) pressure-induced circumferential distention, and the tissue bed-induced deformations of (c) longitudinal stretching, (d) twisting, and (e) flexure. Image from VanEpps and Vorp, [91].

1.3 EFFECTS OF BIOMECHANICS ON ATHEROGENIC RESPONSE OF VASCULAR CELLS AND TISSUE

Mechanical forces and deformations are an important component of the vascular environment. These forces are sensed and communicated to the interior of vascular cells via several different signaling pathways. The mechanism of mechanotransduction is an area of intense research and could provide numerous chemotherapeutic targets. A detailed discussion of the various mechano-signaling pathways is beyond the scope of this document. Regardless, changes in mechanical forces alter cell signaling, which in turn can potentially lead to endothelial activation and/or dysfunction leading to lipid accumulation and inflammatory activation. The mechanosensitivity of each of these pathogenic processes and their associated molecules (described in detail above) is described below and summarized in Table 1.2.

Table 1.2 Summary of atherogenic processes and their mechanosensitivities. * ↓ - denotes decrease or downregulation; ** SS - denotes shear stress; # ↑ - denotes increase or upregulation; ## CS - denotes cyclic stretch; ^ Δ's - denotes changes in. Table from VanEpps and Vorp, [91].

Pathogenic Process	Role in Atherogenesis	Mechanosensitivity
Proliferation	Initial response to endothelial injury (i.e., wound healing)	Abrupt ↓* SS** can ↑# EC## proliferation [92]; ↑ SS ↓ DNA synthesis [93]; Turbulent flow ↑ EC turnover [94, 95]; ↑ SS ↓ EC proliferation [96]; ↑ CS ↑ EC proliferation [97, 98];
Apoptosis	Cause of endothelial dysfunction; found in atherosclerotic lesions	Physiologic SS and CS suppress apoptosis in ECs [99-104]; ↓ SS induces EC apoptosis [105]; ↑ CS ↑ EC apoptosis [106]; Turbulent flow ↑ EC turnover [94]
Permeability	Allows macromolecular (e.g., lipids) uptake into vessel wall	↑ CS ↑ permeability [106]; ↑ SS ↓ permeability [107]; ↑ SS gradient ↑ permeability [108]; Cyclic Δ's^ SS ↑ permeability [95, 107, 109]; ↑ Transmural pressure ↑ permeability [108, 110-112].
LDL uptake	Can cause endothelial injury, lipid accumulation, and inflammatory activation	↓SS can ↑ cholesterol permeability [118-120]; Δ's pulse pressure and flow alter cholesterol uptake [113]; ↑ Pressure alters LDL permeability [112]; ↑ SS ↑ Binding, internalization and uptake of LDL [129-131]
LOX-1 expression	Cellular receptor for ox-LDL uptake	↑ SS ↑ LOX-1 mRNA and protein [114]
Cholesteryl esterase	Allows macrophages and SMCs to digest cholesterol. Dysfunction or loss of expression can lead to cholesterol accumulation and foam cell formation.	SMC phenotypic modulation, which is mechanosensitive (see text), can cause ↓ in cholesteryl esterase activity [115-119]
MCP-1	Leukocyte chemoattractant	↑ SS ↓ MCP-1 expression [120]; ↑ CS ↑ MCP-1 expression [121-123]
IL-8	Leukocyte chemoattractant; facilitates TEM	↑ SS ↓ IL-8 expression [124-126]
P-selectin	Leukocyte rolling	A threshold level of is shear required for P-selectin rolling function [127]
ICAM-1	Leukocyte arrest and activation	↑ SS ↑ ICAM-1 expression [146-150]
VCAM-1	Leukocyte arrest and activation	↑ SS ↓ VCAM-1 expression [149, 151, 152]

1.3.1 Endothelial Dysfunction

Mechanical forces have been shown to lead to EC dysfunction characterized by EC proliferation, apoptosis, and increased permeability. One of the most studied mechanical forces with respect to EC dysfunction is shear stress. Permeability of the vessel wall is increased by cyclic changes in shear stress [95, 107, 109] and high spatial shear stress gradients [108], but decreased by increasing levels of shear [107]. The increase in EC permeability in response to shear forces is potentially mediated through changes in endothelial cell-cell contacts [119, 120]. That is, increasing magnitude and duration of shear stress on ECs leads to enhanced expression of proteins associated with both tight and adherens junctions [128], while exposure to low shear stress causes tight junctions to become discontinuous (i.e., leaky) [129]. This suggests that low or oscillating shear levels facilitate systemic atherogenic factors (e.g., LDL). This is also supported by the observation that low shear stress impairs endothelial wound healing while high shear stress enhances wound repair through increased cell spreading and migration [130]. Shear stress can also alter EC proliferation [92, 94-96, 130-132] and apoptosis [113, 116, 158-160] depending on the magnitude and spatial and time variation of the shear stress. For instance, ECs exposed to 10-15 dynes/cm^2 of shear stress and laminar flow conditions have little or no proliferation or apoptosis [95, 99-102, 104]. On the other hand, low shear stress can cause increased proliferation and apoptosis, hence increased EC turnover [97, 101, 110, 139, 140].

Based on the above data relating shear stress to endothelial dysfunction a hypothetical mapping of shear stress onto an atherogenicity spectrum can be seen in Figure 1.6.

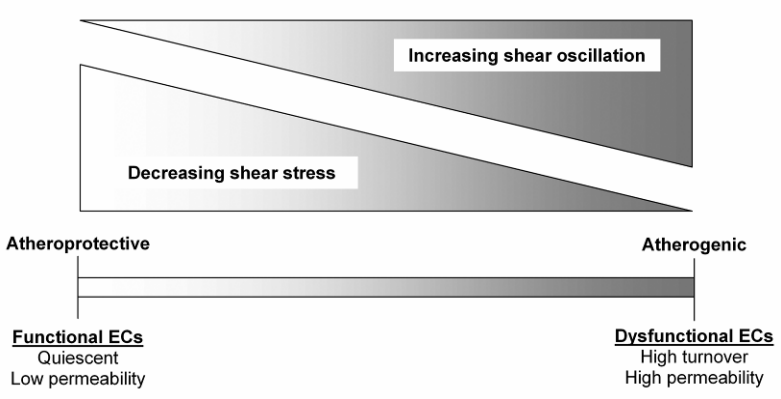

Figure 1.6 Pictorial representation of how the biomechanical stimulus shear stress maps to a continuum between atheroprotection and atherogenicity. If the atherogenicity of shear stress can be characterized by the level endothelial cell dysfunction a map can be drawn relating a given type of shear stress (e.g., low magnitude, high oscillation) to its potential to facilitate atherogenesis. Further research is required to provide quantification to this representation. Figure from VanEpps and Vorp [91].

Of course this scheme must be evaluated with caution since the majority of these studies have been performed in two dimensional mono-culture conditions. SMC/EC co-culture has been shown to dramatically alter the proliferative response of ECs to various stimuli including shear stress [133, 134]. The response is also dependent upon the culture media [135], substrate [135], and type of cells used (venous versus arterial) [136]. A more accurate description of the mitigating effects of shear stress on atherogenesis requires continued research utilizing more physiologic model systems such as three-dimensional EC/SMC co-culture [133, 134], *ex vivo* experimental preparations [137, 138], and *in vivo* trials. This type of paradigm could be extended to all combinations of mechanical stimuli and atherogenic processes as discussed below. Such a description could provide intelligent direction in the search for therapeutic targets.

Other mechanical stimuli that can potentiate or inhibit EC dysfunction manifested by proliferation, apoptosis, and increased permeability are cyclic stretch and hydrostatic pressure.

More specifically, physiological levels of cyclic stretch can increase EC proliferation [82, 103, 147], suppress apoptosis [101], and provide an atheroprotective effect for the endothelium [106]. Although the increased proliferation is a contradictory response for atheroprotection there does seem to be an analogous effect of moderate levels of cyclic stretch to the protective effect of moderate levels (10-15 dyne/cm^2) of shear stress [99-104, 139]. On the other hand, supra-physiologic levels of cyclic stretch can cause increased permeability and apoptosis [106]. That hydrostatic or transmural pressure is also an important determinant of endothelial dysfunction is suggested from the well-known fact that hypertension is a risk factor for atherosclerosis. Indeed, increased pressure has been implicated in mass transport of material (e.g., lipids) from the lumen to the vessel wall [110], as well as alterations in EC proliferation and apoptosis [140].

1.3.2 Lipid Accumulation

Accumulation of lipids in atherogenesis is also modulated by mechanical forces. For instance, lipids accumulate at the luminal surface in areas where blood flow velocity and wall shear stress are low [127, 171] and where particle residence times and the permeability of the endothelial layer are enhanced (a known manifestation of EC dysfunction as detailed above) [171-175]. Lipid accumulation is also mediated by shear-sensitive receptors. The expression of LOX-1, a key modulator of LDL-induced endothelial insult and lipid accumulation (recall Figure 2), has been shown to be regulated by physiologic levels of shear stress [114]. Also, the binding, internalization, and degradation of unmodified LDL by the vessel wall is highly dependent on shear stress [129-131]. Cyclic strain and pressure also effect lipid accumulation. For example, cyclic stretch causes an increase in reactive oxygen species [141] and oxidative stress [142] in ECs, which increase the oxidation of LDL and increase EC permeability and uptake of ox-LDL.

Hypertension (i.e., increased intraluminal pressure) has been predicted to increase convective pressures or the driving force for the transport of material (e.g., LDL) from the lumen to the vessel wall [124, 178, 179]. This is substantiated by data showing that increased transmural pressure leads to increased filtration velocity [143] and uptake of cholesterol [113]. Cytoskeletal rearrangement has been implicated as a factor in both shear and stretch mediated LDL accumulation [144].

Loss of expression of cholesteryl esterase by SMCs that have been phenotypically altered from a contractile to a synthetic phenotype (a common event in atherogenesis, see above) is another means by which lipids are accumulated in the vessel wall. The phenotypic state of SMCs is regulated at least in part by mechanical forces, as demonstrated by the observation that cyclic stretch creates a substrate-dependent modulation of proliferation and h-caldesmon expression *in vitro* [115]. *In vivo* studies have also shown the importance of mechanical injury in the phenotype of vascular SMCs. For example, balloon inflation injury to the media was shown to promote extracellular matrix synthesis and decrease α-actin content in SMCs [116]. Zhang et al showed that neointimal smooth muscle cells of external jugular veins transposed to the carotid artery position display a more primitive synthetic phenotype [119], supporting the notion that the change from the venous to the arterial biomechanical milieu triggers phenotypic alteration. Further evidence comes from *ex vivo* organ culture studies wherein cyclic stretch was found to be necessary to maintain the contractile function of SMCs in cultured rat portal veins [118]. Goldman et al. exposed rat vena cava to arterial pressures [117], leading to a large increase in medial circumferential strain and a concomitant reduction in the SMC filamentous actin coverage. Taken together, these previous studies demonstrate that mechanical forces are important modulators of lipid accumulation, another important event in atherogenesis.

1.3.3 Inflammatory Cell Infiltrate

Shear forces in conjunction with apical chemokines promote the migration of leukocytes across the endothelium [58, 59]. Both chemokines described above (IL-8 and MCP-1) have been shown to be responsive to mechanical stimuli. For example, human umbilical vein endothelial cells showed increased production of IL-8 mRNA and protein under low flow as compared to those exposed to high flow [143, 144, 181, 182]. IL-8 is also upregulated in response to cyclic stretch [145]. Similarly for MCP-1, steady shear (ramp flow and the steady component of step flow) diminishes protein [120] and mRNA [146] expression, while cyclic strain induces protein and mRNA expression [139-141, 183].

The adhesion molecules are also mechanosensitive, in that oscillatory flow induces up-regulation of adhesion molecules and cytokines that mediate monocyte/EC interactions [156, 157]. More specifically, those adhesion molecules described above (i.e., P-selectin, ICAM-1, and VCAM-1) have very specific responses to biomechanical forces. Fluid shear above 0.5 dyne/cm^2 significantly enhances HL-60 myelocyte rolling on P-selectin at site densities of 200/μm^2 and below [127]. Shear stress can also modulate expression of VCAM-1 and ICAM-1 [185, 187]. Laminar flow generated shear stress (>2.5 dyne/cm^2) directly and selectively upregulates ICAM-1 expression on the surface of endothelial cells and promotes leukocyte adhesion in a dose-independent fashion[147-149]. VCAM-1, on the other hand, is downregulated by shear stress in a dose-dependent manner [151, 152]. While we are not aware of any studies specifically relating mural stresses or cyclic strains with the expression of adhesion molecules, veins subjected to arterial flow show increases in ICAM-1 expression [150] which is abolished by stretch activated cation channel blockers [151], suggesting the role of cyclic stretch in the expression ICAM-1. This data demonstrates that the expression of

mediators of the inflammatory cell recruitment component of atherogenesis is sensitive to mechanical stimulation.

1.4 CORRELATIONS BETWEEN BIOMECHANICS AND LESION LOCALIZATION

Prior to our more detailed understanding of the mechanobiology of vascular cells several groups began to find correlations between physiologic biomechanical forces or deformations and the location of atherosclerotic lesions in attempts to find the mitigating factor that accounted for the heterogeneous distribution of atherosclerosis [138, 152-156]. These studies can be grouped into those that examine shear stress and those that examine mural stress. In addition, several groups have investigated correlations between biomechanics and vein graft stenosis by intimal hyperplasia (an accelerated form of atherogenesis). This work has demonstrated that anastomosis angle, graft diameter, and graft compliance are all important mechanical factors in determining the likelihood of intimal hyperplasia and subsequent graft failure [157]. David Vorp's laboratory has also determined that the flow condition in the host artery should also be considered in evaluating the biomechanical status and failure potential of a vein graft [158]. Although this work is germane to the topic of cardiovascular mechanopathobiology, the details of these and other similar studies and their implications are beyond the scope of this document.

1.4.1 Shear Stress

Areas of low or oscillating shear stress within the arterial tree have been correlated with atherogenesis in a variety of models including the carotid bifurcation [194-197], abdominal aorta [168, 169], and coronary vasculature [81, 86, 200, 201]. The lower wall shear rate near the carotid artery bifurcation is associated with larger intimal/medial thickness than at a more proximal site, suggesting accelerated atherosclerotic lesion formation for the bifurcation region [159]. The suprarenal abdominal aorta, which tends to have a lower incidence of plaque formation, has an uncomplicated, laminar flow pattern while the more atherosclerosis-prone infrarenal abdominal aorta has a more complicated flow pattern characterized by flow separation, vortices, and flow reversal [160]. In the coronary circulation, lesion location also depends on geometric factors such as curvature, bifurcation angle, and position of the ostia of branches [81, 83, 161-163], all of which can affect shear stress. Furthermore, the rate of progression of atherosclerosis, which is highly variable among lesions in the same patient, has been related to variations in shear stress [164]. Clearly, shear stress has been shown to be an important contributor to atherogenesis both in correlative and mechanistic type studies.

1.4.2 Mural Stress

Much attention has been given to the correlations between shear stress and atherogenesis. However, this neglects an extremely important component of the vascular biomechanical milieu, namely mural stress. The previous discussion has demonstrated that cyclic stretch and hydrostatic pressure have the capacity to potentiate or inhibit pathogenic features of atherosclerosis. Furthermore, we are just beginning to understand the degree to which tissue-

beds induce vascular deformations and therefore mural stresses. Nowhere is this clearer than in the coronary arteries which seem to be exquisitely susceptible to atherosclerosis [165]. Given the effects of mural stress on vascular cells, the effects of shear stress alone cannot account for the high susceptibility of coronary arteries to atherosclerosis. Indeed, *in vivo* studies of mural deformations have demonstrated that regions of coronary arteries that undergo increased levels of cyclic flexion exhibit a greater degree of atherosclerotic lesion formation [152, 154]. On the contrary, the intramyocardial coronary arteries, which experience cyclic radial compression due to contraction of the surrounding myocardial muscle, have a low occurrence of atherosclerosis, indicating a protective effect of mechanical compression [77, 78]. A similar phenomenon has been seen in the vertebral arteries where the portions of the vessel that are surrounded by bone tend to be free of lesions while the intervertebral portions are more prone to atherogenesis [78, 177].

The protective effect provided by external radial support as seen in the intramyocardial arteries and the vertebral arteries presents an ideal situation that may be an excellent avenue for clinical intervention. Indeed, Thubrikar et al. used rigid casts to reduce circumferential wall distension in rabbit arteries which resulted in a reduction in atherosclerotic lesion development [166]. On the other hand, nonconstrictive (those that do not impede circumferential distension) perivascular supports have been shown to induce intimal growth in arteries and are a common method for experimental induction of arterial injury and atherosclerosis [210]. There clearly is a need for further work to investigate this particular mechanical phenomenon in order to develop safe clinical interventions.

1.5 SUMMARY

The biomechanical environment of the vasculature is extremely complex including temporal and spatial variations as well as fluid and solid stresses. This complex pattern of biomechanical stimuli provides a mechanism by which systemic insults such as diabetes mellitus, smoking, and dyslipidemia can result in a highly localized heterogeneous distribution of disease such as atherosclerosis (Figure 1.7).

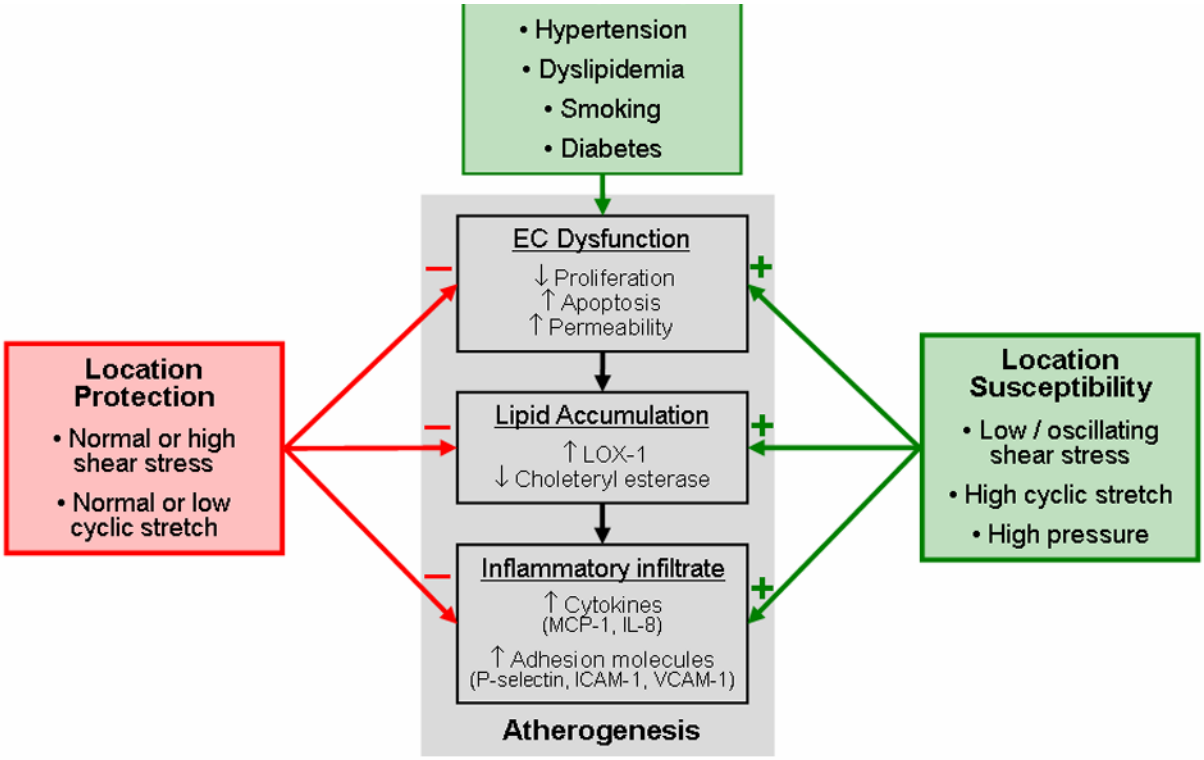

Figure 1.7 Summary schematic demonstrating how established risk factors provide a systemic preponderance toward atherogenesis while location-specific biomechanical factors may influence lesion localization by stimulating (red) or inhibiting (green) atherogenic processes. Image from VanEpps and Vorp, [91].

Biomechanical forces can either facilitate vascular insult/injury or protect against it. The next major innovation in the prevention and treatment of CVD must come from the basic understanding of the complex biomechanical milieu of the vasculature and the mechanism by which this environment affects the pathological processes of atherogenesis. Furthering our understanding of this relationship is the motivation behind the work described here.

1.6 SPECIFIC AIMS

The research described above characterizing the mechanopathobiology of atherogenesis led to the formation of the following hypothesis:

Working Hypothesis: *Local variations in shear and mural stress associated with dynamic deformation of arterial segments influence the distribution of early markers of atherogenesis.*

Specific Aim 1: Experimentally determine the extent and spatial distribution of early markers of atherogenesis (i.e., endothelial injury, lipid accumulation, and inflammatory activation) in intact arterial segments exposed to physiologically realistic *ex vivo* perfusion conditions and controlled, biomechanical stimuli (i.e., cyclic flexure, stretch, and twist).

Specific Aim 2: Estimate the distribution of deformation-induced (mural) stresses specifically for each perfused arterial segment using computational solid stress analysis.

Specific Aim 3: Estimate the distribution of flow-induced (shear) stress specifically for each experimentally perfused arterial segment using computational fluid dynamics techniques.

Specific Aim 4: Determine the correlative relationships (positive and negative) between the mural stress and shear stress distributions determined computationally (**Specific Aims 2 and 3 respectively**) and the spatial variation of atherogenic endpoints determined experimentally (**Specific Aim 1**).

This research project was a combined experimental/computational study. The experimental portion of the work consisted of perfusion of intact arterial segments *ex vivo* under well-controlled biochemical and biomechanical conditions (**Specific Aim 1**). The computational portion consisted of finite element (**Specific Aim 2**) and computational fluid dynamics (**Specific Aim 3**) simulation of each individual *ex vivo* experiment. These two arms of the study were combined by location specific pairing of biological endpoints determined experimentally in **Specific Aim 1** and mechanical stress measures estimated computationally (**Specific Aims 2 and 3**) in a multiple linear regression analysis (**Specific Aim 4**). This study design allows for distinct and unique coupling between each perfusion experiment and its associated computational simulation.

The goal of this study was to develop a more detailed understanding of how the biomechanical milieu of the vasculature contributes to location-specific atherogenic processes. Such understanding may have two significant long-term benefits. First, it provides clinicians with some insight into lesion-prone and lesion-protective areas of the vasculature. This insight will allow them to focus their monitoring and intervention to the most vulnerable sites. Second,

providing a direct link between biomechanical stimuli and specific pathogenic mechanisms in atherosclerosis narrows the search for specific signaling pathways for potential pharmacological intervention.

While the original research plan included evaluation of all the atherogenic endpoints listed in this section, the protein and gene expression levels for LOX-1, cholesteryl esterase and the inflammatory chemokines (IL-8 and MCP-1) and adhesion molecules (P-Selectin, ICAM-1 and VCAM) proved to be experimentally difficult. A description of those experimental difficulties, the preliminary findings, and recommendations to overcome those obstacles can be found in Appendix A. The rest of the dissertation will focus specifically on three atherogenic endpoints which represent the earliest observable pathobiologic events: intimal permeability, cellular apoptosis, and proliferation.

2.0 *EX VIVO* VASCULAR PERFUSION SYSTEM (EVPS)

The vascular biomechanics laboratory has focused on vascular bioengineering and vascular pathobiology over the years by developing unique, state-of-the-art, bioengineering tools to study vascular disease. One such tool is a device to allow the application of various physiologically-consistent dynamic deformations to intact vascular segments perfused *ex vivo*[167, 191]. To paraphrase from the recent book by Jay Humphrey[167] (pp 316-317):

> *"the device reported by Vorp et al,[156] allows continuous perfusion of a vascular segment within a 'bioreactor environment'. This is an important experimental advance, for it may allow one to study remodeling of vessels under well-controlled multiaxial loads."*

Experiments utilizing this device have demonstrated that (1) vein segments exposed arterial hemodynamics and cyclic axial stretch and twist (coronary bypass environment) have increased platelet deposition when compared to controls [137]; (2) cyclic flexure of arterial segments leads to differential expression of MMP-1 and E-Selectin (two important players in many vascular diseases) [138]; and (3) hemodynamics conditions influence the localization of immediate early gene (Erg-1. c-jun, c-fos) expression in arterial vein graft end-to-side anastomoses [168].

While this device has demonstrated near-physiologic biomechanical and biochemical conditions there were a few limitations that needed to be addressed before the proposed aims could be thoroughly examined. This section will describe the original EVPS with dynamic

mechanical deformation capabilities, the limitations of that device, and the actions that were taken to address those limitations. These technical improvements were incorporated for all subsequent *ex vivo* experiments in this study.

2.1 DESCRIPTION OF THE ORIGINAL EVPS

Central to this project is *ex vivo* exposure of arterial segments to precisely controlled hemodynamics, biomechanical wall motion, and dissolved gases (pH, pO_2, pCO_2) to simulate the coronary environment. The EVPS originally described by Labadie et al., [169] and further modified by Vorp et al., 1996 [156] and Vorp et al., 1999 [138] is a combination of two devices. The first device simulates physiologic hemodynamics on intact vascular segments. The second device can apply additional physiologic heart-induced deformations of cyclic stretch, twist, and flexure.

2.1.1 Simulation of Physiologic Hemodynamics

As described by Labadie et al., pulsatile flow was originally provided by combining a Bio-Medicus® (Model 520D, Medtronic, Minneapolis, MN) centrifugal pump (like those sometimes used for cardiopulmonary bypass) with a gate valve controlled by a linear actuator [169]. In this configuration, the pump provided the bulk flow while the gate valve superimposed a pulsatile pressure / flow waveform Figure 2.1. This device was capable of reproducing the physiologic pressure and flow waveforms with a high degree of accuracy. However, the success was overshadowed by frequent mechanical failure and compromised system sterility. This problem

was addressed by simply removing the gate valve and allowing the Bio-Medicus® centrifugal pump to provide the pulsatility. While this pump does not reproduce the higher order harmonics of a physiologic pressure / flow waveform, its mechanical reliability provides excellent intra-experiment reproducibility.

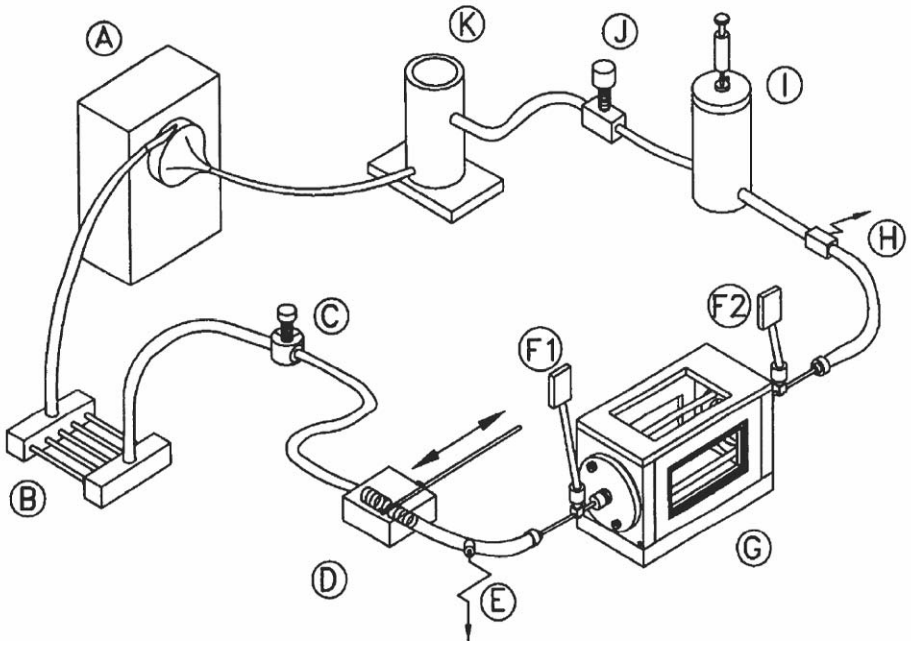

Figure 2.1 The original EVPS described by Labadie et al. [169] consisted of the following elements connected in series: Bio-Medicus®centrifugal pump (A), heat exchanger (B), pressure regulator (C), gate valve (D), temperature probe (E), pressure transducers (F1 and F2), tissue housing chamber (G), flow probe (H), compliance chamber (I), valve (J), and reservoir (K). Components not shown include, adventital bath circuit, He-Ne laser micrometer, and data acquisition system. Image from Labadie et al. [169].

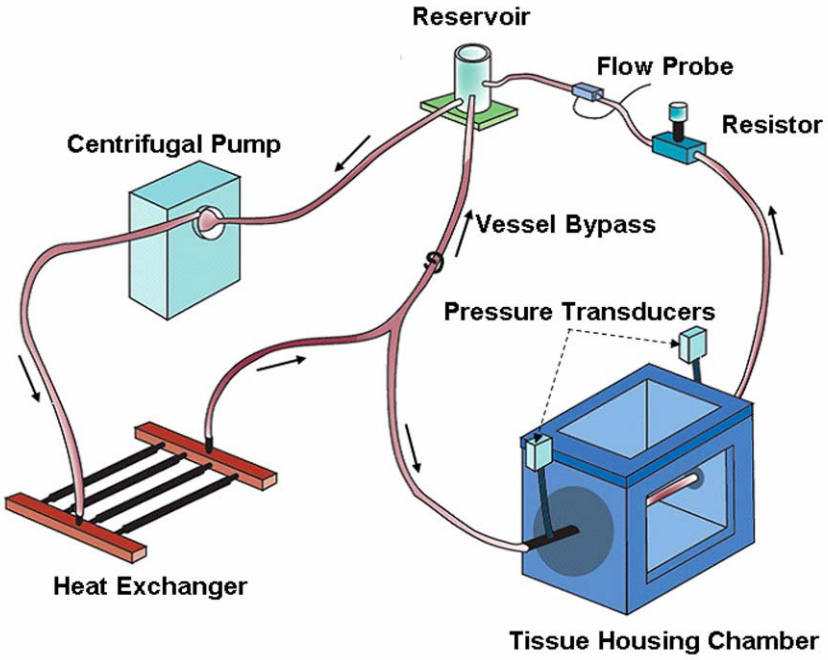

Figure 2.2 Schematic of the current EVPS. The loop is composed of a Bio-Medicus® centrifugal pump that provides pulsatile pressure and flow, heat exchanger, tissue-housing chamber, proximal and distal pressure transducers, a variable resistance valve, flow probe, collection reservoir, and vessel bypass. Components not shown include, adventital bath circuit, He-Ne laser micrometer, and data acquisition system. Image adapted from Labadie et al. [169].

The current EVPS is shown in Figure 2.2. The centrifugal pump provides pulsatile circulation of sterile perfusate (i.e., tissue culture media) through the mounted arterial segment. A separate roller pump circulates an adventitial bath (i.e., tissue culture medium) around the specimen which is mounted in a sealed vessel-housing chamber. Medical grade disposable pressure transducers (Model PX272, Edwards Lifesciences, Irvine, CA) positioned upstream and downstream of the specimen allow accurate estimation of intraluminal pressure. In-line ultrasonic flow probes (Model 4N32, Transonic Systems, Ithaca, NY) measure volumetric flow rate, while vessel outer diameter is measured using a highly accurate He-Ne laser micrometer (Model 162-100, Beta LaserMike, Dayton, OH). A Pentium 4 computer digitizes the analog

signals provided by the laser micrometer and pressure and flow transducers with an analog/digital interface board. A variable resistance valve in the flow circuit allows for the independent adjustment of intraluminal pressure and flow. The bath and perfusate are maintained at 37ºC using heat exchangers immersed in water baths. Injection ports allow for the addition of bioactive and pharmacological agents as well as media sampling. Physiologic pH, pO_2 and pCO_2 are monitored via media sampling using an ABL 5 blood gas measuring device (Radiometer, Copenhagen, Germany) and maintained by purging a filtered mixture of air and CO_2 over the circulating perfusate in the collection reservoir, and over the adventitial bath medium in the vessel housing chamber [137, 138, 144, 156, 169-172].

2.1.2 Simulation of Heart-Induced Mechanical Deformations

To generate the heart-induced deformations of cyclic axial stretch, twist, and flexure, an additional piece of hardware is required. The first generation of this device, developed and described by Vorp et al. [156], was capable of replicating physiologic cyclic stretch and twist deformations of the coronary arteries (Figure 2.3). A custom-designed motion control program systematically operates two stepper motors to simulate these conditions. The first ("Stretching Motor" in Figure 2.3) rotates a precision-threaded lead screw, transmitting longitudinal motion to the two carriages attached to the perfusion tees or cannulae. The ends of the lead screw are threaded in opposite directions generating opposing longitudinal motion of the two cannulae (i.e., axial stretch of the interposed vascular segment specimen). The second motor ("Twisting Motor" in Figure 2.3) is fixed to one of the cannulae which rotates an amount specified by the motion control program. Since the other cannula is fixed against rotation, a twisting deformation is generated.

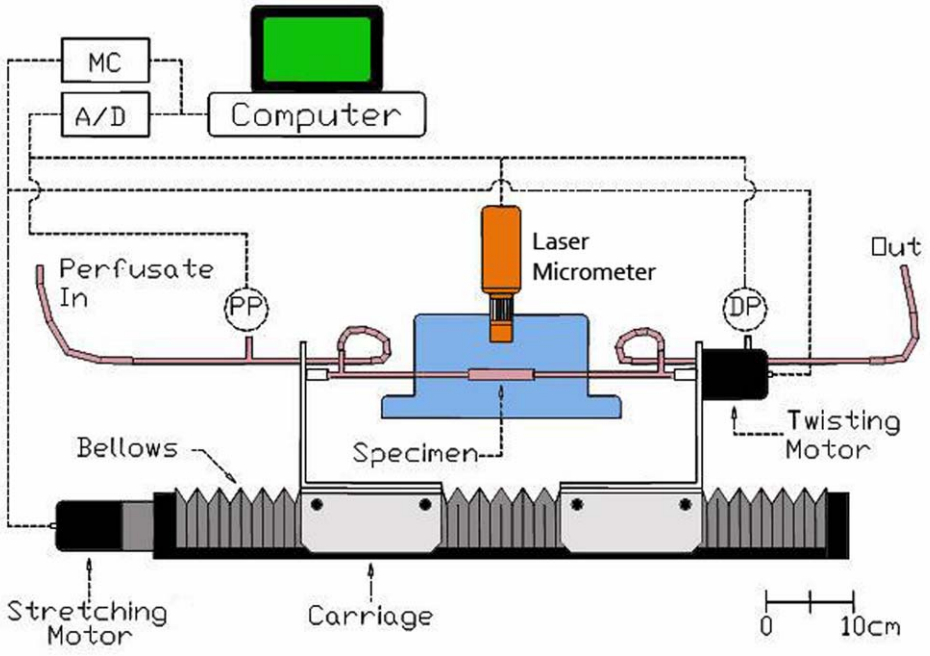

Figure 2.3 Schematic of the first generation device for the simulation of heart-induced coronary artery deformation described by Vorp et al. [156]. Cyclic axial stretch and twist are generated by a pair of computer controlled microstepping motors. The Stretching Motor rotates a precision-threaded lead screw transmitting longitudinal motion to the two carriages. The Twisting Motor is fixed to a perfusion tee which rotates an amount specified by the motion control program. The same computer also records and digitizes the analog output from the Laser Micrometer, proximal (PP) and distal (DP) pressure transducers, and the ultrasonic flow probe (not shown). Image adapted from Vorp et al. [156].

Vorp et al.[138] modified this device in order to replicate the cyclic flexure experienced by the coronary arteries. This device utilized the Stretching Motor and lead screw system in as shown Figure 2.3. However, to generate cyclic flexure, only the distal cannula is attached to the carriage driven by the lead screw and Stretching Motor, while the proximal cannula was held in a fixed position. Movement of the distal cannula toward the proximal cannula causes the vessel segment to flex as shown in Figure 2.4. Back-and-forth motion thus causes cyclic flexure. This

device generated curvatures similar to that seen in the coronary arteries which led to differential expression MMP-1 and E-Selectin when compared to non-flexed vascular segments [138].

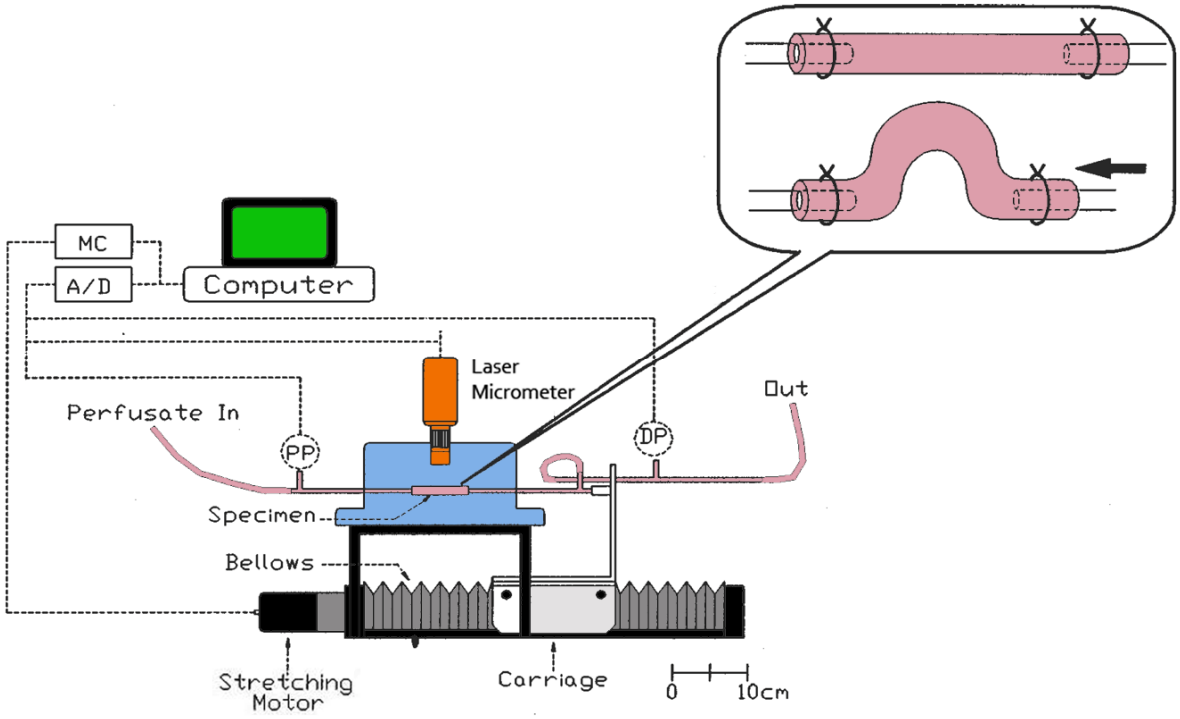

Figure 2.4 Schematic of the device in Figure 2.3 modified to generate cyclic flexure as described by Vorp et al. [138]. Cyclic flexure action is shown in the balloon. Image adapted fromVorp et al. [138].

2.1.3 System Design Limitations

While the EVPS, with heart-induced mechanical stimulation capabilities described above, has demonstrated utility for investigating vascular mechanopathobiology, there are a couple of limitations which have the potential to confound any interpretation of the data generated therein. The first limitation is the presence of multiple, simultaneous, cyclic waveforms being used to

stimulate the vascular segments of interest. For instance, a vascular segment may be subjected to both cyclic pressure and cyclic axial stretch. Given these multiple waveforms, it is important to have the ability to measure and control the phase angle between the waveforms. Moreover, the phase angle should be maintained such that the global mechanical stimulus continues to mimic the physiologic biomechanical milieu.

The second limitation is the method used to generate cyclic changes in curvature. The device shown in Figure 2.4 generated curvature changes by moving the distal end of the vascular segment toward the proximal end until the segment "buckled". While the curvatures values were physiologic in magnitude, this motion did not accurately simulate coronary flexure where the myocardium actually provides a distributed flexure load to an artery that is held in longitudinal tension. Accurate simulation of coronary flexure should provide a true bending deformation via a distributed displacement or load rather than by "buckling".

2.2 TECHNICAL IMPROVEMENTS TO EVPS

To address the limitations highlighted above, two separate technical improvements were made to the EVPS described in Section 2.1. The first was an updated motion control system to allow for the accurate control of the phase angle between the pressure waveform and the cyclic deformation (i.e., stretch, flexure, or twist) waveform. The second was the addition of a flat, flexible strip of inert polymer to provide a distributed flexure load to the vascular segment. The design and validation of these technical improvements are described here.

2.2.1 Maintenance of Physiologic Phase Relationship Between Cyclic Deformation and Pressure Waveforms

Biplane cineangiography of human coronary arteries with simultaneous acquisition of arterial blood pressure has demonstrated that maximum axial stretch occurs during cardiac diastole, and maximum twist and flexure occur during systole [101, 102, 217, 218]. Therefore, the cyclic axial stretch waveform should be imparted 180˚ out of phase with the pressure waveform while cyclic twist and flexure waveforms should be imparted in phase with the pressure waveform. To achieve this design objective, the original motion control system was modified and validated as described below so that the cyclic motion (i.e., stretch, flexure, or twist) waveform was triggered off of the acquired pressure signal.

2.2.1.1 Controller Design

Motion control for the EVPS with cyclic deformation capabilities is provided by a custom designed LabView 7.1 (National Instruments Corporation, Austin, TX) program which interfaces with a Compumotor (Parker, Rohnert Park, CA) multiaxis motion controller (Model 6K4) (Appendix B). The motion controller drives the Stretching Motor and the Twisting Motor shown in Figure 2.3. With this system, a given motion can be described by a displacement, acceleration, and a maximum velocity. The motor accelerates at the given acceleration until the maximum velocity is reached and maintains that velocity until such time that a deceleration equal in magnitude to the input acceleration brings the velocity back to zero when the prescribed displacement is reached. This creates a smooth cyclic motion as shown in Figure 2.5.

The displacement component (d_{max}) of the motion is determined by the particular deformation (i.e., stretch, flexure, or twist) and the magnitude. In the case of cyclic stretch, the

displacement was determined by the desired percent stretch and the vascular segment length. For twist, the desired twist angle was specified as the displacement. For flexure, the displacement required to generate a desired curvature was determined by an empiric model (see Section 2.2.2.1). However, the acceleration (a) and maximum velocity (v_{max}) components were required to specify the time-varying motion profile. These values were determined as functions of d_{max} using standard equations of motion. Since the acceleration is constant (see description of motion control system above), the displacement (d) at a given point in time (t) for a constant acceleration can be written as:

$$d = \frac{1}{2}at^2 + v_0 t + d_0 \tag{2.1}$$

where v_0 and d_0 are the initial velocity and displacement, respectively. Assuming that v_0 and d_0 are both zero at t=0 (beginning of a motion cycle) (2.1) reduces to:

$$d = \frac{1}{2}at^2 \tag{2.2}$$

Given that the frequency of the cyclic motion should be 1 Hz (the frequency of the pressure waveform generated by the centrifugal pumps), then the time (t) required to achieve d_{max} should be 0.5 seconds. However, since each motion cycle is triggered off of the pressure waveform, it is important that each motion cycle be completed before the next trigger signal is received. Otherwise, the cycle would be skipped. Therefore, the time to reach d_{max} was chosen to be 0.475 seconds (Figure 2.5).

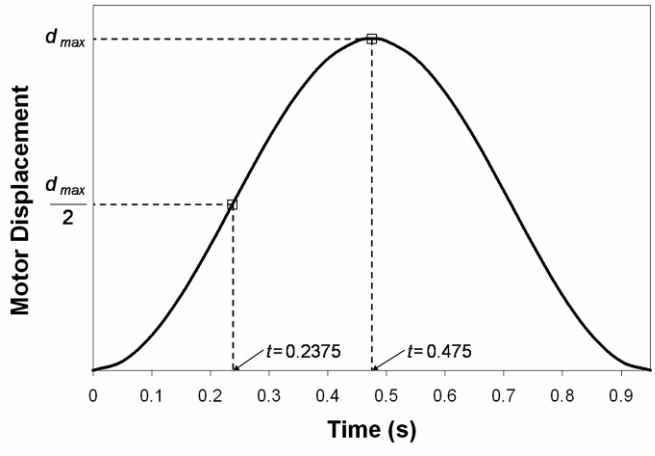

Figure 2.5 Smooth cyclic motion profile of the input motor displacement.

Assuming a symmetric motion profile, v_{max} is reached at one half the time required to reach d_{max} (in this case 0.2375 seconds). Since the acceleration and deceleration rates are equal the motion is symmetric and therefore the displacement at t=0.2375 seconds would be one half d_{max}. Substituting these values into (2.2) the acceleration term can written as a function of d_{max}:

$$d_{max} = a(0.2375\,s)^2 \tag{2.3}$$

$$a = \frac{d_{max}}{0.05640625\,s^2} \tag{2.4}$$

v_{max} can then be determined as the derivative of the displacement function with respect to time:

$$v_{max} = at \;@\; t=0.2375 \text{ seconds} \tag{2.5}$$

$$v_{max} = \frac{d_{max}}{0.2375\,s} \tag{2.6}$$

The functions in (2.4) and (2.6) in conjunction with the user specified d_{max} were used to generate the cyclic motion profile with respect to time (Figure 2.5).

2.2.1.2 Data Collection

The phase angle between the cyclic motion and pressure waveforms was controlled using a peak detection / motion triggering scheme. Since the perfusion pressure is continuously monitored (See Section 2.1.1) it can be used as a reference for triggering the motion control system using the LabView "Peak Detector PtByPt" virtual interface (VI) (Appendix B). This VI monitors continuous input data and returns a Boolean "true" when a peak (or valley) above a threshold amplitude is detected within a given width specified by the user (Figure 2.6). The width describes the number of time points in a region of interest. Since the acquired pressure signal from the EVPS (provided as input to this VI) is relatively smooth (i.e., has a high signal to noise ratio), the detection of a peak is relatively insensitive to the specified width [173]. Therefore, the value of width can serve as a delay. In other words, the VI cannot return a value for peak until the entire specified width or number of time points has been scanned. Varying the width on the Peak Detector VI varies the time between peak detection and triggering of a motion cycle. Thus, adjustment of the width can be used to tune the phase angle between the pressure and motion waveforms the desired physiologic value.

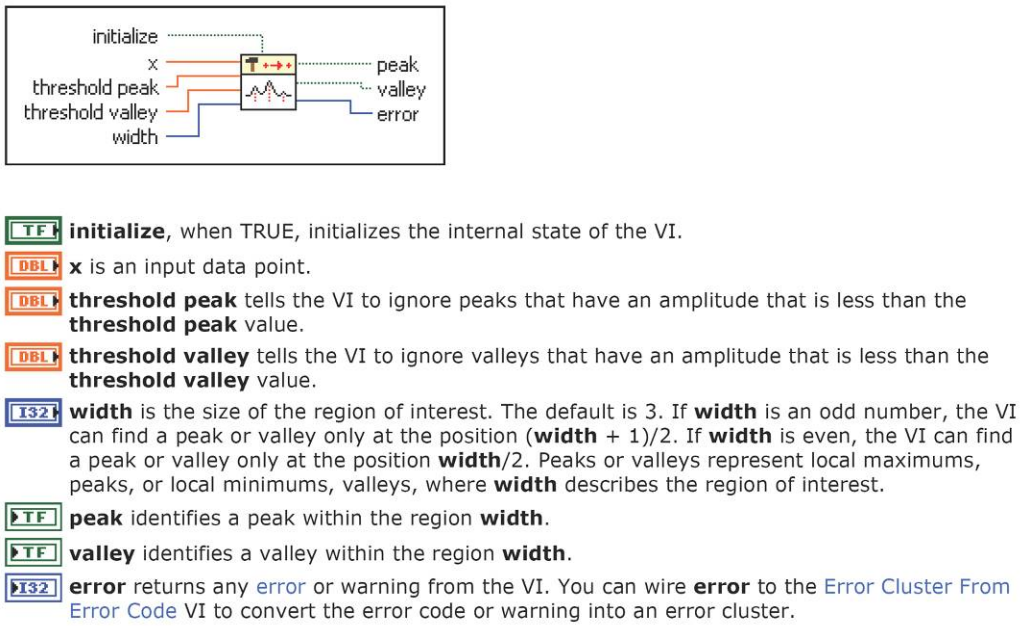

Figure 2.6 Description of the Peak Detector PtByPt VI from the LabView 7.1 Help files [173].

To determine the appropriate width for a zero (flexure and twist) and a 180˚ (stretch) phase angle, the pressure waveform and the cyclic motion waveform were simultaneously acquired at 30 Hz for various widths ranging from the minimum of 3 to 52 points. The average time distance between pressure and displacement peaks was determined for 5 consecutive loading cycles and converted to a phase angle. The phase angle was then plotted as a function width.

2.2.1.3 Results and Discussion

There was a linear relationship between width and phase angle spanning almost an entire cycle period (Figure 2.7). Based on the regression of the phase angle versus width data, it was determined that a width of 33 time points generated a zero degree phase angle, while a width of 5 time points maintained a 180˚ phase angle (Figure 2.8).

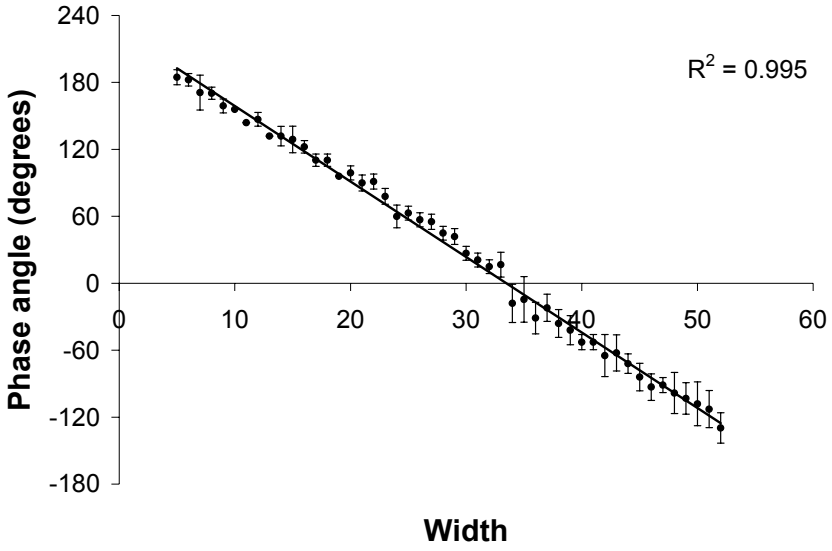

Figure 2.7 Mean phase angle from 5 consecutive loading cycles versus width and the regression line of best fit. Error bars represent standard deviation.

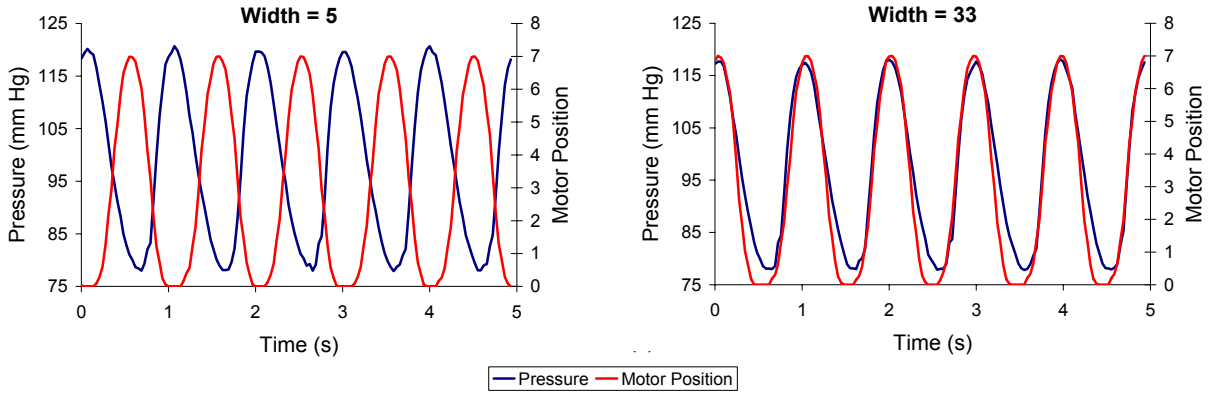

Figure 2.8 Plots of simultaneously acquired pressure and motor position waveforms for peak detector widths corresponding to 0˚ (Width=5) and 180˚ (Width =33) phase angles.

The use of the "Peak Detector PtByPt" VI with variable detection width provided an excellent means to control the phase angle between the pressure and motion waveforms. In addition to recreating the desired physiological phase angles of zero and 180˚ demonstrated in the coronary arteries, it is possible to generate any phase angle in between. This motion control system could be used to investigate the potential effects of altered phase relationship between simultaneous mechanical stimuli. In fact, arteries in other tissue beds have been shown to undergo extraneous dynamic motion similar to the coronaries [92, 93]. However, the frequency and phase relationship of those motions may be significantly different than those for the coronary arteries. This technical improvement to the EVPS provides a means to study not only coronary arterial dynamics but dynamic motion of other arterial segments.

2.2.2 Simulation of Physiologic Cyclic Flexure *Ex Vivo*

The objective of this technical improvement was to modify the original bending component of the EVPS to generate a more physiologically-realistic flexure load on *ex vivo* perfused arterial segments while maintaining a physiologic level of longitudinal tension. To accomplish this, the following design goals were developed for this modification: (1) The device should provide a range of curvatures similar to those measured *in vivo*. (2) Cyclic changes in curvature should occur at the same frequency as the pulsatile perfusion pressure. (3) The curvature waveform should have the appropriate phase relationship with the pressure waveform. (4) Curvature changes should have a minimal effect on the length of the perfused vascular segments in order to maintain longitudinal tension. (5) The integrity of the vascular tissue must be maintained. This section described how these goals were achieved.

2.2.2.1 Design of Cyclic Flexure Device

In order to generate a more realistic flexure load while maintaining physiologic longitudinal tension, the bending component of the EVPS was modified with the addition of a flat, flexible strip of inert polymer (*Durastar* polymer MN611, Eastman Chemical Company, Kingsport, TN) that was fixed to the cannulae holding the vascular segment (Figure 2.9).

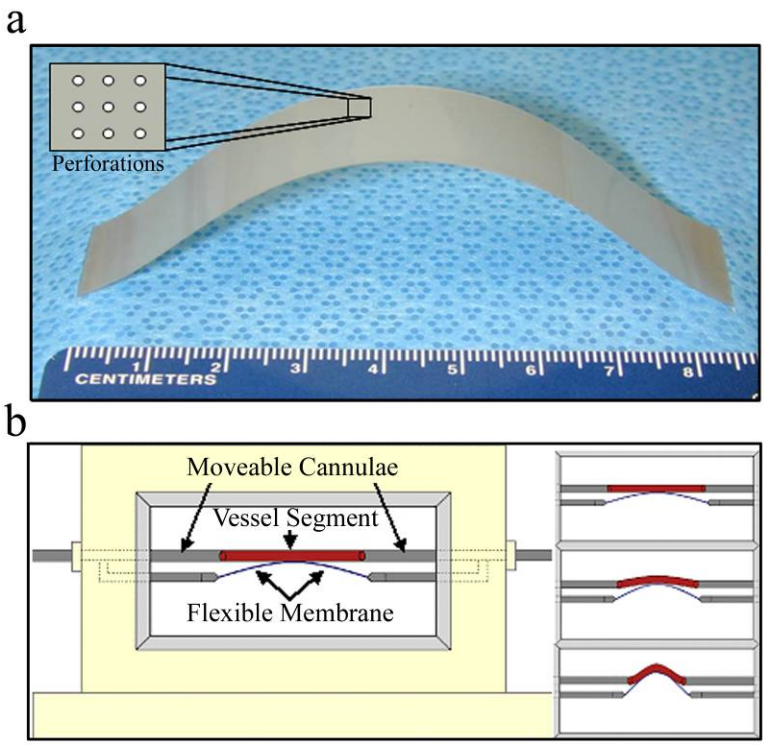

Figure 2.9 (a) Photograph of the polymer membrane. (b) Schematic side view of the tissue housing chamber showing the modified vessel cannulae with attached polymer membrane (left), and conceptual demonstration of the application of a distributed flexure load to a vascular segment (right frames). At rest the vessel is under tension and in gentle contact with the flexible polymer (top frame). As the perfusion tees move toward each other the polymer strip flexes into the vessel applying the distributed displacement. Shown are intermediate (middle frame) and maximal (bottom frame) levels of curvature.

To reduce injury to the vessel during prolonged cyclic flexure, the polymer strip was (1) perforated to allow nutrients to diffuse through it to the outer surface of the tissue, (2) had a low coefficient of friction to prevent contact wear of the tissue, (3) remained in contact with the vessel segment to prevent injury due to sudden impact, and (4) was chemically inert to prevent toxic reactions with the tissue or bathing solution.

In order to control the degree of curvature applied to vascular segments in the system, a mathematical relationship between the applied displacement of the cannulae and the resulting curvature was required. To determine that relationship, three canine femoral arterial segments of varying length (ranging from 7.3-8.6 cm in vivo length) were implanted into the modified EVPS and subjected to pulsatile pressure (120/80 mm Hg) and flow (130/70 ml/min). After a 30 minute equilibration period under these perfusion conditions, various degrees of static flexure were applied to the vascular segment by displacing the Stretch Motor (see Figure 2.3) a known distance. A CCD camera was used to image the vascular segments at the various levels of static motor displacement (Figure 2.10a). Scion Image 4.0.2 (Scion Corporation, Frederick, MD) was used to perform edge detection and map the surfaces of the greater and lesser curvatures of the flexed vascular segments to a series of x-y in-plane coordinate pairs (Figure 2.10b). The arc length was calculated as the sum of the Pythagorean distance between consecutive points for a given curve. To determine the maximum applied curvature, the points near the location of maximal flexure were interpolated with a second order polynomial (Figure 2.10c). That function was then used to calculate the curvature (k) using the following standard relationship [174].

$$k = \frac{\frac{d^2 y}{dx^2}}{\left[1 + \left(\frac{dy}{dx}\right)^2\right]^{3/2}} \tag{2.7}$$

Assuming a linear relationship between radius and circumference, the centerline arc length and curvature were calculated by an arithmetic average of the respective values for the greater and lesser curvatures. This assumption requires that there is no change in inner diameter during the curvature cycle. The result was a set of data points relating curvature to motor displacement and vessel segment length. This relationship was then used to determine d_{max} in the custom-designed motion control program described in Section 2.2.1.1.

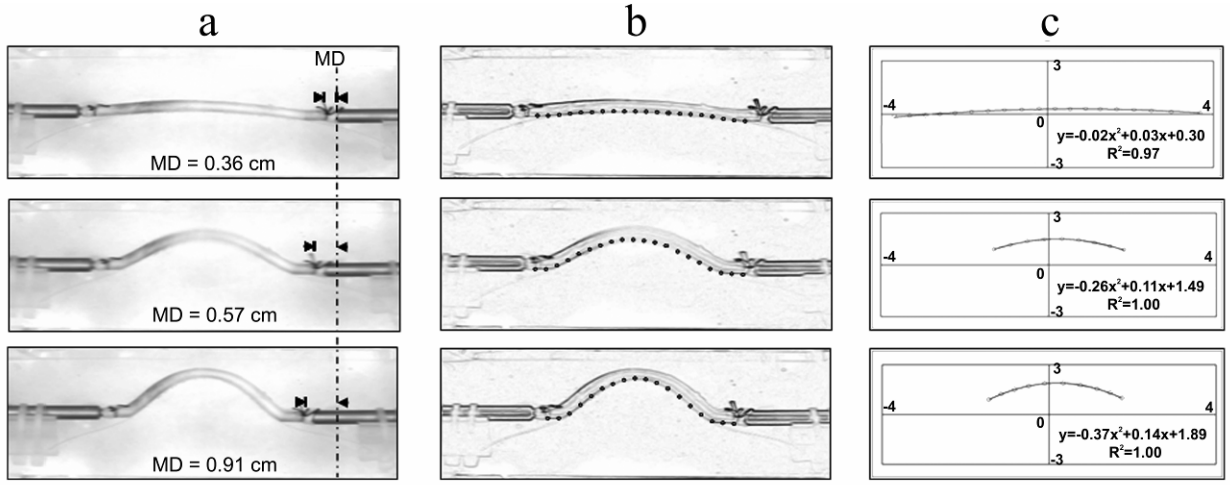

Figure 2.10 (a) Representative CCD camera images of curvatures generated on perfused vascular segments by different motor displacements. (b) Images from A after edge detection and discretization of the lesser curvature. (c) Interpolation of maximal curvature region by second order polynomial interpolation of discretized x-y coordinates (in cm) from images in b. The x-axis is oriented horizontally and the y-axis vertically. Note that only the lesser cruvature is shown for image sets b and c. The same procedure was used for the greater curvature.

Validation of the motion control system was performed on three additional canine femoral arterial segments. These specimens were implanted into the EVPS and equilibrated with pulsatile pressure (120/80 mm Hg) and flow (130/70 ml/min) for ten minutes. Each arterial segment was then subjected to thirty cycles each of three different user-defined maximum curvatures (0.5-1.1 cm^{-1}) with five minutes of no cyclic motion in between each set of thirty cycles. Images of the arterial segments undergoing in-plane flexure were captured at thirty frames per second with a CCD camera. The images from the final three cycles of a given curvature regimen were analyzed for calculating the time-varying curvature as described above. To ensure that the arterial segment was maintained in tension during the curvature cycle, the instantaneous vessel arc length was measured at each time point as described above. Since each arterial segment was a different length and was subjected to three different input curvatures, this experiment generated nine distinct validation points.

To assess the effects of flexure on tissue integrity, bilateral porcine femoral arterial segments were surgically harvested from 30-40 kg pigs (N=3) and implanted into two independent EVPSs. One segment (control) was exposed to normal hemodynamics (120/80 mm Hg; 130/70 ml/min, at 1 Hz) without flexure while the other (flex) was exposed to the same hemodynamic conditions plus cyclic flexure motion (0-0.7 cm^{-1} at 1 Hz) for twelve hours. At the conclusion of the experiment, the flex arterial segments were processed as follows: (1) A longitudinal cut was made separating the greater curvature and the lesser curvature. (2) Each "half-vessel" was then cut transversely into proximal, middle, and distal portions (Figure 2.11).

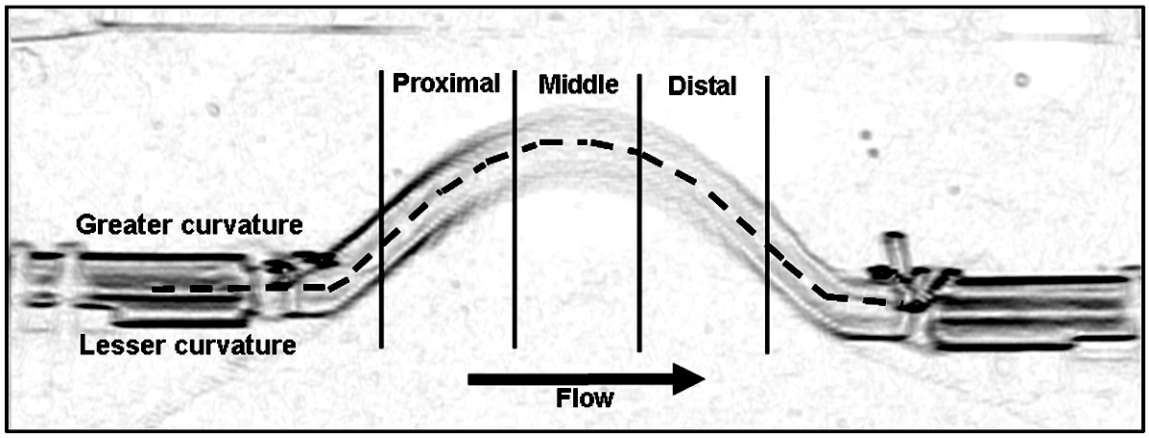

Figure 2.11 Schematic of the post-perfusion tissue processing method.

2.2.2.2 Device Validation Results

Plots of motor displacement versus curvature for various arterial segment lengths demonstrated a linear relationship (Figure 2.12). Furthermore, the slope of that relationship was linearly dependent on the segment length. Based on this data we were able to determine a function relating the motor displacement (MD) required to provide the desired maximum curvature (k) to a vascular segment of length (L):

$$MD = \frac{k}{2.59 - 0.21L} \tag{2.8}$$

The constants 2.59 and 0.21 in the denominator had units cm^{-2} and cm^{-3}, respectively.

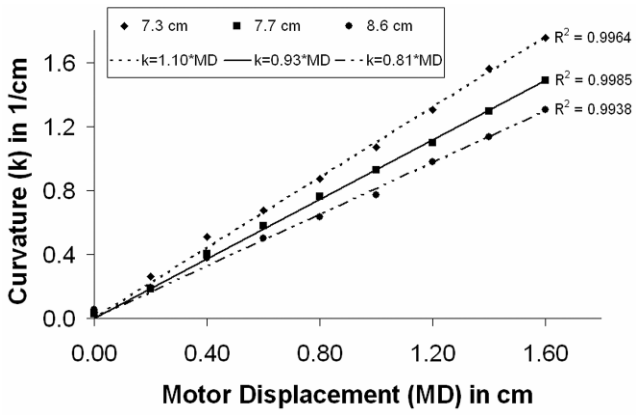

Figure 2.12 Plot of curvature versus motor displacement with least squares linear regression lines for three different vessel segment lengths.

For each of the nine mechanical validation points, the actual measured maximum curvature was plotted versus the specified user-input maximum curvature (Figure 2.13a). The error between the measured and desired maximum curvature for all nine points was less than 9%. Within a given cycle the measured curvature closely followed the motion control set point over time (Figure 2.13b). The maximum change in length during all nine-input curvatures was 2.3% (Figure 2.13b). Since the average *in vivo* stretch ratio for these vessels was measured to be 40%, the longitudinal tension was indeed maintained over the curvature cycle. Simultaneous computer acquisition of pressure and motor displacement, and subsequent calculation of curvature via (2.7) demonstrated that the pressure and curvature waveforms were almost coincident, with a zero phase angle (Figure 2.13c).

Histological examination demonstrated that tissue integrity was maintained, with no morphological signs of cell death due to necrosis, in either the flex or control vessel segment specimens after twelve hours of perfusion (Figure 2.14). In addition, there were no

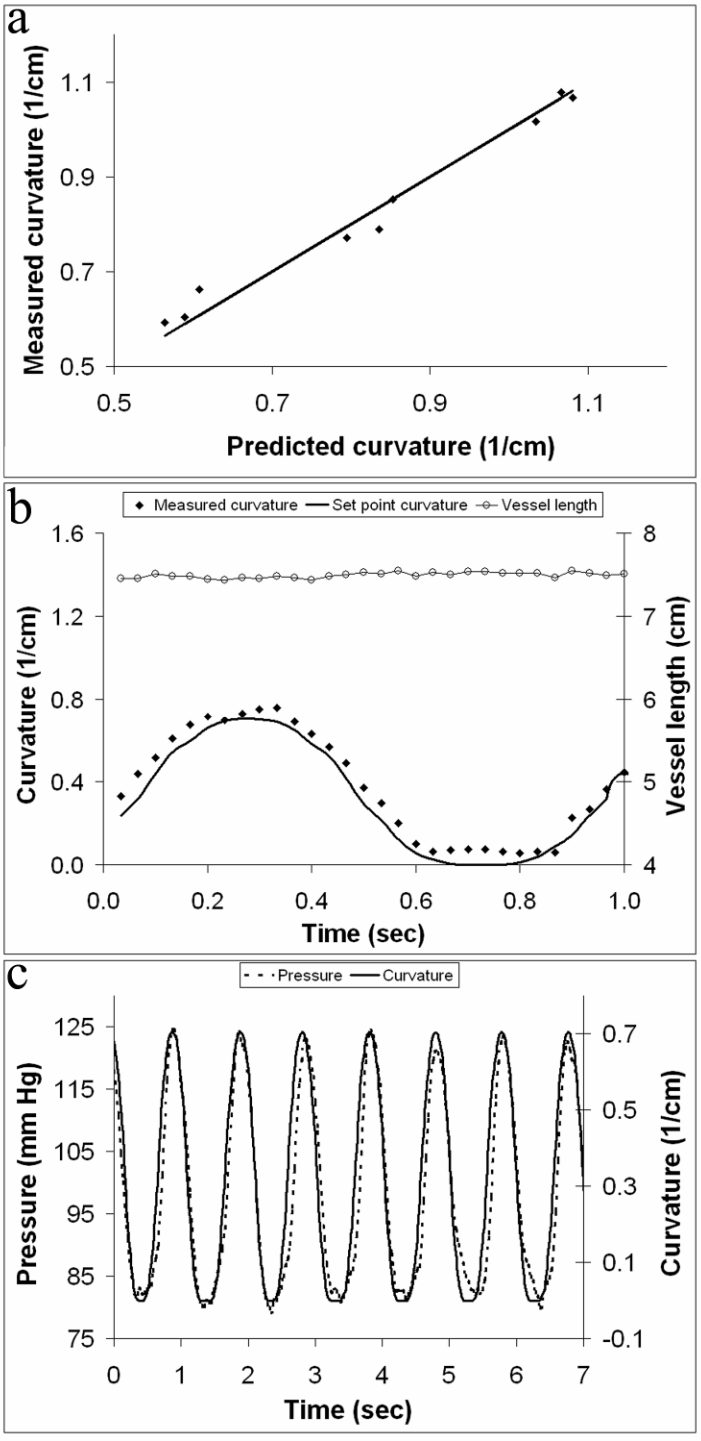

Figure 2.13 (a) Correlation plot comparing the measured curvature to the curvature predicted by the motion control model of the nine validation points. The line represents a plot of unity representing perfect agreement between measured and predicted curvatures. (b) Measured time-varying curvature and vessel length for a representative perfused arterial segment. The set point curvature profile refers to the time-varying curvature predicted by the input motor displacement motion profile. (c) Comparison of the pressure and curvature waveforms demonstrating a zero phase angle between them.

control arterial segments. The surface of vascular tissue from the lesser curvature of the flex arterial segment did not appear to have significant damage due to contact with the membrane (Figure 2.14d-f).

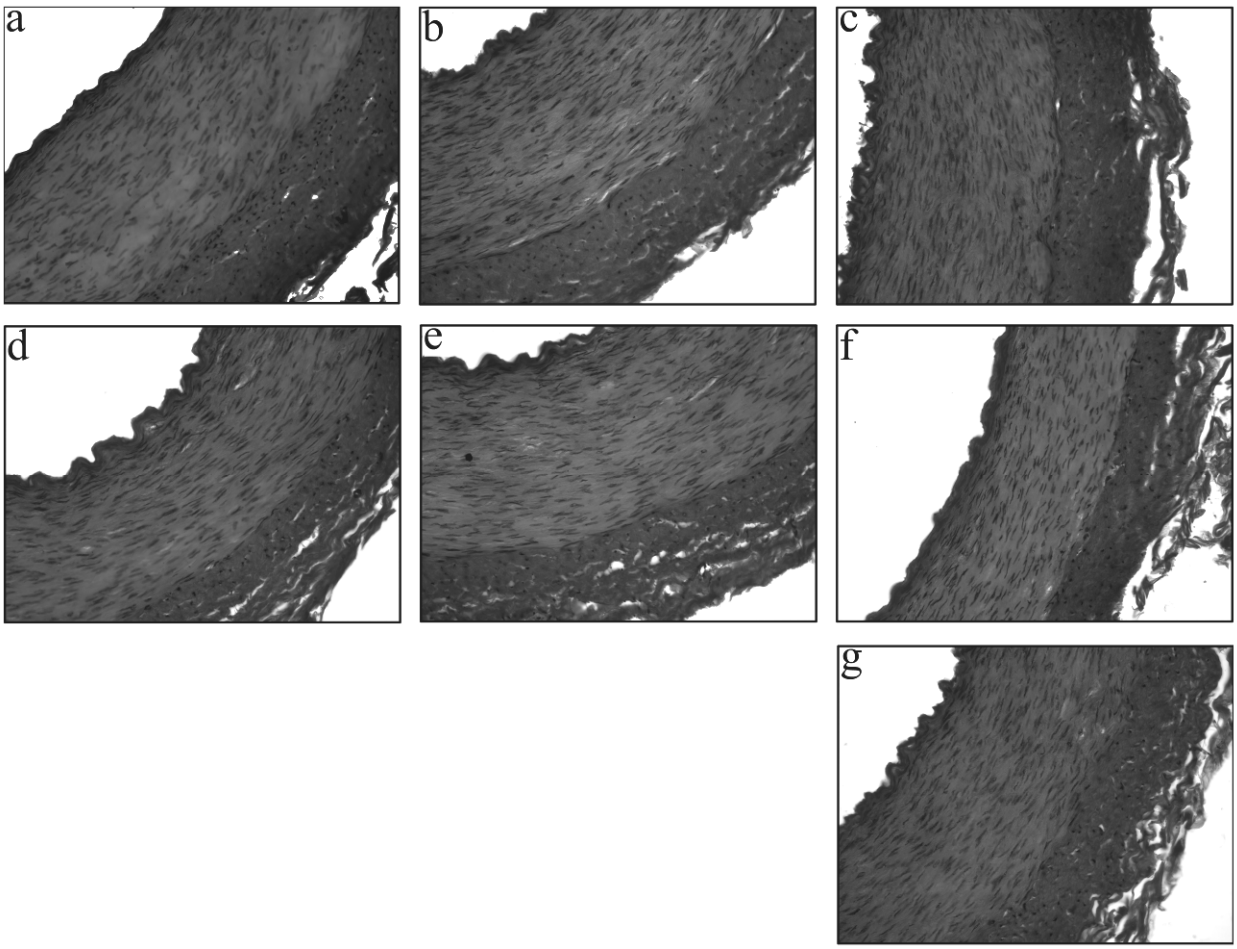

Figure 2.14 Representative 200x photomicrographs of H&E stained sections. (a-f) Specimens from a flexed arterial segment: (a) Poximal, greater curvature; (b) Middle, greater curvature; (c) Distal, greater curvature; (d) Proximal, lesser curvature; (e) Middle, lesser curvature; (f) Distal lesser curvature. (g) Control arterial segment perfused without cyclic flexure.

2.2.2.3 Discussion and Conclusions

The addition of a polymer guiding membrane represents an important improvement from the previous attempt to simulate coronary arterial flexure dynamics *ex vivo*. While the original design provided physiologic changes in curvature, this motion was obtained in a non-physiologic manner by buckling the vessel segment rather than truly flexing it. Flexure requires a distributed displacement load over the length of the segment as seen in the coronary arteries which are tethered to the dynamic, curved surface of the myocardium. The polymer membrane provided that distributed displacement load and provided cyclic changes in curvature in a more physiologic manner.

The success of this modification was determined by its ability to meet the five initially prescribed design constraints listed in Section 2.2.2.1. First, the device was able to generate curvatures between 0.0 and 1.8 cm^{-1}, a range that has been reported for coronary arteries *in vivo* by biplane cineangiographic reconstruction [90-93]. Second, the EVPS provided pulsatile pressure and flow at a frequency of 1 Hz. Since the curvature motion cycle was triggered off of the pressure waveform, the frequency of the curvature waveform was also 1 Hz. Although slightly lower than the average pulse rate in humans, this is a commonly accepted frequency for simulation of the vascular biomechanical milieu [175]. Third, the curvature waveform was approximately in phase with the pressure waveform. Simultaneous measurement of dynamic coronary arterial geometry and arterial pressure demonstrates that maximum curvature occurs at systole or at maximum pressure [176], which means that *in vivo* these waveforms are indeed in phase. Fourth, the coronary arteries, like other arteries, are in tension (stretch ratio = 40% for the arterial segments in this study) *in vivo*, even during dynamic changes in curvature. Because the former design of this system utilized a buckling motion it could not maintain longitudinal

tension. However, the new design was able to maintain the *in vivo* length of perfused arterial segments with a maximum of only 2.3% change in length over a flexure cycle. Finally, twelve hours of contact with the polymer membrane during cyclic flexure did not result in any gross changes in tissue structure.

Although this work represents a major improvement on the former dynamic EVPS, it is important to note a few limitations. First, the curvature profile in time was a simple sinusoidal waveform. Work by several researchers has demonstrated that the *in vivo* curvature waveform contains higher frequency harmonics [85-88]. This simplified model represents a first approximation and is a significant improvement to the only experimental system reported to date that recreates vascular flexure on living, intact vascular segments. Second, the preliminary biological validation experiments described here utilized normal cell culture media as the perfusate. This media has a density and viscosity close to water and therefore is not a good representation of blood. Future experiments concerned with the shear stress distribution within the vessel segment could utilize a variety of supplements (e.g., dextran) to better simulate the viscous properties of blood.

The addition of an inert, polymer membrane was used to better simulate coronary-like flexure motion on arterial segments perfused *ex vivo* in the well-validated dynamic EVPS. This modification was able to mimic coronary flexure curvatures in magnitude, frequency, and phase relationship with the pressure waveform, while maintaining tissue integrity. This new device will be used in the *ex vivo* perfusion experiments described below.

3.0 PERFUSION EXPERIMENTS

Specific Aim 1 was accomplished by performing three sets of *ex vivo* vascular perfusion experiments. Specifically, one set of experiments (N=5 animals per set) was performed for each heart-induced deformation of cyclic axial stretch, cyclic flexure, and cyclic twist to test the effects on early atherogenic endpoints (i.e., permeability, apoptosis, and proliferation). Each experiment was "paired" to account for animal-to-animal variability, and generally, proceeded as follows. Bilateral porcine femoral arteries were surgically harvested from juvenile pigs (see Section 3.1.1) and tied into separate, independent EVPSs (see Section 2.1). One arterial segment was perfused using normal porcine arterial hemodynamic conditions (see Section 3.1.2), while the other was perfused under the same conditions, plus either cyclic axial stretching, twisting, or flexure as described above in Sections 2.1.2 and 2.2.2.1. Vascular perfusion experiments were carried out for 12 hours since the majority of the endpoints under investigation have been successfully detected within a few hours of this time point (see references in Table 1.2). At the conclusion of each experiment, the tissue was processed (see Section 3.1.3) for geometric reconstruction (required for Specific Aims 2 and 3) and biological assays for permeability, apoptosis, and proliferation (see Section 3.1.4). Experiment sets, individual experiments, and specimens within an experiment will be referred to according to the nomenclature shown in Figure 3.1

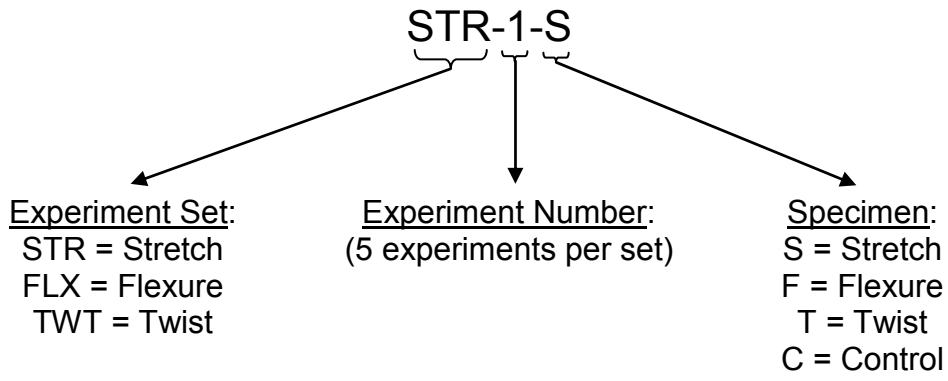

Figure 3.1 A given specimen in this studied was assigned a three part name for reference purposes. The first part is a three letter designation indicating the type of experiment it came from. The second part is the experiment number. Recall 5 experiments were performed for each set. Finally, within a given set there were two specimens, a deformed specimen that was subjected to either cyclic axial stretch, cyclic flexure, or cyclic twist, and a paired control. The third part of the name determines which specimen of the pair.

This chapter will describe in detail the methods used and the results obtained from those *ex vivo* experiments. It will conclude with a discussion of the implication of the results and demonstrate the need for the subsequent computational analyses described for Specific Aims 2 and 3.

3.1 METHODS

3.1.1 Tissue Source and Harvest

The porcine species was chosen because it has been well characterized as a model for studying atherosclerosis [177]. For example, pigs fed a high cholesterol diet demonstrate dramatically elevated LDL cholesterol after 6 weeks [178] and fully developed atheromatous plaques, which resemble those of human atherosclerosis (determined histologically), after 16 weeks [179]. It

should be noted that these effects are seen in the absence of any other acute arterial injury (e.g., wire injury) [179]. Pigs with lipoprotein associated mutations develop marked hypercholersterolemia and atherosclerosis even with a low-fat, cholesterol-free diet [180, 181]. Lesions in these animals resemble those observed in humans, progressing from fatty streaks at 7 months age to advanced lesions with necrotic lipid cores by 2 years [192, 193]. Affected arteries include the coronary, iliac, and femoral arteries [180].

Although it seems counter-intuitive, there are three important reasons why coronary arteries were not used in these *ex vivo* experiments: (1) A major strength of this study was its paired experimental design, which helped reduce the effects of animal-to-animal variability and provided more statistical power. Since it is not possible to get paired sets of coronary arteries that are similar (for example, the right and left coronary arteries are mechanically distinct [88]), use of these vessels would not have preserved the paired design. (2) One of the hypotheses under investigation was that the prevalence of atherosclerotic lesions in the coronary arteries is associated with their dynamic deformation environment. In order to test the effects of cyclic motions, it was important to use an artery that had not previously "experienced" those chronic mechanical deformations. In other words, a “mechanically naïve” artery was required, which precludes the use of coronary arteries that have existed in a complex and unknown dynamic environment. (3) In an effort to maximize the viability of the tissue in the EVPS, arterial samples were surgically harvested from live but anaesthetized animals. Harvesting the coronary arteries in this fashion would have been exceedingly difficult, requiring cardiopulmonary bypass for the animal as well as a much longer surgical time and expense.

Given this rationale, a thorough investigation to find the most appropriate surrogate vessel model (i.e., one that fulfills the three above criteria and has sufficient similarities to the

coronary arteries) was performed. This investigation led to the femoral artery, a muscular artery found in the lower extremity with similar morphology and tissue composition to that of the coronary [211, 225]. This finding was validated by histological examination of porcine coronary and femoral arteries from the same animal (Figure 3.2)

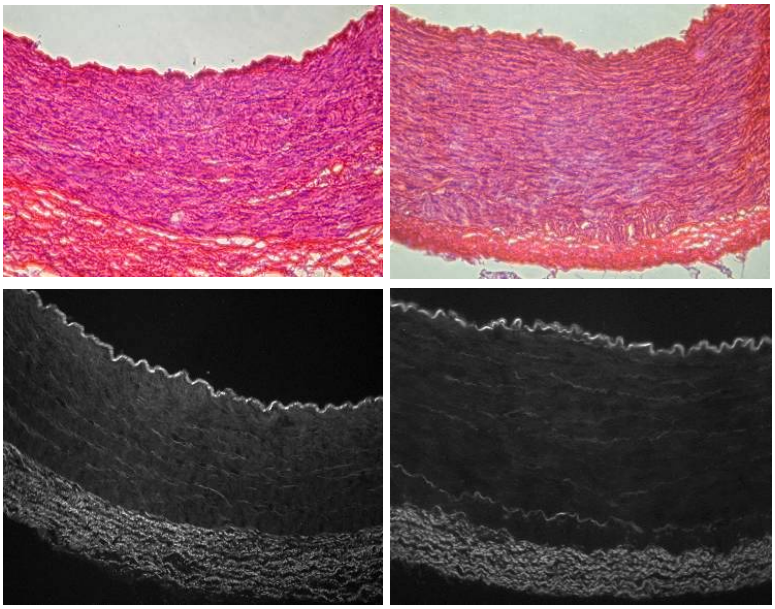

Figure 3.2 Hematoxylin and eosin staining (top) and elastin auto-fluorescence (bottom) of a coronary (left) and femoral (right) artery from the same animal.

Furthermore, it has been demonstrated that the susceptibility of the femoral artery to atherogenesis is similar to that of the coronary independent of risk factors [182]. It was recently demonstrated that the human superficial femoral artery experiences significant changes in length and curvature due to movement at the hip and knee joint [183]. Therefore, we felt that the femoral artery was the most suitable surrogate model of the coronary arteries for the *ex vivo* perfusion studies of Specific Aim 2.

For surgical harvest of porcine femoral arteries, pigs were premedicated with atropin sulfate (0.5 mg) and cefazolin sodium (500mg) and then anesthetized with 10 mg/kg ketamine via IM injection and 1-3% isofluorane via inhalation. They were then intubated and maintained at a surgical plane of anesthesia with isoflurane (1-3% in oxygen) and positive pressure ventilation. Universal antiseptic technique and sterile draping was used prior to start. Groin incisions were made bilaterally, and dissection was done in layers up to the vascular fascia. Common and superficial femoral arteries were identified and dissected proximal to the femoral ring and distal to the branching of the deep femoral artery. All branches were identified and carefully ligated with silk suture to avoid leakage during the *ex vivo* perfusion experiment. Once the desired length (5-7 cm) was exposed, the arterial specimens were clamped at both ends using custom-designed vascular clamps [144, 170] that maintain *in vivo* dimensions. The vessels were ligated on either side of the clamp and then removed. Upon completion of the femoral arterial excision, animals were euthanized according to an approved method set forth by the AVMA panel of euthanasia.

3.1.2 *Ex Vivo* Perfusion Conditions

Pairs of freshly harvested femoral arterial specimens were transported from the surgical facility to the laboratory in a sterile transport box containing lactated ringers solution supplemented with heparin (500 units/liter), papverine (60 mg/liter), and penicillin-streptomycin (10ml/liter) and implanted into separate EVPSs pre-equilibrated (overnight) with the perfusion conditions listed in Table 3.1. Tissue culture Media-199 supplemented with 1% porcine serum, 2.5 g/L sodium bicarbonate, and 10ml/L penicillin-streptomycin was used for the perfusate,

while Dulbecco's Modified Eagle's Media with the same supplements was used for the adventitial bath medium.

Implantation involved cannulating the free ends of the arterial specimens to the perfusion tees mounted within the tissue housing chamber (recall Figure 2.2) and securing with 2-0 silk suture. The time from harvest to implant was always less than one hour. Both segments were allowed to equilibrate at the conditions prescribed in Table 3.1 for 30 minutes prior to the start of the experiment. After the equilibration period, cyclic motion was applied at a frequency of 1 Hz to one of the vessel specimens (chosen at random) according to Table 3.2. Perfusion parameters were maintained by monitoring and recording all parameters every 90 minutes with manual adjustments to the pumps, resistors, water baths, and gas flow rates as necessary.

Table 3.1 *Ex vivo* perfusion conditions

	Set point	**Tolerance**
Systolic Pressure	120 mm Hg	± 5 mm Hg
Diastolic Pressure	80 mm Hg	± 5 mm Hg
Flow Rate	100 ml/min	± 5 ml/min
Temperature	37˚C	± 1˚C
pH	7.40	± 0.05
pO_2	145 mm Hg	± 5 mm Hg
pCO_2	40 mm Hg	± 5 mm Hg
HCO_3	24	± 3

Table 3.2 Coronary-like deformations

Cyclic Deformation	Magnitude
Axial Stretch	0 to 7%
Flexure	0 to 0.7cm^{-1}
Twist	0 to 20˚

3.1.3 Post-Perfusion Sample Processing

After 12 hours of *ex vivo* perfusion, arterial specimens were decannulated by cutting the 2-0 suture and placed on an RNase free cutting board. The unloaded length (L) was measured prior to cutting and discarding any tissue that had been in contact with the steel cannulae. For the axisymmetric deformation cases of axial stretch and twist, the specimen was divided as follows (Figure 3.3): (1) 5mm rings were cut from the proximal and distal ends and used to obtain dimensional measurements for the geometric reconstructions and subsequent computational analysis (see Section 4.1); (2) The remainder was divided into 3-5 equally sized segments, depending on the length; (3) Each of the segments generated in step (2) was cut into two unequal sub-segments. The proximal 20% (sub-segment 1) was earmarked for histological analysis while the remaining 80% (sub-segment 2) was dedicated for total RNA and protein isolation. All segments from step (3) were placed into individual RNase free 1.5ml microfuge tubes and snap frozen in liquid nitrogen and stored at -80˚C.

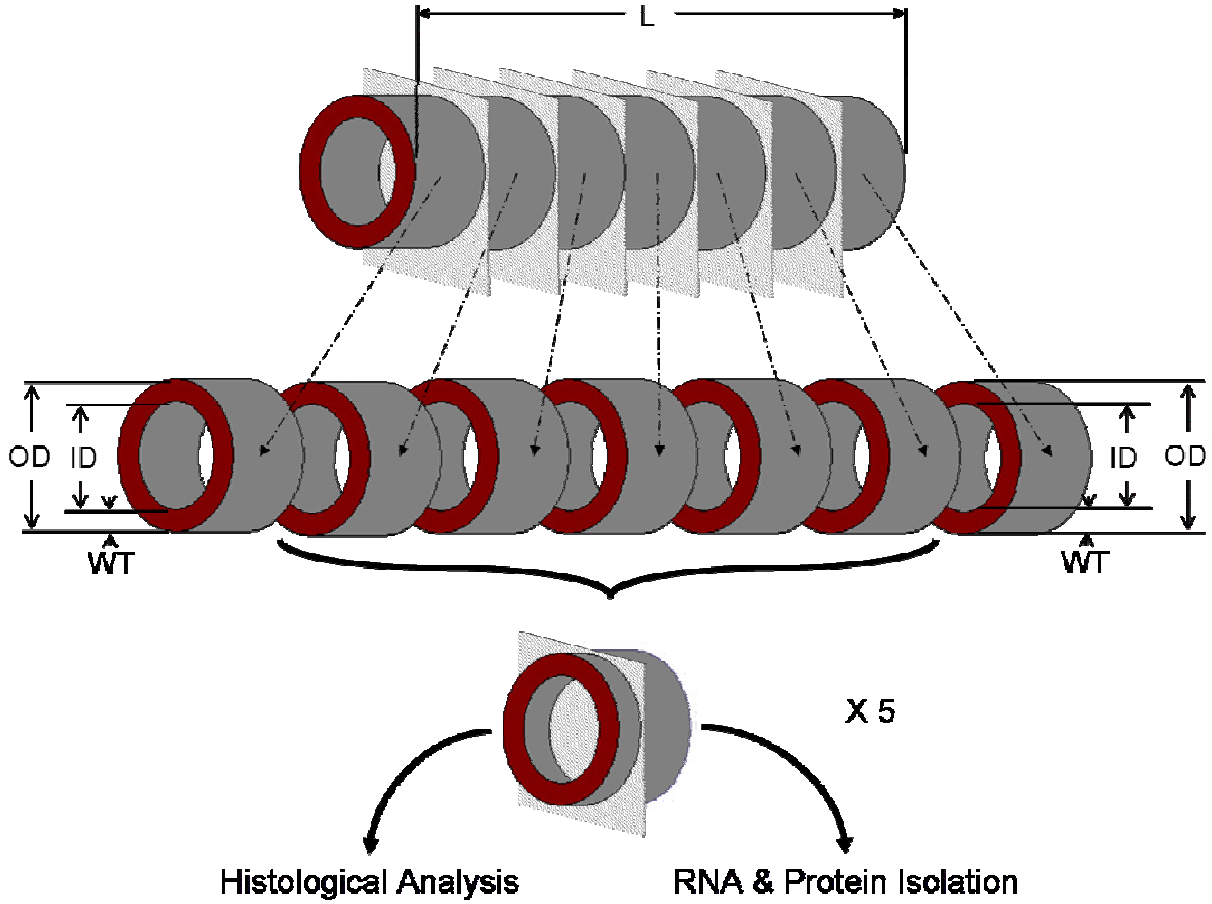

Figure 3.3 Axisymmetic tissue processing procedure. Vessel specimens were cut into 5 - 7 segments as shown. The end segments were used to determine the outer (OD) and inner diameter (ID) and wall thickness (WT) for geometric reconstruction and subsequent finite element (see Chapter 4) and computational fluid dynamics simulations (see Chapter 5). Each of the remaining segments were further subdivided into a 20% sub-segment used for histological analysis and an 80% sub-segment from which total RNA and Protein could be isolated.

For the asymmetric flexure deformation case, this tissue was divided as described in section 2.2.2.1 (recall Figure 2.11 and see Figure 3.4). Each segment (Proximal, Middle, and Distal each from the Greater and Lesser Curvature) was further subdivided, frozen, and stored according to step (3) described above for the axisymmetric cases.

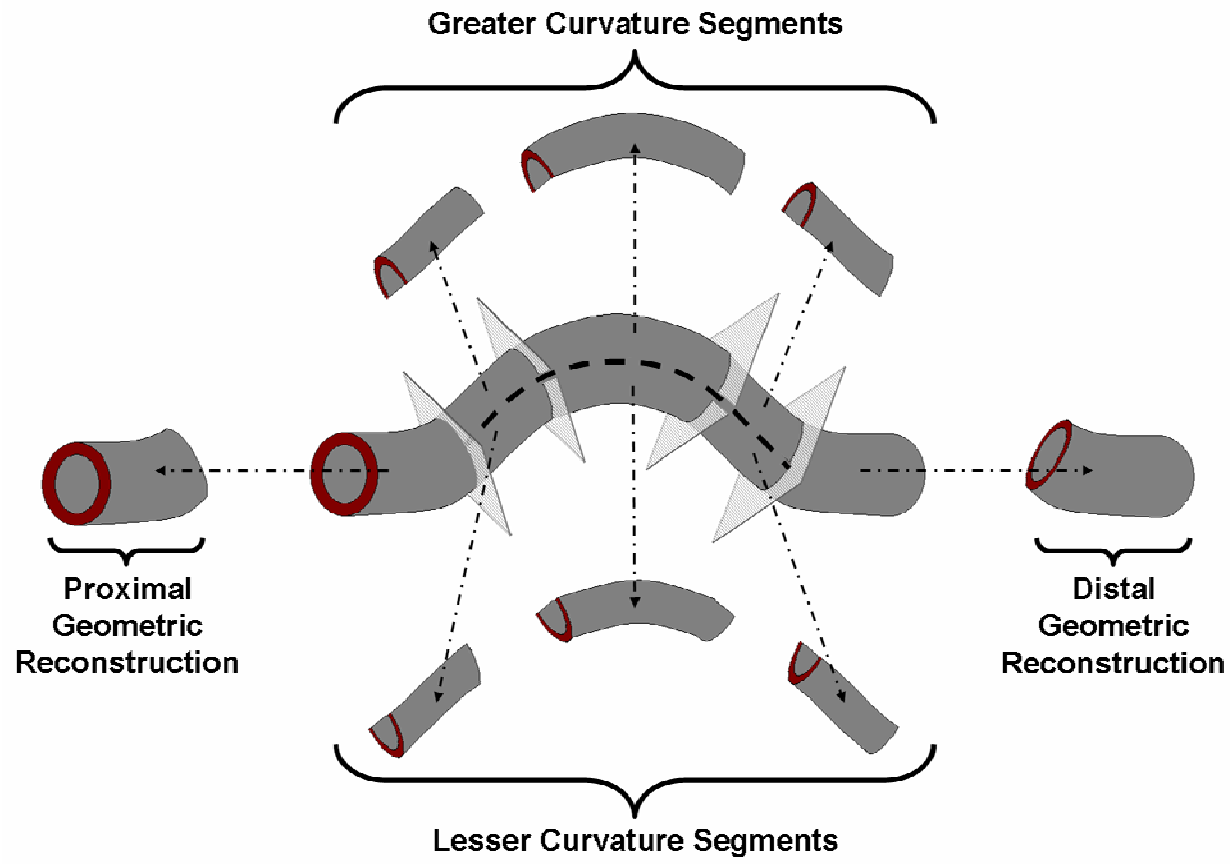

Figure 3.4 Asymmetric tissue processing procedure. Vessel specimens were cut into 8 segments as shown. First, the proximal and distal ends were cut and used for geometric reconstruction measurements (as shown in Figure 3.3) and subsequent finite element (see Section 4.0) and computational fluid dynamics simulations (see Section 5.0). Second, a longitudinal cut was made separating the greater curvature and the lesser curvature. (2) Each "half-vessel" was then cut transversely into proximal, middle, and distal segments. Each of these segments were further subdivided into a 20% sub-segment used for histological analysis and an 80% sub-segment from which total RNA and Protein could be isolated as show in Figure 3.3.

3.1.4 Biological Analyses

The biological endpoints proposed for Specific Aim 1 can be characterized as either histological or molecular-based with repect to the type of assay required. The histological endpoints include permeability, apoptosis, and proliferation. The protein and gene expression endpoints required isolation of protein and RNA and are classified as molecular. As stated in Section 1.6, the molecular endpoints considered were experimentally difficult to obtain. Further description of the methods, experimental difficulties, preliminary results, and recommendations for future investigation with regards to the molecular endpoints can be found in Appendix A.

The samples earmarked for histological analysis (Figure 3.3) were taken from the freezer and immediately embedded in Tissue Freezing Medium™ (Triangle Biomedical Sciences, Durham, NC) and frozen at -65˚C. Five-micron cross-sections were cut using a cryotome and placed on positively charged, glass microscope slides. Slides were stored at -80˚C until they could be processed for assays of permeability, apoptosis, or proliferation.

3.1.4.1 Permeability

During the last hour of each 12-hour perfusion experiment, the perfusate media was supplemented with a physiologic concentration of porcine serum albumin mixed with a 1:1 molar concentration of Evan's blue dye (EBD). Five-micron cross-sections (see Section 3.1.4) were dried at 37˚C for 45 minutes, fixed in 2% paraformaldehyde for 20 minutes, washed and mounted with Gel/Mount (Biomeda, Burlingame, CA). Detection of EBD-labeled albumin permeation into the vessel wall was performed using fluorescent microscopy. EBD has very broad spectrum fluorescent properties. Of note, it emits in the far-red region of the spectrum when excited with a Cy5 excitation wavelength (620-660nm). The benefit of this property is that

blood vessels, which generate significant auto-fluorescence, have very little far-red fluorescence. Most recently, the trend has been to perform EBD permeability assays on *en face* preparations [107, 109] rather than in cross-sections. However, it has also been successfully performed on cross-sections [184, 185]. The limitation of the *en face* preparation is that it forces the experiment to be dedicated solely to the permeability endpoint. Using cross-sections allowed a larger number of endpoints to be investigated for a given perfusion experiment.

Image quantification was performed using a custom Matlab® v7.0 script (Appendix C). This program calculated the sum of pixel intensities from each of four fields of view (FOV) from a given 5 μm cross-section and averaged them to define the mean intensity for that cross-section. The mean intensity for one segment (defined in Figure 3.3) was determined by averaging the mean intensity from 6 non-serial, randomly placed cross-sections within the segment. All intensities were normalized to the wall thickness to account for different diffusion distances. Wall thickness was determined from the geometric reconstruction protocol described in Section 4.1.

3.1.4.2 Apoptosis

Apoptosis was assessed using the In Situ Cell Death Kit, fluorescein (TUNEL) (Roche Applied Science, Indianapolis, IN). This assay uses the TUNEL technology which identifies the genomic DNA cleavage component of apoptosis. Briefly, cross-sections were dried at 37˚C for 20 minutes, fixed in 2% paraformaldehyde for 20 minutes, and rehydrated in phosphate buffered saline (PBS) for 30 minutes. Samples were then incubated at room temperature for 10 minutes each in 10μg/ml Proteinase K followed by a freshly prepared solution of 0.1% Triton X-100 and 0.1% sodium citrate for permeabilization of membranes. DNA strand breaks were identified by incubation at 37˚C for one hour with Terminal deoxynucleotidyl transferase and fluorescein

labeled dUTP (both provided in the kit from Roche). Nuclei were counterstained with Hoechst 33258. A small set of samples was treated with 100U/ml of DNase I to serve as positive controls each time the assay was performed to ensure efficacy. All sample preparation parameters including incubation times, temperatures, and reagent concentrations were optimized using DNase I treated positive controls. Negative controls were incubated with labeled dUTP without the transferase enzyme.

Quantification of the percent of TUNEL positive cells was performed using a custom Matlab® v7.0 script (Appendix C). This program calculated the number of positive staining cells and divided by the total number of cells from each of four FOVs from a given 5 μm cross-section and averaged them to define the mean percent positive cells for that cross-section. The mean percent TUNEL positive cells from one segment (Figure 3.3) was determined by averaging the mean intensity from 3 non-serial, randomly placed cross-sections within the segment.

3.1.4.3 Proliferation

Proliferation was assessed by the expression of proliferating cell nuclear antigen (PCNA) determined by immunohistochemistry. Five-micron cross-sections were dried, fixed, and permeabilized as described for the TUNEL assay above. Nonspecific binding of antibodies was blocked by incubating the samples for 15 minutes with 1% horse serum in PBS. Following this, the samples were incubated with a primary mouse monoclonal antibody against PCNA (Clone PC10, Chemicon, Temecula, CA) for 60 min at room temperature in a moist chamber to prevent sample drying. Unbound primary antibody was removed by subsequent washes in PBS. Next, cross-sections were incubated with rabbit anti-mouse secondary antibody conjugated to Cy2 for 60 minutes at room temperature in a moist chamber and then rinsed 3 times for 15 minutes with PBS. For nuclear visualization, cells were counter-stained with Hoechst 33258. Porcine small

intestine was used as a positive control for proliferating cells [186]. Quantification of the percent PCNA positive cells was performed using the same methodology as for TUNEL (above)

3.1.5 Statistics

This study utilized a paired experimental design. Therefore, all averaged endpoint results are normalized and reported as relative fold-increase or -decrease in the deformed (i.e, stretch, twist, or flexure) specimen or segment (see Figure 3.3) versus its paired control. The average change for a given whole vessel specimen was determined by averaging the fold changes of its constitutive segments. Statistical differences between deformed and control groups were determined using a Student's paired t-test. Analysis of variance (ANOVA) with a post hoc Tukey's honestly significant difference test was performed on raw endpoint values averaged for the replicate cross-sections (6 for permeability, and 3 or apoptosis and proliferation) for each experimental vessel specimen to assess the endpoint distribution within that specimen. This same analysis was also used on the average normalized endpoint values for each experimental deformation to reveal any distribution trends related solely to the individual deformations. For the axi-symmetric deformations, (i.e., stretch and twist) a one-factor ANOVA was used where the longitudinal segment position was the independent factor. For flexure, a two-factor ANOVA was used with longitudinal position (proximal, middle, and distal) as one factor and circumferential position (greater and lesser curvature) as the other factor. In all cases, a significance value of 0.05 was used.

3.2 RESULTS

3.2.1 Perfusion Conditions

For the most part, e*x vivo* perfusion conditions were maintained within the preset tolerances given in Table 3.1 (Figure 3.5 and Figure 3.6). In a few experiments the temperature and pH were outside the tolerances at the first monitoring time point. This was due to the time required for implantation, during which the system was open to ambient conditions. In all cases, these values fell within the tolerance range by the next time scheduled recording. However, there were no significant differences in any of these parameters between the deformed (i.e., stretch, twist, and flexure) and the control specimens or between time points. This demonstrates the well-controlled experimental environment and isolation of the specific experimental variables of interest within the EVPS.

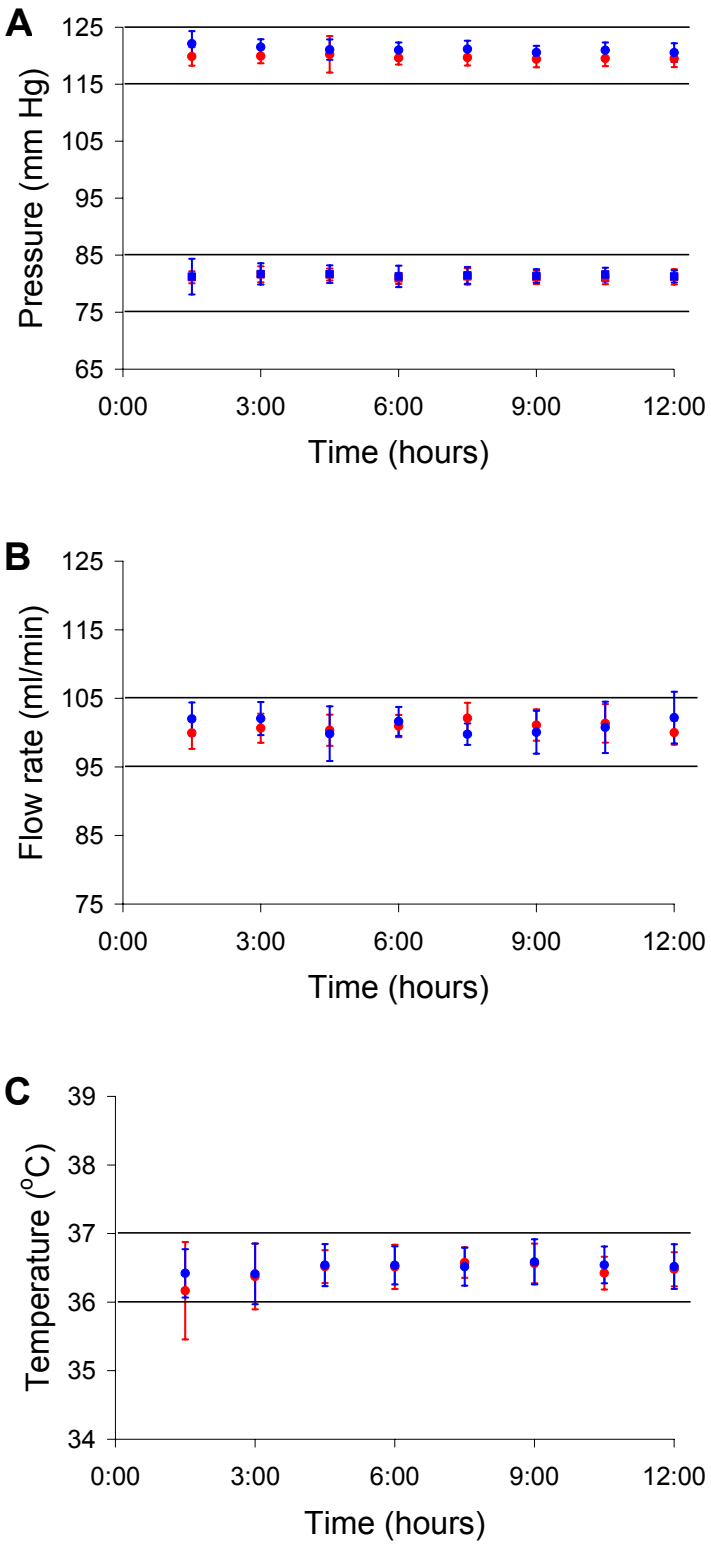

Figure 3.5 Average monitored hemodynamic perfusion conditions versus time for all experiments: A) Systolic and diastolic pressure; B) Flow rate; and C) Temperature. Deformed (i.e., stretch, flexure, or twist) conditions are shown in blue, while control conditions are shown in red. Error bars represent the standard deviation.

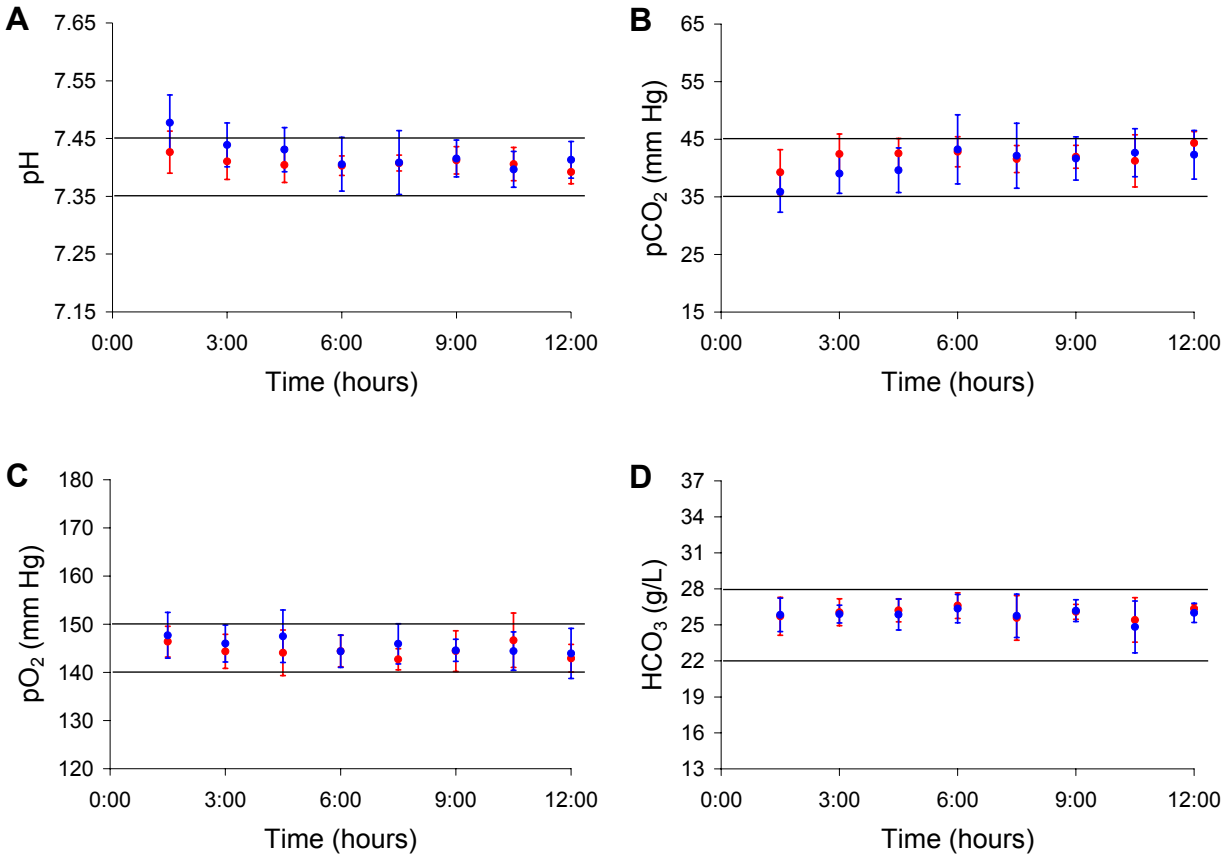

Figure 3.6 Average monitored dissolved gases in the EVPSs versus time for all experiments: A) pH; B) pCO_2; C) pO_2; and D) HCO_3. Deformed (i.e., stretch, twist, or flexure) conditions are shown in blue, while control conditions are shown in red. Error bars represent the standard deviation.

3.2.2 Permeability

Microscopic examination of samples prepared for EBD visualization demonstrated that albumin permeation rarely extended beyond the internal elastic lamina in vessel segments exposed to normal hemodynamics without cyclic deformation. On the other hand, samples subjected to cyclic stretch had EBD fluorescence which extended into the vessel wall (Figure 3.7). Similar results were seen for cyclic flexure and twist. Quantification using custom image analysis software (Appendix C) demonstrated a significant increase in EBD intensity in the vessel wall for stretch (1.24±0.07 fold, p=0.025) and flexure (1.14±0.04 fold p=0.026) compared to control but not for twist (1.31±0.18, p=0.126) (Figure 3.8).

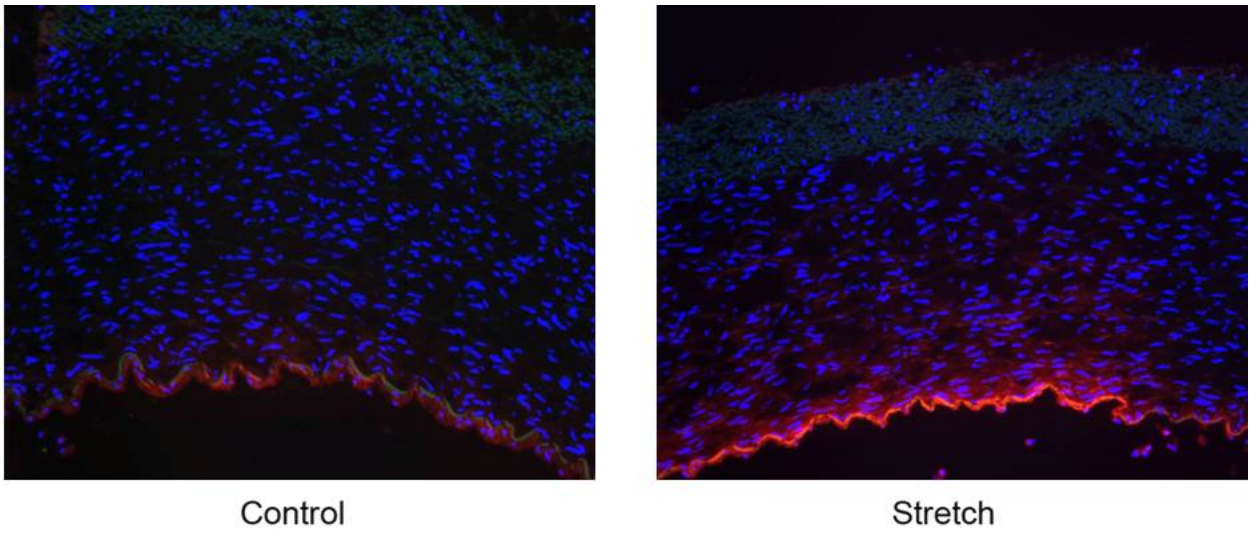

Figure 3.7 Representative 200x fluorescent micrographs from control and stretch samples with nuclei in blue, tissue autofluorescence in green, and EBD in red. In both images the vessel lumen is oriented toward the bottom of the picture.

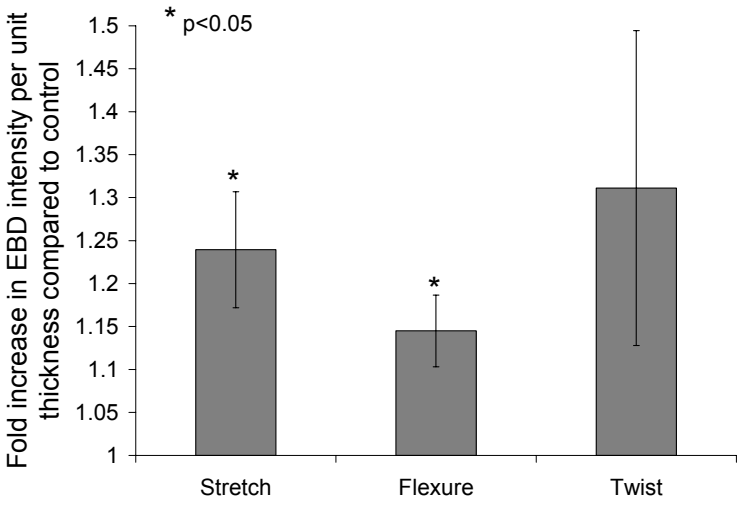

Figure 3.8 Whole vessel specimen fold increase in EBD bound albumin normalized to vessel wall thickness for each type of deformation compared to control. Bars represent mean ± standard error of the mean (N=5). Statistically significant differences with respect to control are indicated by an asterisk.

The average, normalized spatial distributions (determined via the tissue processing methods described in Section 0) of permeability for each experiment set are shown in Figure 3.9. Each experiment had a different number of segments depending on the vessel segment length obtained during the surgery. For statistical analysis and comparison purposes, the values for all the segments in between the first segment (Proximal) and the last segment (Distal) were grouped together, averaged, and referred to as the Middle segments. No significant differences within or between deformation groups were observed for the average normalized distributions.

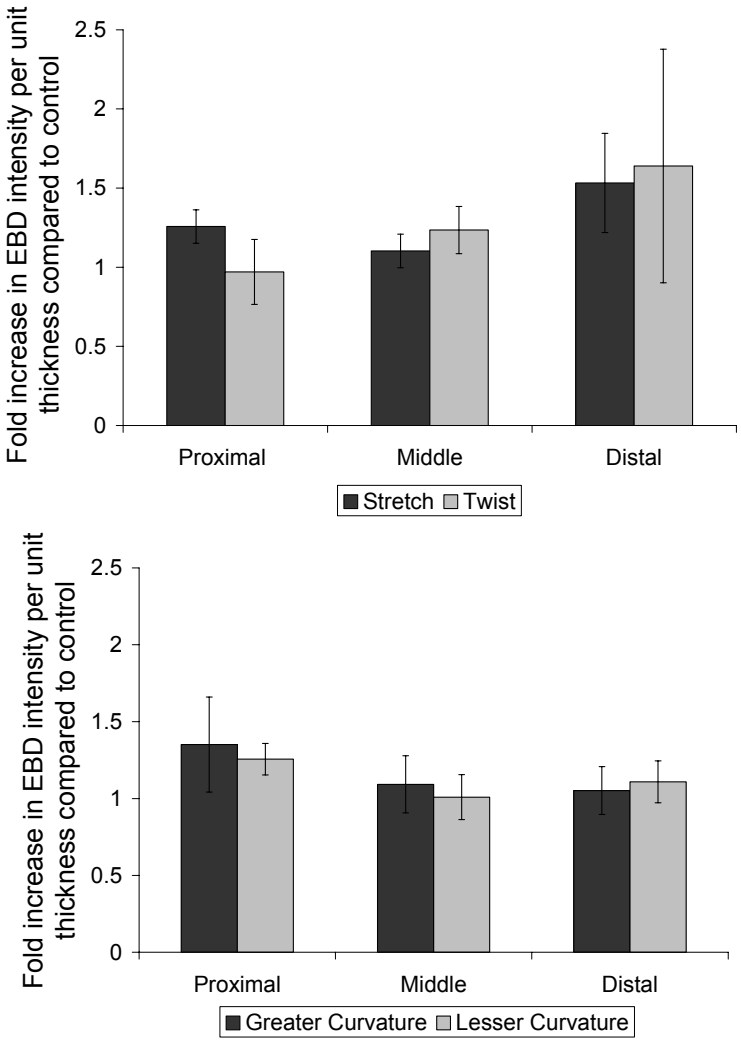

Figure 3.9 Distribution of EBD bound albumin normalized to vessel wall thickness for stretch and twist (top) and flexure (bottom). Bars represent mean ± standard error of the mean (N=5).

However, significant differences in permeability were observed within individual vessel specimens, indicating significant spatial variability in permeability. In other words, within a given specimen there were significant differences in permeability between the individual segments of that specimen. The spatial distribution of permeability for each perfused vascular specimen (determined by the tissue processing methods described in Section 0) are shown in Figure 3.10 - Figure 3.14 for the STR experiments; Figure 3.15 - Figure 3.19 for the TWT

experiments; and Figure 3.20 - Figure 3.24 for the FLX experiments. Each specimen from each experiment is shown to highlight specimen-to-specimen variations in the magnitudes and distributions of permeability. All but one vessel specimen from the five STR experiment pairs had significant changes in permeability over their length. For FLX, significant variation in permeability was observed in all flexed specimens when both longitudinal and circumferential positions were included as factors. However, only 2 of 5 paired controls for the flexure experiments had significant spatial variation. In the TWT experiments, 4 of 5 twist specimens had significant distributions of permeability; only 3 of the paired control specimens had significant distributions. In all three experimental sets, the shape of the distribution varied significantly between specimens and imposed mechanical deformation.

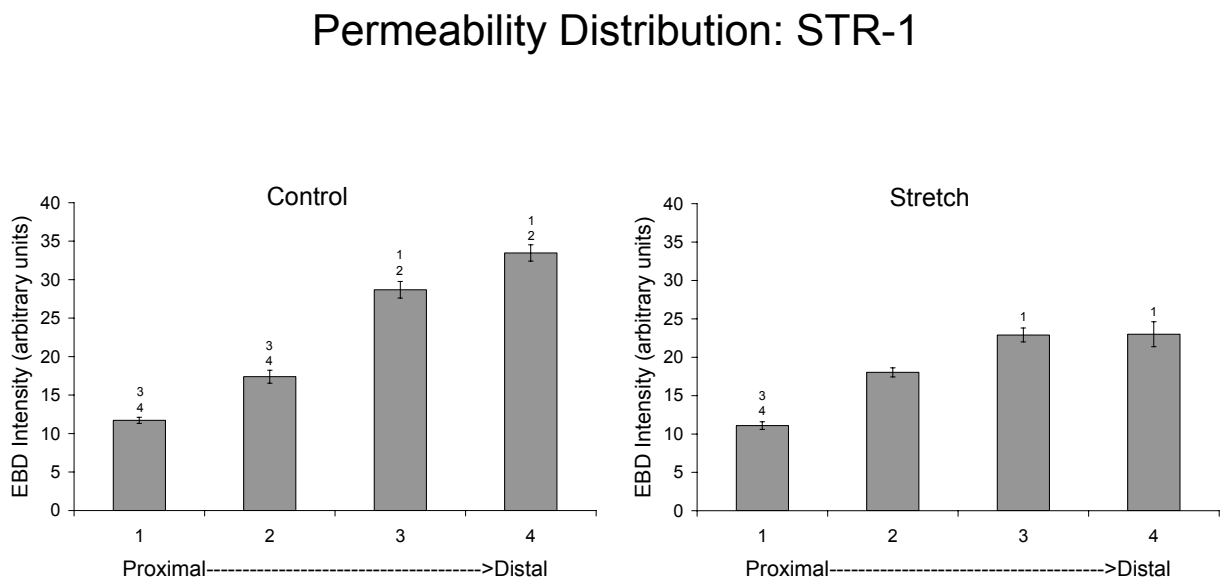

Figure 3.10 Permeability distribution for each specimen (Control and Stretch) in experiment STR-1. Bars represent that average EBD intensity for the six cross-sections sampled in the segment. Error bars represent the standard error of the mean. The numbers above the bars indicate which other segments in the given spcimen had significant differences in permeability from that segment.

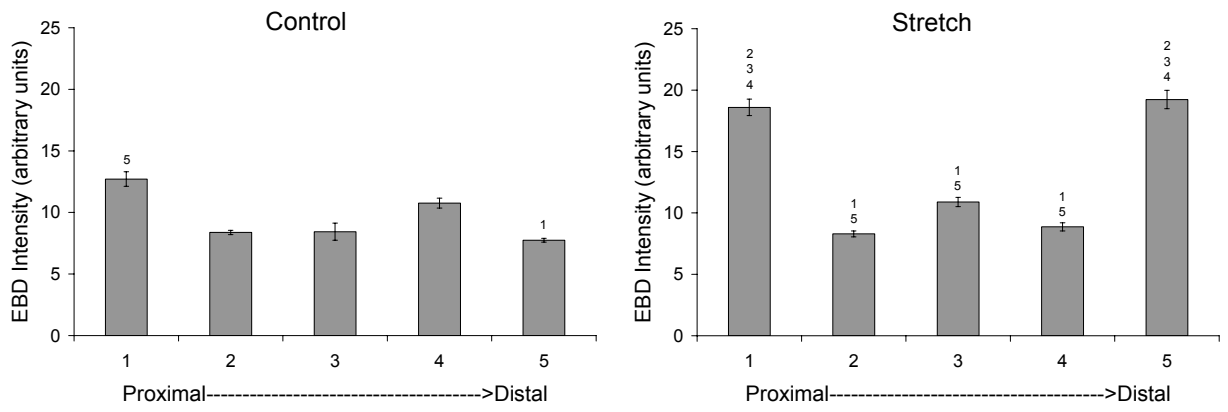

Figure 3.11 Permeability distribution for each specimen (Control and Stretch) in experiment STR-2. Bars represent that average EBD intensity for the six cross-sections sampled in the segment. Error bars represent the standard error of the mean. The numbers above the bars indicate which other segments in the given specimen had significant differences in permeability from that segment.

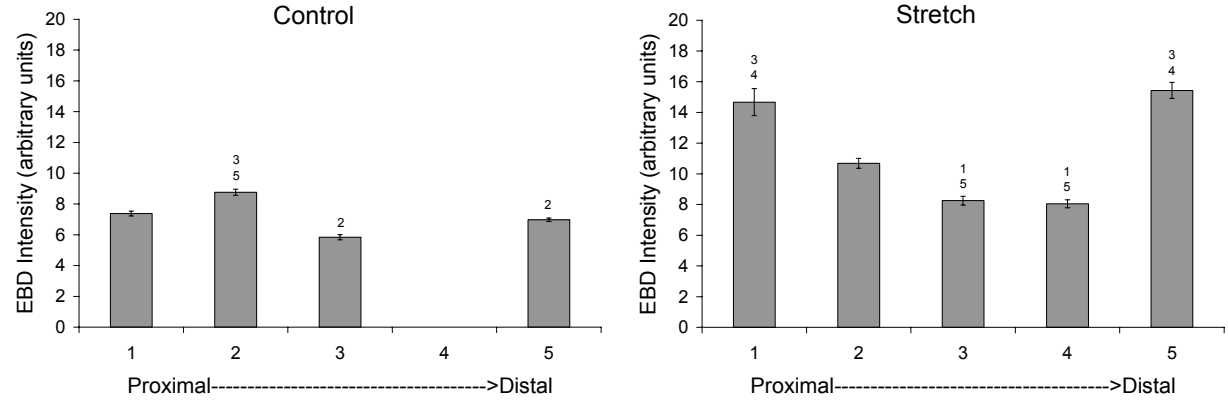

Figure 3.12 Permeability distribution for each specimen (Control and Stretch) in experiment STR-3. Bars represent that average EBD intensity for the six cross-sections sampled in the segment. Error bars represent the standard error of the mean. The numbers above the bars indicate which other segments in the given specimen had significant differences in permeability from that segment.

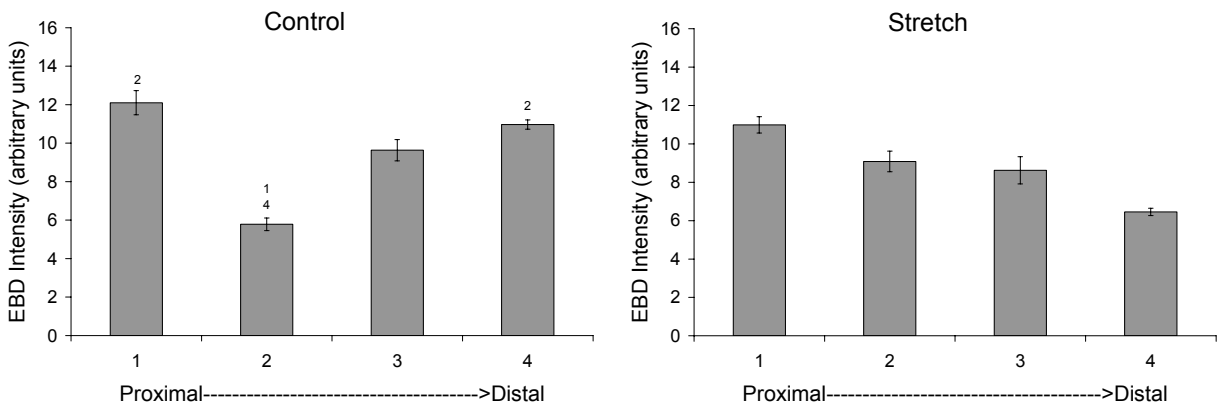

Figure 3.13 Permeability distribution for each specimen (Control and Stretch) in experiment STR-4. Bars represent that average EBD intensity for the six cross-sections sampled in the segment. Error bars represent the standard error of the mean. The numbers above the bars indicate which other segments in the given specimen had significant differences in permeability from that segment.

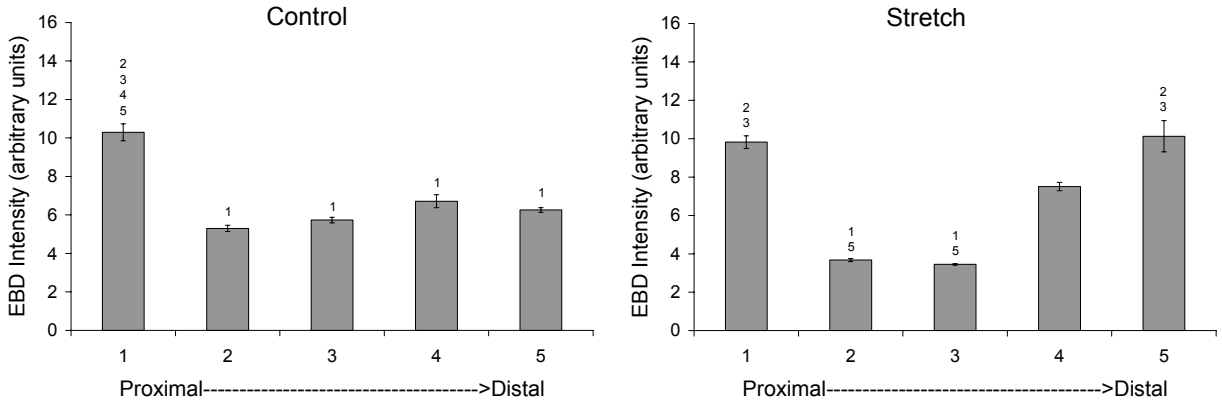

Figure 3.14 Permeability distribution for each specimen (Control and Stretch) in experiment STR-5. Bars represent that average EBD intensity for the six cross-sections sampled in the segment. Error bars represent the standard error of the mean. The numbers above the bars indicate which other segments in the given specimen had significant differences in permeability from that segment.

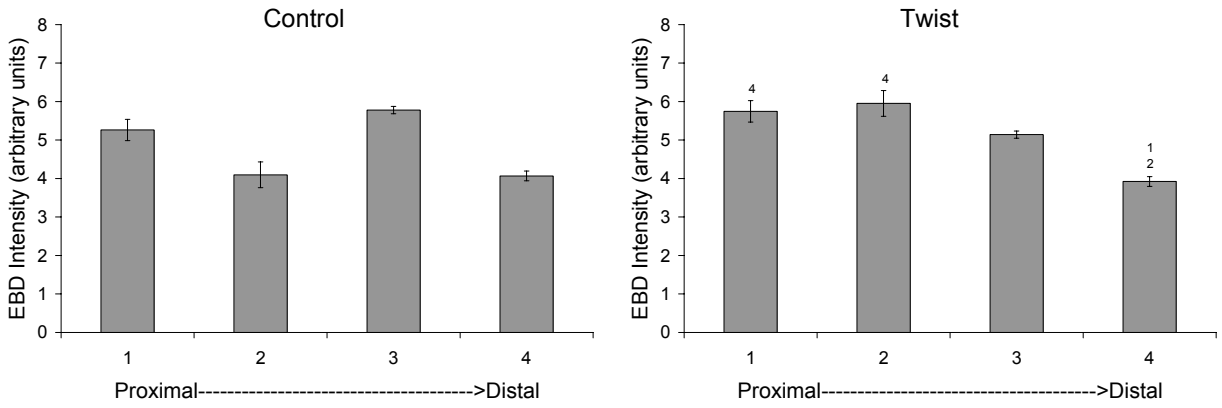

Figure 3.15 Permeability distribution for each specimen (Control and Twist) in experiment TWT-1. Bars represent that average EBD intensity for the six cross-sections sampled in the segment. Error bars represent the standard error of the mean. The numbers above the bars indicate which other segments in the given specimen had significant differences in permeability from that segment.

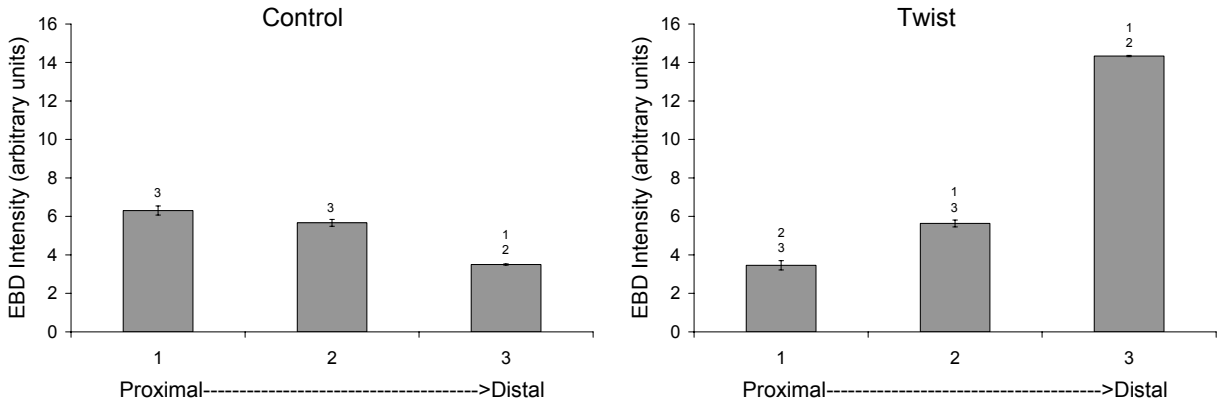

Figure 3.16 Permeability distribution for each specimen (Control and Twist) in experiment TWT-2. Bars represent that average EBD intensity for the six cross-sections sampled in the segment. Error bars represent the standard error of the mean. The numbers above the bars indicate which other segments in the given specimen had significant differences in permeability from that segment.

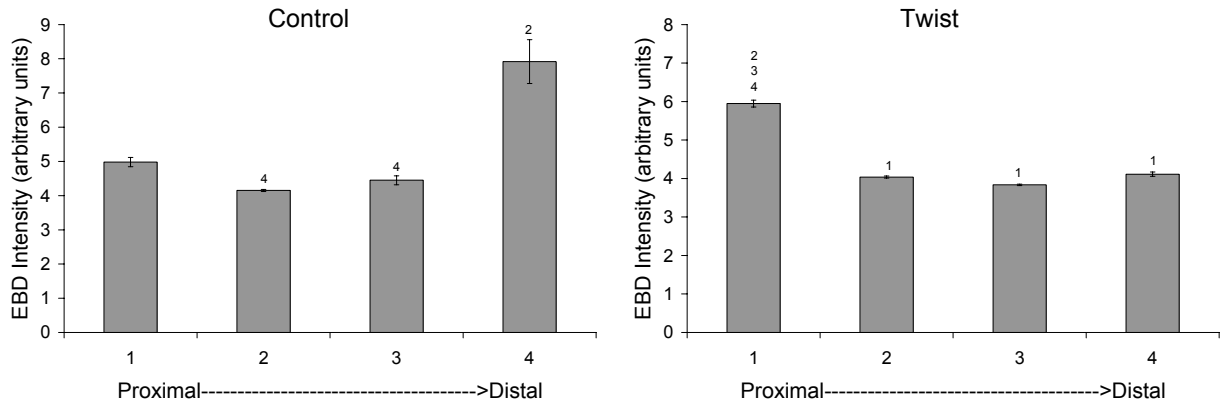

Figure 3.17 Permeability distribution for each specimen (Control and Twist) in experiment TWT-3. Bars represent that average EBD intensity for the six cross-sections sampled in the segment. Error bars represent the standard error of the mean. The numbers above the bars indicate which other segments in the given specimen had significant differences in permeability from that segment.

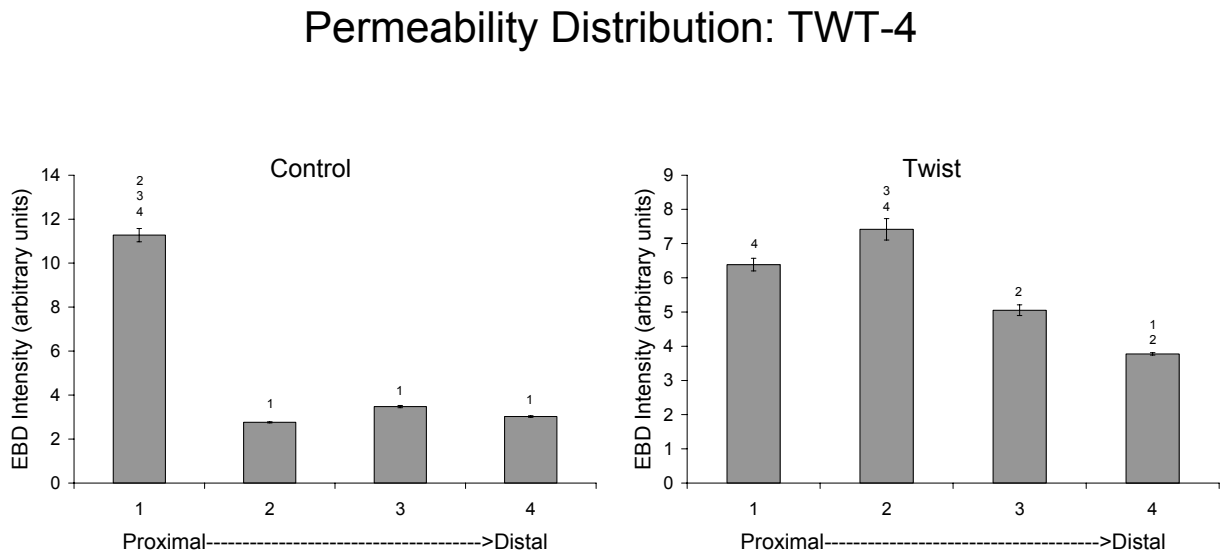

Figure 3.18 Permeability distribution for each specimen (Control and Twist) in experiment TWT-4. Bars represent that average EBD intensity for the six cross-sections sampled in the segment. Error bars represent the standard error of the mean. The numbers above the bars indicate which other segments in the given specimen had significant differences in permeability from that segment.

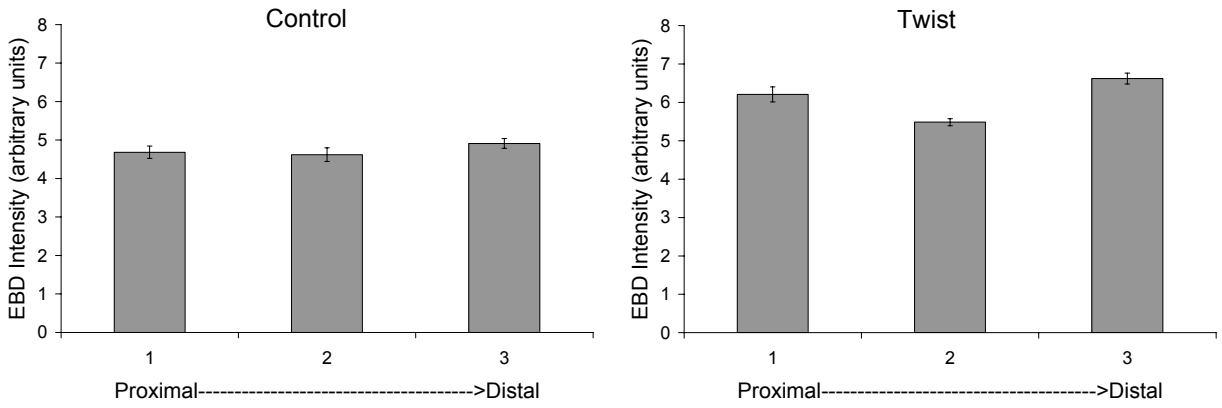

Figure 3.19 Permeability distribution for each specimen (Control and Twist) in experiment TWT-5. Bars represent that average EBD intensity for the six cross-sections sampled in the segment. Error bars represent the standard error of the mean. The numbers above the bars indicate which other segments in the given specimen had significant differences in permeability from that segment.

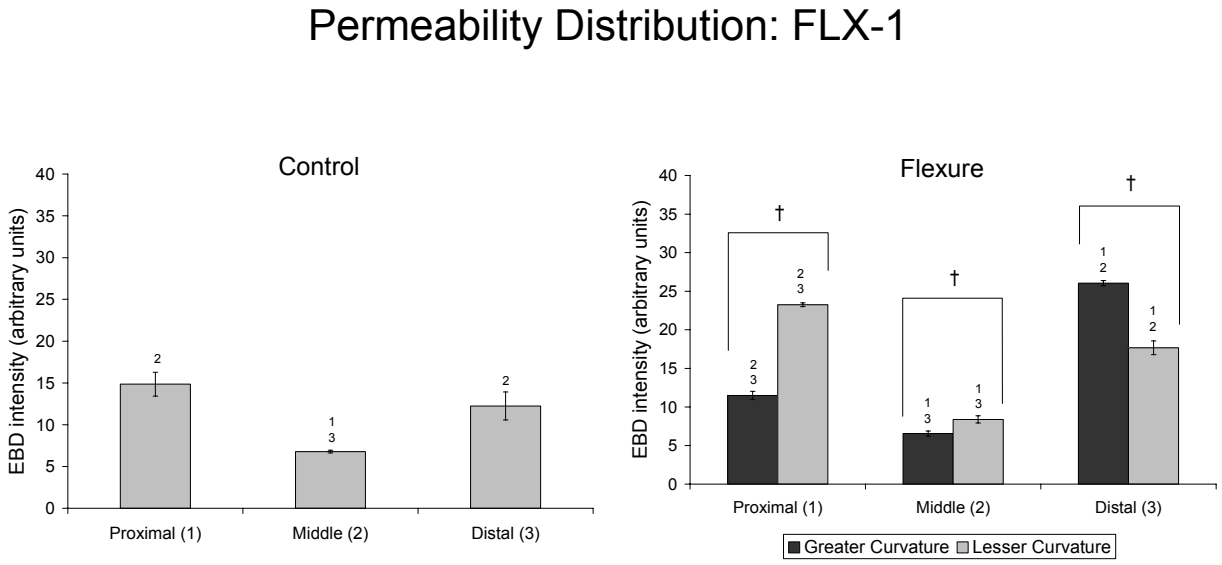

Figure 3.20 Permeability distribution for each specimen (Control and Flexure) in experiment FLX-1. Bars represent that average EBD intensity for the six cross-sections sampled in the segment. Error bars represent the standard error of the mean. The numbers above the bars indicate which other segments in the given specimen had significant differences in permeability from that segment. For flexure significant differences between the greater and lesser curvature are noted by †.

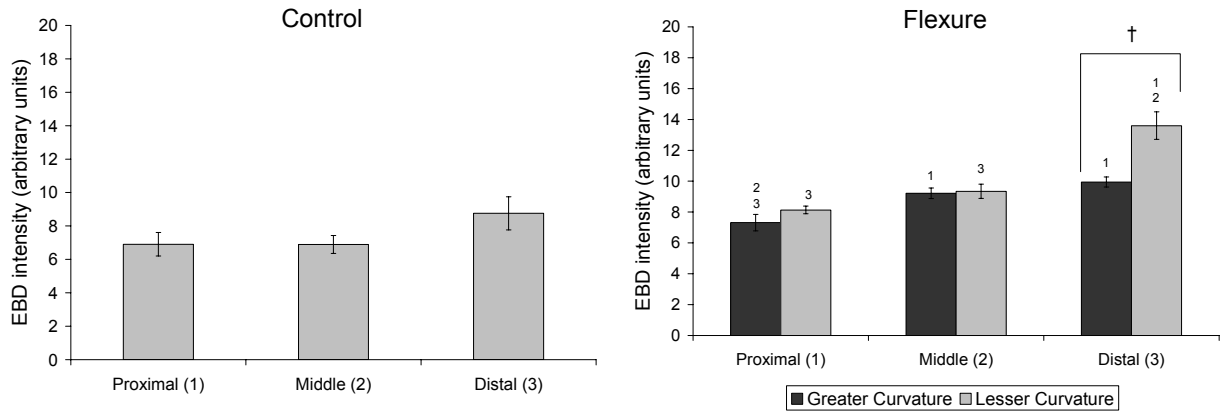

Figure 3.21 Permeability distribution for each specimen (Control and Flexure) in experiment FLX-2. Bars represent that average EBD intensity for the six cross-sections sampled in the segment. Error bars represent the standard error of the mean. The numbers above the bars indicate which other segments in the given specimen had significant differences in permeability from that segment. For flexure significant differences between the greater and lesser curvature are noted by †.

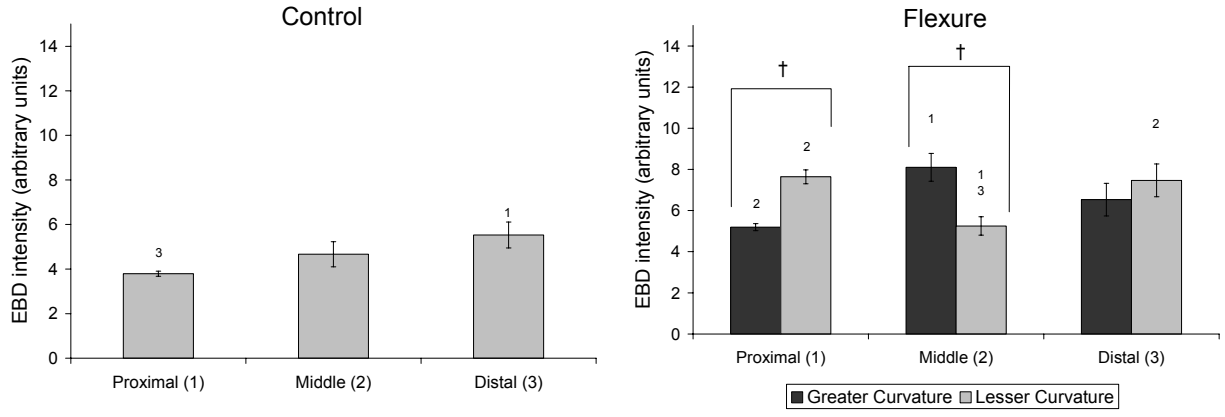

Figure 3.22 Permeability distribution for each specimen (Control and Flexure) in experiment FLX-3. Bars represent that average EBD intensity for the six cross-sections sampled in the segment. Error bars represent the standard error of the mean. The numbers above the bars indicate which other segments in the given specimen had significant differences in permeability from that segment. For flexure significant differences between the greater and lesser curvature are noted by †.

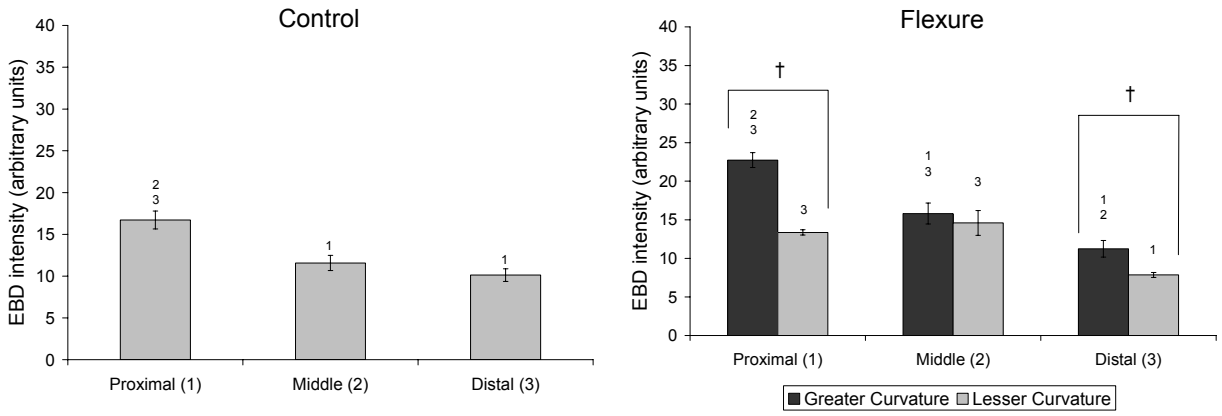

Figure 3.23 Permeability distribution for each specimen (Control and Flexure) in experiment FLX-4. Bars represent that average EBD intensity for the six cross-sections sampled in the segment. Error bars represent the standard error of the mean. The numbers above the bars indicate which other segments in the given specimen had significant differences in permeability from that segment. For flexure significant differences between the greater and lesser curvature are noted by †.

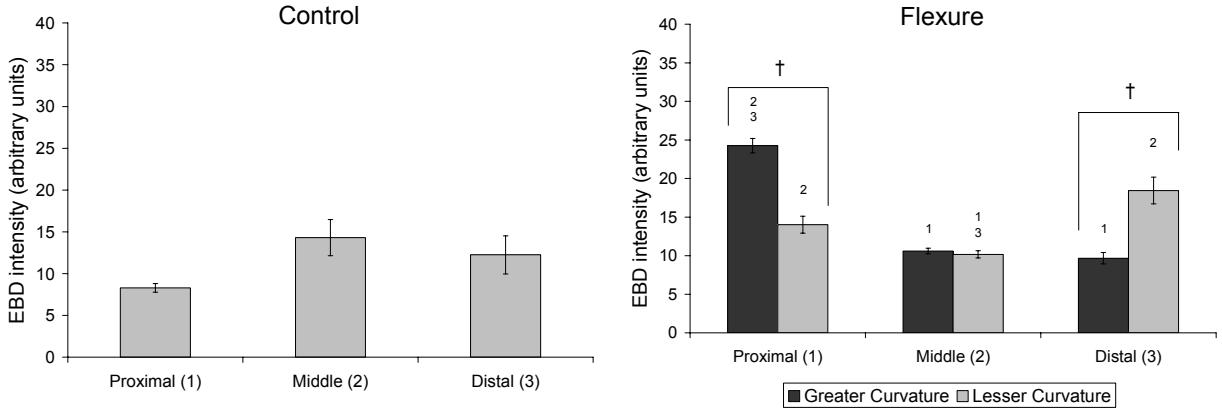

Figure 3.24 Permeability distribution for each specimen (Control and Flexure) in experiment FLX-5. Bars represent that average EBD intensity for the six cross-sections sampled in the segment. Error bars represent the standard error of the mean. The numbers above the bars indicate which other segments in the given specimen had significant differences in permeability from that segment. For flexure significant differences between the greater and lesser curvature are noted by †.

3.2.3 Apoptosis

Apoptotic cells determined by TUNEL were few in number and confined to the adventitia in vessel segments exposed to normal hemodynamics without cyclic deformation (Figure 3.25). The addition of cyclic stretch and flexure caused an increase in the proportion of cells positive for DNA fragmentation. Furthermore, apoptotic cells were present in both the medial and intimal areas of the wall of specimens exposed to these deformations. Quantification using custom image analysis software (Appendix C) demonstrated a significant increase in EBD intensity in the vessel wall for stretch (2.91±0.71 fold, $p=0.015$) and flexure (3.42±1.02 fold $p=0.029$) compared to controls but not for twist (2.30±1.21, $p=0.129$) (Figure 3.26).

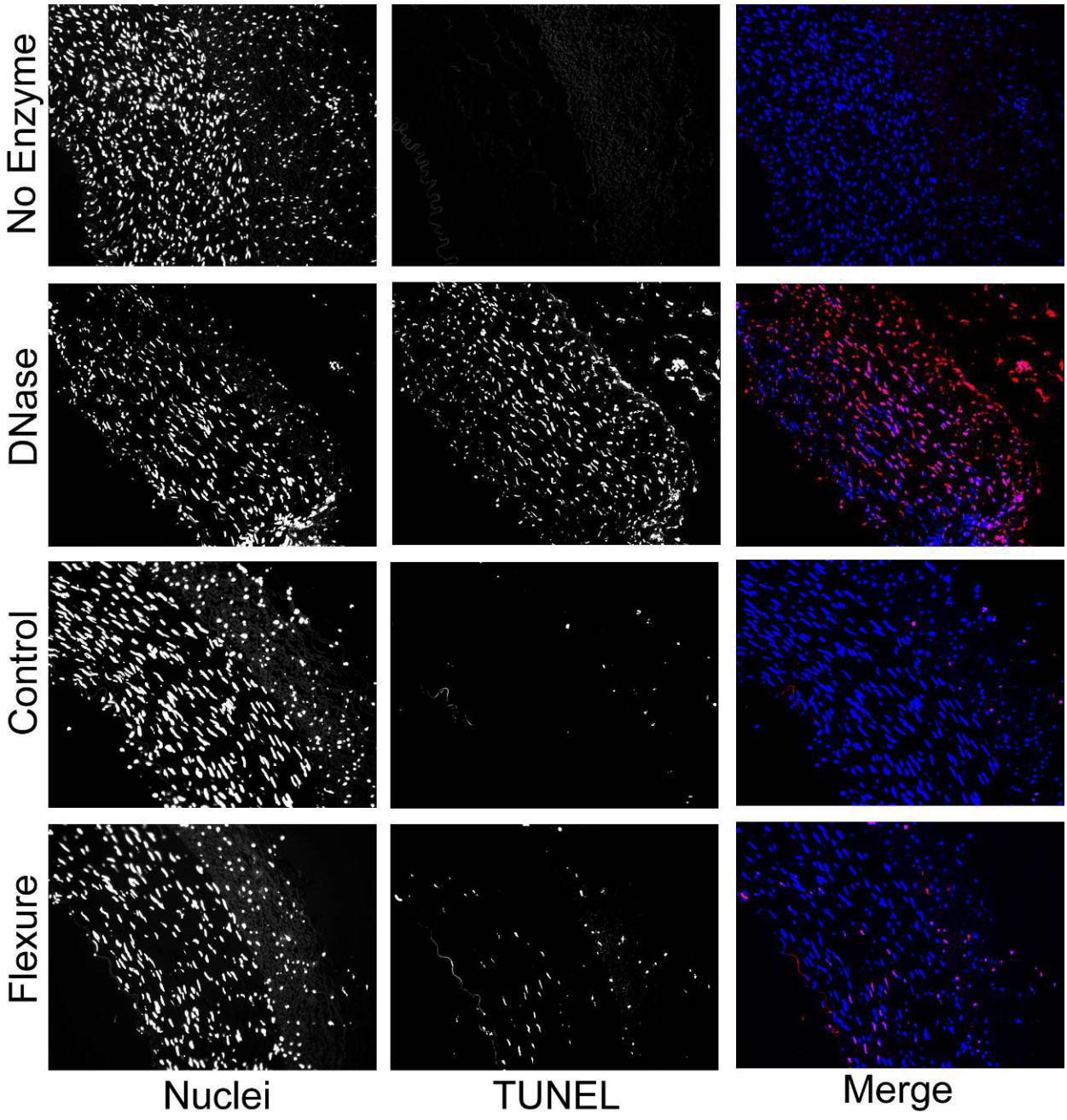

Figure 3.25 Representative 200x photomicrographs of apoptosis determined by the TUNEL assay. Four sets of images are shown: A negative control (No Enzyme), positive control (DNase), representative control sample from a flexure experiment (Control), and its paired flexure sample (Flexure). Each set of images consist of a nuclear stain (Nuclei), a TUNEL stain (TUNEL) and a color merge of the two (MERGE). In the color merge nuclei are blue and TUNEL stain is red. In all images the vessel lumen is oriented in the bottom left corner.

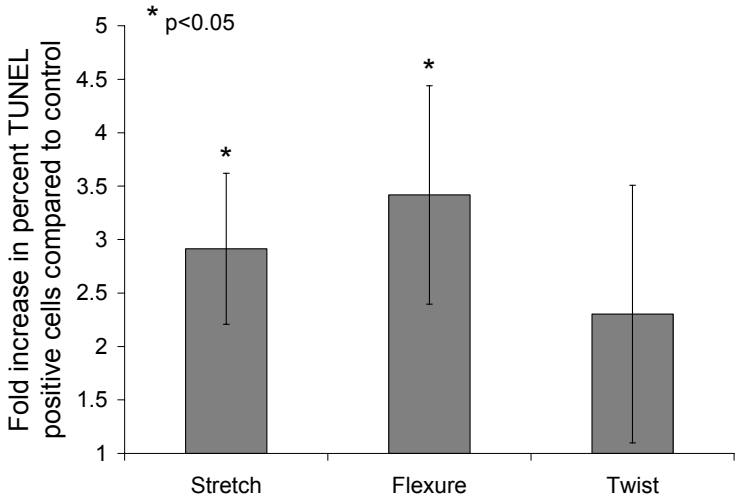

Figure 3.26 Whole vessel specimen fold increase in apoptosis for each type of deformation compared to control. Bars represent mean ± standard error of the mean (N=5). Statistically significant differences with respect to control are indicated by an asterisk.

The average, normalized spatial distributions of apoptosis for each experiment set are shown in Figure 3.27. No significant differences were observed for the average normalized distributions within or between deformation groups. However, like permeability, significant spatial variation in apoptosis was observed within individual vessel segments. The spatial distributions of apoptosis for each perfused vascular specimen are shown in Figure 3.28-Figure 3.32 for the STR experiments, Figure 3.33-Figure 3.37 for the TWT experiments, and Figure 3.38-Figure 3.42 for the FLX experiments. In the STR experimental set, 3 of 5 stretch and 2 of 5 control specimens had significant spatial variation in apoptosis. For the FLX set, 2 of 5 flexed specimens had significant variation in both the longitudinal and circumferential directions. None of the control samples from that set had significant variation within them. Only one control sample from all of the TWT experimental set specimens showed significant variation in apoptosis.

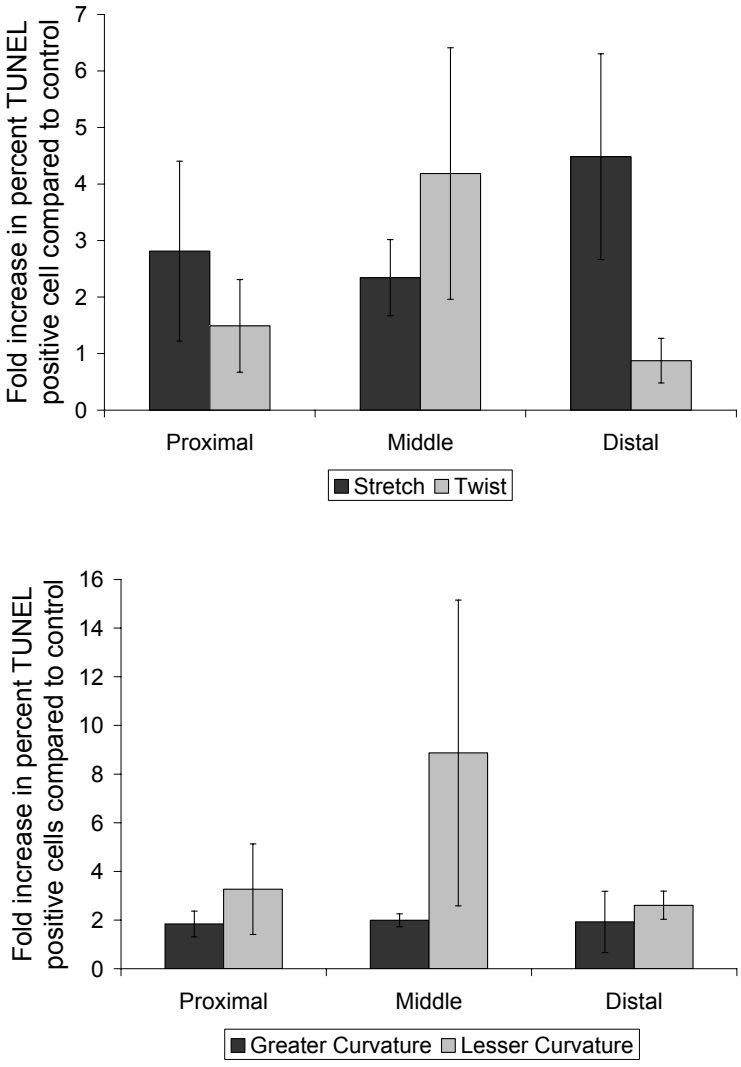

Figure 3.27 Distribution of apoptosis for stretch and twist (top) and flexure (bottom). Bars represent mean ± standard error of the mean (N=5).

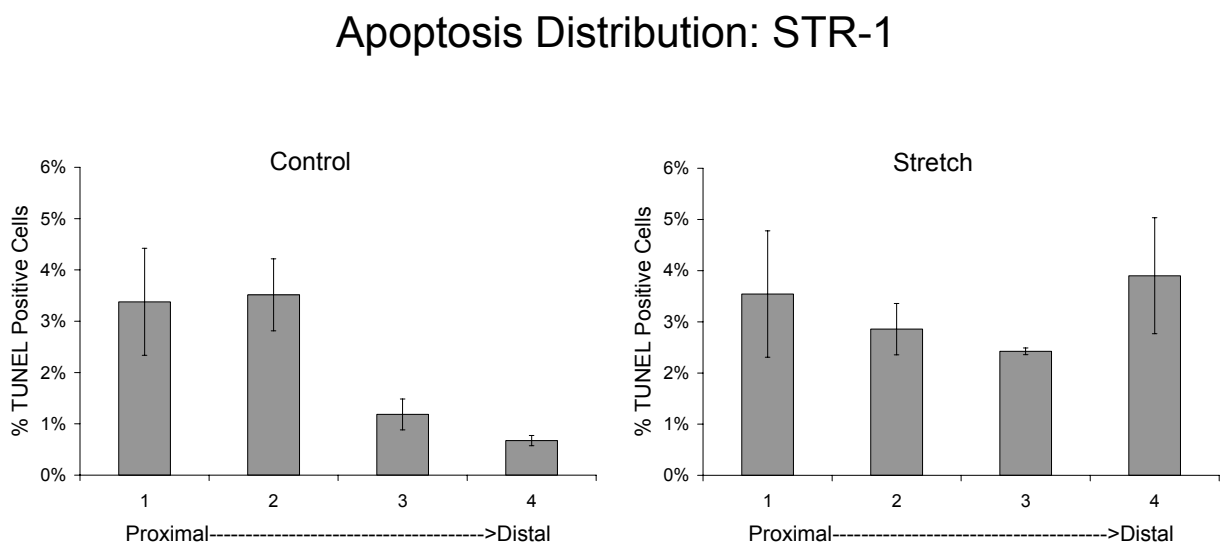

Figure 3.28 Apoptosis distribution for each specimen (Control and Stretch) in experiment STR-1. Bars represent that average % TUNEL positive cells for the three cross-sections sampled in the segment. Error bars represent the standard error of the mean. The numbers above the bars indicate which other segments in the given specimen had significant differences in apoptosis from that segment.

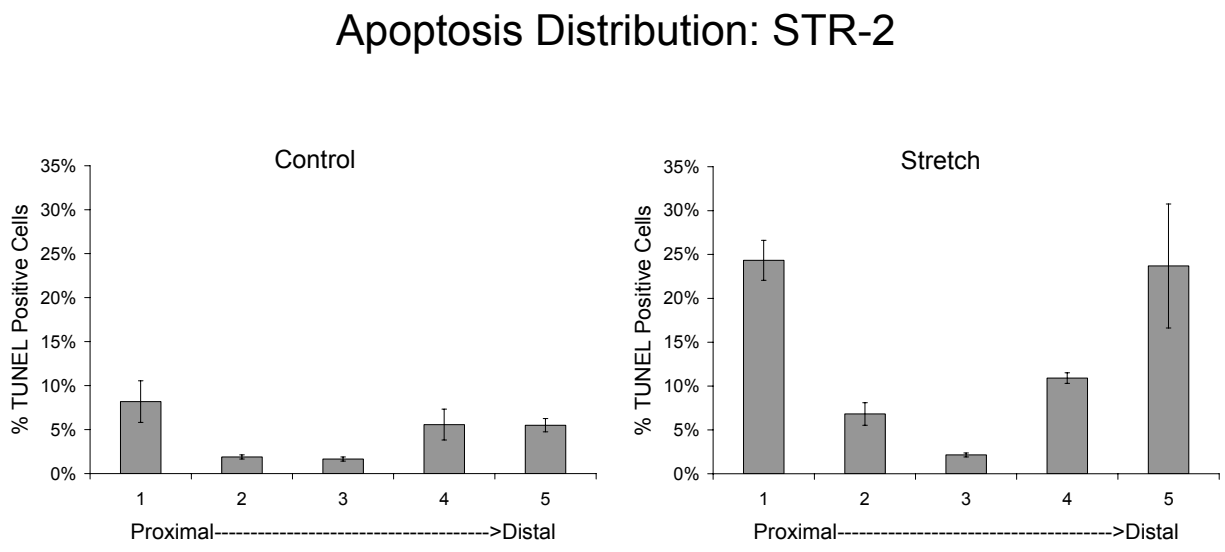

Figure 3.29 Apoptosis distribution for each specimen (Control and Stretch) in experiment STR-2. Bars represent that average % TUNEL positive cells for the three cross-sections sampled in the segment. Error bars represent the standard error of the mean. The numbers above the bars indicate which other segments in the given specimen had significant differences in apoptosis from that segment.

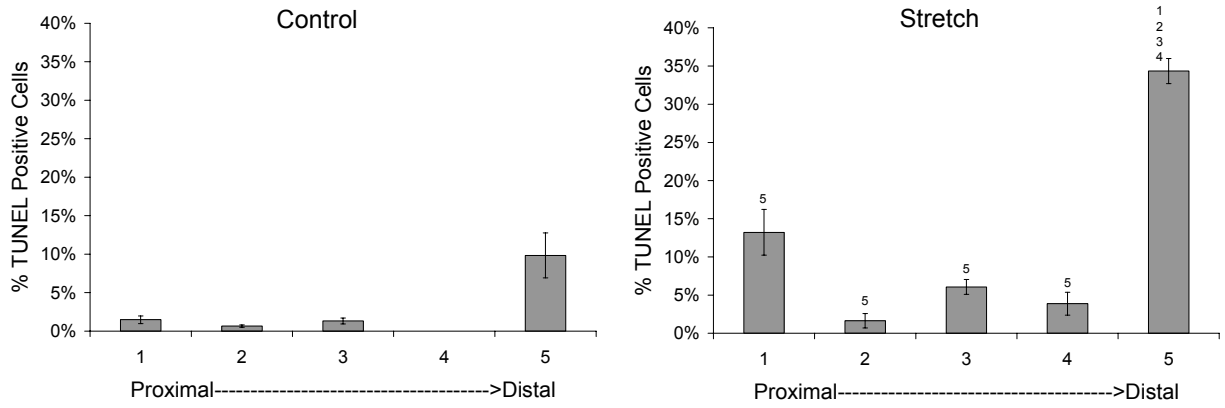

Figure 3.30 Apoptosis distribution for each specimen (Control and Stretch) in experiment STR-3. Bars represent that average % TUNEL positive cells for the three cross-sections sampled in the segment. Error bars represent the standard error of the mean. The numbers above the bars indicate which other segments in the given specimen had significant differences in apoptosis from that segment.

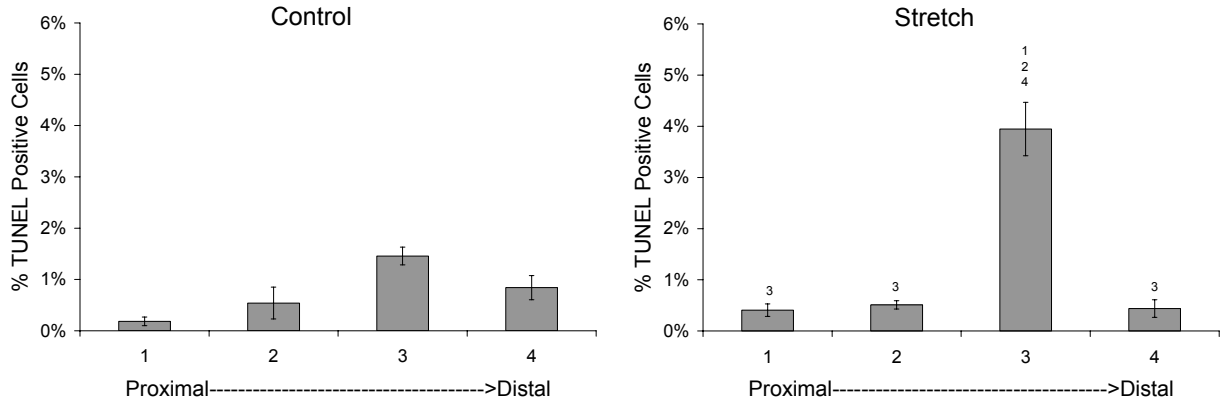

Figure 3.31 Apoptosis distribution for each specimen (Control and Stretch) in experiment STR-4. Bars represent that average % TUNEL positive cells for the three cross-sections sampled in the segment. Error bars represent the standard error of the mean. The numbers above the bars indicate which other segments in the given specimen had significant differences in apoptosis from that segment.

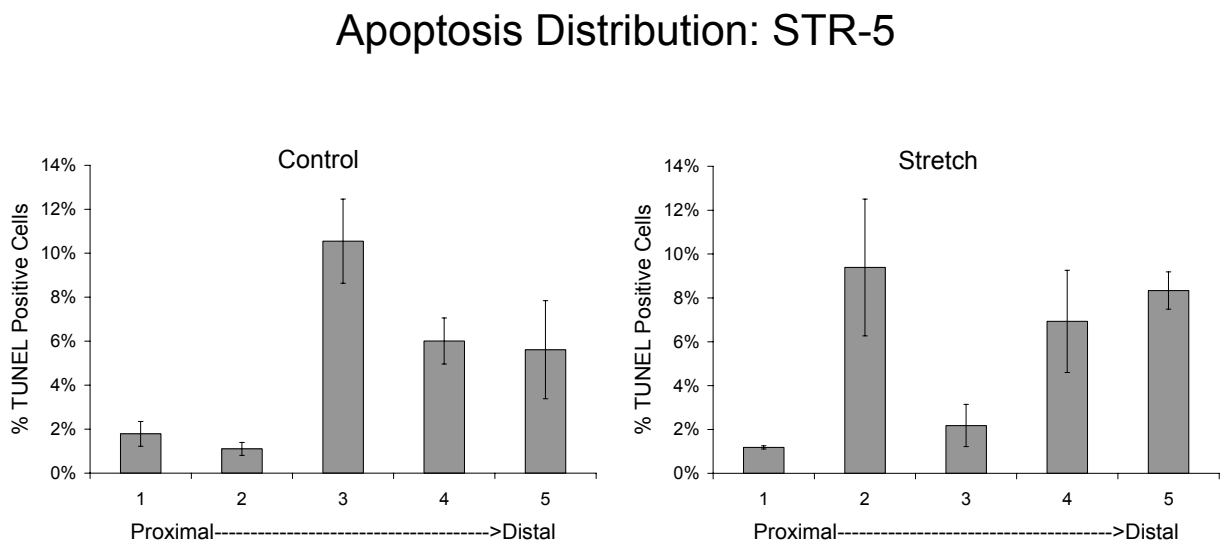

Figure 3.32 Apoptosis distribution for each specimen (Control and Stretch) in experiment STR-5. Bars represent that average % TUNEL positive cells for the three cross-sections sampled in the segment. Error bars represent the standard error of the mean. The numbers above the bars indicate which other segments in the given specimen had significant differences in apoptosis from that segment.

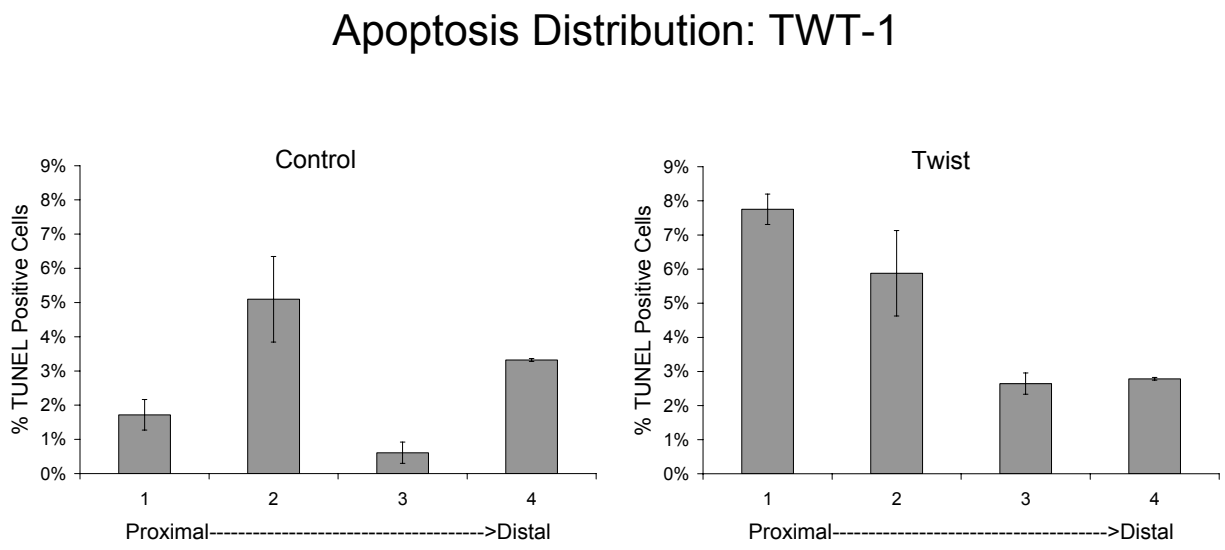

Figure 3.33 Apoptosis distribution for each specimen (Control and Twist) in experiment TWT-1. Bars represent that average % TUNEL positive cells for the three cross-sections sampled in the segment. Error bars represent the standard error of the mean. The numbers above the bars indicate which other segments in the given specimen had significant differences in apoptosis from that segment.

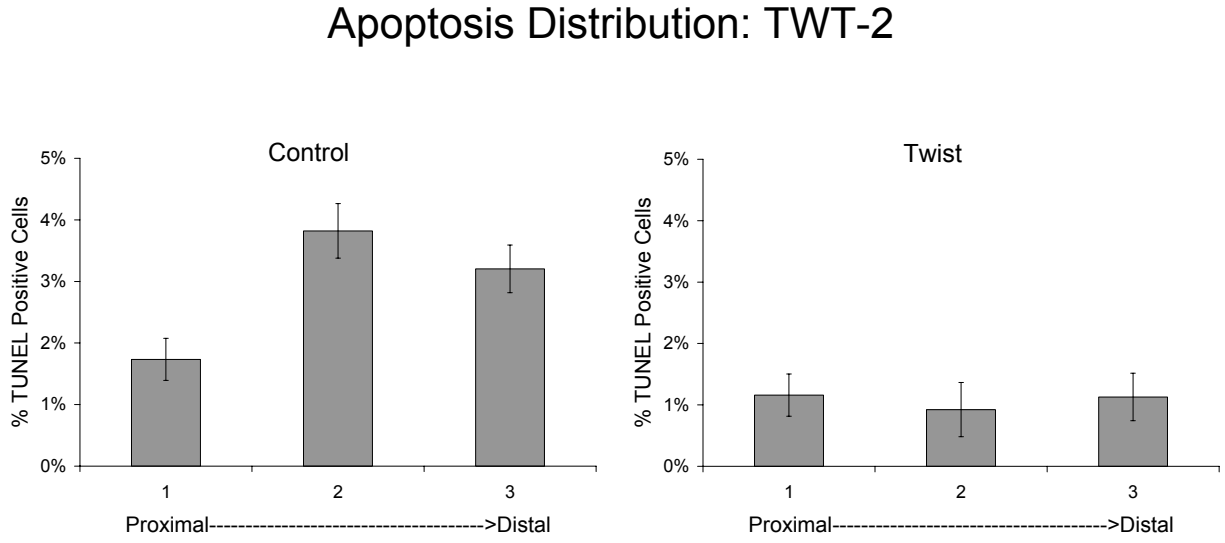

Figure 3.34 Apoptosis distribution for each specimen (Control and Twist) in experiment TWT-2. Bars represent that average % TUNEL positive cells for the three cross-sections sampled in the segment. Error bars represent the standard error of the mean. The numbers above the bars indicate which other segments in the given specimen had significant differences in apoptosis from that segment.

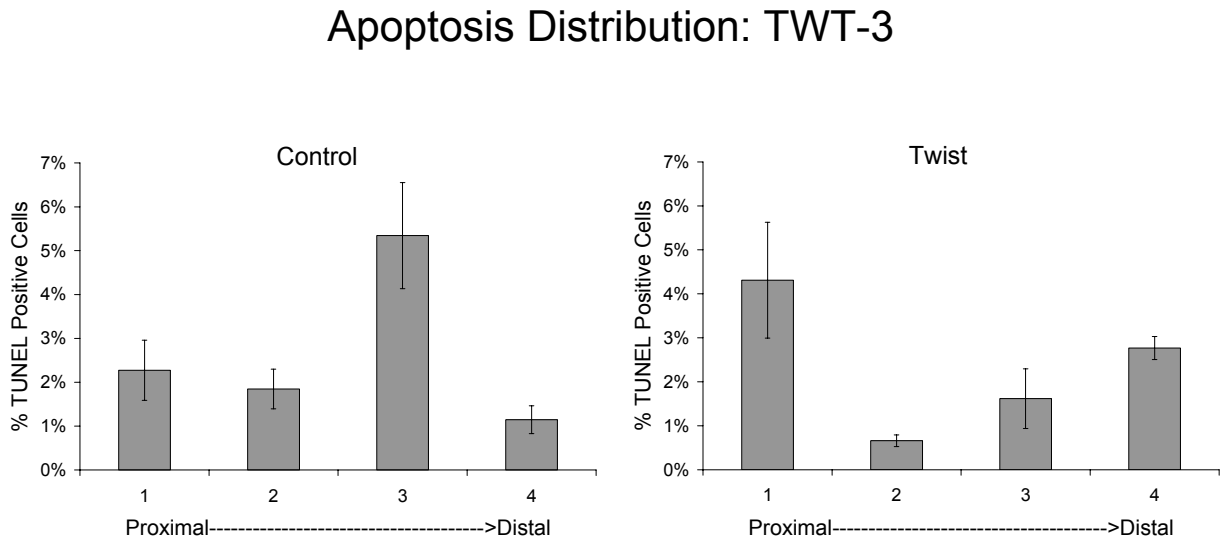

Figure 3.35 Apoptosis distribution for each specimen (Control and Twist) in experiment TWT-3. Bars represent that average % TUNEL positive cells for the three cross-sections sampled in the segment. Error bars represent the standard error of the mean. The numbers above the bars indicate which other segments in the given specimen had significant differences in apoptosis from that segment.

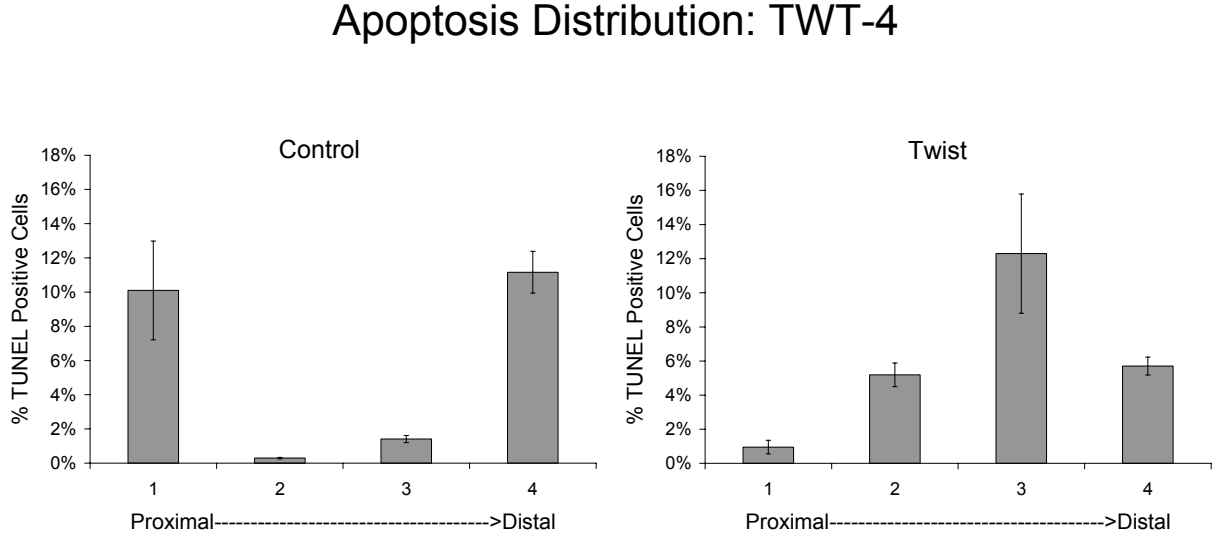

Figure 3.36 Apoptosis distribution for each specimen (Control and Twist) in experiment TWT-4. Bars represent that average % TUNEL positive cells for the three cross-sections sampled in the segment. Error bars represent the standard error of the mean. The numbers above the bars indicate which other segments in the given specimen had significant differences in apoptosis from that segment.

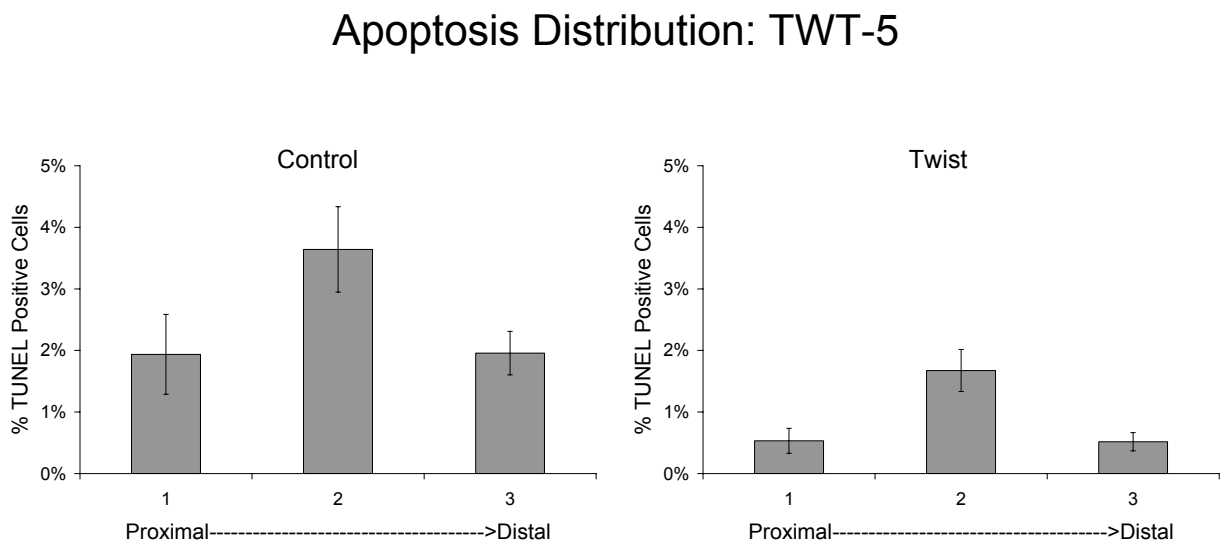

Figure 3.37 Apoptosis distribution for each specimen (Control and Twist) in experiment TWT-5. Bars represent that average % TUNEL positive cells for the three cross-sections sampled in the segment. Error bars represent the standard error of the mean. The numbers above the bars indicate which other segments in the given specimen had significant differences in apoptosis from that segment.

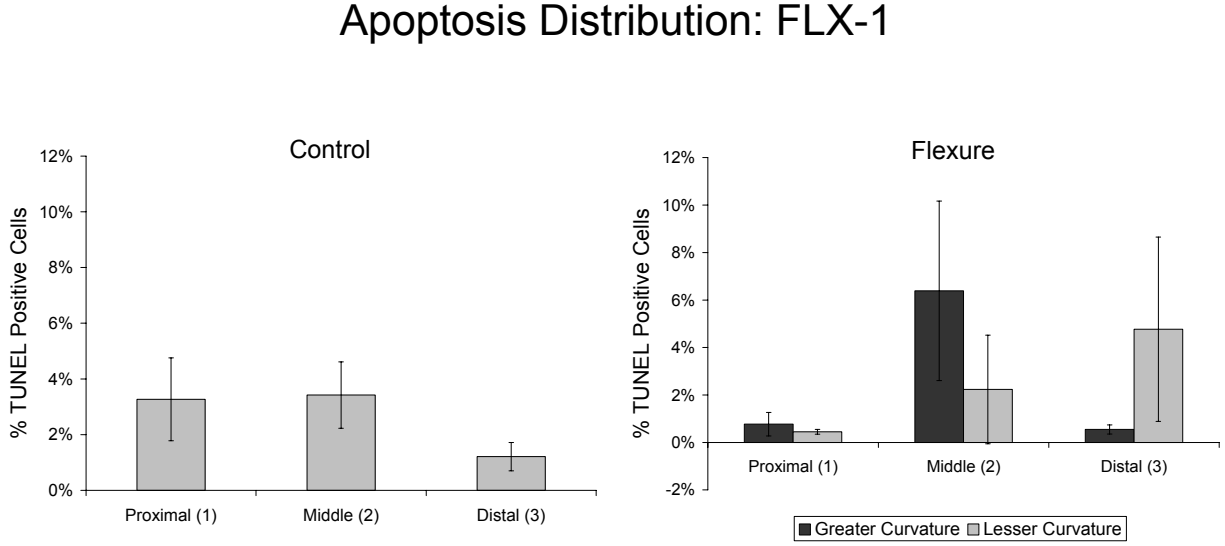

Figure 3.38 Apoptosis distribution for each specimen (Control and Flexure) in experiment FLX-1. Bars represent that average EBD intensity for the six cross-sections sampled in the segment. Error bars represent the standard error of the mean. The numbers above the bars indicate which other segments in the given specimen had significant differences in apoptosis from that segment. For flexure significant differences between the greater and lesser curvature are noted by †.

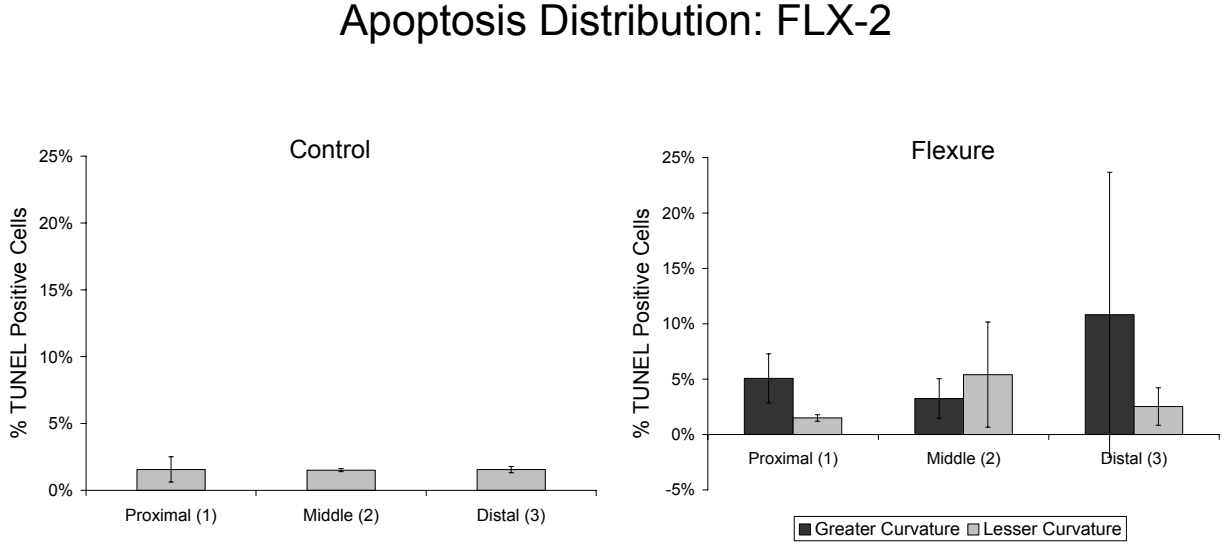

Figure 3.39 Apoptosis distribution for each specimen (Control and Flexure) in experiment FLX-2. Bars represent that average EBD intensity for the six cross-sections sampled in the segment. Error bars represent the standard error of the mean. The numbers above the bars indicate which other segments in the given specimen had significant differences in apoptosis from that segment. For flexure significant differences between the greater and lesser curvature are noted by †.

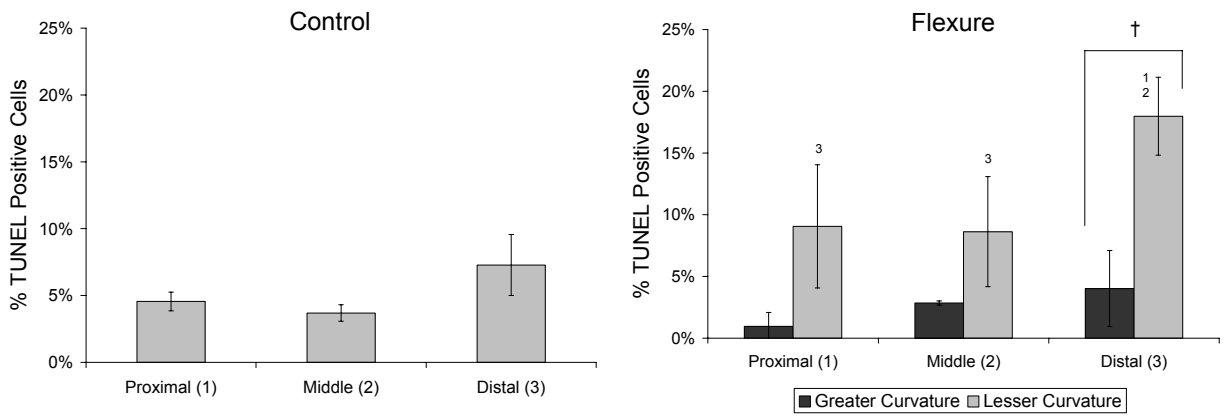

Figure 3.40 Apoptosis distribution for each specimen (Control and Flexure) in experiment FLX-3. Bars represent that average EBD intensity for the six cross-sections sampled in the segment. Error bars represent the standard error of the mean. The numbers above the bars indicate which other segments in the given specimen had significant differences in apoptosis from that segment. For flexure significant differences between the greater and lesser curvature are noted by †.

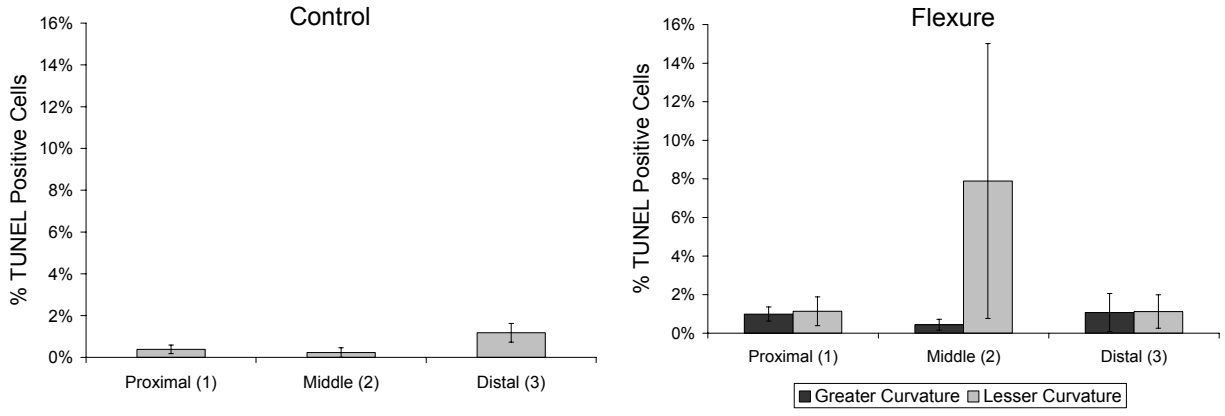

Figure 3.41 Apoptosis distribution for each specimen (Control and Flexure) in experiment FLX-4. Bars represent that average EBD intensity for the six cross-sections sampled in the segment. Error bars represent the standard error of the mean. The numbers above the bars indicate which other segments in the given specimen had significant differences in apoptosis from that segment. For flexure significant differences between the greater and lesser curvature are noted by †.

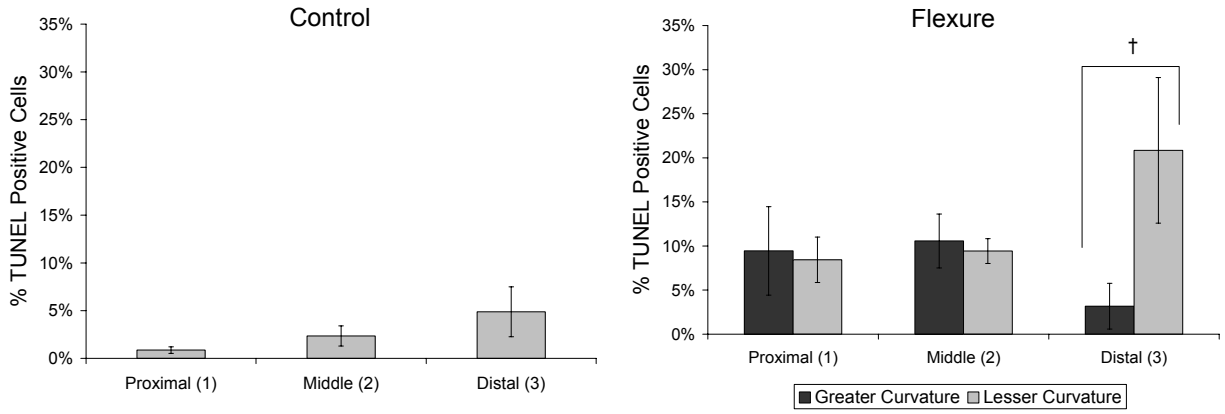

Figure 3.42 Apoptosis distribution for each specimen (Control and Flexure) in experiment FLX-5. Bars represent that average EBD intensity for the six cross-sections sampled in the segment. Error bars represent the standard error of the mean. The numbers above the bars indicate which other segments in the given specimen had significant differences in apoptosis from that segment. For flexure significant differences between the greater and lesser curvature are noted by †.

3.2.4 Proliferation

PCNA expression was not detectable by immunohistochemistry in samples from all deformations experiments (Figure 3.43). Efficacy of the staining methodology and protocol described in Section 3.1.4.3 was determined using porcine small bowel tissue (Figure 3.43).

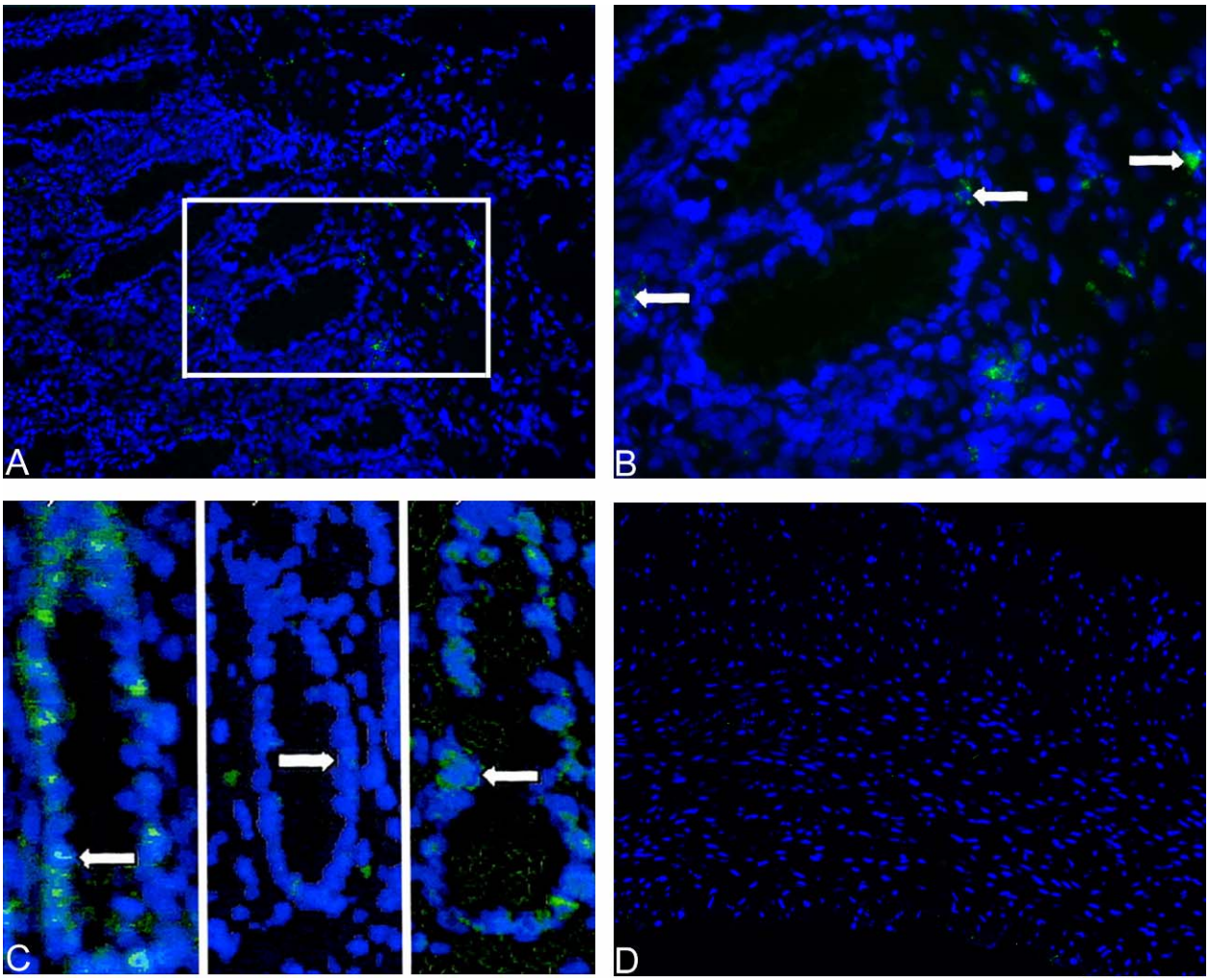

Figure 3.43 Photomicrographs of PCNA immunohistochemistry: A) 200x image of porcine small intestinal crypts; B) 400x image from inset in A; C) Representative images of PCNA-stained crypt epithelial cells from piglets on various nutrition regimens (Image from [186]); D) Representative image of an *ex vivo* perfused vascular segment, which showed no PCNA staining. The lumen is oriented to the bottom left corner. Arrows in B and C indicated PCNA-positive cells.

3.3 DISCUSSION

3.3.1 Cyclic Mechanical Deformation and Atherogenic Potential

These results demonstrate that vascular specimens exposed to normal hemodynamics plus cyclic axial stretch or flexure *ex vivo* have increase macromolecular permeability and apoptosis. Given the tight control over perfusion conditions (recall Figure 3.5 and Figure 3.6) and the paired study design, the increases in permeability and apoptosis can be attributed directly to the addition of either cyclic stretch or flexure. This general finding supports the hypothesis that the coronary arteries are more susceptible to atherosclerosis due to the added heart-induced deformations of cyclic stretch and flexure. Increased permeability indicates possible EC dysfunction and could allow for the convection of lipids and oxidized lipids such as LDL to enter the vessel wall and incite an inflammatory response. The increased numbers of apoptotic cells in stretch and flexed specimens localized to the intimal layers of the vessel wall provide a potential mechanism for this EC dysfunction. EC death with impaired wound healing can cause transient loss of endothelial barrier function leading to increased permeability. In addition, SMC apoptosis could indicate mechanical micro-damage, increased cell turnover, and the beginning of a fibroproliferative response. While no proliferation was detected in these experiments, apoptosis appears to be an important contributor to increased permeability and may precede a proliferative response.

Keeping in mind the highly localized and heterogeneous nature of atherosclerosis, a specific tissue processing protocol was used to characterize the spatial distribution of atherogenic endpoints. The distribution of permeability and apoptosis for an *ex vivo* perfused vascular segments exposed to either cyclic stretch, flexure, or twist was non-uniform and varied greatly

between individual specimens within experimental sets. This indicates the potential for global deformations such as stretch and flexure to generate spatially variable mechanical stresses which influence the spatial distribution of cellular responses including permeability and apoptosis. The spatial distribution of normalized permeability averaged within experimental sets showed only small non-significant spatial variations (recall Figure 3.9). In the case of stretch, the proximal and distal segments appeared to have slightly more permeability than the middle portion. For flexure, the proximal segment had the greatest permeability and within in this area the greater curvature had a greater proportion. Twist demonstrated a linear increase in permeability from proximal to distal. The lack of significance comes from high variability among specimens within an experimental group. Examination of the permeability distribution within individual specimen demonstrates significant spatial variation. The shapes of these distributions appear to be unique to a given specimen. Similarly, for apoptosis the average normalized distributions were not significant and therefore difficult to interpret (recall Figure 3.27). Although, there was generally an increase in apoptosis in the lesser curvature of the middle sub-segment which could be attributed to large stress changes in that region of maximal curvature. However, like permeability, non-normalized individual distributions were significant and unique to a given specimen. These results highlight the immense variation in vascular tissue response to global stimuli. Further understanding in vascular pathobiology requires investigation into how global stimuli (e.g., hyperlipidemia, cyclic stretch, etc.) perturb the local biomechanical and biochemical milieu that influence the local cellular / tissue response.

3.3.2 Limitations and Experimental Concerns

As with any *ex vivo* or *in vitro* experimental setup several simplifications from the *in vivo* state are required. First, the cyclic pressure waveform provided by the centrifugal pump only captures the first harmonic of a physiologic pressure signal. Likewise, the cyclic deformations had a sinusoidal motion profile which would not contain the higher frequency content of the physiologic state. Lastly, because of the difficulties in making, sterilizing, and maintaining a cell culture medium with physiologic viscosity, the perfusate medium used in this study was normal cell culture medium with a density and viscosity similar to that of water. With this type of medium it would be impossible to generate the flow rates required for a physiologic shear stress. Therefore, the flow rate was set to recreate a physiologic shear rate. The implications of this are discussed in more detail in Section 6.3.2.

Cyclic twist appeared to increase both permeability and apoptosis, though it was not statistically significant. A power analysis on the twist experiment set indicates that an additional 9 experiments would be required to detect significant changes in permeability and an additional 23 experiments for apoptosis. The addition of that many experiments calls into question the biological significance of any effect seen.

The microscopic TUNEL assay not only provides the ability to quantify the number of apoptotic cells but also their location within a tissue. Almost all sections had some degree of apoptosis in the adventitial layer. This amount of apoptosis may be slightly elevated compared to normal healthy tissue but can be attributed to the surgical harvest of the vessel segments. Since vessel segments were always harvested in pairs this effect should been removed in the paired normalization.

The sparse staining for PCNA is a concern. Without this information (in conjuction with the apoptosis data) it is impossible to determine the net change in cell turn over and potential proliferative response of the tissue. Unfortunately, 12 hours may be too soon to detect changes in proliferation, given the number of gene expression changes required to activate the cell cycle machinery. This time point was chosen to maximize the detection of all endpoints including the gene and protein expression endpoints originally proposed. The expression of PCNA was just on the threshold of that time point [96, 98]. To confirm the lack of PCNA staining was indeed real, a thorough check on the experimental technique was performed (see Figure 3.43). While the PCNA signal for the porcine small intestine was less than expected, it can be explained by the fact that the animal had been been NPO for 12 to 18 hours prior to surgery. It is likely, that with the lack of active digestion the need to continue to replenish the intestinal epithelium is diminished and with it the expression of PCNA. Indeed, the level of PCNA staining was similar to the middle panel of C in Figure 3.43 which is from a piglet that had been on total parental nutrition [186].

3.4 CONCLUSIONS

Cyclic axial stretch and cyclic flexure play an important role in the biomechanical environment of the coronary vasculature. These deformations can lead to increases in intimal and medial apoptosis with comcomitant increases in permeability. Such changes indicate an increased potential for atherosclerotic lesion development. The spatial variations of these responses are complicated and appear to be vessel specimen specific. To better understand how global mechanical stimuli such as cyclic axial stretch and flexure contribute to the local biomechanical

milieu and potentially influence these biologic processes, experiment specific computational solid and fluid stress analyses are required. These analyses can provide the local distribution of mechanical stress which can then be correlated with distribution of biological response.

4.0 COMPUTATIONAL SOLID STRESS ANALYSIS

The goal of Specific Aims 2 and 3 was to estimate the distribution of mechanical stresses specifically for each perfused arterial segment from Specific Aim 1. Two types of mechanical stress have been implicated in arterial pathology – mural (solid) stresses and fluid or shear stresses. Both were considered in this project. The fluid (shear) stresses are the focus of Chapter 5, while the solid stresses are the focus of this chapter.

Finite element analysis was employed on an experiment-specific basis to estimate the mural stresses associated with each vessel segment perfused in the experiments described in Chapter 3. These analyses provided insight into the spatial distribution of stresses within the arterial wall created by the cyclic deformations of pulsatile pressure, axial stretching, flexure, and twist. Several items are required to perform finite element analysis. First, a geometric reconstruction or solid model of the body of interest is needed. In this case, the geometry of each perfused vessel specimen from Specific Aim 1 was reconstructed (see Section 4.1). Second, a description of the material behavior that relates deformation or strain to stress is required. For vascular tissue, several types of constitutive material models have been described in the literature [167, 187-189]. For this application, two types of material models were employed (see Section 4.2. In addition, a new model was developed to account for shear stresses due to torsion (see Section 4.2). Third, appropriate boundary or loading conditions must be applied to recreate the mechanical environment utilized in each experiment. To simulate the loading regimens provided

by the EVPS, experiment-specific displacement and loading schemes were generated (see Section 4.3).

The following sections describe the development of the finite element models, the results of the individual experiment-specific simulations, and the implications for understanding the distribution of mural stresses within the vascular segments under various mechanical deformations.

4.1 GEOMETRIC RECONSTRUCTION

Geometric reconstruction was carried out in two steps. First, geometric measurements were made on each perfused vascular specimen. Second, those measurements were used to develop a three-dimensional model of the arterial wall that could be discretized into elements for subsequent finite analysis.

4.1.1 Measurement of Vascular Segment Dimensions

As described in the tissue processing procedure (recall Section 0 and Figure 3.3) the unloaded length (L) of each vascular segment was measured following each EVPS experiment, after removal of tissue that had been in contact with the cannulae, but prior to tissue processing. Ring-shaped specimens were cut from the proximal and distal ends of the arterial specimen, placed in small culture dishes filled with normal saline, and transferred to a warming plate set at 37˚C. After 30 minutes of incubation to ensure physiologic temperature was reached, pictures of the cross-section of the segments were taken with a digital camera (Nikon, Coolpix 950, Japan)

(Figure 4.1A). JPEG images were converted to uncompressed 8-bit grayscale TIFF images and imported into Scion Image v4.0 (Scion Corporation, Frederick, MD). Edge detection was performed using the Scion Image edge detection filter. This filter performs a Sobel edge detection operation using 3 x 3 spatial convolutions, where the value of each pixel in the selection is replaced with the weighted average of its 3 x 3 neighborhood. Two convolutions are done using the kernels shown in (4.1), generating vertical and horizontal derivatives.

$$\begin{matrix} 1 & 2 & 1 \\ 0 & 0 & 0 \\ -1 & -2 & -1 \end{matrix} \qquad \begin{matrix} 1 & 0 & -1 \\ 2 & 0 & -2 \\ 1 & 0 & -1 \end{matrix} \tag{4.1}$$

The results are then combined by using the square root of the sum of the squares of the two derivatives. After performing edge detection (Figure 4.1B), the inner and outer diameters were measured in pixels and converted to centimeters using a calibration ruler that was submerged in each culture dish. A set of orthogonal pairs of inner and outer diameter measurements were made on each segment (Figure 4.1 C and D).

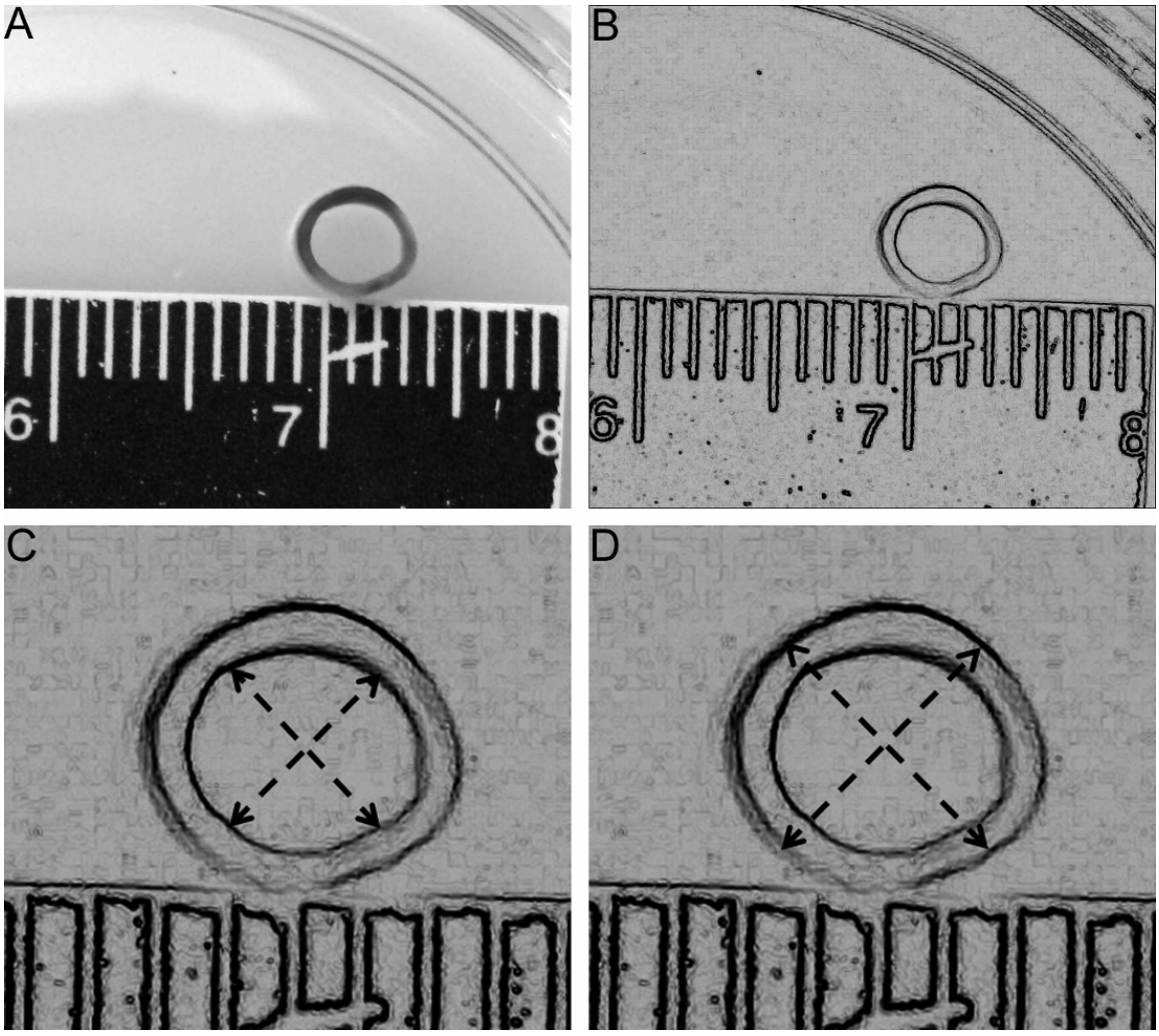

Figure 4.1 Digital images of vascular segments used for geometric measurements. A) Raw image; B) Image in A after edge detection; C) Close-up of B with a set of orthogonal inside diameter lines; and D) Close-up of B with a set of orthogonal outside diameter lines.

4.1.2 Volume Reconstruction

To reconstruct the entire vascular specimen volume, the shape was assumed to have a circular cross-section with linear taper in diameter (both inner and outer) and wall thickness. Therefore, the orthogonal diameter measurements were averaged to calculate a single, mean inner and outer diameter for the proximal and distal ends. The wall thickness was calculated as half the difference between the mean inner and outer diameters. The diameters and wall thickness for any point along the length of the vessel specimen was determined via simple linear interpolation (Figure 4.2). Given the axi-symmetry of these reconstructions the geometries were easy to build directly within the ABAQUS v6.5 CAE part module. Based on this reconstruction method, a "taper parameter" was defined. The taper of a given geometric measure (i.e., OD, ID, and WT) was defined as the difference between the proximal and distal values divided by L. For example, the taper in OD would be

$$\text{Taper}_{OD} = \frac{OD_{proximal} - OD_{distal}}{L} \tag{4.2}$$

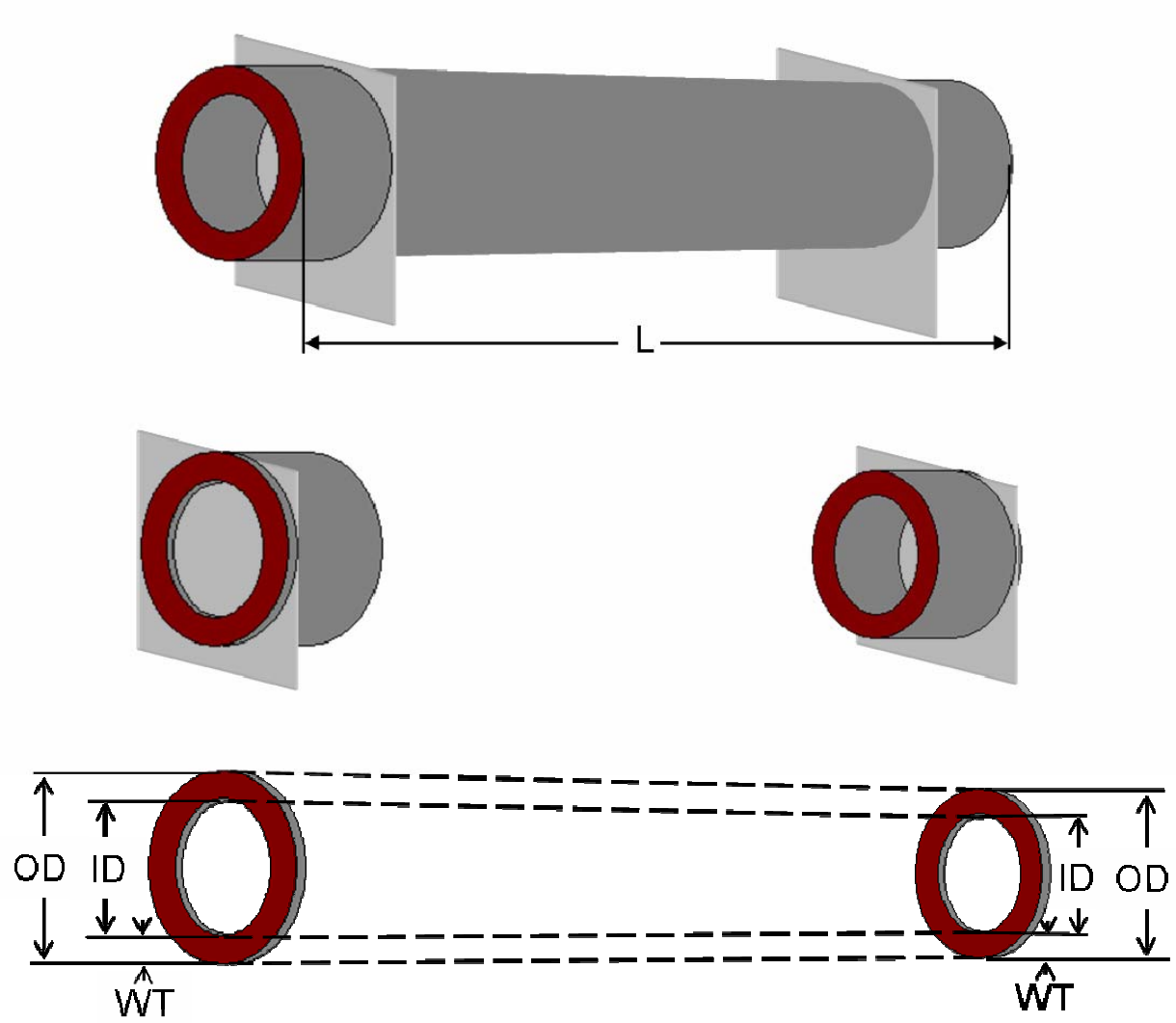

Figure 4.2 Schematic of the 3D reconstruction scheme. Mean inner diameter (ID), outer diameter (OD), and wall thickness (WT) were calculated from orthogonal measurements taken on rings from the the proximal and distal ends. Intervening diameter and wall thickness values were determined by linear interpolation along the length of the vessel segment (L).

4.2 MATERIAL MODEL

To date, no material characterization of porcine femoral arteries has been published in the literature. In light of the close morphology between femoral and coronary arteries (see Section 3.1.1 and Figure 3.2), the material properties of coronary arteries, which have been described in the literature, were used [187, 189]. Two different types of strain energy functions were utilized to model the constitutive material properties of porcine femoral arteries. The first type was a specific form of the generalized Mooney-Rivlin relation. This function assumes the material to be incompressible, hyperelastic, and isotropic. It is expressed as a polynomial of the form:

$$W = \sum_{i=0,j=0}^{\infty} a_{ij} (I_1 - 3)^m (I_2 - 3)^n, \quad a_{00} = 0 \tag{4.3}$$

where I_1 and I_2 are the strain invariants and a_{ij} are the hyperelastic material parameters [188]. Specifically,

$$I_1 = tr\mathbf{C} \tag{4.4}$$

and

$$I_2 = \frac{1}{2}\left[(tr\mathbf{C})^2 - tr\mathbf{C}^2\right] \tag{4.5}$$

where **C** is the right Cauchy-Green strain tensor [188]. The specific form of this strain energy function and the associated material parameters utilized in this study were originally described by Lally et al. [187]. They fit a third-order Mooney-Rivlin strain energy function of the form:

$$W = a_{10}(I_1 - 3) + a_{01}(I_2 - 3) + a_{20}(I_1 - 3)^2 + a_{11}(I_1 - 3)(I_2 - 3) + a_{30}(I_1 - 3)^3 \tag{4.6}$$

to porcine coronary arteries using biaxial test data. The derived material parameters in kPa were: a_{10}=11.438, a_{01}=21.296, a_{20}=601.245, a_{11}=1205.260, and a_{30}=0 [187]. While this model shows

good agreement with experimental mechanical testing data in certain loading cases, it cannot describe the anisotropic characteristics of vascular tissue.

To incorporate anisotropy, a second type of strain energy model was investigated in this analysis. Chuong and Fung [190] described a pseudoelastic strain energy model of the form:

$$W = \frac{1}{2} c_0 \left(e^Q - 1 \right) \tag{4.7}$$

where

$$Q = c_1 E_r^2 + c_2 E_\theta^2 + c_3 E_z^2 + 2c_4 E_\theta E_r + 2c_5 E_\theta E_z + 2c_6 E_z E_r \tag{4.8}$$

E_r, E_θ, and E_z are the principle components of the Green's strain tensor. This strain energy formulation differs from the Mooney-Rivlin model in that it does not assume isotropy. Instead the material is said to be cylindrically orthotropic. Wang et al. [189], determined the material constants c_0-c_6 for the porcine left anterior descending (LAD) artery and the right coronary artery. The parameters for the LAD, c_0=8.92 kPa, c_1=0.55, c_2=1.25, c_3=2.46, c_4=0.08, c_5=0.36, and c_6=0.06, were used in this study.

A limitation of the Fung-type exponential model in (4.7) and (4.8) is that is does not include any shear terms. Specifically, it does not include an $E_{\theta z}$ term to account for shear due to torsion. Since twisting is one of the deformations under investigation here, this posed a significant obstacle to understanding the stress distribution in arteries under torsion. Therefore, the development of a new exponential material model was undertaken to include torsion shear stresses. The following sections describe this development and the implementation of both material models into the finite element solver package, ABAQUS v6.5.

4.2.1 Calculation of the Torsion Shear Parameter For the Fung-type Strain Energy Model

While the shear moduli due to twisting have been determined for pig coronary arteries [191], they were not constant, varying with the longitudinal stretch ratio and the applied internal pressure. Therefore, in order to develop a finite element simulation of the arterial wall under torsion, a material model that incorporates this relationship between shear modulus and the other mechanical stimuli is required. As detailed in the following sections, we utilized previously-reported shear moduli to calculate a shear strain parameter in a Fung-type exponential strain energy model of the arterial wall and determined if this single constant can account for the observed behavior of arterial segments under torsion.

4.2.1.1 Methods

Biomechanical Principles

In this analysis, the coronary artery is assumed to be a straight cylinder with circular cross-section (Figure 4.3A). Therefore, the dimensions of a segment of this artery can be defined by the length (L), the inner radius (r_i) and the outer radius (r_o). It is acted upon by a pressure (P) (i.e., blood pressure), a longitudinal tension which generates a stretch ratio (λ), and a torque (T), which causes the vessel to twist by angle (θ). As previously demonstrated, the zero-stress state (the configuration in which all loads are zero) of an artery is determined by making a radial cut in an arterial ring, allowing the ring to open into a sector [192, 193]. The inner (R_i) and outer radii (R_o) and opening angle (Φ) of that sector represent the zero-stress or reference configuration (Figure 4.3B).

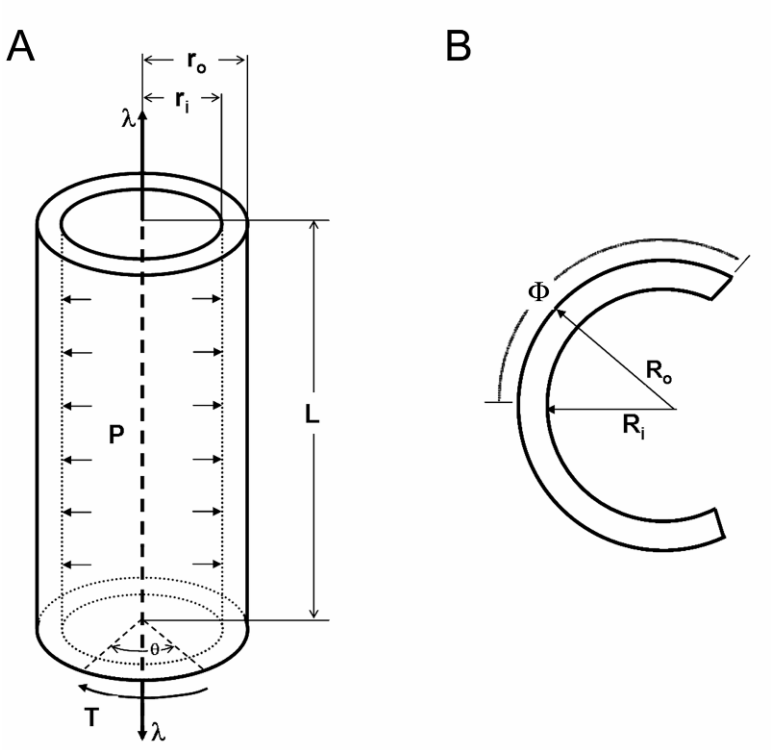

Figure 4.3 A) Schematic of an arterial segment of length L and inner and outer radii r_i and r_o respectively, acted upon by a longitudinal stretch λ, an intraluminal pressure P, and a torque T which generates a twist angle θ. B) Schematic of a sector of an arterial ring with inner and outer radii R_i and R_o respectively, and opening angle Φ.

The deformation gradient **F** of an intact, loaded arterial segment would be [167]:

$$\mathbf{F} = \begin{bmatrix} \frac{\partial r}{\partial R} & 0 & 0 \\ 0 & \frac{\pi r}{\Phi R} & r\gamma \\ 0 & 0 & \lambda \end{bmatrix} \tag{4.9}$$

where γ is the twist per unit length or θ/L. Assuming that arterial tissue is incompressible requires that the determinant of **F** is 1. Thus,

$$\det \mathbf{F} = \frac{\partial r}{\partial R} \cdot \frac{\pi r}{\Phi R} \cdot \lambda \tag{4.10}$$

$$\frac{\partial r}{\partial R} = \frac{\Phi R}{\pi r \lambda} \tag{4.11}$$

The deformation of a given point in this arterial segment can be characterized by the Green's strain tensor (**E**), which is given by

$$\mathbf{E} = \frac{1}{2}\left(\mathbf{F}^{T} \cdot \mathbf{F} - \mathbf{I}\right) = \frac{1}{2}\begin{pmatrix} \left(\frac{\Phi R}{\pi r \lambda}\right)^2 - 1 & 0 & 0 \\ 0 & \left(\frac{\pi r}{\Phi R}\right)^2 - 1 & \frac{r^2 \pi \gamma}{\Phi R} \\ 0 & \frac{r^2 \pi \gamma}{\Phi R} & r^2\gamma^2 + \lambda^2 - 1 \end{pmatrix} \tag{4.12}$$

where **I** is the identity matrix [167].

Humphrey described a generalized form of a strain energy function to describe the elasticity of finite deformations in arterial tissue:

$$W = \frac{1}{2} c_0 \left(e^{Q} - 1\right) \tag{4.13}$$

where

$$\begin{aligned} Q = {} & c_1 E_r^2 + c_2 E_\theta^2 + c_3 E_z^2 + 2c_4 E_\theta E_r + 2c_5 E_\theta E_z + 2c_6 E_z E_r \\ & + c_7\left(E_{\theta z}^2 + E_{z\theta}^2\right) + c_8\left(E_{rz}^2 + E_{zr}^2\right) + c_9\left(E_{\theta r}^2 + E_{r\theta}^2\right) \end{aligned} \tag{4.14}$$

E_r, E_θ, and E_z are the principle components and $E_{\theta z}$, etc., are the shear components of the Green's strain tensor shown in (4.12) [167]. Note that a more specific form of this model was originally put forth by Chuong and Fung (see equations (4.7) and (4.8)) [190]. They assumed a cylindrically orthotropic material symmetry and normal loads, and therefore determined constants for only the first 6 terms in (4.14) [190].

The loading case described in (4.12) allows simplification of the general exponential strain energy function in (4.13) and (4.14). Specifically, E_{rz}, E_{zr}, $E_{\theta r}$ and $E_{r\theta}$ are zero. Also, E is symmetric (i.e., $E=E^T$) which makes $E_{\theta z} = E_{z\theta}$. Therefore, the simplified form of Q becomes

$$Q = c_1 E_r^2 + c_2 E_\theta^2 + c_3 E_z^2 + 2c_4 E_\theta E_r + 2c_5 E_\theta E_z + 2c_6 E_z E_r + 2c_7 E_{\theta z}^2 \tag{4.15}$$

The Cauchy stress tensor ($\boldsymbol{\sigma}$) can then be determined from the strain energy function via

$$\boldsymbol{\sigma} = -p\mathbf{I} + \mathbf{F} \cdot \frac{\partial W}{\partial \mathbf{E}} \cdot \mathbf{F}^T \tag{4.16}$$

where p is the Lagrangian multiplier.

Experimental Data

Values for parameters c_0-c_6 have been previously determined for porcine coronary arteries [189]. No values have been reported for the proposed parameter c_7, but the work by Lu et al. describing the shear modulus properties of porcine coronary arteries provide the necessary information to determine its value [191]. They demonstrated that the torque required to twist an artery varied linearly with γ. Therefore, the relationship between torsion shear stress and shear strain can be described by

$$\overline{\sigma_{\theta z}} = G\, r\, \gamma \tag{4.17}$$

where G is the shear modulus. G was found to be linearly proportional to the mean circumferential stress, such that

$$G = \alpha + \beta\, \overline{\sigma_\theta} \tag{4.18}$$

where $\overline{\sigma_\theta}$ is determined from the Law of Laplace [191]. The linear constants (α and β) were found to depend on the longitudinal stretch ratio λ (Table 4.1). The result was a family of linear functions describing the relationship between G, λ, and $\overline{\sigma_\theta}$.

Table 4.1 Average linear constants ± standard deviation for the family of linear functions for shear modulus determined experimentally in [191]. Shear moduli versus circumferential wall stress and longitudinal stretch ratio is given in (4.18).

λ	α (kPa)	β (unitless)
1.2	19.4 ± 2.87	0.553 ± 0.101
1.3	24.7 ± 3.86	0.825 ± 0.172
1.4	33.1 ± 7.98	1.47 ± 0.369

Derivation of an expression for c_7

While these previous experiments by Lu et al. [191] provide the necessary data for developing a finite element model of arterial segments under torsion, the form of the relationship is not conducive for finite element analysis. Ideally the relationship would be encompassed in the strain energy function, specifically in the value of the parameter c_7. To do this, the Cauchy torsion shear stress component was derived from equations (4.12), (4.13), (4.15), and (4.16) and written as

$$\sigma_{\theta z} = \left(\frac{\pi\, r\, \lambda}{\Phi\, R}\right)\frac{\partial W}{\partial E_{\theta z}} + r\,\gamma\,\lambda\frac{\partial W}{\partial E_z} \tag{4.19}$$

Evaluating the derivatives yields

$$\sigma_{\theta z} = c_0 c_7\left(\frac{\pi r}{\Phi R}\right)^2 r\,\gamma\,\lambda\, e^Q + c_0\left(c_5 E_\theta + c_6 E_r + c_3 E_z\right) r\,\gamma\,\lambda\, e^Q \tag{4.20}$$

Setting (4.20) equal to the expression derived by Lu et al. (4.17) [191] gives:

$$\left(\alpha + \beta\,\overline{\sigma_\theta}\right) = c_0 c_7\left(\frac{\pi\, r}{\Phi\, R}\right)^2 \lambda\, e^Q + c_0\left(c_5 E_\theta + c_6 E_r + c_3 E_z\right)\lambda\, e^Q \tag{4.21}$$

Solving for c_7 gives:

$$c_7 = \left(\frac{\Phi R}{\pi r}\right)^2\left[\frac{\left(\alpha + \beta\,\overline{\sigma_\theta}\right)}{c_0 \lambda e^Q} - \left(c_5 E_\theta + c_6 E_r + c_3 E_z\right)\right] \tag{4.22}$$

Note that (4.22) is not a closed form solution because c_7 appears in the expression for Q (see (4.15)). However, it was assumed that c_7 makes a negligible contribution to Q and therefore Q was calculated without the c_7 term in the evaluation of (4.22). The validity of this assumption was confirmed once values of c_7 were determined.

Finite element analysis-based calculation of c_7

Based on (4.22) the data on the strain state of an arterial segment under circumferential (pressure) and longitudinal (stretch) load is required to calculate c_7. This information was obtained by finite element analysis using ABAQUS v6.5. The user-defined subroutine UMAT was used for incorporation of custom material properties; i.e., W given by (4.13) and (4.15) (see Section 4.2.2 and Appendix C). The parameters used in (4.15) were previously determined by Wang et al. [189] for intact porcine left anterior descending artery (LAD): c_0=8.92 kPa, c_1=0.55, c_2=1.25, c_3=2.46, c_4=0.08, c_5=0.36, c_6=0.06. The specific gravity was assumed to be 1.0 and arterial tissue was assumed to be incompressible. This constraint was applied by the use of the penalty function

$$\varphi(\mathrm{J}) = (\mathrm{J}-1)^2 \tag{4.23}$$

where J is the determinant of the deformation gradient F. This constraint was used in place of the Lagrangian multiplier in (4.16) making the Cauchy stress

$$\boldsymbol{\sigma} = \mathbf{F} \cdot \frac{\partial \mathrm{W}}{\partial \mathbf{E}} \cdot \mathbf{F}^{\mathrm{T}} + \eta \frac{\partial \varphi}{\partial \boldsymbol{\varepsilon}} \tag{4.24}$$

where ε is the logarithmic strain tensor and η is the penalty parameter. Incompressibility was maintained with $\eta=10^6$. Three different geometries representing the mean ("Medium") porcine LAD dimensions plus ("Large") or minus ("Small") one standard deviation (Table 1) [194] were constructed and meshed using 8-node biquadratic, axi-symmetric, hybrid quadrilateral elements.

All geometries had the same length (20 mm) and opening angle (2.97 rad). The residual stress and strain fields (determined from the opening angle) were applied as initial conditions using the ABAQUS user-defined functions SDVINI and SIGINI shown in Appendix E.

The analyses for the calculation of c_7 were performed in two static loading steps. The first step was a linear ramp in the longitudinal stretch until the desired λ was achieved. The second was a linear ramp in pressure from 0 to 16 kPa. The resulting inner and outer radii were computed during this pressurization step and used in the calculation of c_7 at the 21 combinations of applied pressure and stretch. It should be noted that by using a static analysis, all inertial effects were ignored.

Mean values for the parameter c_7 of the arterial segment were determined at pressures of 0, 3, 5, 8, 10.7, 13.3, and16 kPa (corresponding to 0, 22.5, 60, 80, 100, and 120 mm Hg respectively) with longitudinal stretch ratios of 1.2, 1.3, and 1.4, thus generating 21 distinct values which were then averaged. This was repeated for each of the three geometries in Table 4.2.

Table 4.2 Porcine LAD dimensions from [194].

	Small	Medium	Large
Inner radius (mm)	0.817	0.963	1.108
Outer radius (mm)	1.047	1.219	1.390
Wall thickness (μm)	230	256	282

In silico triaxial experiments

Each value determined for c_7 was validated through *in silico* simulation of the triaxial experiments performed by Lu et al [191]. As before, finite element analysis was performed using ABAQUS v6.5 with the UMAT (see Section 4.2.2 and Appendix D) user-defined subroutine on the three geometries indicated in Table 4.2. However, in this case, the strain energy function utilized by UMAT was that defined in equations (4.13) and (4.15) incorporating the newly calculated value for c_7. The simulated experiments had three loading steps (Figure 4.4). There was a sequential linear ramp first in stretch and then in pressure to desired values. Following this, one end of the vessel segment was fixed in position while a clockwise circumferential displacement was applied to the other end, generating a twist angle of -25°. The displacement was then reversed; i.e., a counter-clockwise circumferential displacement was applied until the twist angle reached 25°. The shear stress ($\sigma_{\theta Z}$) evaluated at the nodes of the end being displaced circumferentially was recorded throughout the twist loading cycle. These values were used to calculate the torque (T) required to achieve this twist via

$$T = 2\pi \int_{r_i}^{r_o} \sigma_{\theta z} r^2 dr \tag{4.25}$$

This integral was estimated via the trapezoid rule evaluated at the finite element nodes. Substituting the relationship between shear stress and shear modulus (see (4.17)), determined by Lu et al. [191] and evaluated the integral in (4.25) gives

$$T = G\, K\, \gamma \tag{4.26}$$

where K is the polar moment of inertia given by

$$K = \frac{\pi}{2}\left(r_o^4 - r_i^4\right) \tag{4.27}$$

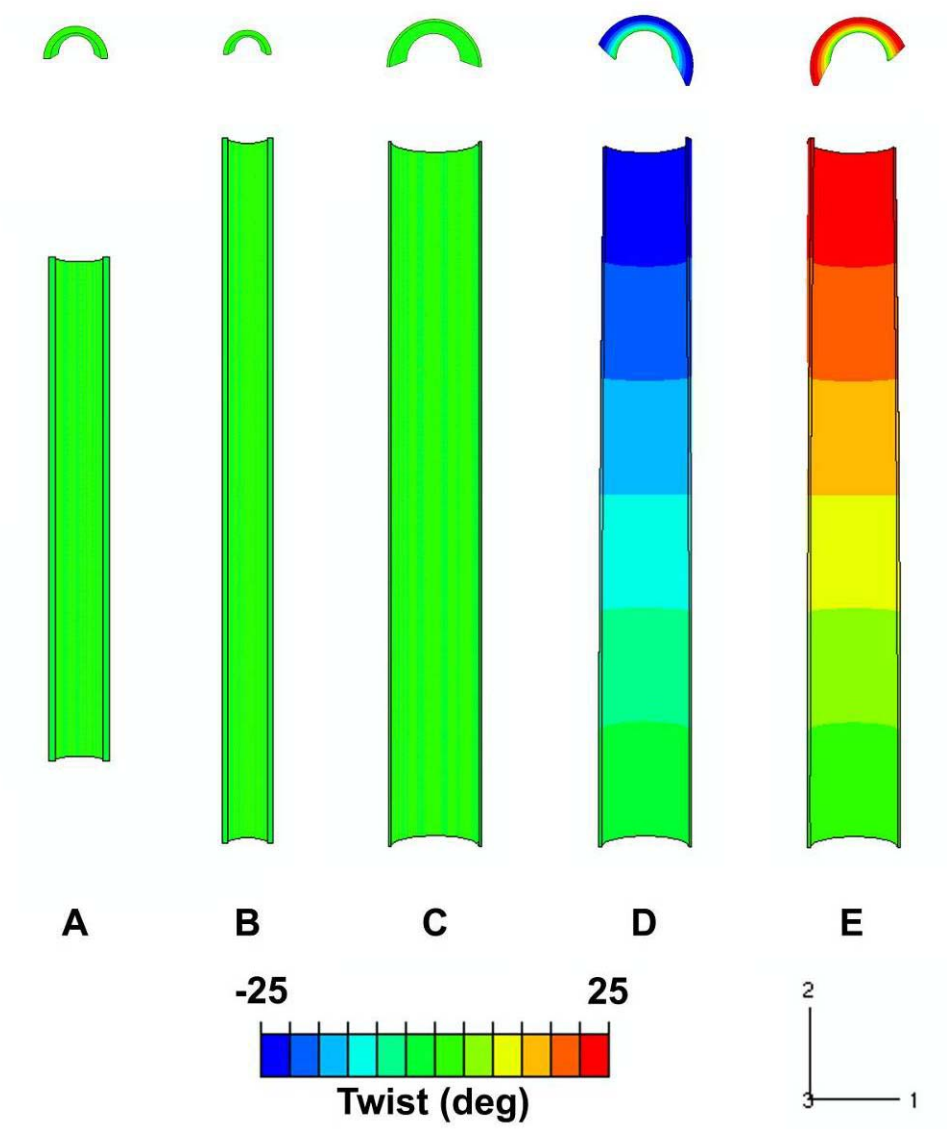

Figure 4.4 *In silico* triaxial experimental protocol demonstrated by a representative vessel geometry. Two views are shown of a hemi-vessel at each step with angle of twist plotted as the color map: An end view (top) and a side view into the open end of the hemi-vessel (bottom). A) Vessel segment in the unloaded configuration; B) stretched to the desired λ; C) pressurized to the desired P; D) twisted on upper end by $\theta = -25^{\circ}$; E) returned to a zero twist; F) and twisted in the opposite direction, $\theta = 25^{\circ}$.

Plots of torque (T) versus polar moment of inertia times the twist per unit length ($K\gamma$) were generated for each combination of stretch ratio and pressure. The shear modulus (G) was then determined from the slope of these lines and compared to the moduli determined experimentally by Lu et al [191].

4.2.1.2 Results

Values for the parameter c_7

The inner and outer radii computed via finite element analysis for each of three porcine LAD geometries in Table 4.2 for a given longitudinal stretch and pressure combination are shown in Figure 4.5. The average values of c_7 calculated according to (4.22) for each longitudinal stretch and pressure combination for a given geometry are shown in Figure 4.6. The average value for c_7 across the three geometries was 0.0759±0.0009 (mean ± standard deviation).

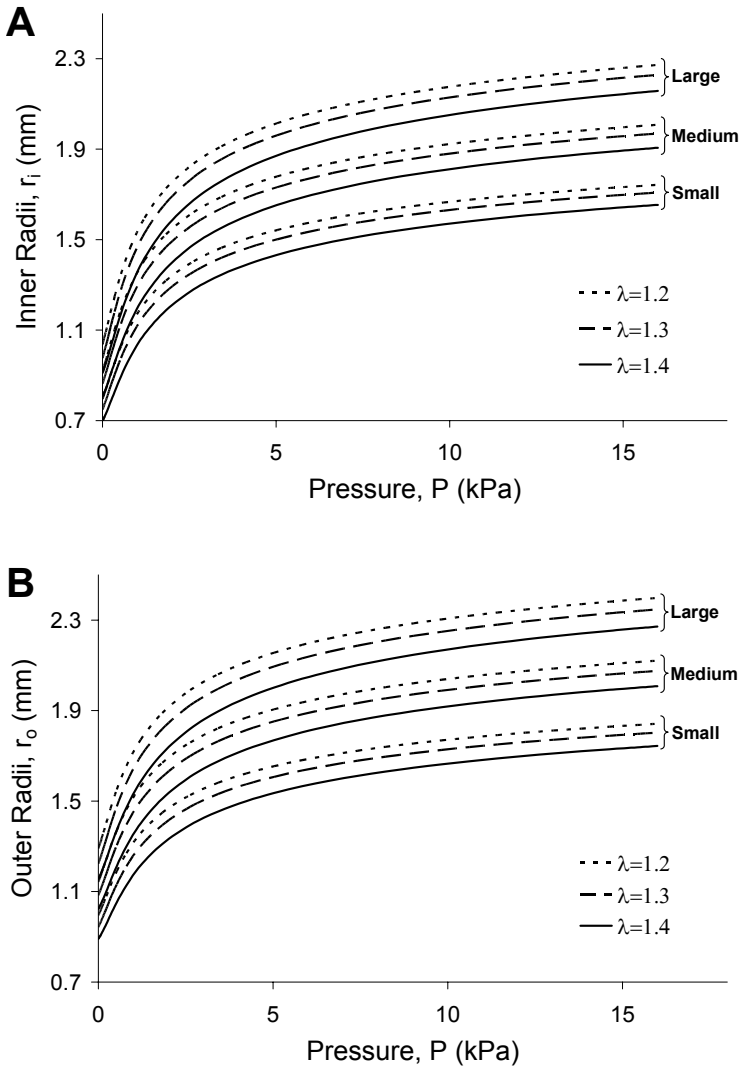

Figure 4.5 Plots of computed inner (A) and outer (B) radii versus pressure for the three porcine LAD geometries (Small, Medium and Large) at stretch ratios of 1.2, 1.3 and 1.4.

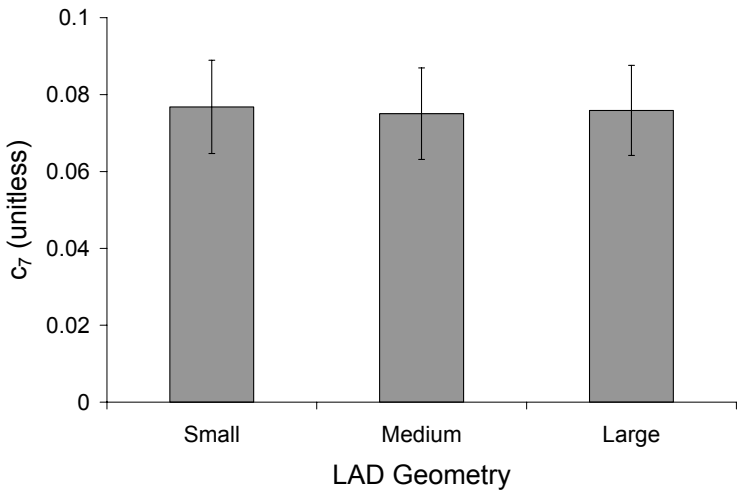

Figure 4.6 Calculated values for the parameter c_7 for each porcine LAD geometry (Small, Medium and Large). Bars represent the average value from each combination of pressure (0, 3, 5, 8, 10.7, 13.3, and 16 kPa) and stretch ratio (1.2, 1.3, and 1.4), a total of 21 combinations. Error bars represent the standard error of the mean.

In silico triaxial experiments

Incorporation of the average value for the c_7 term into the finite element simulation employing the exponential strain energy function defined by (4.13) and (4.15) generated linear relationships between torque and polar moment of inertia times twist per unit length shown in Figure 4.7. These plots are similar to those determined experimentally by Lu et al. [191]. A comparison of the family of linear functions used to describe the shear moduli by Lu et al. [191] (described by equation (4.18) and constants in Table 4.1) and the single exponential model with c_7 term shows close agreement (R^2>0.98) independent of the vessel segment geometry (Figure 4.8).

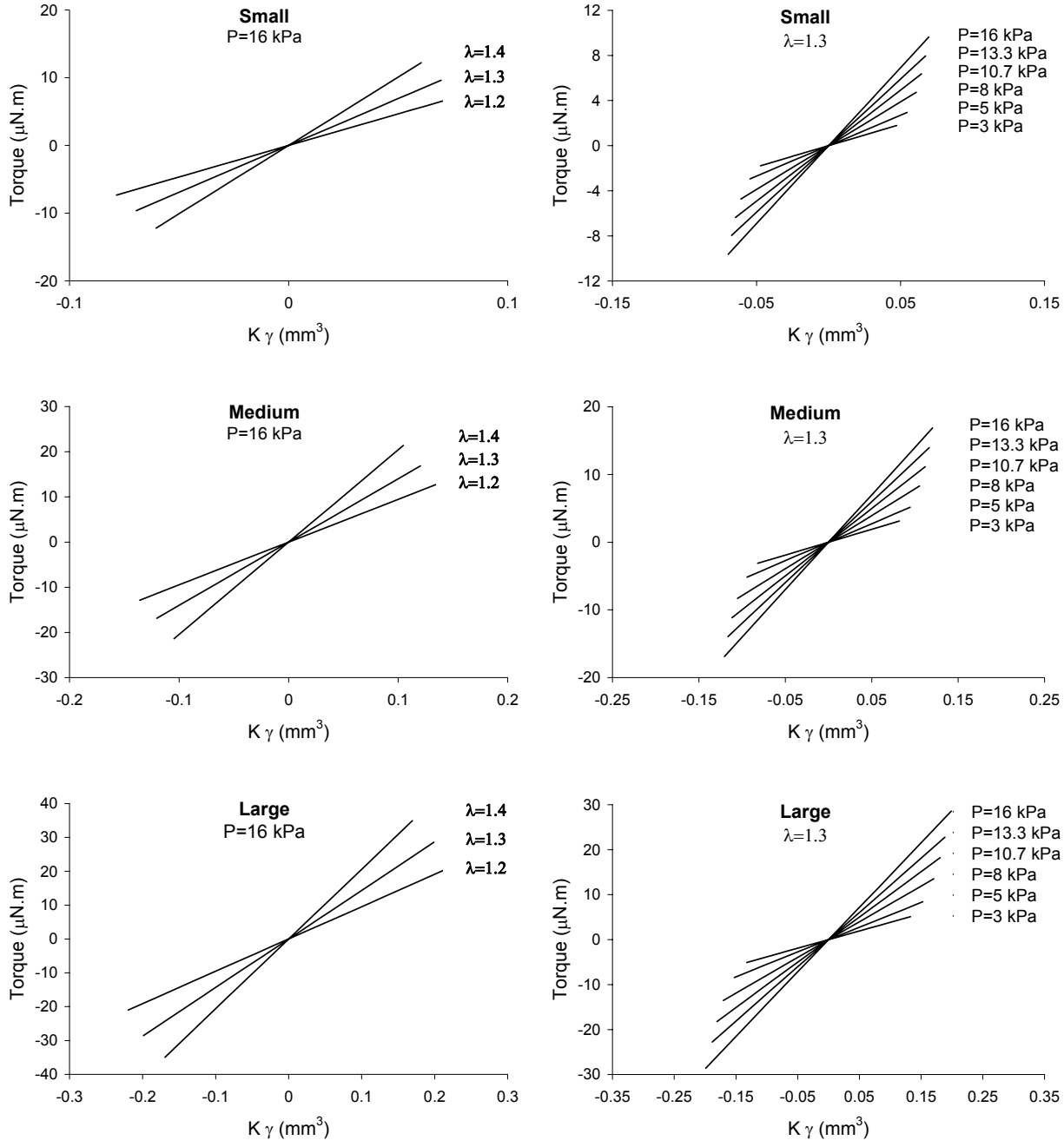

Figure 4.7 Plots of torque versus polar moment of inertia (γ) for various stretch ratios at constant pressure (left) and various pressures at constant stretch ratio (right) for each of three vessel geometries (Small, Medium, and Large).

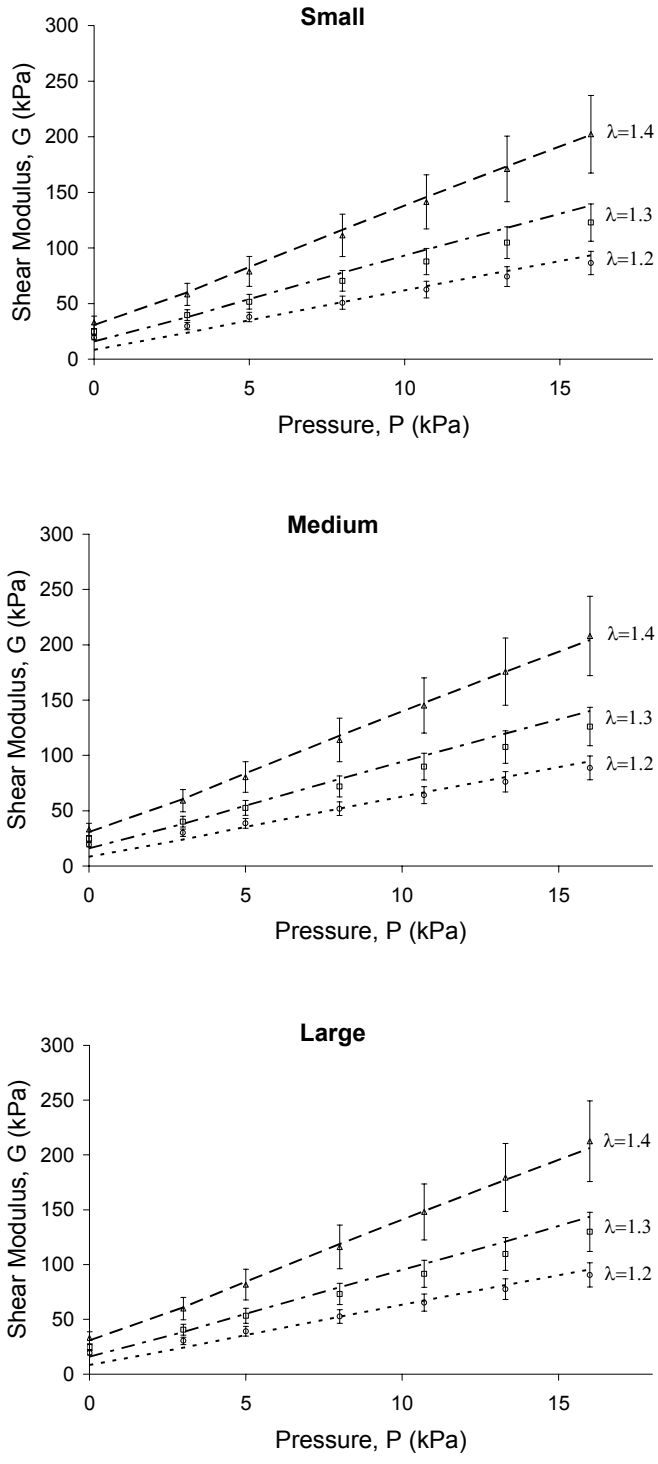

Figure 4.8 Shear modulus (G) as a function of pressure for various stretch ratios for each of three vessel geometries (Small, Medium, and Large). Individual points represent shear moduli determined by linear functions of mean circumferential wall stress from Lu et al [191] (see equation (4.18) and Table 4.1. Error bars represent a 95% confidence interval. The lines represent shear moduli predicted from the in silico triaxial experiments using W defined by (4.13) and (4.15); i.e., including the shear strain term (c7 = 0.0759).

Validation of assumptions and simulation quality

The difference between the values of Q at the maximum and minimum loading conditions of the mean LAD geometry with and without the c_7 term was found to be less than 0.02%, suggesting that c_7 does indeed have a negligible contribution to Q. The determinant (J) of the deformation gradient was monitored throughout the analysis and found to range from 0.9998-1.0004, suggesting that incompressibility assumption was met.

Valid finite element analysis requires that the results be independent of the mesh size. To ensure mesh independence, the shear stress $\sigma_{\theta Z}$ at the end nodes used in the evaluation of the torque from (4.25) were determined to be nearly the same for three different mesh densities (Figure 4.9). All reported results utilized the medium mesh density.

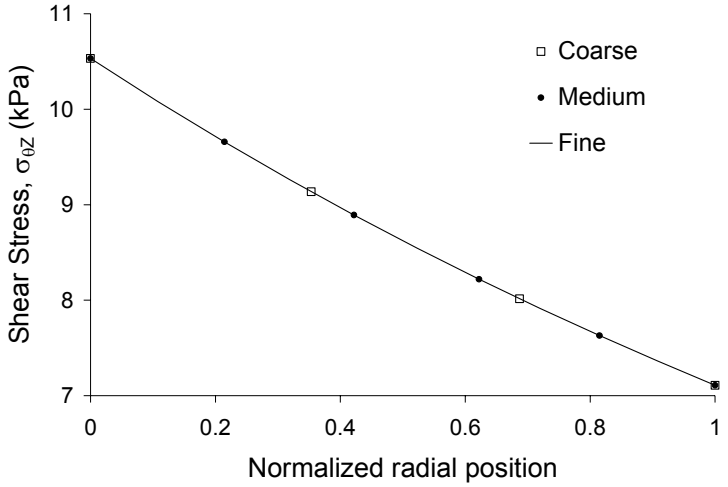

Figure 4.9 Mesh independence analysis. The radial distribution of shear stress ($\sigma_{\theta z}$) for the nodes at the twist end of the vessel is shown for three different mesh densities (coarse, medium, and fine).

4.2.1.3 Discussion

Characterization of the mechanical stress distribution in the coronary arterial bed could provide insight into the mechanisms underlying atherosclerotic lesion localization. The torsion shear component of that stress distribution has been understudied due to the lack of a well-defined material model of the arterial wall that includes this component of mechanical deformation. The benefits of this work to that end are multi-fold. Lu et al. previously used triaxial mechanical testing to determine a family of linear functions for the shear modulus of porcine coronary arteries [191]. In all, 6 linear parameters were required to describe the torsion shear properties of one porcine coronary artery. While this model provided a continuous distribution for shear modulus with respect to circumferential stress it could only describe a discrete distribution with respect to longitudinal stretch ratio. That is, if the vessel of interest had a stretch ratio between 1.2 and 1.3, a potentially non-linear interpolation would be necessary. The model described here solves that problem by providing a single constant that characterizes the entire physiologic spectrum of shear moduli for pressures between 0 and 120 mm Hg and longitudinal stretch ratios between 1.2 and 1.4. In addition, a material model that is invertible, such as the one described by the Fung-type exponential strain energy function used here, allows for its use in finite element analysis. This is significant in that it allows one to characterize the stress distribution in arterial tissue under torsion.

In silico simulation of triaxial experiments demonstrated that this single parameter captures the dependence of torsion shear stress on circumferential and longitudinal stress. Furthermore, the values of the shear modulus calculated for the porcine LAD from this study agreed with those published previously [191]. While this study focused specifically on the porcine LAD, shear moduli data have been reported for the right coronary artery in the pig [191]

and the aorta in the rat [195]. This methodology could easily be employed to determine the value of c_7 for those particular vessels as well.

The validity of this methodology can be evaluated with a few key observations. The first is that the value of c_7 is independent of the vessel segment size. Second, the value of c_7 is small relative to other parameters in the model. In fact, it is small enough to be negligible in the calculation of the exponent Q, which is appropriate, since the twisting deformation is expected to have a very small contribution to the other non-torsion stresses in the arterial wall. Third, the results are independent of mesh density indicating appropriate mesh size and boundary conditions in the finite element analysis.

Like all simulation studies, the results are limited by the assumptions made. First, the analysis assumes an axi-symmetric geometry with constant diameter and wall thickness over the length. However, the coronary arteries have a complex geometry with significant branching and a continuous distribution of both diameter and wall thickness over the length [196]. Furthermore, the zero stress state, characterized by the opening angle, also varies longitudinally [196]. For this analysis, the dimensions were assumed to be constant and equal to those of the porcine left coronary artery prior to the first major branch. The straight, axi-symmetric assumption has been previously employed by Lu et al. as well as others to evaluate the torsion shear properties of vascular tissue [203, 207]. Our results can therefore be interpreted with respect to these previous studies. Second, extrapolation of our results beyond the conditions tested should be performed with care. Residual analysis demonstrates an increase in error toward the ends of the testing range, indicating that this model may not be valid at pressures above 120 mm Hg and stretch ratios below 1.2 or above 1.4. A higher order model may be required to characterize the shear stress behavior under these more extreme loading conditions.

In summary, the description of the torsion shear properties of the porcine LAD was condensed from a family of linear functions to a single parameter added to a well-validated Fung-type exponential material model. Finite element analyses utilizing this model can more accurately predict the various components of stress within the wall of vessels undergoing torsional deformation, such as the coronary arteries. Such computational modeling using accurate material models could aide in determining the mechanistic link between biomechanical stimuli and the localization of atherogenesis.

4.2.2 Implementation of Material Models Into ABAQUS Finite Element Solver

ABAQUS v6.5 contains a built-in material property definition for hyperelastic materials. The generalized Mooney-Rivlin model in (4.1) is described as a polynomial function. The user specifies the order of the polynomial and the material constants. As part of this built-in matieral property definition, incompressibility is automatically enforced by requiring the use of hybrid elements specifically designed for incompressible materials. On the other hand, there is no built-in function for exponential pseudoelastic strain energy functions. ABAQUS does provide the user-defined subroutine, UMAT, for custom definition of material constitutive properties. This subroutine can be used to update the Jacobian matrix and stress tensor from the provided deformation gradient at each increment. UMAT utilizes the Cauchy "true" definition of stress and defines the Jacobian matrix as [197]

$$\frac{\partial \Delta \boldsymbol{\sigma}}{\partial \Delta \boldsymbol{\varepsilon}} \tag{4.28}$$

where ε is the logarithmic strain tensor defined by

$$\boldsymbol{\varepsilon} = \ln \mathbf{F} \tag{4.29}$$

Implementation of this subroutine for incorporation of the Fung-type exponential strain energy models required two expressions. First, an expression for the Cauchy stress tensor was derived as a function of the deformation gradient (see equations (4.9)-(4.16)). Second, the Jacobian matrix was determined from the Cauchy stress tensor. Since the strain energy function is given in terms of the Green's strain, the Cauchy stress tensor is also in terms of the Green's strain. The Jacobian matrix with respect to the logarithmic strain can be determined by application of the chain rule:

$$\frac{\partial \boldsymbol{\sigma}}{\partial \boldsymbol{\varepsilon}} = \frac{\partial \mathbf{E}}{\partial \boldsymbol{\varepsilon}} \frac{\partial \boldsymbol{\sigma}}{\partial \mathbf{E}}$$

$$\frac{\partial \boldsymbol{\sigma}}{\partial \boldsymbol{\varepsilon}} = (\mathbf{I} + 2\mathbf{E}) \frac{\partial \boldsymbol{\sigma}}{\partial \mathbf{E}} \tag{4.30}$$

For all loading cases, it was assumed that $E_{\theta z}$ is the predominant shear strain and that the other shear strains (E_{rz} and $E_{\theta r}$) were negligible. To enforce this constraint two additional terms had to be added to the exponent Q in the strain energy function such that

$$Q = c_1 E_r^2 + c_2 E_\theta^2 + c_3 E_z^2 + 2\left(c_4 E_\theta E_r + c_5 E_\theta E_z + c_6 E_z E_r + c_7 E_{\theta z}^2 + c_8 E_{rz}^2 + c_9 E_{\theta r}^2\right) \tag{4.31}$$

These terms were added to aide in computational stability and force a near zero shear strain in the r-z and r-θ planes. Therefore, the parameters c_8 and c_9 were not true material constants. Rather, their values were arbitrarily chosen to be large enough to prevent shear deformations in the respective planes. Zhang et al. employed a similar technique in their axi-symmetric fluid-structure analysis of the effect of surrounding tissue on fluid and solid mechanics in the vasculature [198].

Pseudoelastic strain energy models do not have an inherent assumption of incompressibility. This assumption has to be applied either directly (via a lagrange multiplier) or indirectly (via a penalty function). For all the finite element analyses in Specific Aim 2 utilizing

the Fung model, incompressibility was enforced via a penalty function as described above in Section 4.2.1.1 (See Appendix D for more details on the development of the UMAT file).

4.3 BOUNDARY AND LOADING CONDITIONS

Once the material properties were appropriately defined, boundary and loading conditions that simulate the mechanical loading regimens generated in the individual EVPS experiments described in Chapter 3.0 were developed. The experiments can be grouped based on the symmetry of the mechanical loading applied. Cyclic axial stretch and cyclic twist are axi-symmetric type deformations while flexure is a three-dimensional deformation.

4.3.1 Axi-symmetric simulations

Cyclic stretch was modeled in a 4 step process. First, a linear ramp in longitudinal displacement was applied to the proximal and distal boundary nodes in order to stretch the vessel from unloaded to *in vivo* length (measured prior to explant from the EVPS). Second, a linear ramp in pressure from 0 to 120 mm Hg was applied to the inner surface nodes while maintaining the longitudinal stretch. Third, a sinusoidal pressure wave with an 80mm Hg minimum and 120 mm Hg maximum was applied to the inner surface nodes to simulate normal pressure hemodynamics. Again, the longitudinal stretch was maintained. Fourth, a sinusoidal longitudinal displacement was added to the proximal and distal nodes to generate cyclic axial stretching of 0-7% of *in vivo* length. The sinusoidal pressure load on the inner surface nodes was maintained 180˚ out of phase with the stretch waveform as applied in the EVPS (see Figure 2.8 and Section 2.2.1.3).

Cyclic twist was also modeled in a 4 step process identical to cyclic stretch but with 2 modifications. The first is that the pressure load applied in step 2 was only 80 mm Hg. This change was required to accommodate the zero phase angle between pressure and twist (see Section 2.2.1). Second, in step 4, instead of a longitudinal displacement, a sinusoidal circumferential displacement was applied to the distal boundary nodes while the proximal boundary nodes were fixed in position. This displacement cycled between 0 and 20˚.

4.3.2 Three-dimensional (asymmetric) simulations

The deformation generated by the bending membrane in the EVPS is not axi-symmetric and therefore requires simulation in three-dimensions. However, there is one symmetry plane that can be utilized to reduce computational expense. That is, vessel segment can be bisected in the bending plane so that only half of the vessel segment volume is analyzed. Utilizing this symmetry, the flexure simulation was modeled in a 5 step process. First, a linear ramp in longitudinal displacement was applied to the proximal and distal boundary nodes to stretch the vessel segment from its unloaded to its *in vivo* length. Second, a linear ramp in pressure from 0 to 80 mm Hg was applied to the inner surface nodes while maintaining the longitudinal stretch. Third, a sinusoidal pressure wave with an 80mm Hg minimum and 120 mm Hg maximum was applied to the inner surface nodes to simulate normal pressure hemodynamics. Again, the longitudinal stretch was maintained. Fourth, the vertical displacement for a subset of nodes on the outer surface of the vessel segment was set to zero. These nodes included 25% of the outer surface nodes and represented the portion of the vessel segment in contact with the flexure membrane. This step simulates the initial vessel contact to the membrane. Fifth, a custom, periodic, vertical displacement field was applied to the subset of nodes in step 4. The periodic

pressure load from step 3 was also applied during step 5 such that the phase angle between pressure and curvature waveforms was zero (see Figure 2.8 and Section 2.2.1.3).

To apply a custom displacement field in ABAQUS the user-defined subroutine DISP was attached to the analysis job (Appendix F). The time profile for vertical displacement in the finite element simulation was assumed to be sinusoidal requiring specification of only the amplitude (one half the maximum displacement) of the sine function for each node along the vessel length. The maximum vertical displacement along the length of the vessel was determined empirically as a function of the toal vessel length and applied maximum curvature from the dynamic image data taken for the mechanical validation of the cyclic flexure device (see Section 2.2.2). That relationship was determined by assuming that the vertical displacement had a sinusoidal shape with respect to longitudinal position. Therefore, the entire vertical displacement field (H) with respect to time and longitudinal position could be generated from the maximal vertical displacement of the center point or point of maximum curvature (denoted as H_{max}). The CCD camera images obtained to validate the cyclic flexure device (see Section 2.2.2) provided x-y data points of the outer surface of the vessel segment at various time points including the time of maximal curvature. Maximum vertical displacement was related to vessel segment length (L) and applied maximum curvature (k) for each the validation experiments described in Section 2.2.2.1. Second order polynomials were fit to the data and used to determine the maximal vertical displacement for subsequent flexure experiments based on the vessel length and applied curvature (0.7 cm^{-1} for all the flexure experiments in this study):

$$H_{max} = C_1 k^2 + C_2 k + C_3 \tag{4.32}$$

where

$$C_1 = 0.21\,L^2 - 0.35\,L + 13.57$$
$$C_2 = -0.55\,L^2 + 9.16\,L - 35.70 \quad (4.33)$$
$$C_3 = 0.18\,L + 1.18$$

This function was then used to determine the maximum H for each node along the vessel length (denoted $H_t(z)$). Orienting the coordinate system in the center of the vessel longitudinally, and using the assumption stated earlier that the vertical displacement has a sinusoidal shape gives

$$H_t(z) = -\frac{H_{max}}{2}\,COS\left(\frac{\pi z}{L}\right) + \frac{H_{max}}{2} \quad (4.34)$$

where z represents the longitudinal position. The time profile for H (denoted H(t,z)), which was also sinusoidal, was then equal to

$$H(t,z) = -\frac{H_t(z)}{2}\,COS(2\pi t) + \frac{H_t(z)}{2} \quad (4.35)$$

The vertical displacement field described by equations (4.32)-(4.35) was applied to each of the flexure specimens in the FLX experiment set with k=0.7 cm^{-1} and L equal to the *in vivo* length of the specimen via unique DISP user subroutine files (Appendix F). An example displacement field is shown in Figure 4.10.

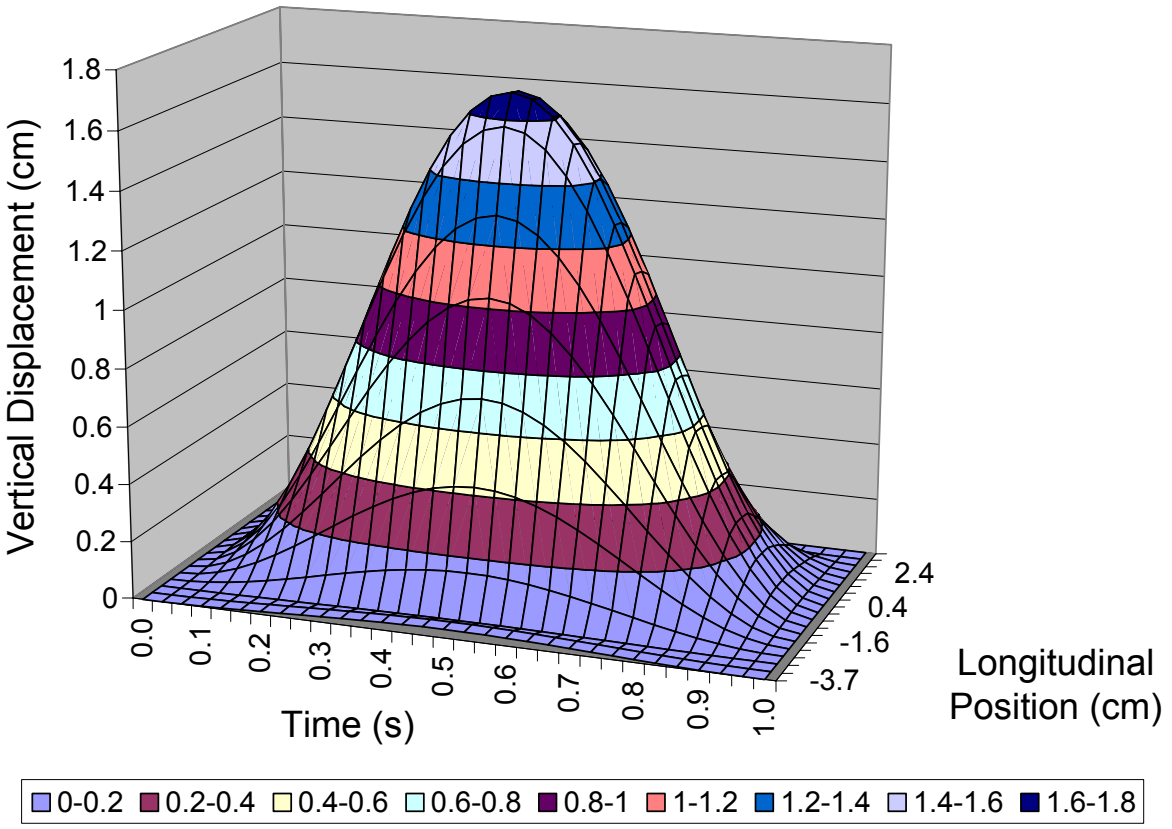

Figure 4.10 Representative vertical displacement field as a function of time and longitudinal position.

4.4 MESH GENERATION

Element types were chosen to ensure accurate estimation of stresses, mesh independence, and computational stability. In other words, the simplest element type that provided stable solution convergence, realistic stress values (i.e., radial stress at the inner surface nodes equal to the applied internal pressure), and results independent of mesh density was used. Each type of deformation (stretch, flexure, and twist) had a specific element type based on these criteria.

Furthermore, a representative geometry from each experiment set was discretized at three different mesh densities to determine the appropriate mesh size. For each deformation, the element type and mesh densities used to test for mesh independence are listed below.

4.4.1 Cyclic Axial Stretch

For cyclic stretch, vessel geometries were meshed with 4-node, bilinear, axisymmetric, hybrid quadrilateral elements. The mesh densities are shown in Figure 4.11 and listed in Table 4.3.

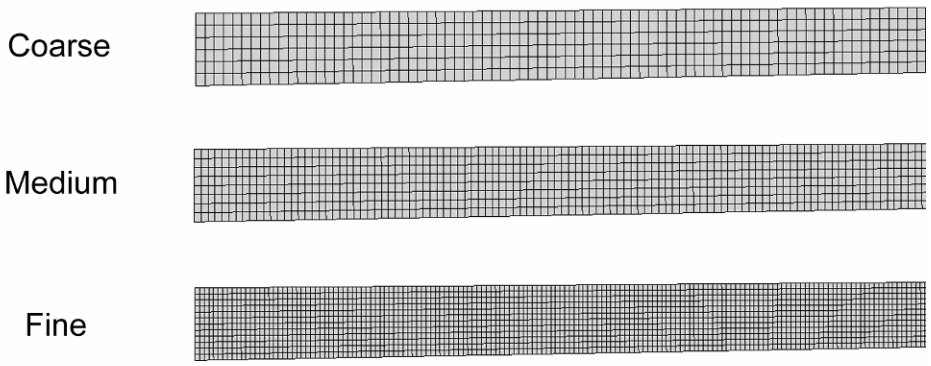

Figure 4.11 Mesh densities used for finite element analysis of cyclic stretch. Images represent only a fraction of the total vessel geometry.

Table 4.3 Mesh parameters for cyclic stretch finite element analysis

Mesh	Element Size	# of Nodes	# of Elements
Coarse	0.1	2527	2160
Medium	0.075	4329	3840
Fine	0.05	9373	8640

4.4.2 Cyclic Twist

For cyclic twist, vessel geometries were meshed with 8-node, biquadratic, axi-symmetric, hybrid quadrilateral elements. The mesh densities are shown in Figure 4.12 and listed in Table 4.4.

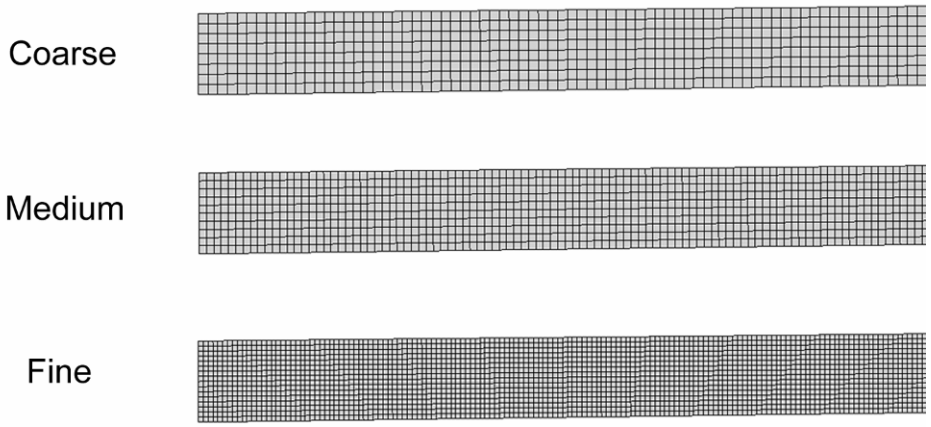

Figure 4.12 Mesh densities used for finite element analysis of cyclic twist. Images represent only a fraction of the total vessel geometry.

Table 4.4 Mesh parameters for cyclic twist finite element analysis

Mesh	Element Size	# of Nodes	# of Elements
Coarse	0.1	8077	2480
Medium	0.075	13269	4140
Fine	0.05	31033	9920

4.4.3 Cyclic Flexure

For cyclic flexure, vessel geometries were meshed with 8-node, linear, hybrid, 3D hexahedral (brick) elements. The mesh densities are listed in Table 4.5 and shown in Figure 4.13.

Table 4.5 Mesh parameters for cyclic flexure finite element analysis

Mesh	Element Size	# of Nodes	# of Elements
Coarse	0.5	2628	1728
Medium	0.4	12240	9520
Fine	0.3	27650	22608

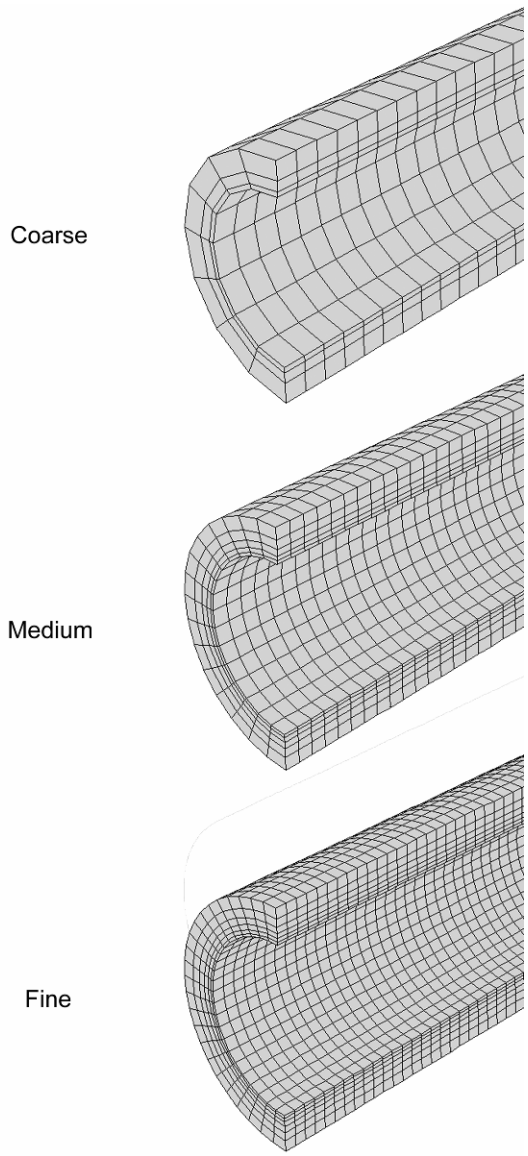

Figure 4.13 Mesh densities used for finite element analysis of cyclic flexure. Images represent only a fraction of the total vessel geometry.

4.5 RESULTS

4.5.1 Mooney-Rivlin Versus Fung Strain Energy Functions

The finite element-predicted changes in outer diameter for the two types of strain energy function described in Section 4.2 were compared with outer diameter data acquired from the laser micrometer during the *ex vivo* perfusion experiments. An example of that comparison is shown in Figure 4.14. These results demonstrate that the Fung model is a better estimator of the material behavior of porcine femoral arteries. Furthermore, exploration of wide range of material parameters for the Mooney-Rivlin relation indicated that this model would never predict diameters greater than the unloaded diameter once the vessel segments were stretched to *in vivo* length. Therefore, the Fung exponential model with the material constants determined by Wang et al. [189] (see Section 4.2) was used for estimation of stress distributions for the STR and TWT experiment sets. However, it was determined that the Fung model was not suitable for simulation of cyclic flexure.

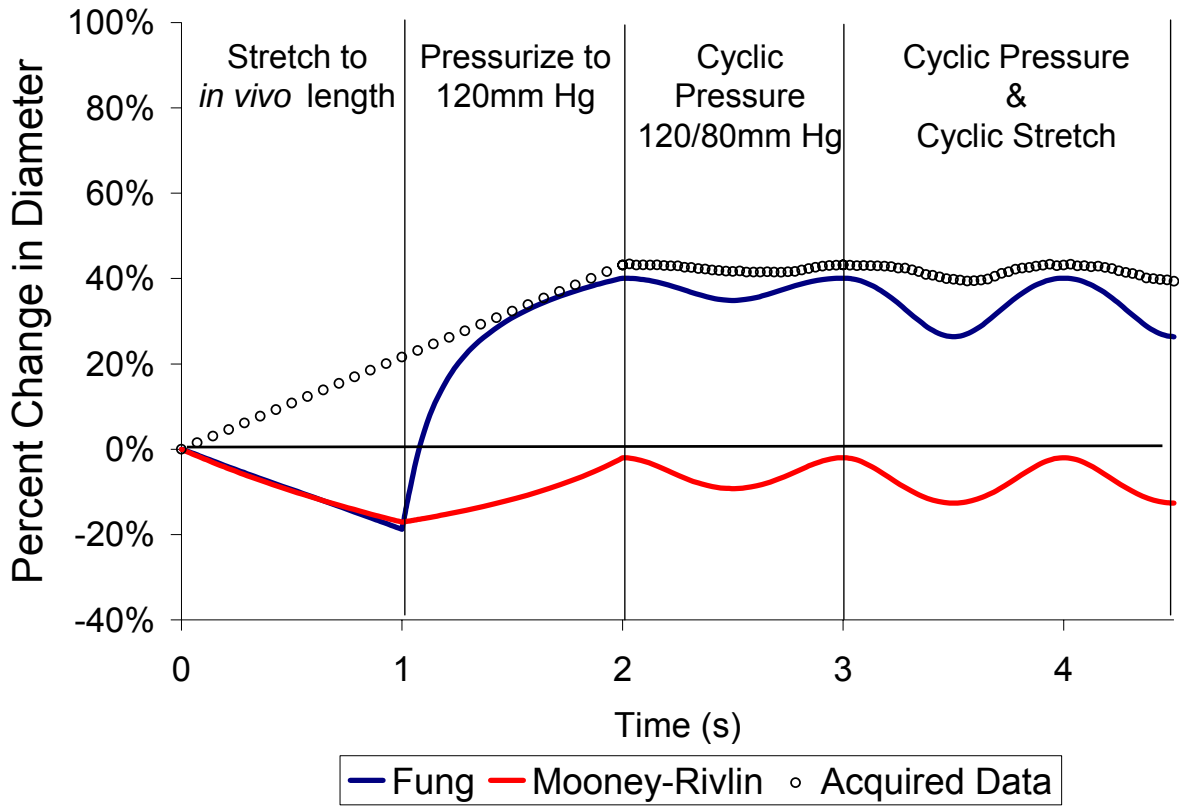

Figure 4.14 Comparison of experimentally acquired outer diameter data with that predicted by the Fung and Mooney-Rivlin strain energy functions. All four steps of the cyclic stretching simulation are depicted. 1) Stretch to *in vivo* length (0-1s); 2) Pressurize to 120 mm Hg (1-2s); 3) Cyclic pressure loading at 120/80 mm Hg at 1 Hz (2-3s); 4) Cyclic pressure plus cyclic axial stretch 0-7% of *in vivo* length at 1 Hz (3-4s). In reality, during the experiment the initial stretch and pressurization were applied simultaneously.

The deformations created by the flexure membrane are complex, three-dimensional, and asymmetric. The original Fung model and the one developed in Section 4.2.1 to include torsional shear (see Section) are incomplete in that they do not account for additional shear deformations (e.g., shear in the r-z and r-θ planes). It was assumed that these shear strains are negligible, and this assumption was enforced using relatively large values of the constants c_8 and c_9 in (4.31) (see Section 4.2.2). While this method was effective for stretch and twist, it was ineffective for flexure. In the case of flexure, values of c_8 and c_9 large enough to reduce shear in

the r-z and r-θ planes to near zero led to computation instabilities and convergence difficulties. These problems could be alleviated by lowering the values of c_8 and c_9. This in turn led to large shear strains which dominated the total strain energy of the system and generated unrealistic shear stress values. This shear effect can be seen in Figure 4.15A.

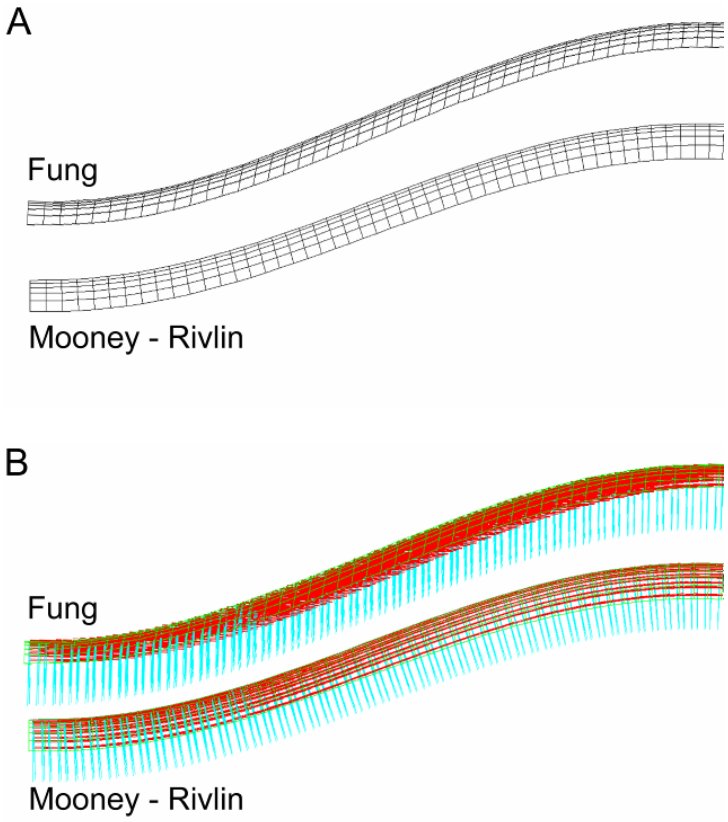

Figure 4.15 Comparison of the deformed mesh (A) and material orientation (B) for the Fung and Mooney-Rivlin strain energy functions in the flexure simulations. In B, the red vectors are the longitudinal axes and the cyan vectors are the radial axes. In the Fung model the radial axes remain vertical and the longitudinal axes remain horizontal. In the Mooney-Rivlin model the radial axis are perpendicular to the vessel contour and the longitudinal axes are parallel.

Notice that the sides of the elements in the Fung model remain vertical as the bending deformation occurs. In the isotropic Mooney-Rivlin model there is very little shearing of the elements. In fact, the material orientation of the elements rotates with the deformation, unlike the Fung model where it remains constant (Figure 4.15B). Therefore, the Mooney-Rivlin constitutive relation was used for the estimation stress distribution in the cyclic flexure experiments.

4.5.2 Cyclic Axial Stretch

The average dimensions of the stretch and control vessel specimens perfused in the STR experiment set and their coefficients of variation (CV) are shown in Table 4.6. While there is little difference between stretch and control specimens, there is a high degree of variability in the taper between all experimental specimens (indicated by a CV greater than one). The longitudinal distributions of Von Mises stress predicted by the three mesh densities listed in Table 4.3 were nearly identical (Figure 4.16). Therefore, the medium mesh size was used for all finite element simulations of stretch experiments.

Contour plots of the stretch specimen simulations demonstrate that the global mechanical deformation of axial stretch leads to a non-uniform distribution of Von Mises, longitudinal, and circumferential stress that is time dependent (Figure 4.17-Figure 4.21). Since the material properties and load are uniform, this non-uniform distribution is purely a product of the taper in the specimen. Indeed, the specimen-to-specimen variability in taper seen in Table 4.6 is manifested in a high degree of variability in the stress distributions. For example, specimens STR-1-S (Figure 4.17), STR-2-S (Figure 4.18), and STR-4-S (Figure 4.20) had increasing longitudinal stress over their length, while specimens STR-3-S (Figure 4.19) and STR-5-S

(Figure 4.21) had a more pronounced decreasing trend in longitudinal stress. The finite element simulation results for all the stretch and control specimens from the STR experiment set are listed in Table 4.7 and Table 4.8.

Table 4.6 Average dimensions (mm) for the vessel specimens perfused in the STR experiment set. Coefficients of variation (CV) are shown to demonstrate the variability within a given dimension. CVs greater than one, indicating high variability, are marked with asterisks.

		Mean ± Standard Deviation		Coefficient of Variation	
		Stretch	Control	Stretch	Control
Proximal	OD	4.35 ± 0.63	4.38 ± 0.55	0.14	0.12
	ID	3.11 ± 0.38	3.10 ± 0.59	0.12	0.19
	WT	0.62 ± 0.22	0.64 ± 0.25	0.35	0.4
Distal	OD	3.85 ± 0.63	4.07 ± 0.65	0.16	0.16
	ID	2.68 ± 0.21	2.89 ± 0.5	0.08	0.17
	WT	0.61 ± 0.27	0.59 ± 0.13	0.44	0.23
Taper	OD	0.01 ± 0.01	0.01 ± 0.01	1.12*	1.41*
	ID	1.00 ± 0.78	0.90 ± 2.19	0.78	2.43*
	WT	16.05 ± 37.20	4.31 ± 29.08	2.32*	6.75*
% Stretch		43 ± 9%	39 ± 13%	0.22	0.33

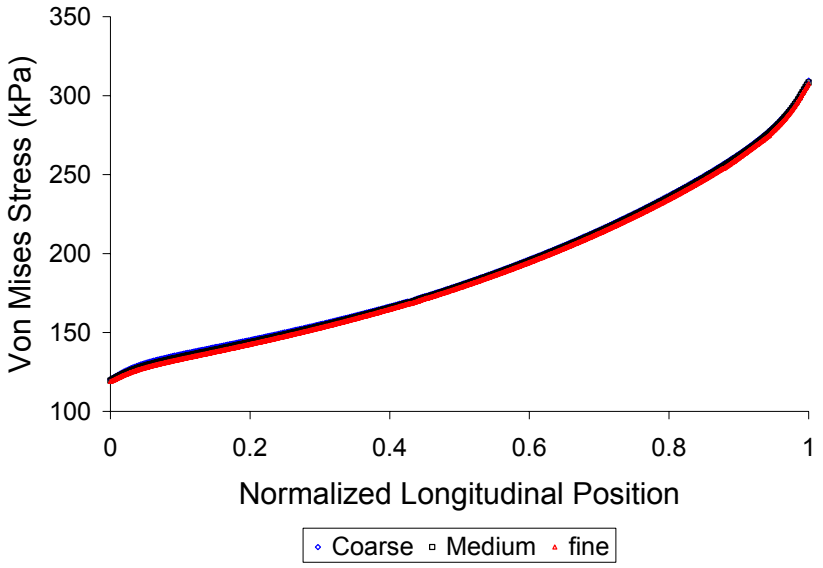

Figure 4.16 Von Mises stress distribution over the specimen length for the three mesh densities in Table 4.3.

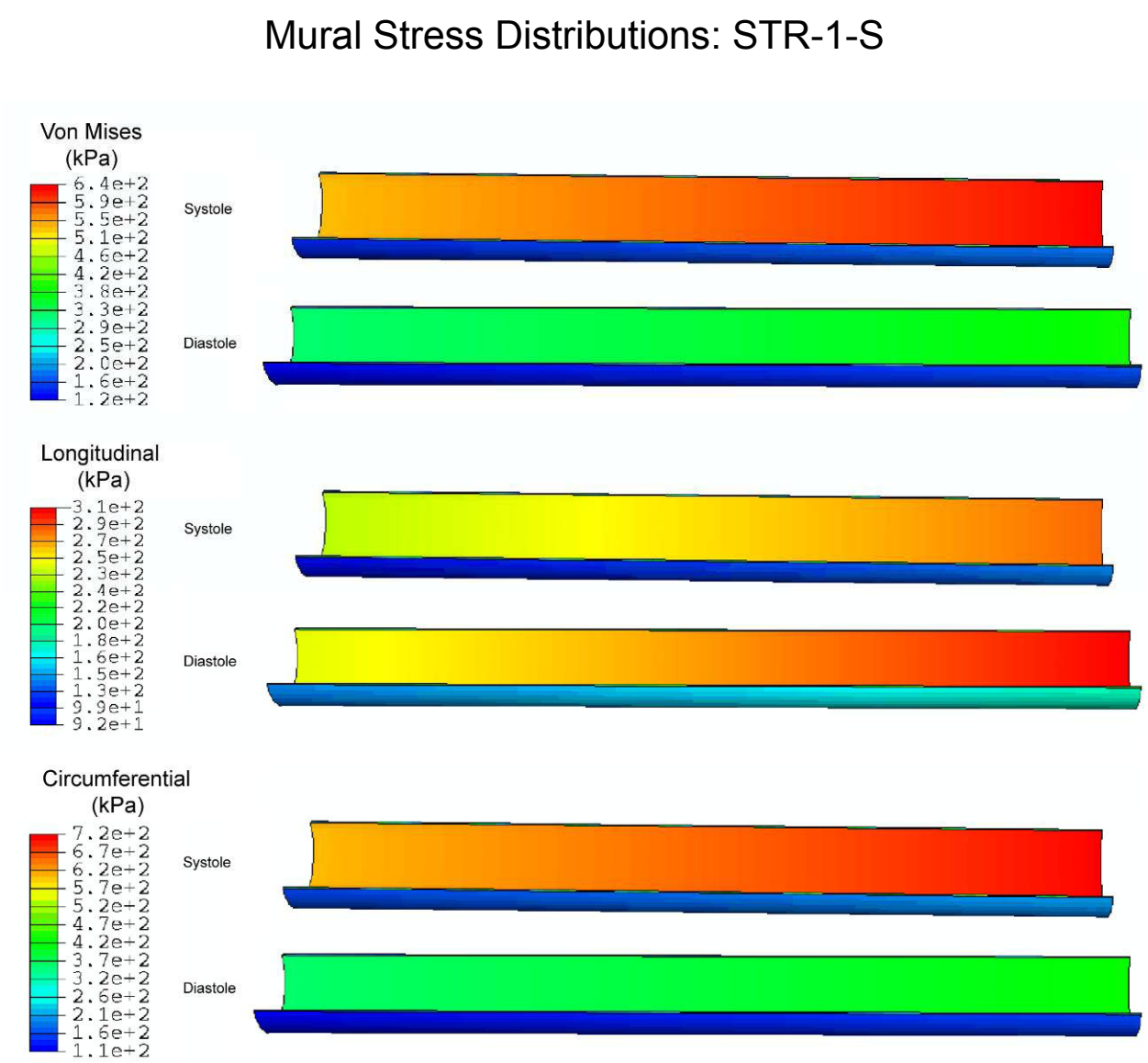

Figure 4.17 Contour plots of Von Mises, longitudinal, and circumferential stress in the STR-1-S specimen at systole (maximum pressure, minimum axial stretch) and diastole (minimum pressure, maximum axial stretch).

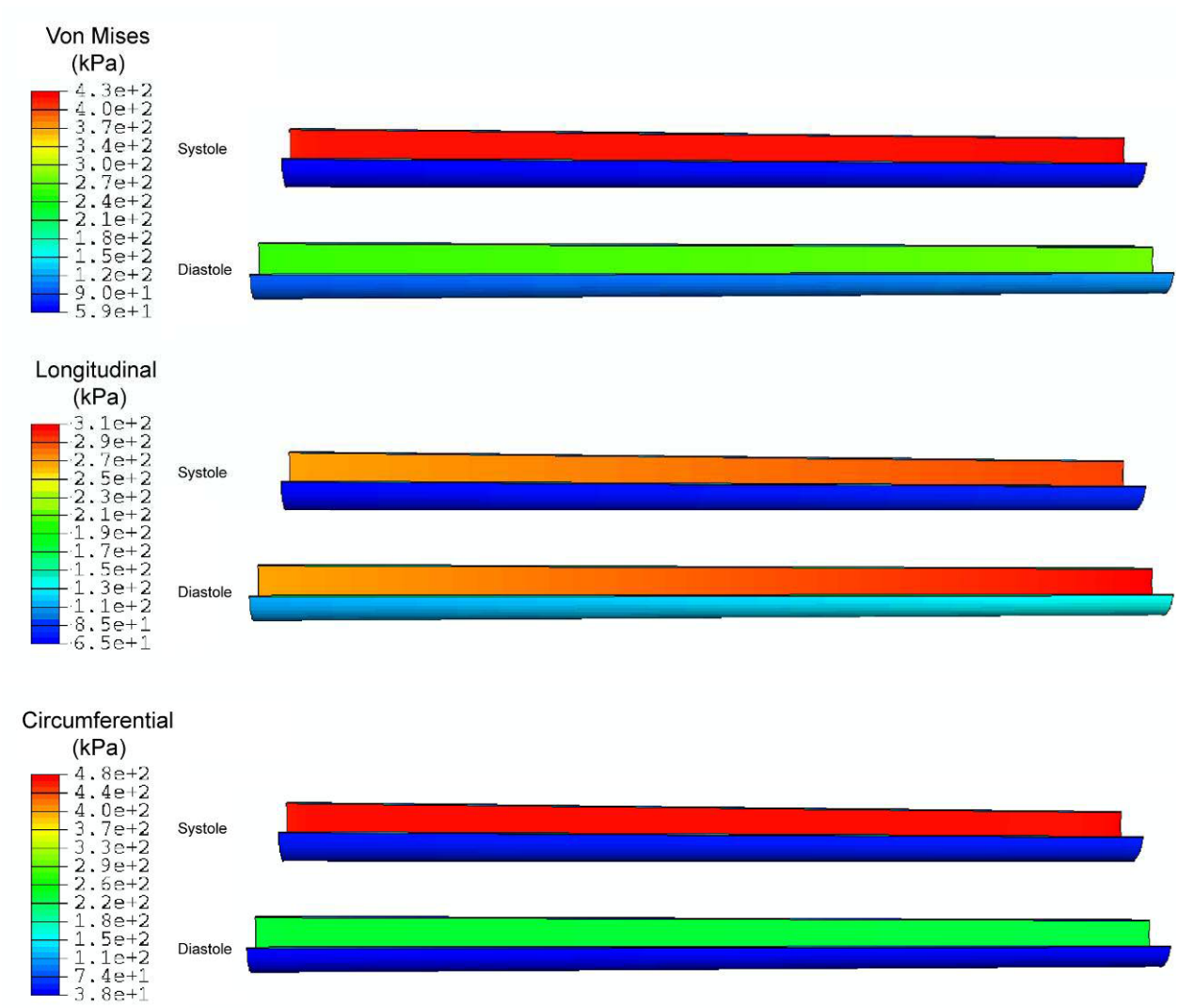

Figure 4.18 Contour plots of Von Mises, longitudinal, and circumferential stress in the STR-2-S specimen at systole (maximum pressure, minimum axial stretch) and diastole (minimum pressure, maximum axial stretch).

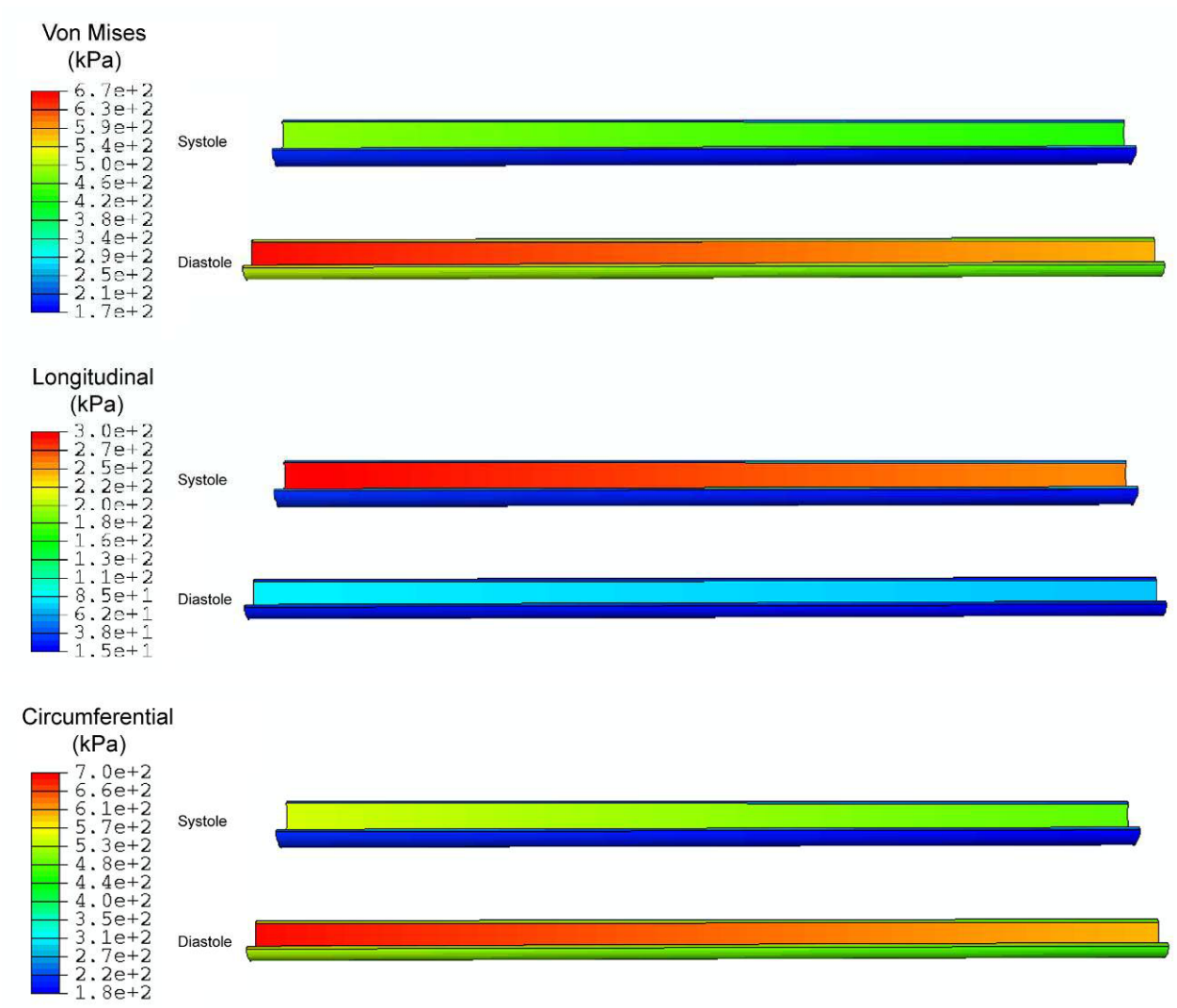

Figure 4.19 Contour plots of Von Mises, longitudinal, and circumferential stress in the STR-3-S specimen at systole (maximum pressure, minimum axial stretch) and diastole (minimum pressure, maximum axial stretch).

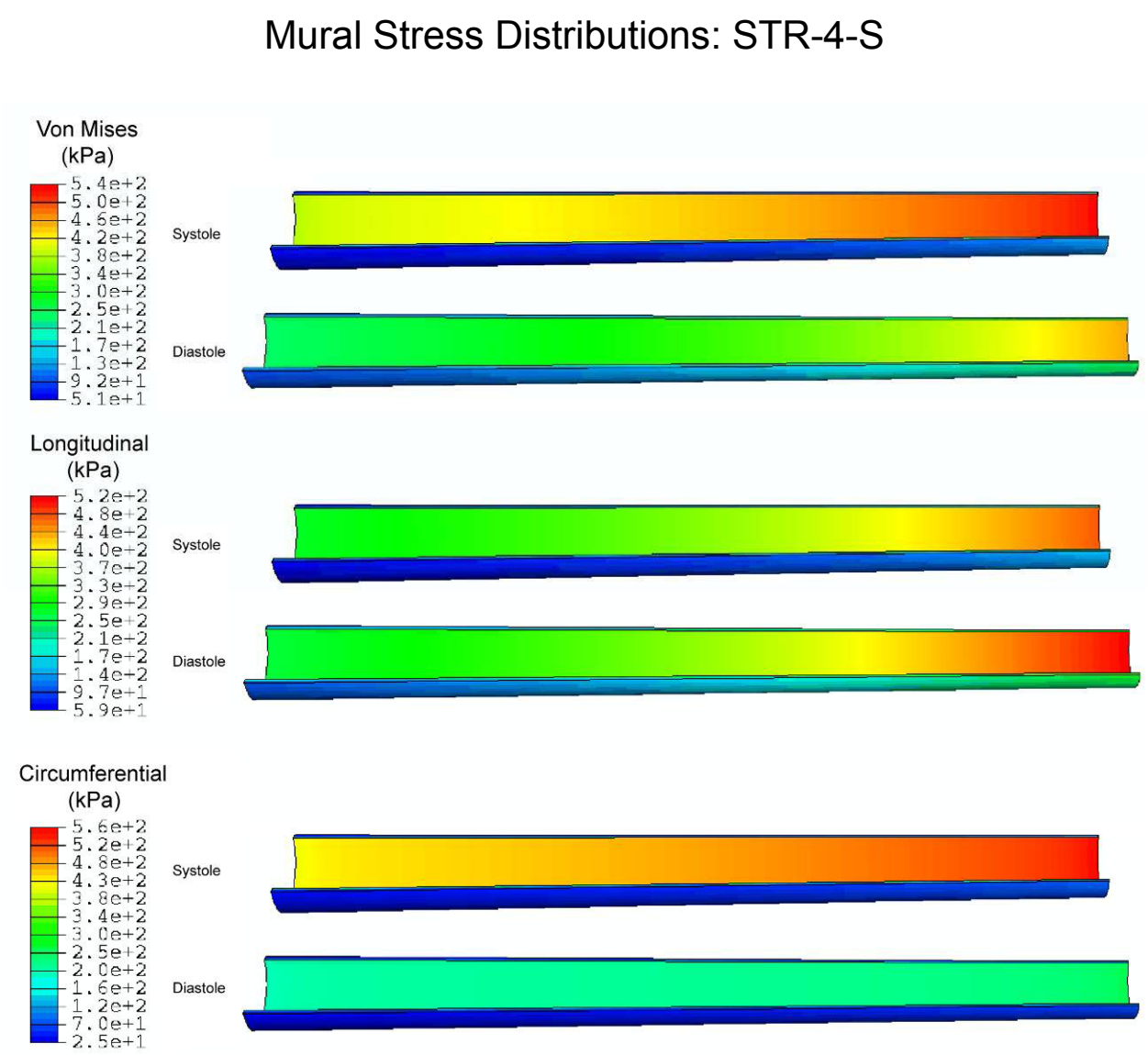

Figure 4.20 Contour plots of Von Mises, longitudinal, and circumferential stress in the STR-4-S specimen at systole (maximum pressure, minimum axial stretch) and diastole (minimum pressure, maximum axial stretch).

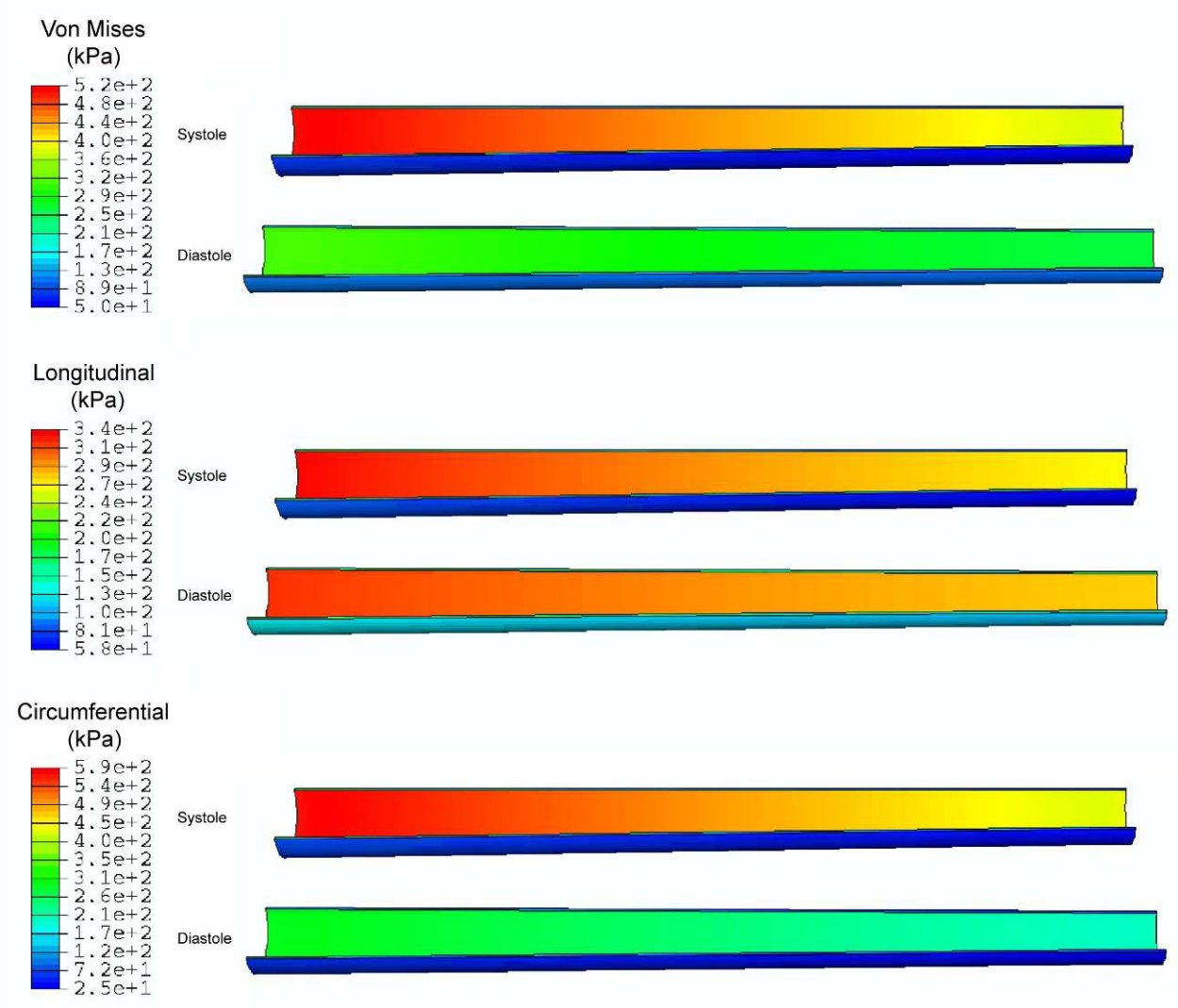

Figure 4.21 Contour plots of Von Mises, longitudinal, and circumferential stress in the STR-5-S specimen at systole (maximum pressure, minimum axial stretch) and diastole (minimum pressure, maximum axial stretch).

Table 4.7 Mean stress values (in kPa) for the ROIs corresponding to the experiment specific biological specimen processing segments for each stretch specimen in the STR experiment set. ROIs are numbered proximal to distal.

Stretch							
		Diastole			Systole		
		Von Mises	σ_{zz}	$\sigma_{\theta\theta}$	Von Mises	σ_{zz}	$\sigma_{\theta\theta}$
STR-1-S	1	219	188	232	328	165	371
	2	228	197	241	341	172	386
	3	238	206	251	354	179	401
	4	248	216	261	369	186	418
STR-2-S	1	158	173	109	180	140	189
	2	161	176	109	180	142	189
	3	163	180	109	181	143	189
	4	166	183	109	181	145	190
	5	169	187	109	182	147	190
STR-3-S	1	553	569	40	268	295	96
	2	542	558	38	263	289	93
	3	532	548	37	258	283	90
	4	523	537	36	253	278	87
	5	514	528	34	249	273	84
STR-4-S	1	167	185	90	165	146	161
	2	188	210	95	178	163	172
	3	216	242	102	195	183	185
	4	253	283	109	216	209	201
STR-5-S	1	175	191	124	201	158	213
	2	169	186	115	189	151	198
	3	165	181	106	178	144	185
	4	160	177	98	168	138	173
	5	157	174	91	159	132	161

Table 4.8 Mean stress values (in kPa) for the ROIs corresponding to the experiment specific biological specimen processing segments for each control specimen in the STR experiment set. ROIs are numbered proximal to distal.

Control							
		Diastole			Systole		
		Von Mises	σ_{zz}	$\sigma_{\theta\theta}$	Von Mises	σ_{zz}	$\sigma_{\theta\theta}$
STR-1-C	1	182	101	205	295	146	333
	2	167	93	188	271	132	305
	3	152	84	171	247	118	278
	4	137	75	153	222	103	248
STR-2-C	1	129	63	144	211	89	235
	2	124	60	138	203	84	226
	3	119	57	133	195	80	217
	4	114	55	127	187	75	208
	5	110	52	122	180	71	200
STR-3-C	1	277	300	65	337	372	114
	2	273	296	67	333	368	118
	3	269	293	69	329	364	121
	4	266	290	71	325	361	124
	5	262	287	73	322	357	127
STR-4-C	1	76	65	72	117	87	120
	2	86	74	83	132	98	138
	3	98	84	96	152	113	160
	4	114	98	114	176	132	188
STR-5-C	1	337	300	65	277	372	114
	2	333	296	67	273	368	118
	3	329	293	69	269	364	121
	4	325	290	71	266	361	124
	5	322	287	73	262	357	127

4.5.3 Cyclic Flexure

The average dimensions and CVs of the flexure and control vessel specimens perfused in the cyclic flexure experiment set are shown in Table 4.9. Like in the stretch experiment set, there is little difference between flexure and control specimen dimensions but a high degree of variability in the taper.

Table 4.9 Average dimensions (mm) for the vessel specimens perfused in the FLX experiment set. Coefficients of variation (CV) are shown to demonstrate the variability within a given dimension. CVs greater than one, indicating high variability, are marked with asterisks.

		Mean ± Standard Deviation		Coefficient of Variation	
		Flexure	Control	Flexure	Control
Proximal	OD	4.78 ± 0.88	4.05 ± 0.63	0.18	0.15
	ID	3.07 ± 0.85	2.55 ± 1.00	0.28	0.39
	WT	0.85 ± 0.17	0.75 ± 0.21	0.20	0.28
Distal	OD	3.97 ± 0.69	4.17 ± 0.19	0.17	0.05
	ID	2.27 ± 0.93	2.81 ± 0.44	0.41	0.16
	WT	0.85 ± 0.20	0.68 ± 0.19	0.23	0.28
Taper	OD	0.02 ± 0.03	0.00 ± 0.01	1.55*	5.28*
	ID	1.50 ± 2.69	-0.38 ± 0.96	1.79*	2.55*
	WT	-3.91 ± 66.11	-6.21 ± 15.35	16.90*	2.47*
% Stretch		60 ± 14%	65 ± 13%	0.23	0.20

The von Mises stress values along the greater (Figure 4.22) and lesser curvatures (Figure 4.23) for the three mesh densities listed in Table 4.5 had similarly shaped distributions with only slight variations in magnitude. Therefore, the medium mesh size was used for all finite element simulations of flex experiments.

The application of a distributed flexure displacement provided by the EVPS with the flexure membrane generates time-varying, non-uniform distributions of Von Mises, longitudinal, circumferential, and radial stress. While a non-uniform stress distribution is expected from this type of distributed load, there is significant specimen-to-specimen variability in the shape of those distributions and the magnitude of the stresses (Figure 4.24-Figure 4.28). Like the stretch experiments, this variability can be attributed to the high specimen-to-specimen variability in taper. Figure 4.29 demonstrates how the distributed displacement and the geometric variability both contribute to the spatial distribution of stress. In FLX-4-F (Figure 4.27) and FLX-5-F (Figure 4.28), there is a significant decrease in longitudinal stress in the lesser curvature half of the middle segment. This distribution is present in all experiments indicating a contribution of the displacement load which is relatively preserved among specimens. However, examination of the distribution of stress in the greater curvature shows some specimen-to-specimen variability. In FLX-4-F the longitudinal stress peaks in the middle segment along the greater curvature with decreased stress in the proximal and distal segments. On the other, FLX-5-F has a more uniform distribution of longitudinal stress in the greater curvature. The finite element simulation results for all the flexure and paired control specimens from the 5 FLX experiments are listed in Table 4.10 and Table 4.11.

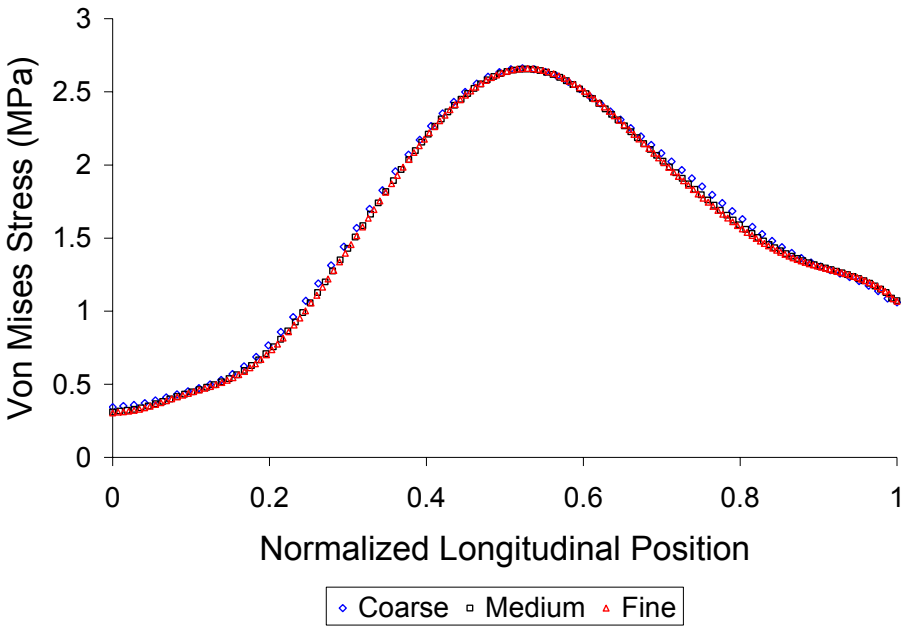

Figure 4.22 Von Mises stress distribution along the greater curvature of a representative flexure simulation for the three mesh densities listed in Table 4.5.

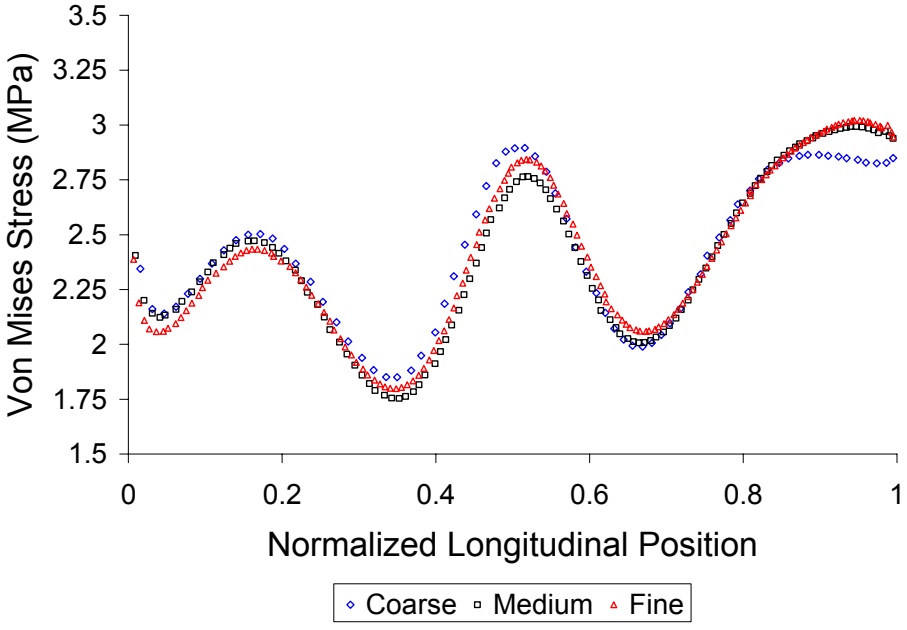

Figure 4.23 Von Mises stress distribution along the lesser curvature of a representative flexure simulation for the three mesh densities listed in Table 4.5.

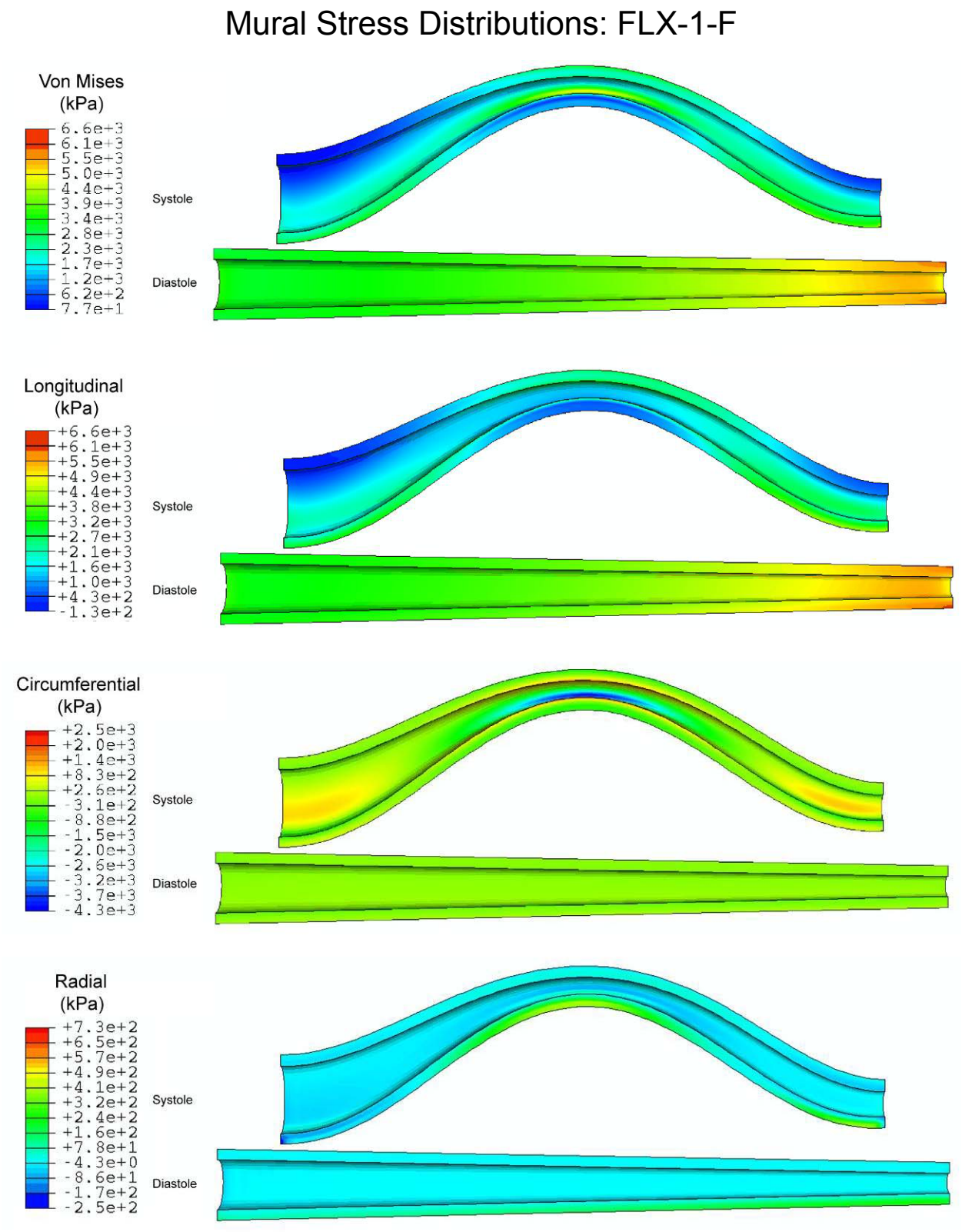

Figure 4.24 Contour plots of Von Mises, longitudinal, circumferential, and radial stress in the FLX-1-F specimen at systole (maximum pressure, maximum curvature) and diastole (minimum pressure, minimum curvature).

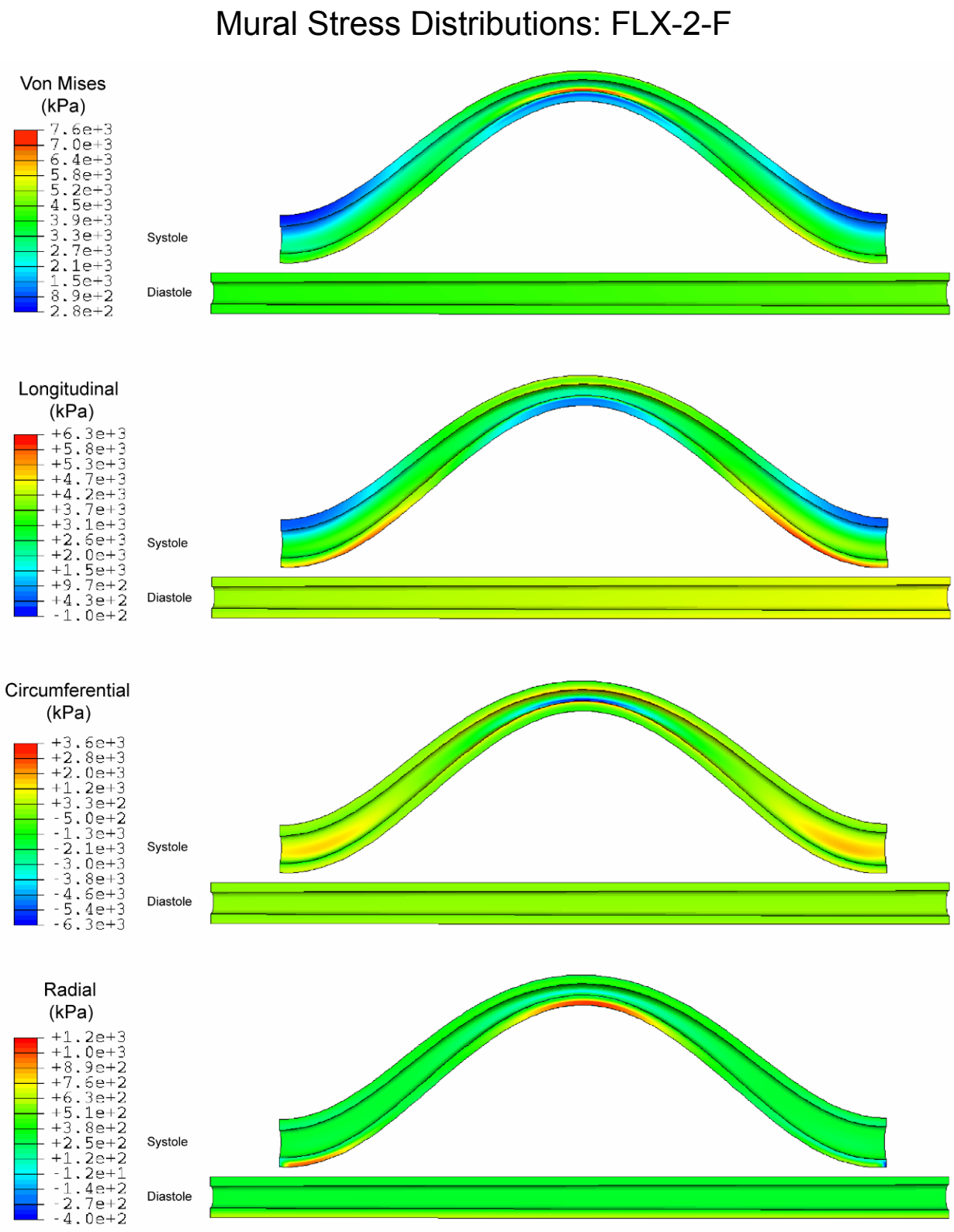

Figure 4.25 Contour plots of Von Mises, longitudinal, circumferential, and radial stress in the FLX-2-F specimen at systole (maximum pressure, maximum curvature) and diastole (minimum pressure, minimum curvature).

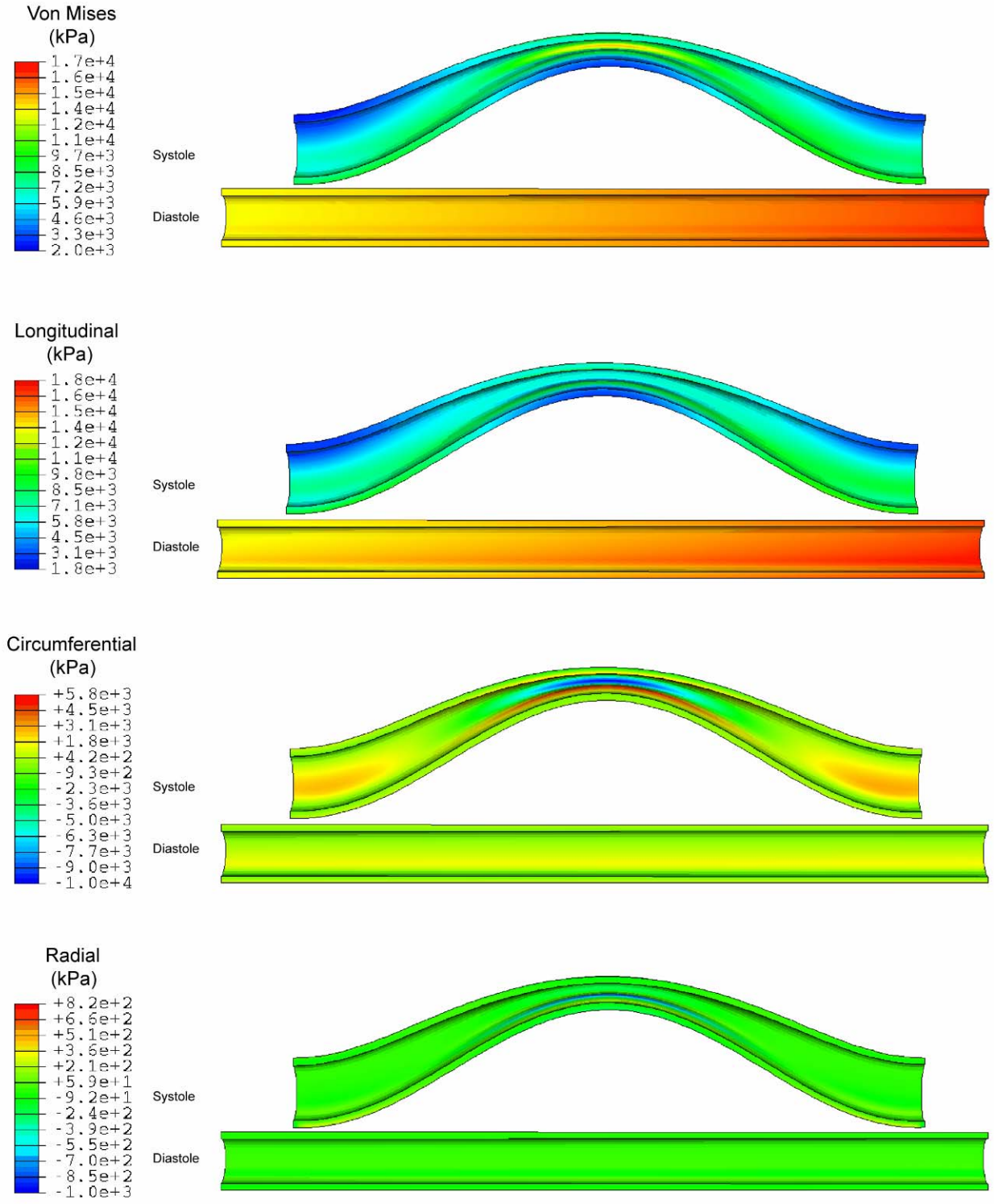

Figure 4.26 Contour plots of Von Mises, longitudinal, circumferential, and radial stress in the FLX-3-F specimen at systole (maximum pressure, maximum curvature) and diastole (minimum pressure, minimum curvature).

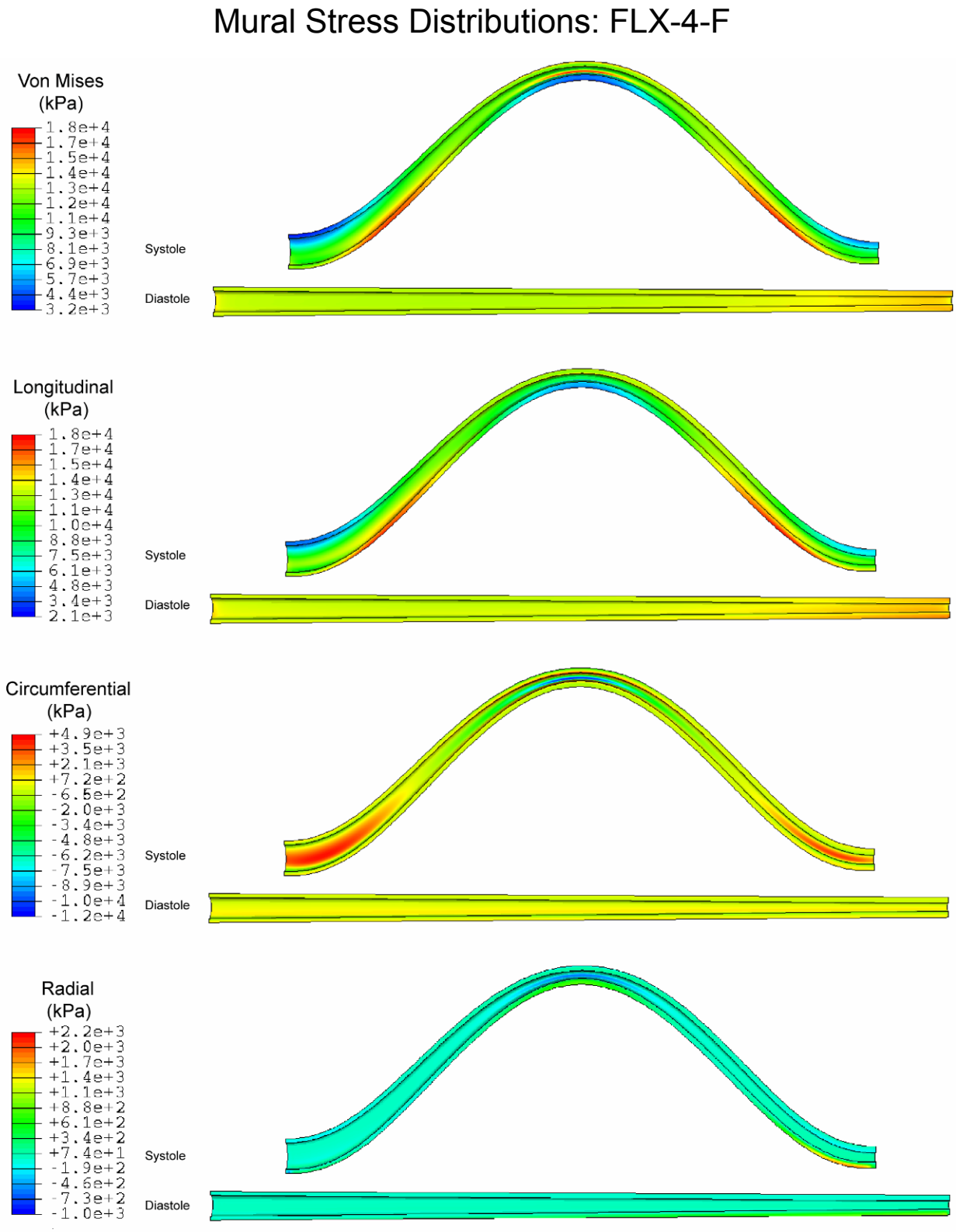

Figure 4.27 Contour plots of Von Mises, longitudinal, circumferential, and radial stress in the FLX-4-F specimen at systole (maximum pressure, maximum curvature) and diastole (minimum pressure, minimum curvature).

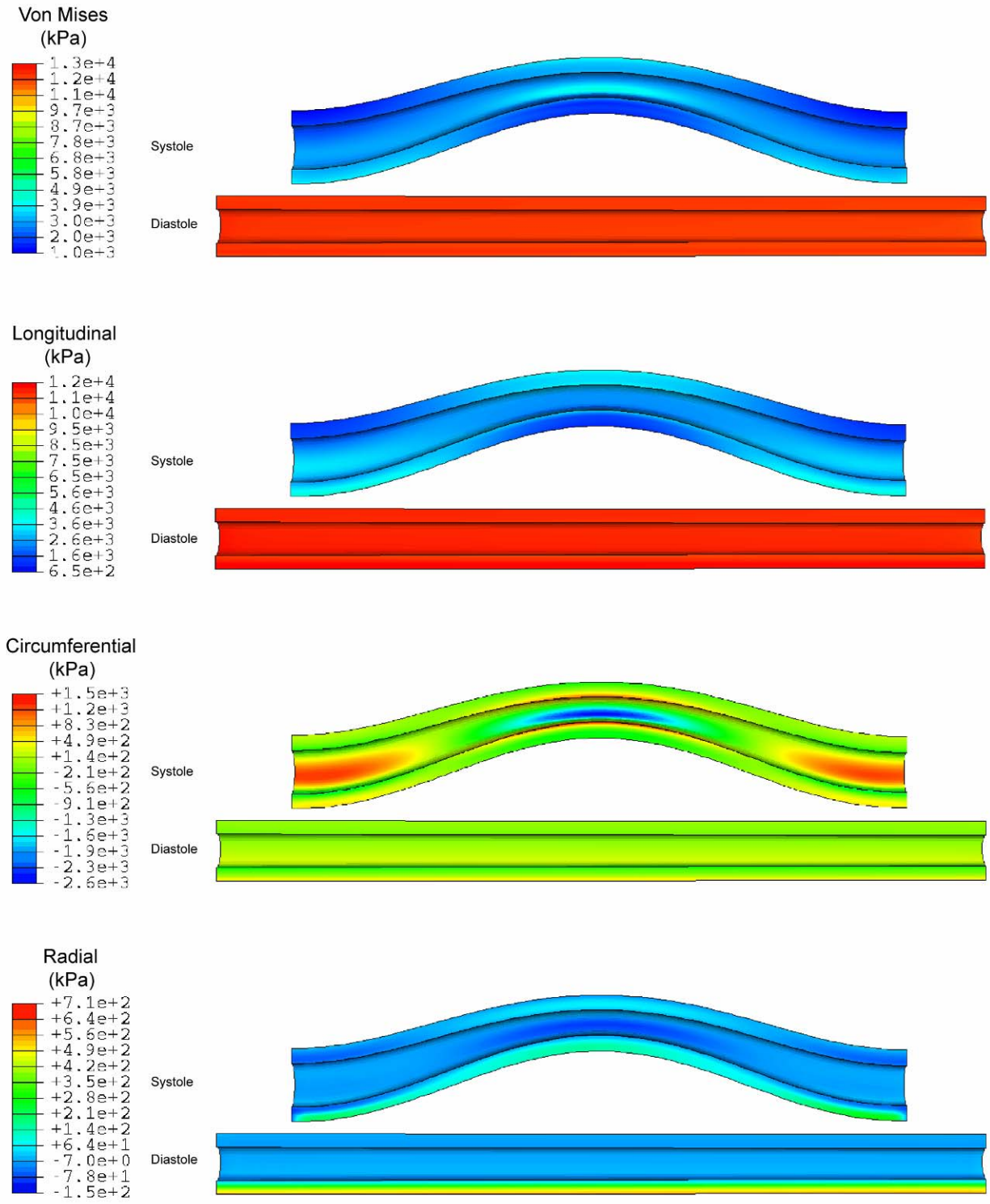

Figure 4.28 Contour plots of Von Mises, longitudinal, circumferential, and radial stress in the FLX-5-F specimen at systole (maximum pressure, maximum curvature) and diastole (minimum pressure, minimum curvature).

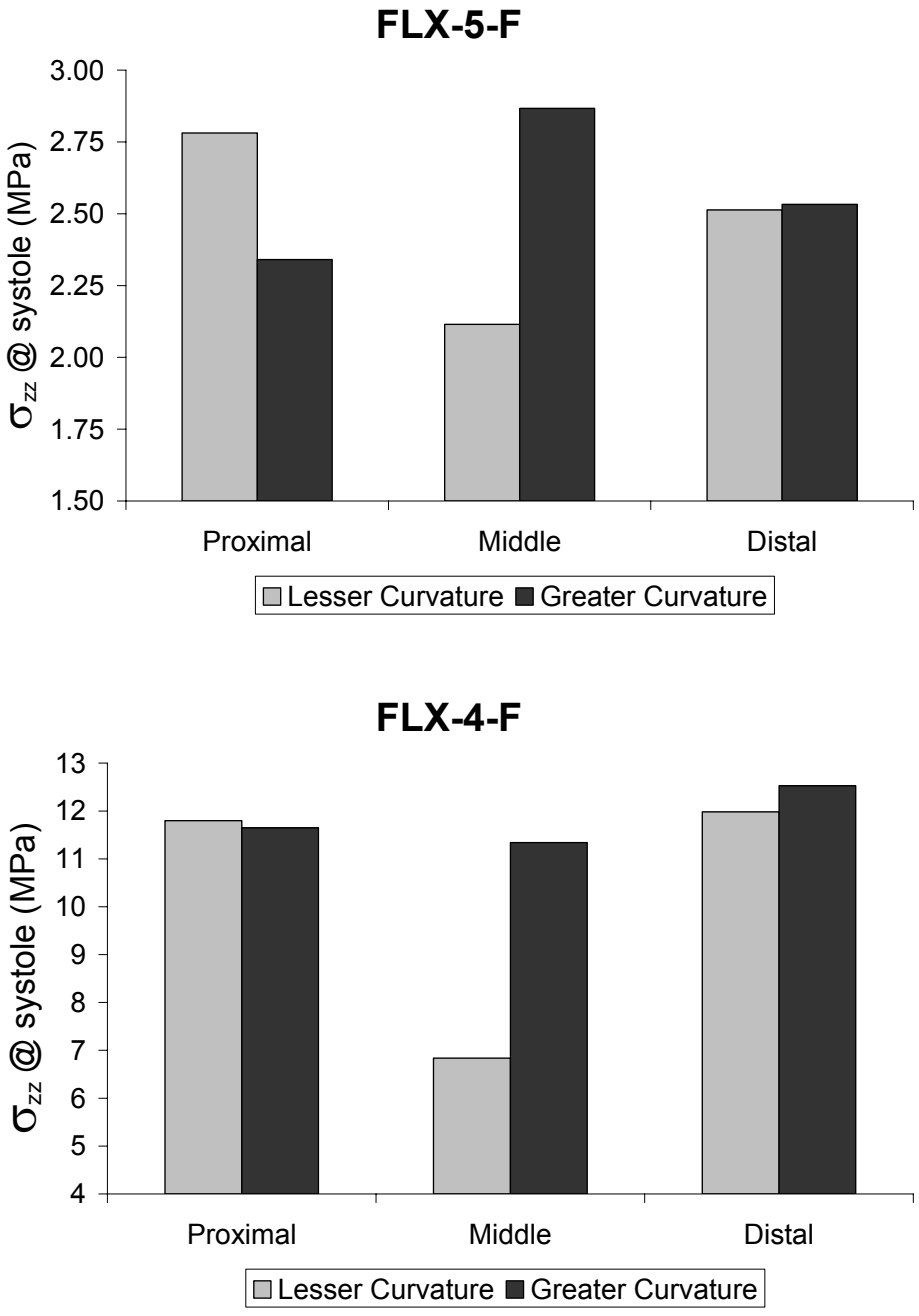

Figure 4.29 Mean longitudinal stress (σ_{zz}) for all nodes within 6 regions of interest (ROIs) in the flexure specimens. These ROIs correspond directly to the segments taken for biological analysis (see Section 0 and Figure 3.3). Values represent σ_{zz} at systole (maximum pressure, maximum curvature). Two experimental specimens are shown for comparison purposes.

Table 4.10 Mean stress values (in kPa) for the ROIs corresponding to the experiment specific biological specimen processing segments for each flexure specimen in the FLX experiment set. ROIs are numbered proximal to distal.

Flexure										
			Diastole				Systole			
			Von Mises	σ_{rr}	$\sigma_{\theta\theta}$	σ_{zz}	Von Mises	σ_{rr}	$\sigma_{\theta\theta}$	σ_{zz}
FLX-1-F	Lesser	1	11978	-6	-1	11974	2389	-8	56	2340
		2	11952	-6	-1	11948	2954	-33	-29	2867
		3	11921	-6	-2	11917	2594	-17	22	2533
	Greater	1	11988	13	36	12009	2840	-5	74	2781
		2	11961	13	36	11982	2401	-103	-222	2115
		3	11928	13	36	11949	2650	-40	-36	2514
FLX-2-F	Lesser	1	13170	-6	-25	13149	11753	-31	-68	11647
		2	13322	-6	-36	13295	11757	-171	-243	11342
		3	13781	-6	-46	13749	12624	-27	-106	12529
	Greater	1	13221	7	104	13258	12068	-65	-176	11800
		2	13378	16	113	13421	7813	-331	-680	6839
		3	13842	27	123	13895	12219	-63	-184	11981
FLX-3-F	Lesser	1	4226	-6	9	4228	3003	-21	7	2939
		2	4325	-6	10	4327	3469	-74	18	3301
		3	4434	-6	11	4436	3116	-23	14	3049
	Greater	1	4229	1	22	4239	3067	-57	-102	2891
		2	4328	1	23	4339	2351	-214	-246	1689
		3	4437	1	24	4448	3239	-59	-103	3050
FLX-4-F	Lesser	1	3510	-2	18	3512	1410	-18	45	1321
		2	3952	-2	14	3952	364	35	309	338
		3	4539	-1	10	4536	10	1	9	10
	Greater	1	3517	2	27	3524	1835	-40	-44	1648
		2	3955	3	25	3961	426	120	472	459
		3	4542	6	23	4548	12	3	13	13
FLX-5-F	Lesser	1	14421	-11	-28	14398	6664	-89	-175	6337
		2	14924	-11	-27	14901	7586	-225	-169	7038
		3	15463	-11	-26	15441	7129	-96	-175	6785
	Greater	1	14495	-5	195	14567	6759	-105	-79	6318
		2	14997	-6	197	15070	5777	-286	-203	4971
		3	15540	-6	200	15614	7179	-114	-79	6703

Table 4.11 Mean stress values (in kPa) for the ROIs corresponding to the experiment specific biological specimen processing segments for each control specimen in the FLX experiment set. ROIs are numbered proximal to distal.

Control									
		Diastole				Systole			
		Von Mises	σ_{rr}	$\sigma_{\theta\theta}$	σ_{zz}	Von Mises	σ_{rr}	$\sigma_{\theta\theta}$	σ_{zz}
FLX-1-C	1	15424	-5	21	15431	15424	-8	31	15435
	2	15424	-5	21	15431	15127	-8	32	15139
	3	14833	-5	22	14840	14833	-8	34	14845
FLX-2-C	1	108	-5	15	111	112	-8	25	116
	2	114	-5	19	118	118	-8	32	124
	3	128	-9	39	136	128	-9	39	136
FLX-3-C	1	3709	5	3714	4	3709	8	3716	6
	2	3609	5	3614	4	3610	8	3616	6
	3	3514	5	3518	4	3514	8	3520	6
FLX-4-C	1	12547	-5	20	12554	12547	-5	20	12554
	2	12467	-5	21	12475	12467	-5	21	12475
	3	12401	-5	22	12409	12401	-5	22	12409
FLX-5-C	1	11552	-5	49	11572	11553	-8	73	11583
	2	11921	-5	47	11939	11921	-8	71	11950
	3	12312	-4	46	12330	12312	-7	69	12340

4.5.4 Cyclic Twist

The average dimensions of the twist and control vessel specimens perfused in the cyclic TWT experiment set and their CVs are shown in Table 4.12. There were no significant differences between the twist and control vessel dimensions. As for the STR and FLX experiment sets, there was significant specimen-to-specimen variability in the vessel taper parameters.

Table 4.12 Average dimensions (mm) for the vessel specimens perfused in the TWT experiment set. Coefficients of variation (CV) are shown to demonstrate the variability within a given dimension. CVs greater than one, indicating high variability, are marked with asterisks.

		Mean ± Standard Deviation		Coefficient of Variation	
		Twist	Control	Twist	Control
Proximal	OD	4.90 ± 0.53	4.80 ± 0.38	0.11	0.08
	ID	3.28 ± 0.47	3.17 ± 0.47	0.14	0.05
	WT	0.81 ± 0.16	0.82 ± 0.19	0.20	0.23
Distal	OD	4.26 ± 0.24	4.37 ± 0.51	0.06	0.12
	ID	2.85 ± 0.11	3.05 ± 0.11	0.04	0.03
	WT	0.71 ± 0.13	0.66 ± 0.23	0.19	0.35
Taper	OD	0.02 ± 0.01	0.01 ± 0.02	0.71	1.57*
	ID	0.75 ± 0.79	0.22 ± 0.26	1.06*	1.18*
	WT	34.32 ± 71.40	12.26 ± 3.08	2.08*	0.25
% Stretch		67 ± 11%	61 ± 14%	0.17	0.23

The longitudinal distribution of torsion shear stress was independent of mesh density (Figure 4.16). Since the elements used in these simulations were second order and incur a significant computational cost, the coarse mesh size was used for all the finite element simulations of the twist experiments.

Contour plots of torsion shear stress revealed a non-uniform, time-varying distribution (Figure 4.31). Unlike the STR and FLX experiments sets, there was very little specimen-to-specimen variation in the shape of the distribution of torsion shear stress (Figure 4.32). All specimens had increasing torsion shear stress from proximal to distal. However, there were large differences in the magnitude of that shear stress (Figure 4.32) which can be attributed to geometric differences. The finite element simulation results for all the twist and paired control specimens from the 5 TWT experiments are listed in Table 4.13 and Table 4.14.

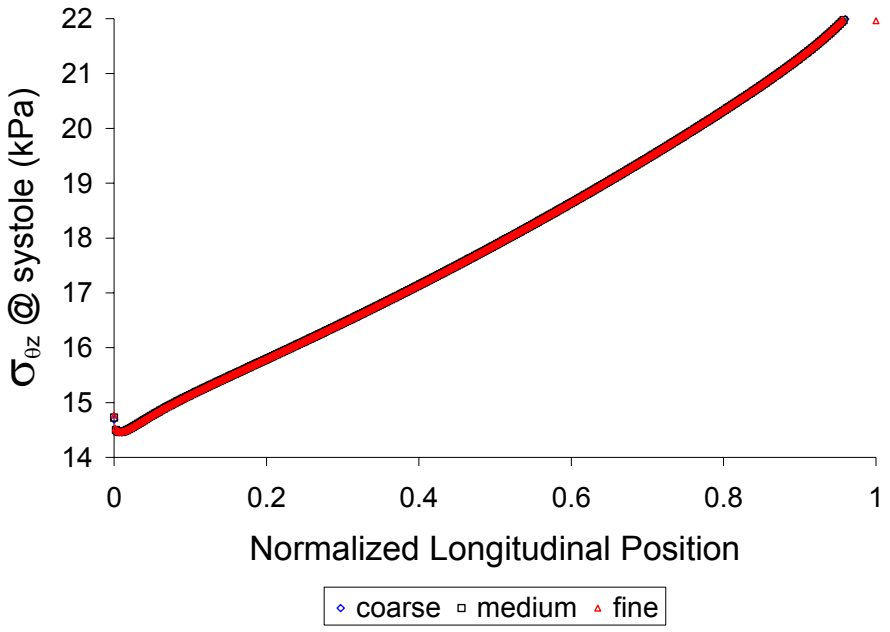

Figure 4.30 Torsion shear stress distribution over the specimen length for the three mesh densities in Table 4.4.

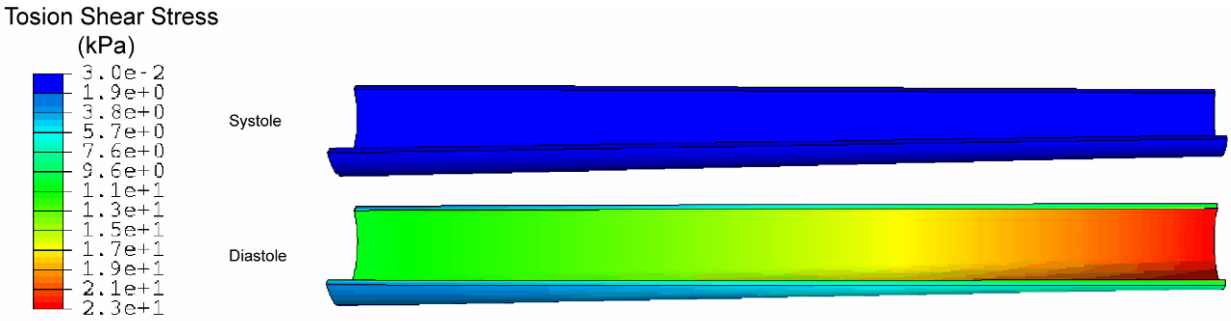

Figure 4.31 Contour plots of torsion shear stress in a representative twist specimen (TWT-2-T) at systole (maximum pressure, maximum twist) and diastole (minimum pressure, minimum twist).

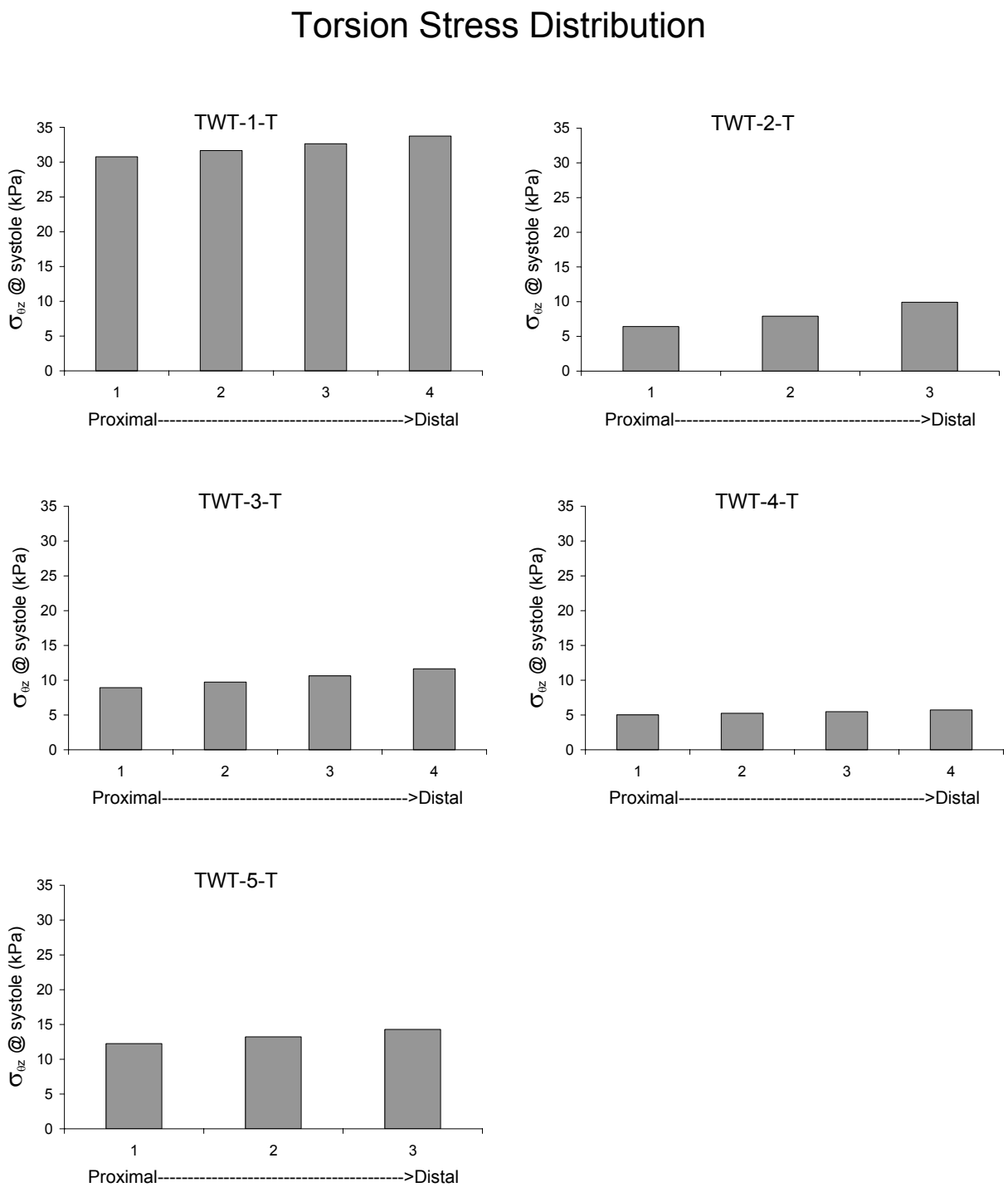

Figure 4.32 Mean torsion shear stress ($\sigma_{\theta z}$) for all nodes within the regions of interest (ROIs) correspond directly to the segments taken for biological analysis (see Section 0 and Figure 3.3). Values represent $\sigma_{\theta z}$ at systole (maximum pressure, maximum twist). All twist specimens from the TWT experiment set are shown with identical vertical axis scales for comparison purposes.

Table 4.13 Mean stress values (in kPa) for the ROIs corresponding to the experiment specific biological specimen processing segments for each twist specimen in the TWT experiment set. ROIs are numbered proximal to distal.

Twist									
		Diastole				Systole			
		Von Mises	$\sigma_{\theta\theta}$	σ_{zz}	$\sigma_{\theta z}$	Von Mises	$\sigma_{\theta\theta}$	σ_{zz}	$\sigma_{\theta z}$
TWT-1-T	1	3191	3196	15	0.01	3262	3273	29	-30.77
	2	3313	3318	17	0.01	3386	3398	32	-31.67
	3	3446	3453	18	-0.01	3522	3535	34	-32.65
	4	3594	3601	19	-0.02	3673	3687	37	-33.74
TWT-2-T	1	203	225	81	0.00	260	288	139	-6.43
	2	225	249	77	0.00	284	315	133	-7.92
	3	253	277	73	0.00	314	348	126	-9.91
TWT-3-T	1	276	302	78	0.00	341	378	135	-8.94
	2	289	315	76	0.00	355	393	132	-9.73
	3	303	329	74	0.00	371	410	129	-10.63
	4	318	344	72	0.00	388	427	126	-11.64
TWT-4-T	1	130	142	72	0.00	174	183	123	-5.01
	2	131	143	70	0.00	174	184	120	-5.24
	3	132	144	68	0.00	174	185	116	-5.48
	4	133	146	66	0.00	175	187	113	-5.74
TWT-5-T	1	352	390	118	0.00	447	502	202	-12.25
	2	364	402	114	0.00	460	516	196	-13.22
	3	377	415	110	0.00	475	530	189	-14.30

Table 4.14 Mean stress values (in kPa) for the ROIs corresponding to the experiment specific biological specimen processing segments for each control specimen in the TWT experiment set. ROIs are numbered proximal to distal.

Control									
		Diastole				Systole			
		Von Mises	$\sigma_{\theta\theta}$	σ_{zz}	$\sigma_{\theta z}$	Von Mises	$\sigma_{\theta\theta}$	σ_{zz}	$\sigma_{\theta z}$
TWT-1-C	1	1160	1174	32	0.00	1452	1481	67	0.00
	2	1354	1369	35	0.00	1452	1481	67	0.00
	3	1609	1625	38	0.00	1723	1755	73	0.00
	4	1952	1971	43	0.00	2090	2125	81	0.00
TWT-2-C	1	213	236	75	0.00	268	297	129	0.00
	2	200	220	71	0.00	251	279	123	0.00
	3	188	207	68	0.00	237	262	118	0.00
TWT-3-C	1	409	428	49	0.00	472	505	88	0.00
	2	414	433	49	0.00	478	510	88	0.00
	3	419	439	49	0.00	483	516	89	0.00
	4	424	444	49	0.00	489	522	89	0.00
TWT-4-C	1	200	223	93	0.00	262	290	159	0.00
	2	210	234	95	0.00	273	303	162	0.00
	3	220	245	97	0.00	285	317	165	0.00
	4	231	258	99	0.00	298	332	168	0.00
TWT-5-C	1	328	364	114	0.00	418	470	195	0.00
	2	348	386	118	0.00	442	497	202	0.00
	3	370	411	122	0.00	469	528	209	0.00

4.6 DISCUSSION

4.6.1 Vessel Geometry, Stress Distribution, and Atherogenesis

The experiment specific finite element simulations performed in this Specific Aim have demonstrated that even simple global deformations such as axial stretch or twist can generate a non-uniform distribution of stresses over the length of an arterial segment. Since the material properties and loading remain spatially constant, the local geometry alone governs how a global mechanical deformation will distribute the stress load. The differences in absolute geometric parameters such as OD, ID, and WT may be subtle but relative geometric parameters such as the taper in OD, ID, and WT may have significant variation leading significant stress variation.

Vascular geometry has long been studied as a potential mediator of location specific vascular disease. Vorp et al. demonstrated that both maximum diameter and aneurysm shape are determinants of maximal wall stress and potential for rupture [199]. Geometric and morphometric analysis of the coronary arteries has led to several key correlations between geometry and early remodeling events associated with atherogenesis prior to disease development [81]. The work by Ding et al to characterize the dynamic motion of the coronary arteries demonstrated significant variation within and between individuals in those motion parameters [87]. While these studies have elucidated these correlations, they have not revealed the mechanism by which geometry impacts the biological response of the vascular cells. The computational analyses in this study provide one possible mechanism connecting geometry with vascular cell response. That is, the local geometry dictates how various mechanical loads distribute over the vascular segment. The next step is to determine how those local stresses influence biological processes involved in vascular disease, specifically atherosclerosis.

4.6.2 Limitations

Interpretation of the results described here must be done with consideration given to the limitations of the study. First, to the author's knowledge, there has been no published study characterizing the mechanical properties of the porcine femoral artery with subsequent constitutive model development. Therefore, constitutive models of the porcine coronary arteries were used instead. The histological analysis in Figure 3.2 demonstrates that these two arteries are very similar in morphology and composition. Therefore, it is possible that the mechanical properties are similar. In addition, the conclusions made in this analysis are in terms of relative trends and changes in mechanical stress within a vascular segment rather than absolute stress values. Indeed, the basic shear modulus behavior of porcine coronary arteries [191] and rat aortas [195] are almost identical, with differences only in absolute value. Therefore, minor inaccuracies in the model should not affect the conclusions drawn from this work, provided that the global trends are preserved.

Second, even though it was determined that the Mooney-Rivlin strain energy function for porcine coronary arteries was not a good predictor of femoral artery behavior in our *ex vivo* system, it was a much more suitable material model for the complex, three-dimensional, asymmetric flexure deformation. Computational convergence with the Fung model required arbitrary adjustment of the material parameters c_8 and c_9 in (4.31). While this is a valid approach for deformations with little or no shear strain [198], it generated unrealistic shear strain values for the more complicated flexure deformation. New finite element friendly material models of the vasculature that include anisotropic shear strains should eliminate the impact of this limitation.

Third, the vessel geometry was idealized in that it assumed a linear taper and circular cross-section. The assumption of circular cross-section is fairly accurate for medium, muscular arteries such as the femoral artery [200]. In addition, violation of this assumption is likely to produce radial and circumferential stress variations. The effect of these distributions on the biological endpoints would not be detected since the tissue processing scheme was aimed at perceiving longitudinal distributions of endpoints (see Figure 3.3). There was a circumferential component to the tissue processing scheme for the flexure experiments (see Figure 2.11). However, the non-uniform displacement load is likely to overshadow the subtle effects of non-circular cross-section. The assumption of linear taper is of greater concern. The femoral arteries supply blood to the surrounding muscles of the lower extremity and therefore have several branches. These branches influence the diameter and wall thickness which could generate additional variations in stress that were not accounted for in this model. If the wall stresses are in fact an influential modulator of vascular cell response, it is likely that any unexplained variation in biological data could be due to the non-linear taper generated by these branches.

4.7 CONCLUSIONS

The relatively simple mechanical deformations of axial stretch, flexure, and twist, generated by the EVPS, result in non-uniform wall stress distributions within arterial segments. The shape of the distribution and the stress magnitudes depend heavily on the vessel specimen geometry. The high specimen-to-specimen variability in stress distribution mimics the high variability in biological endpoint distribution from Specific Aim 1 (see Section 3.2). Multiple regression analyses as proposed for Specific Aim 4 will determine if and how these two distributions are

related. Such information has the potential to characterize how local mural stresses influence the localization of early atherogenic processes. The mural stresses however, are only half the story with regards to the mechanical milieu of an artery. The shear stresses due to fluid flow are the second half. To understand how dynamic mechanical deformation alters the distribution of fluid shear stress, computational fluid dynamics techniques are required and this is the topic of Chapter 5.

5.0 COMPUTATIONAL FLUID DYNAMICS

The objective of Specific Aim 3 was to estimate the distribution of fluid-induced shear stresses specifically for each arterial specimen from Specific Aim 1 based on the deformed geometries determined in Specific Aim 2. Computational fluid dynamics techniques were used to solve the Navier-Stokes equations for fluid flow within the vessel specimens. These analyses demonstrated how the dynamic wall motions created in the EVPS affect the fluid flow characteristics. As stated in Section 3.3.2 the working fluid for the EVPS was cell culture media (viscosity ~ water), which did not allow for generation of physiologic shear stress values. Since flow conditions were set to recreate physiologic shear rate, all subsequent fluid analyses were made with respect to shear rate rather than shear stress.

The application of cyclic twist had no appreciable effect on the vessel specimen diameter. Moreover, the maximum tangential wall velocity reached during the twist deformation is at least two orders of magnitude less than the average fluid velocity. Based on these two observations it is unlikely that cyclic twist has any significant contribution to the flow characteristics. Therefore, only cyclic axial stretch and flexure were considered in the fluid dynamics analyses.

The development of a computational fluid dynamics simulation of fluid flow in a compliant tube with dynamic motion and pulsatile flow required several pieces of information. First, like in the finite element analysis, a geometric model is needed. However, in this case, the fluid volume, rather than the solid vessel wall volume had to be reconstructed. Fluid volumes

from the finite element solutions at the end of the loading step just prior to the cyclic loading step(s) in Section 4.0 were used for geometric reconstructions (see Section 5.1.1). Second, a mathematical description of the volume deformation created by the cyclic loading was required to characterize the mesh deformation over time. Again the finite element simulations in Section 4.0 were used to map the change in volume dimensions over time to the reconstructed mesh geometries (see Section 5.1.2). Third, the inlet and outlet boundary conditions need to be specified such that the fluid dynamic environment of the EVPS is accurately simulated. Pressure and flow data acquired during the *ex vivo* perfusion experiments were used to describe these boundary conditions (see Section 5.2). The next sections describe how these three pieces of information were used to develop computational fluid dynamics simulations of the perfusion experiments, the results of the individual experiment specific analyses, and the implications for understanding the distribution of fluid-induced shear stresses on the endothelium in vascular segments under various mechanical deformations.

5.1 MESH GENERATION

The generation of a mesh for a given vessel geometry was a two-step process. First, the initial loaded geometry was determined from the finite element results, reconstructed, and meshed. Second, the dynamic changes in fluid volume geometry (determined from the finite element analyses) were incrementally applied to the mesh at each time step in the analysis.

5.1.1 Initial Geometric Reconstruction

For the stretch experiment set, the initial geometry was specified as the geometry at diastole. This time point corresponds to the point of maximal stretch in the cyclic stretch cycle. Even though this is the point of maximal axial load, the fluid analysis was significantly more stable and had faster convergence when the simulations were started when flow velocity was a minimum (i.e., diastole). The assumptions of circular cross-section and linear taper made in the finite element reconstruction were maintained in these constructions. Therefore, a given geometry was defined by the proximal inner radius (IR), the distal inner radius (IR) at and the length. These values were extracted at t=0.5 (diastole) for the last loading step in the finite element analyses of the stretch and paired control simulations (see Figure 4.14 and Section 4.3.1). Table 5.1 contains all of the extracted geometric data used for geometric reconstruction. The mesh generation software Gambit v2.2.30 was used to develop an axi-symmetric model that interpolated all inner radii between the proximal and distal IR. To allow flow to become fully developed, 10 diameter flow extensions were added to the inlet and outlet of the vessel model. An example geometric reconstruction is shown in Figure 5.1. Gambit was then used to generate a quadrilateral mesh which included a fine boundary layer near the vessel wall to allow for accurate estimate of the shear stress (Figure 5.2). Control specimens for the stretch and flexure experiments were reconstructed and meshed as described for the stretch specimens.

Table 5.1 Fluid volume dimensions extracted from finite element analyses for geometric reconstruction of fluid phase. Values (in mm) for each individual vessel specimen are listed by experiment ID (see Figure 3.1)

Experiment ID	Proximal IR	Distal IR	Length
STR-1-S	2.40	2.33	40
STR-1-C	2.97	2.00	60
STR-2-S	2.88	2.54	70
STR-2-C	3.69	3.09	66
STR-3-S	1.75	1.59	73
STR-3-C	1.85	2.21	77
STR-4-S	2.56	2.01	52
STR-4-C	2.35	2.98	55
STR-5-S	3.00	2.19	66
STR-5-C	2.79	2.38	60
FLX-1-F	2.18	0.90	55
FLX-1-C	1.25	1.43	52
FLX-2-F	1.23	1.43	70
FLX-2-C	1.08	1.15	60
FLX-3-F	1.70	1.78	50
FLX-3-C	2.10	1.75	50
FLX-4-F	1.49	0.58	85
FLX-4-C	0.77	1.38	80
FLX-5-F	1.10	1.01	40
FLX-5-C	1.18	1.33	38

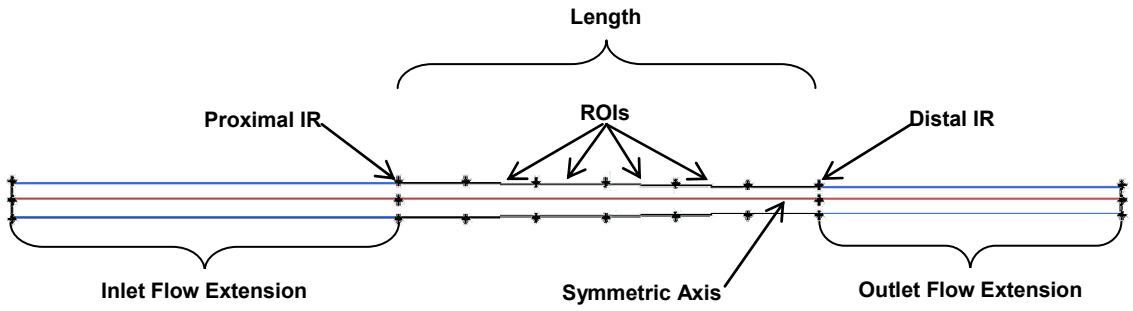

Figure 5.1 Schematic of an axi-symmetric representative fluid volume reconstruction. The proximal and distal inner radii (IR), specimen length, flow extensions, axis of symmetry, and regions of interest (ROIs) corresponding to the biological samples taken in the post perfusion processing protocol (see Section 0) are shown.

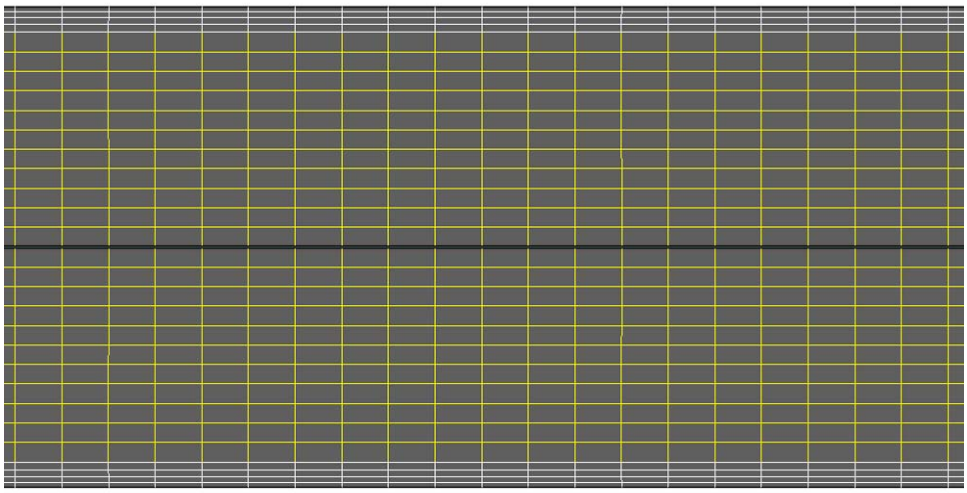

Figure 5.2 Magnified view of a representative initial mesh. The boundary layer is in white, symmetry axis is in black, and the rest of the mesh is in yellow.

For flexure, the initial geometry was specified as the geometry at diastole (i.e., 80mm Hg pressure and zero curvature). Proximal and distal IR and length were extracted from t=0 of the cyclic curvature loading step of the flexure simulation (see Section 4.3.2). The procedure for fluid volume reconstruction of the flexure experiments was the same as for the stretch experiment except that an axi-symmetric mesh was not employed. Because the bending deformation is not axi-symmetric a full three-dimensional mesh was required (Figure 5.3). However, like the solid stress analysis the curvature plane can be used as a symmetry plane to reduce computational cost (see Section 4.3.2). Two types of elements were used in the meshing of the three-dimensional hemi-cylinder. A boundary layer along the outer wall was generated with quadrilateral elements and the inner portion of the volume was meshed with wedge elements (Figure 5.4).

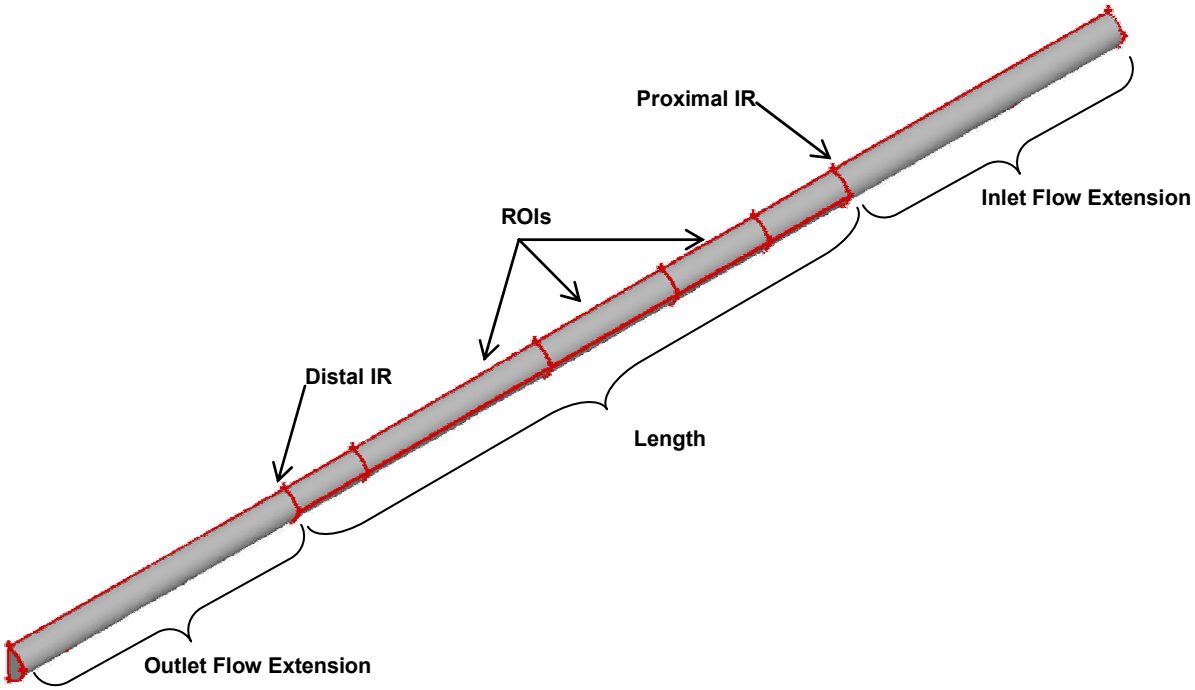

Figure 5.3 Schematic of a three-dimensional representative fluid volume reconstruction for the flexure simulations. The proximal and distal inner radii (IR), specimen length, flow extensions, and regions of interest (ROIs) corresponding to the biological samples taken in the post perfusion processing protocol (see Section 0) are shown.

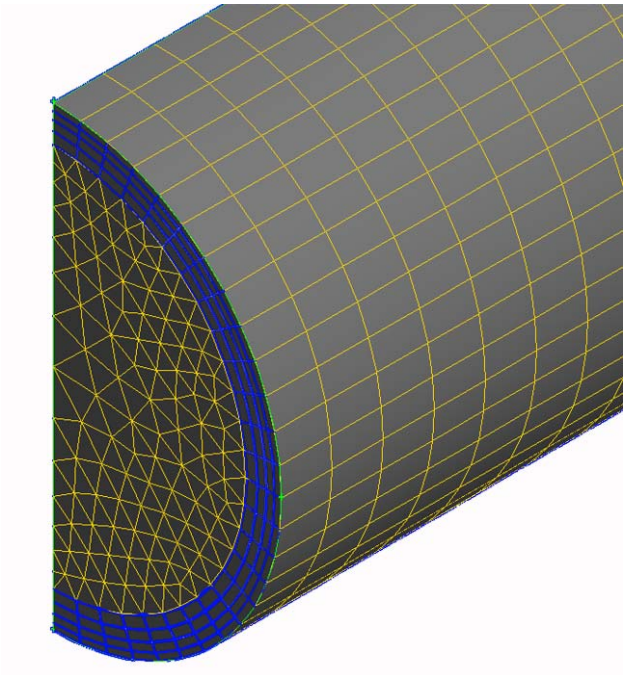

Figure 5.4 Magnified view of a representative initial three-dimensional mesh for the flexure simulations. The boundary layer is in blue, edges are in green, and the rest of the mesh is in yellow.

5.1.2 Specification of Deforming Mesh

Three types of deforming mesh were utilized to model the control, stretch, and flexure specimens, respectively. The control specimens had radial deformation due to pressure distension only. The stretch specimens had both axial and radial deformation, while the flexure experiments had deformations in all three coordinate directions. The following sections provide detailed descriptions of how these axi-symmetric (control and stretch) and three-dimensional (flexure) deformations were applied to the finite volume meshes. In all cases, displacements were applied to the boundary nodes representing the vessel wall, flow extension walls, and the symmetry axis. All interior node positions were updated by a spring smoothing algorithm provided by FLUENT v6.2. The custom displacement fields described below were incorporated into user defined-functions written in the programming language C (see Appendix G). These functions were compiled and added to the solver routine such that the mesh was updated at every time step in the analysis.

5.1.2.1 Axi-symmetric simulations

The temporal profile of proximal and distal IR during the stretch and / or pressure cycles were extracted from the finite element simulations for both the control and stretch simulations in Section 4.3.1. The percent change in radius from the beginning of the 1 Hz loading cycle for each experiment in the stretch set is shown in Figure 5.5.

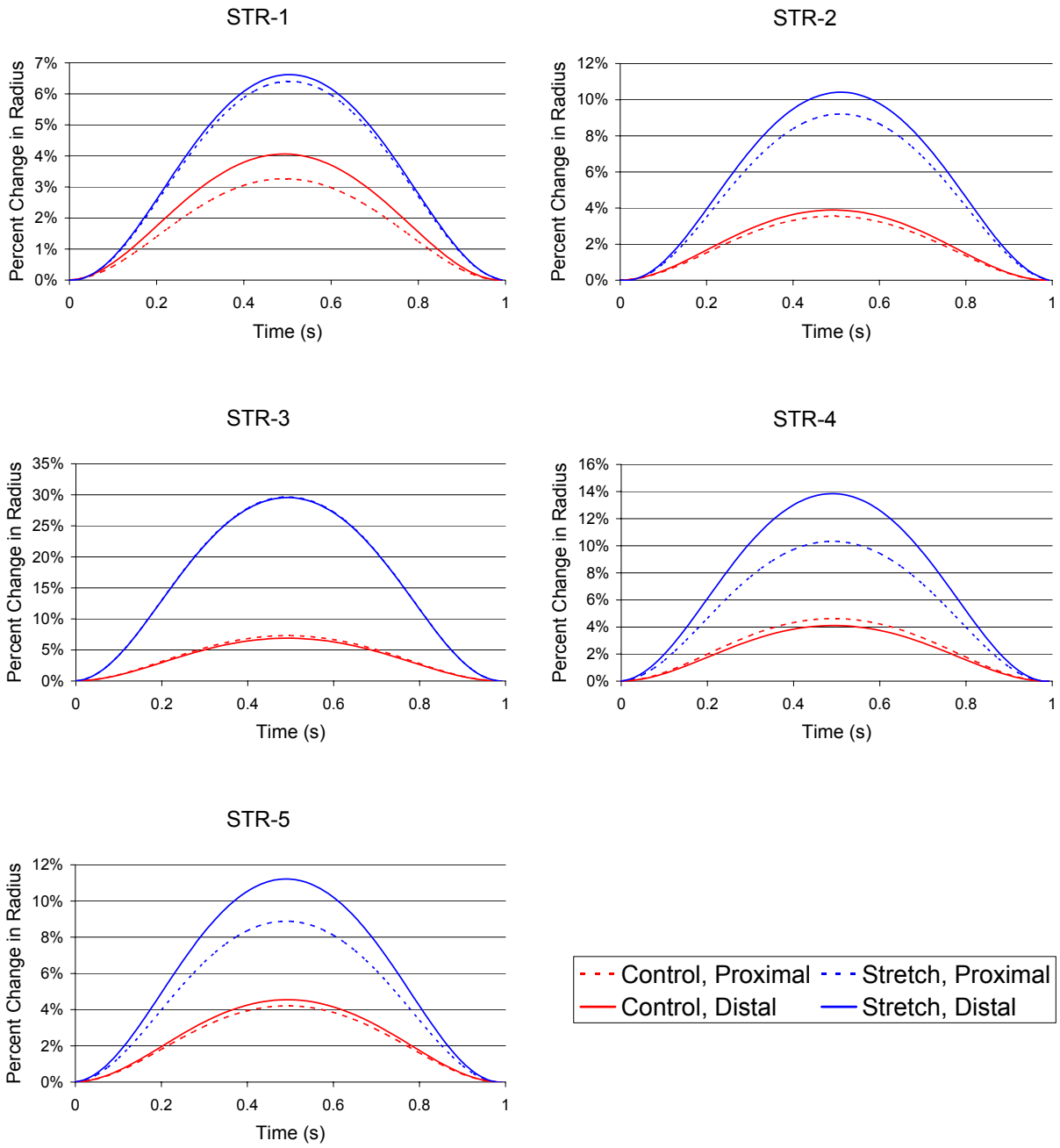

Figure 5.5 Percent change in the proximal and distal radius over the loading cycle for the stretch and control specimens from each experiment in the stretch set.

As expected, there is specimen-to-specimen variability in the radial deformation due to geometry differences (recall Table 4.6 in Section 4.5.2).

Since all loading cycles were applied via sinusoidal functions the deformations were also sinusoidal. Therefore, simple trigonometric functions were used to model the radius changes in the deforming mesh. For each specimen, two wave amplitudes corresponding to the radial displacement were calculated, a proximal amplitude and a distal amplitude. The formula for the amplitude was:

$$\text{Amplitude} = \frac{\text{IR}_{\text{Maximum}} - \text{IR}_{\text{Minimum}}}{2} \tag{5.1}$$

The amplitude of the 1 Hz radial displacement waveform for all points between the proximal and distal ends was then determined using simple linear interpolation as described for the geometric reconstructions (see Section 4.1.2). The proximal and distal radial displacement amplitudes for the stretch and paired control specimens from the stretch experiment set and the control specimens from the flexure experiment set are shown in Table 5.2.

For the stretch specimens there was an additional axial displacement. However, unlike the radial displacement, this deformation was known prior to the finite element simulations. In the EVPS and the finite element simulations, equal and opposing axial displacements were applied to the ends of the vessel segment to generate a maximum stretch of 7%. Again, the time profile of the loading was sinusoidal requiring specification of only the amplitude (one half the maximum displacement) of the sine function. The amplitude for a given node was determined as follows: The coordinate system for the reconstructed geometry was centered along the vessel axis such that half the vessel was on one side of the radial axis and half was on the other (Figure 5.6). Then, assuming a uniform vessel stretch of 7% throughout the length, the maximal nodal

displacements were prescribed as the axial coordinate times 0.07. The axial displacement as a function of time and axial position (D(t,z)) is then given by

$$D(t,z) = -\left(\frac{0.07\,z}{2}\right)\mathrm{Cos}(2\,\pi\,t) + \frac{0.07\,z}{2} \tag{5.2}$$

Negative axial coordinates (i.e., those toward the proximal side), would have negative displacement values while mirror points on the other side of the radial axis would have equal positive displacement (Figure 5.6). This generated a uniform 7% stretch across the length of the vessel segment. The inlet and outlet flow extensions were given rigid displacement motions with amplitudes equal to those of the proximal and distal nodes of the vessel, respectively.

Table 5.2 Radial displacement amplitudes (in mm) for the axi-symmetric fluid simulations.

Experiment ID	Radial Displacement Amplitiudes	
	Proximal	Distal
STR-1-S	0.077	0.077
STR-1-C	0.045	0.041
STR-2-S	0.133	0.133
STR-2-C	0.066	0.060
STR-3-S	0.259	0.235
STR-3-C	0.068	0.076
STR-4-S	0.132	0.140
STR-4-C	0.054	0.061
STR-5-S	0.134	0.123
STR-5-C	0.059	0.054
FLX-1-C	3.2×10^{4}	4.0×10^{4}
FLX-2-C	5.5×10^{4}	6.5×10^{4}
FLX-3-C	1.1×10^{3}	7.4×10^{4}
FLX-4-C	0.015	0.052
FLX-5-C	2.6×10^{4}	3.3×10^{4}

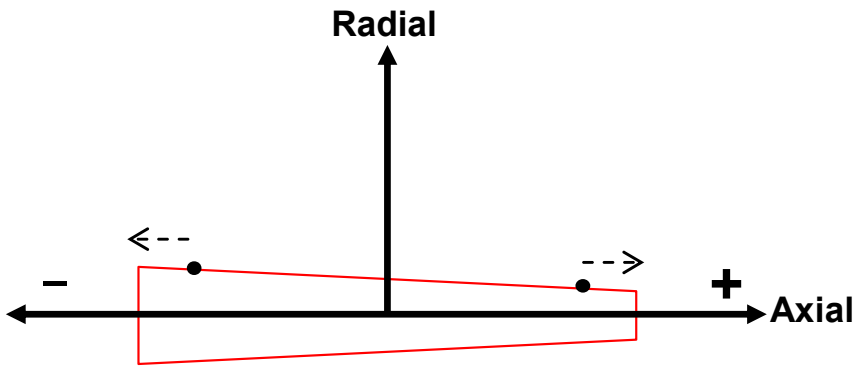

Figure 5.6 Diagram of the axial displacement field model. The vessel geometry (in red) is centered along the vessel axis allowing the axial displacements (as a function of the axial coordinate) to be symmetric about the vessel center.

5.1.2.2 Three-dimensional simulations

The displacement field for the fluid volume under cyclic flexure was quite complex. There were noticeable displacements that varied with position in all three coordinate directions. The most noteworthy variations in displacement are seen in the vertical direction of the curvature plane (Figure 5.7). However, given the significant computational cost of three-dimensional, dynamic, deforming mesh fluid dynamics analyses, two simplifying assumptions were made, based on the data in Figure 5.7, to obtain results in a timely manner: 1) The radial distension due to the pressure pulse is small in comparison to the vertical deflections caused by the flexure displacement and thus can be neglected. The vertical displacement field specified a zero displacement at the proximal and distal end nodes in contact with the membrane (including those of the lesser curvature). Therefore, any vertical displacement in the proximal and distal greater curvature end nodes is a result of radial displacement due to the pressure pulse. Comparing the blue dashed (Greater, Proximal) and black dashed (Greater, Distal) lines to the red dashed lines

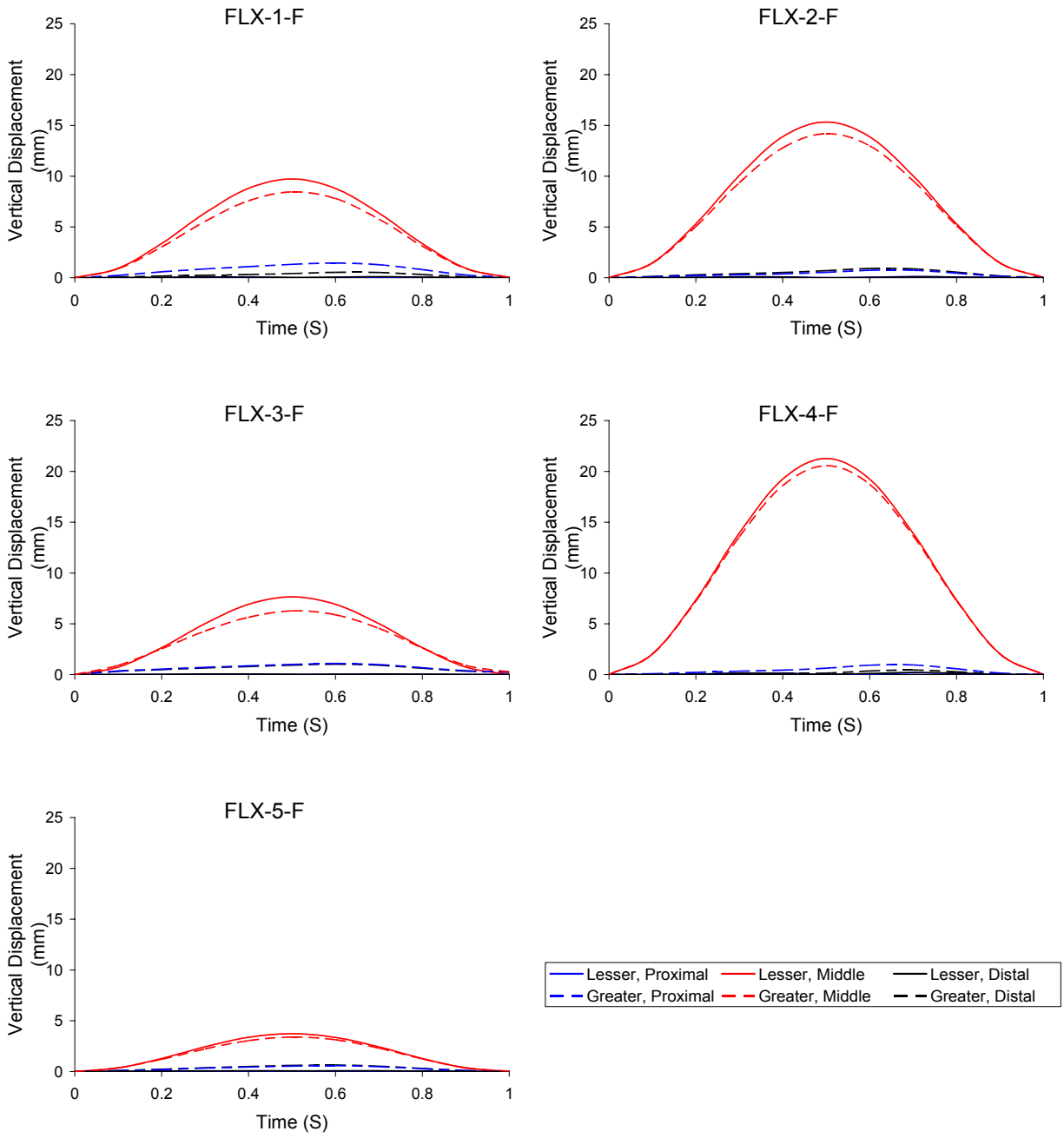

Figure 5.7 Vertical displacement for 6 key points of interest in the 5 flexure specimens from the FLX experiment set. Points included the most proximal points on the greater (Greater, Proximal) and lesser curvatures (Lesser, Proximal); the midpoints (point of maximal curature) of the greater (Greater, Middle) and lesser curvatures (Lesser, Middle); and the most distal points on the greater (Greater, Distal) and lesser (Lesser, Distal) curvatures. The Lesser, Distal and Lesser, Proximal lines are essentially zero and therefore, are difficult to visualize.

(Greater, Middle) in Figure 5.7 confirms that the displacement is dominated by the imposed curvature deflection. 2) The vertical displacement along the lesser curvature is equal to that along the greater curvature. Comparing the solid red line (lesser curvature) to the dashed red line (greater curvature) demonstrates only small differences in displacement along the greater and lesser curvatures. This second assumption essentially preserves a circular-cross section throughout the fluid analysis.

Mathematical models describing the in-plane motion of the fluid boundary were adapted from the custom displacement field functions generated for each of the individual cyclic flexure finite element analyses (see equations (4.32)-(4.35) in Section 4.3.2). Two displacement functions were required: one for the vertical displacement prescribed by the flexure membrane; and one for the horizontal displacement prescribed by the motion of the cannulae. The vertical displacement field was determined to be the same as that provided in the finite element simulation (recall Figure 4.10). That is, the vertical displacement function (with respect to axial position and time) used in each finite element simulation of flexure (see equations (4.32)-(4.35) in Section 4.3.2) was applied to all boundary nodes of the vessel wall. The flow extension boundaries were fixed in the vertical direction.

The horizontal displacement in the finite element simulation was only applied to the proximal and distal end nodes. In the case of the fluid volume, the horizontal displacement field for all nodes on the fluid boundary must be specified. Recall that flexure was applied by equal movement of the two cannulae toward each other, allowing the membrane to flex into the vessel. Therefore, the horizontal displacement field was symmetric about the vertical axis as in the stretch displacement (see Section 5.1.2.1). Using the same methodology as for stretch (see Section 5.1.2.1 and equation (5.2), the vessel was center along the horizontal axis. Then the

maximal horizontal displacement for a given node was calculated as a percent of its axial coordinate. Unlike the stretch case, the displacement was inverted such that the nodes moved toward the vertical axis rather than away. To maintain the symmetry (i.e., the equal displacement of the two cannulae) the percent for a given vessel segment must be constant over its length and was determined as the total cannula displacement prescribed by the motion control program (recall equation (2.3) in Section 2.2.2.1) divided by the vessel segment length. The horizontal displacement field then becomes:

$$D(t, z) = \left(\frac{MD}{2L} z \right) Cos(2 \pi t) - \frac{MD}{2L} z \tag{5.3}$$

where MD is the motor displacement of the cannulae given in (2.3). This deformation function was applied to the boundary nodes of the vessel wall. The inlet and outlet flow extensions were treated as rigid bodies with displacements amplitudes equal to those of the proximal and distal end nodes of the vessel, respectively.

5.2 BOUNDARY CONDITIONS

The accuracy of computational fluid dynamics solutions is highly dependent upon providing accurate boundary conditions. Pressure and flow data acquired during the *ex vivo* perfusion experiments (see Sections 2.1 and 3.2.1) provided detailed information used to define the inlet and outlet boundary conditions for each fluid simulation. The only other boundary condition specified was a no slip condition (i.e., all components of velocity are zero at the wall) applied to the flow extension and vessel walls.

5.2.1 Inlet Boundary Condition

For all fluid simulations the time varying fluid velocity profile at the inlet to the inlet flow extension was specified. Since the velocity profile in the EVPS was unknown, a uniform profile was specified. This is valid since inlet flow extensions were used to ensure full flow profile development prior to the vessel entrance. The velocity profile magnitude was sinusoidal and specified by the amplitude and magnitude shift. Since velocity was not measured directly in the EVPS, velocity values were calculated from the flow waveform. As stated in Section 3.1.2 the perfusion conditions were set to a pulsatile pressure of 120/80 mm Hg with an average volumetric flowrate of 100 ml/min. In all experiments these conditions generated a flow waveform of 130/70 ml/min (Figure 5.8).

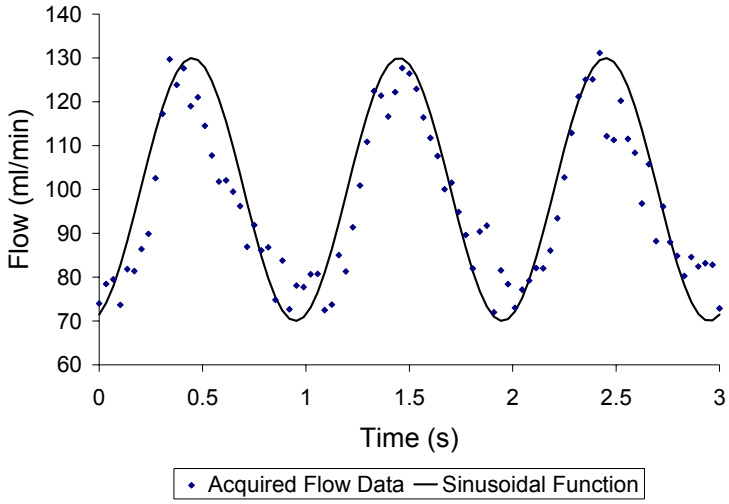

Figure 5.8 Representative time-varying flowrate in the EVPS. Data acquired during a perfusion experiment is compared with a sinusoidal function for idealized 130/70 ml/min pulsatile flow.

The maximum and minimum average (over the cross-sectional area) velocities were calculated from the maximum and minimum flowrates and the inlet cross-sectional area using:

$$v = \frac{Q}{A} \tag{5.4}$$

where v is average velocity, Q is the flowrate, and A is the cross-sectional area. The periodic amplitude and magnitude shift of the sinusoidal velocity function were then calculated using:

$$\text{amplitude} = \frac{v_{\text{maximum}} - v_{\text{minimum}}}{2} \tag{5.5}$$

and

$$\text{magnitude shift} = \frac{v_{\text{maximum}} + v_{\text{minimum}}}{2} \tag{5.6}$$

The generalized, uniform, time-profile for velocity is then given by:

$$v = (\text{-amplitude})\ \text{Cos}(2\pi t) + \text{magnitude shift} \tag{5.7}$$

The amplitudes and magnitude shifts for each specimen-specific simulation are given in Table 5.3.

Table 5.3 Specimen specific velocity profile amplitudes and magnitude shifts given in m/s.

Experiment ID	Amplitude	Magnitude Shift
STR-1-S	0.027	0.092
STR-1-C	0.018	0.060
STR-2-S	0.019	0.064
STR-2-C	0.012	0.039
STR-3-S	0.052	0.174
STR-3-C	0.046	0.155
STR-4-S	0.024	0.081
STR-4-C	0.029	0.096
STR-5-S	0.018	0.059
STR-5-C	0.020	0.068
FLX-1-F	0.034	0.112
FLX-1-C	0.102	0.339
FLX-2-F	0.107	0.354
FLX-2-C	0.137	0.458
FLX-3-F	0.055	0.184
FLX-3-C	0.036	0.120
FLX-4-F	0.072	0.241
FLX-4-C	0.228	0.863
FLX-5-F	0.132	0.438
FLX-5-C	0.115	0.384

5.2.2 Outlet Boundary Condition

A pressure outlet boundary condition was applied to the outflow extension outlet. The time varying proximal and distal pressures (recall Figure 2.2) acquired during the *ex vivo* perfusion experiments were averaged to determine the actual vessel internal pressure time-profile. These values were fit to a sinusoidal function to generate a pressure wave of 120/80 mm Hg as provided in the EVPS (Figure 5.9).

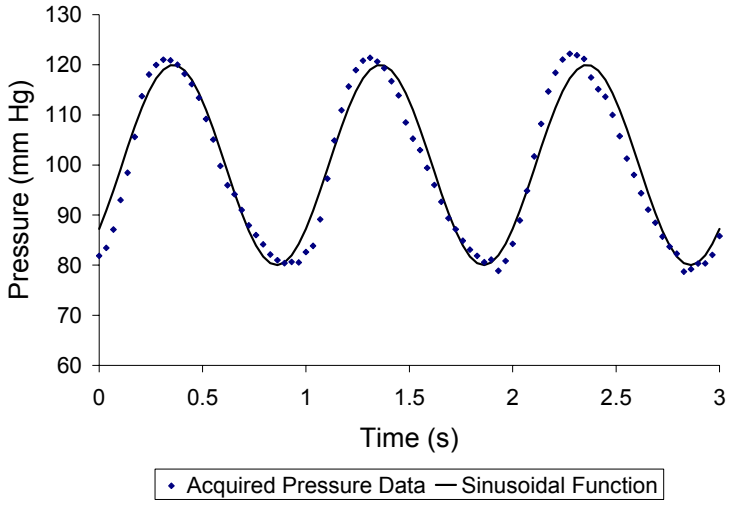

Figure 5.9 Representative time-varying pressure in the EVPS. Data acquired during a perfusion experiment is compared with a sinusoidal function for idealized 120/80 mm Hg pulsatile pressure.

5.3 RESULTS

5.3.1 Cyclic Axial Stretch

The cyclic axial stretch simulations were axi-symmetric with uni-directional flow. Therefore, the total shear rate was dominated by the axial component of shear. The radial component was usually 1-2 orders of magnitude less than the axial component. Consequently, only the total shear rate is reported for the axi-symmetric analyses. The shear rate varied with both time and axial position (Top of Figure 5.10-Figure 5.14). Due to phase lag in the velocity waveform over the length of the vessel, the maximum and minimum shear rates did not always occur at systole and diastole. The distributions of the maxima and minima over the ROIs corresponding to the segments taken for biologic processing for each stretch and paired control specimens in the

stretch experiment set are shown in the Bottom of Figure 5.10-Figure 5.14. There are noticeable specimen-to-specimen differences in the time profiles as well as the distribution of maximal and minimal shear rate. However, this variation is less extreme than that seen for the solid stresses in Section 4.0 . The maximum and minimum shear rates for each ROI from each specimen were tabulated with the shear rates at systole and diastole as endpoints for the regression analyses of Specific Aim 4 (Table 5.4 and Table 5.5). In addition, in order to capture the time variation of these shear measures, two additional parameters were calculated. First, the shear rate range was calculated as the difference between the maximum and minimum shear rate. Second, the shear rate pulse was calculated as the difference between the systolic and the diastolic shear rate. Those values are also included in Table 5.4 and Table 5.5.

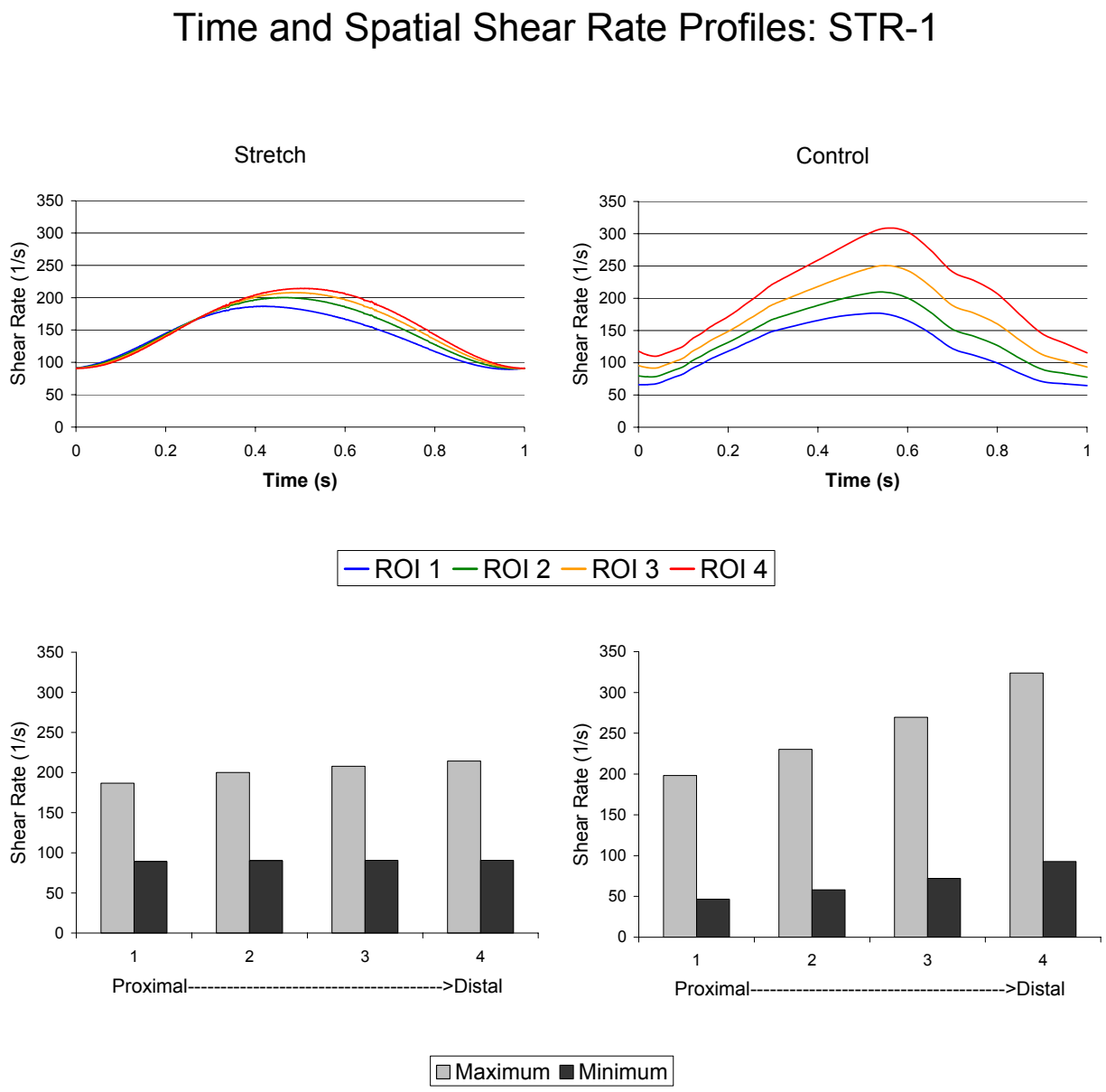

Figure 5.10 Time and spatial shear rate profiles for STR-1: Top - Area weighted average shear rate for the ROIs corresponding to the segments taken for biological analyses in Section 3.0 as a function of time for the stretch (left) and control (right) specimens from STR-1. Segments are numbered from proximal to distal. Bottom - Bar charts of maximum and minimum shear rate for the ROIs in the stretch (left) and control (right) specimens STR-1.

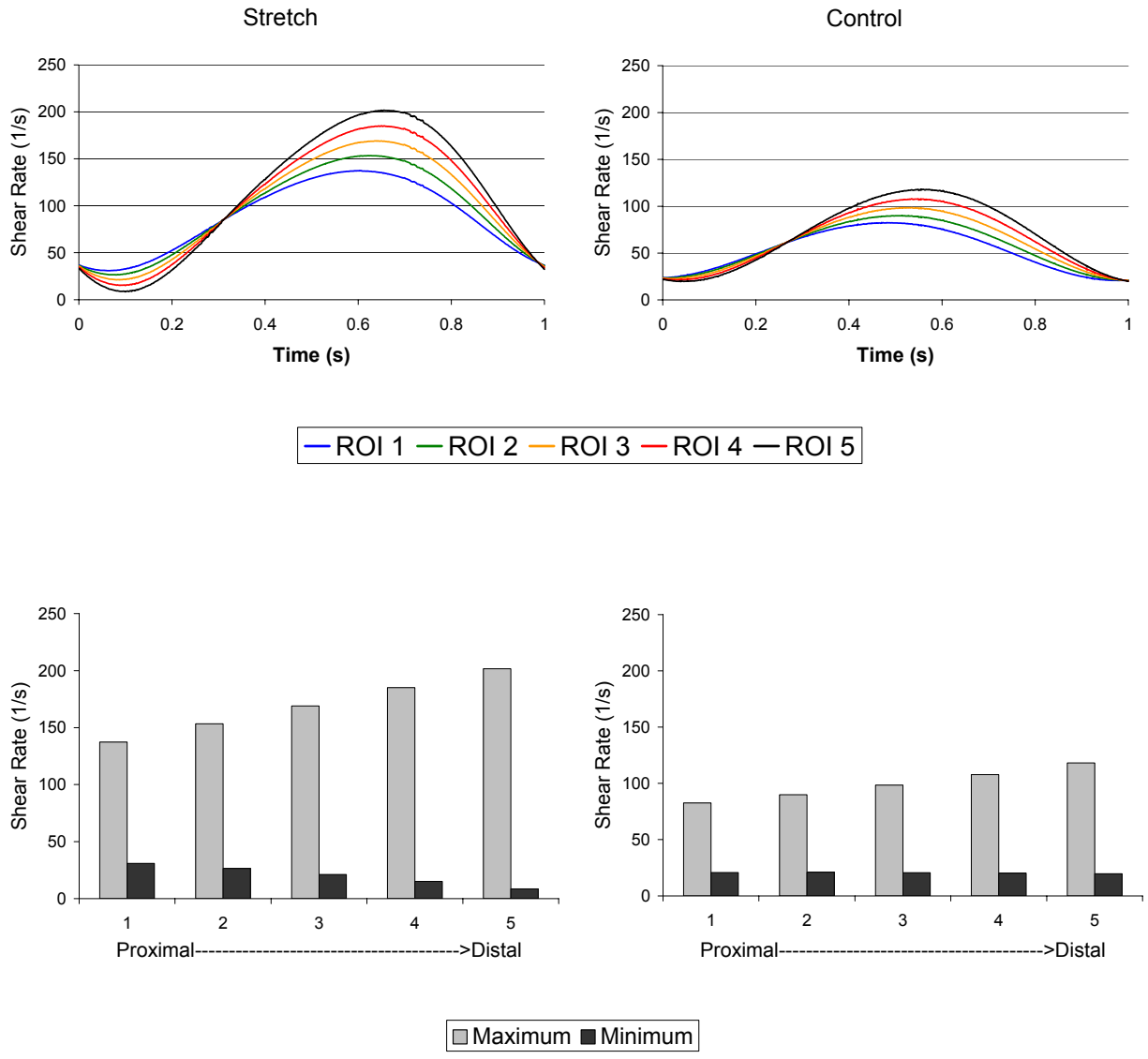

Figure 5.11 Time and spatial shear rate profiles for STR-2: Top - Area weighted average shear rate for the ROIs corresponding to the segments taken for biological analyses in Section 3.0 as a function of time for the stretch (left) and control (right) specimens from STR-2. Segments are numbered from proximal to distal. Bottom - Bar charts of maximum and minimum shear rate for the ROIs in the stretch (left) and control (right) specimens STR-2.

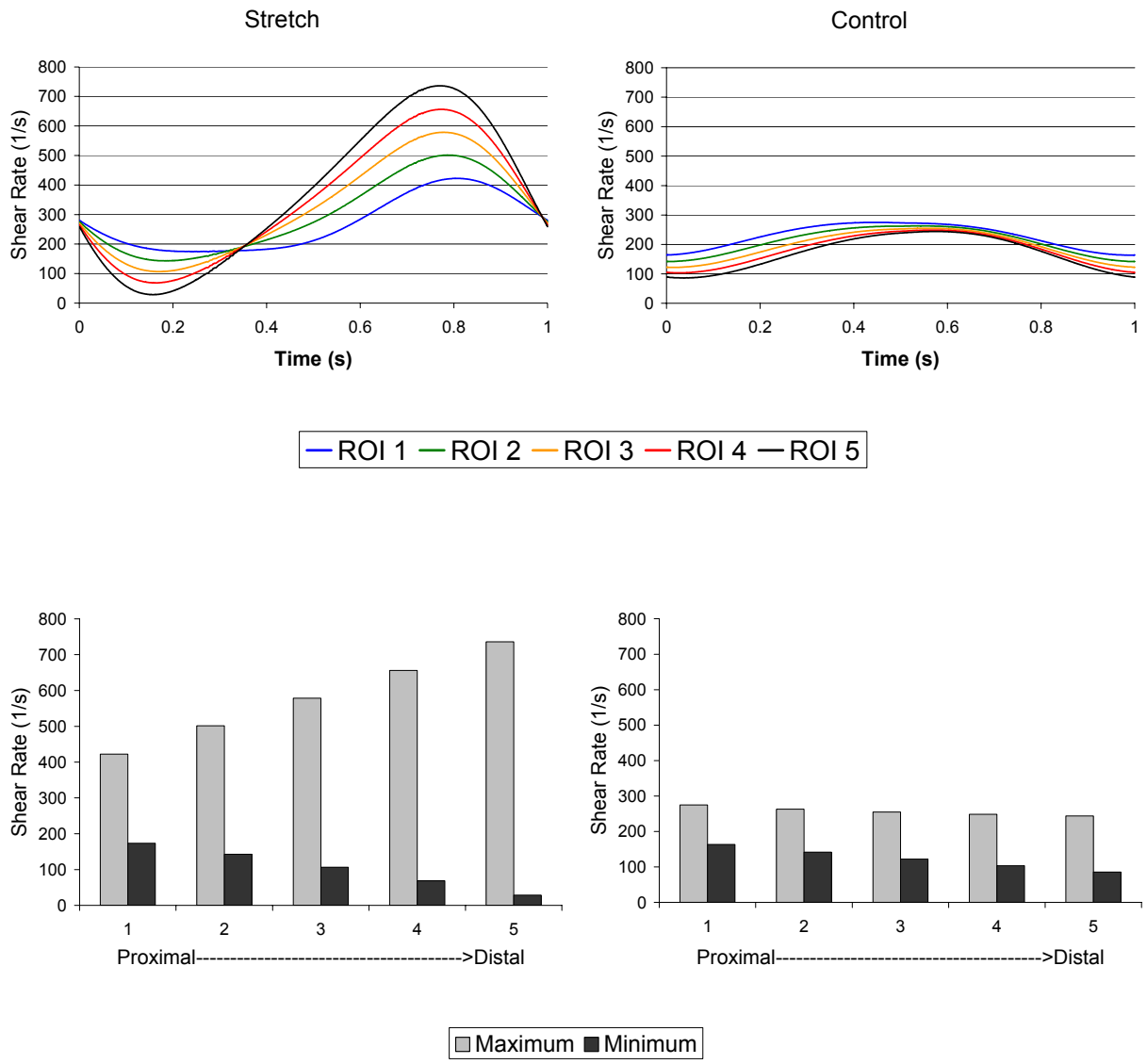

Figure 5.12 Time and spatial shear rate profiles for STR-3: Top - Area weighted average shear rate for the ROIs corresponding to the segments taken for biological analyses in Section 3.0 as a function of time for the stretch (left) and control (right) specimens from STR-3. Segments are numbered from proximal to distal. Bottom - Bar charts of maximum and minimum shear rate for the ROIs in the stretch (left) and control (right) specimens STR-3.

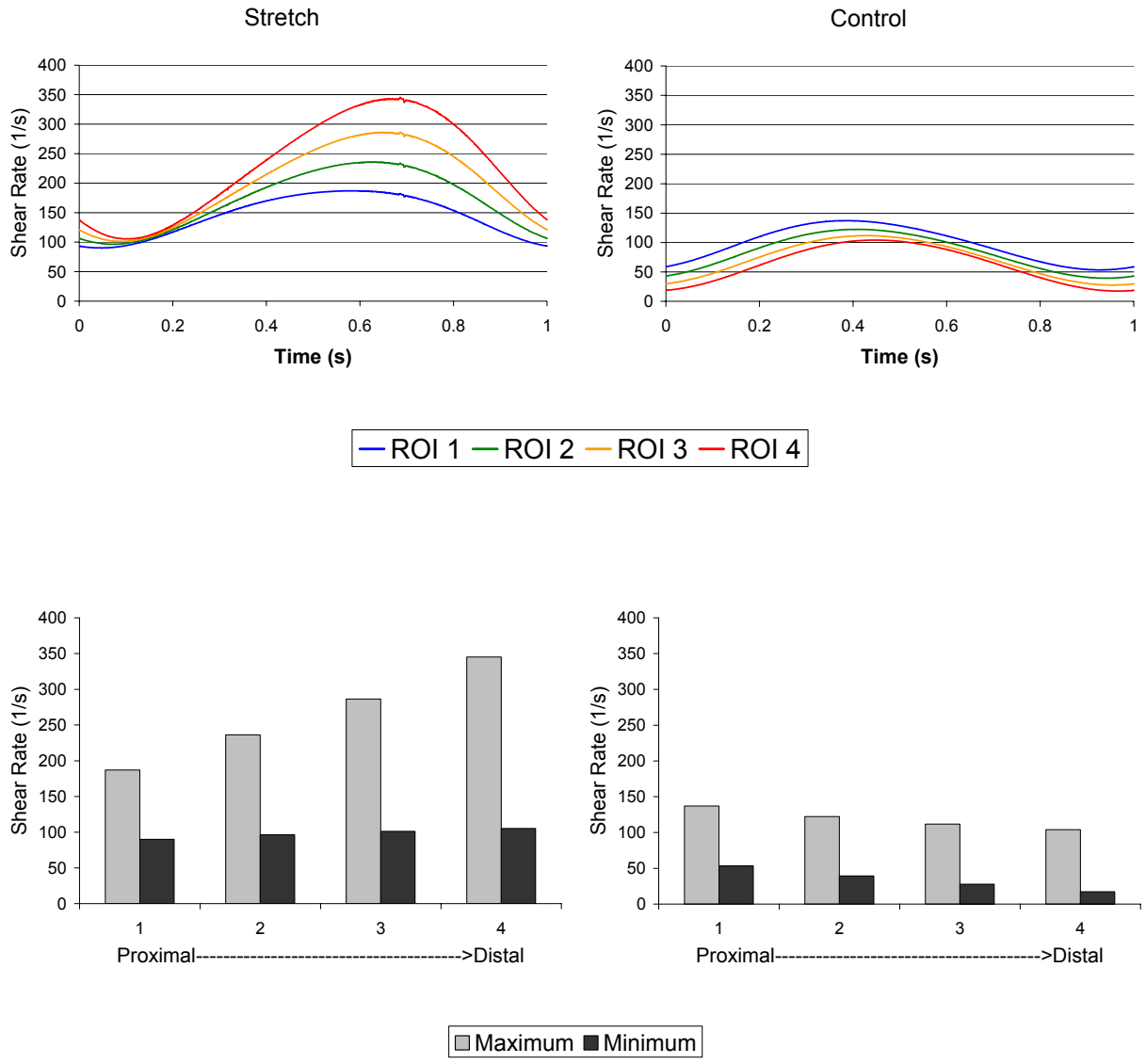

Figure 5.13 Time and spatial shear rate profiles for STR-4: Top - Area weighted average shear rate for the ROIs corresponding to the segments taken for biological analyses in Section 3.0 as a function of time for the stretch (left) and control (right) specimens from STR-4. Segments are numbered from proximal to distal. Bottom - Bar charts of maximum and minimum shear rate for the ROIs in the stretch (left) and control (right) specimens STR-4.

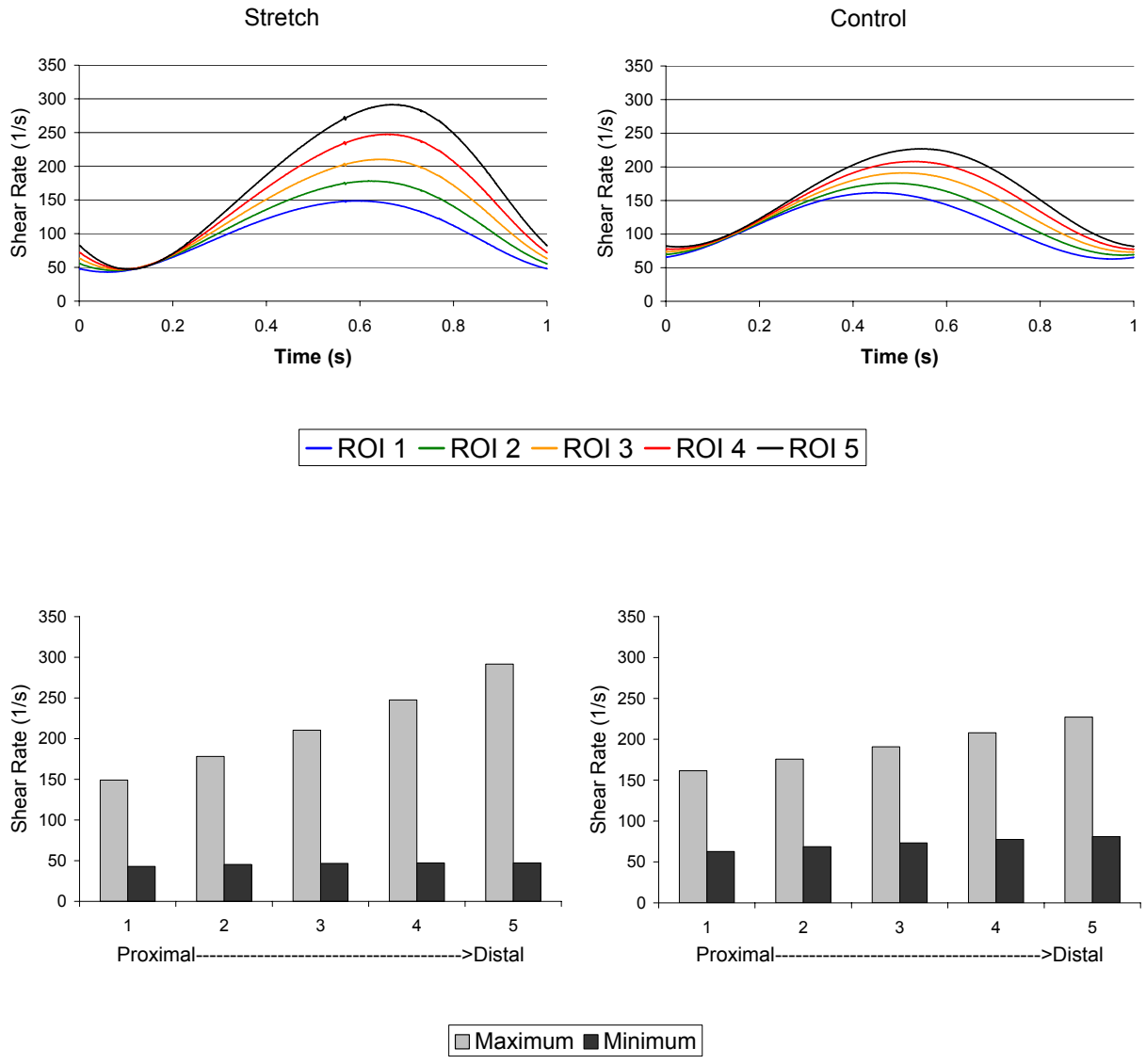

Figure 5.14 Time and spatial shear rate profiles for STR-5: Top - Area weighted average shear rate for the ROIs corresponding to the segments taken for biological analyses in Section 3.0 as a function of time for the stretch (left) and control (right) specimens from STR-5. Segments are numbered from proximal to distal. Bottom - Bar charts of maximum and minimum shear rate for the ROIs in the stretch (left) and control (right) specimens STR-5.

Table 5.4 Shear rate parameters for the ROIs from each stretch specimen from the STR experiment set. ROIs are numbered from proximal to distal.

Stretch							
		Shear Rate (1/s)					
		@ Diastole	@ Systole	Maximum	Minimum	Range	Pulse
STR-1-S	1	91	182	187	89	98	91
	2	91	199	200	90	110	108
	3	91	208	208	91	117	117
	4	91	214	214	91	124	123
STR-2-S	1	37	129	137	31	106	92
	2	36	139	153	26	127	103
	3	36	149	169	21	148	113
	4	35	159	185	15	170	124
	5	33	169	202	9	193	136
STR-3-S	1	280	212	422	173	249	-69
	2	275	274	501	143	358	-2
	3	270	320	578	106	472	49
	4	265	358	656	68	588	94
	5	259	394	736	28	708	135
STR-4-S	1	93	183	187	90	97	90
	2	106	221	236	96	140	114
	3	121	256	286	101	185	135
	4	138	293	345	105	240	156
STR-5-S	1	48	142	149	43	106	93
	2	56	163	178	45	133	107
	3	63	186	210	47	164	122
	4	72	212	248	47	200	139
	5	83	242	292	47	245	159

Table 5.5 Shear rate parameters for the ROIs from each control specimen from the STR experiment set. ROIs are numbered from proximal to distal.

Control							
		Shear Rate (1/s)					
		@ Diastole	@ Systole	Maximum	Minimum	Range	Pulse
STR-1-C	1	66	176	198	47	152	110
	2	79	206	230	58	172	127
	3	96	244	270	72	197	148
	4	118	296	324	93	231	178
STR-2-C	1	23	82	83	21	62	59
	2	23	90	90	21	69	66
	3	23	98	98	21	78	75
	4	23	106	108	20	88	84
	5	22	115	118	20	99	93
STR-3-C	1	164	273	275	163	111	109
	2	142	262	263	142	121	120
	3	123	252	255	122	133	130
	4	105	245	249	103	145	140
	5	89	239	244	86	158	150
STR-4-C	1	59	128	137	53	84	70
	2	43	117	122	39	83	74
	3	30	108	112	28	84	78
	4	19	102	104	17	87	83
STR-5-C	1	65	159	161	63	99	94
	2	70	175	176	69	107	106
	3	74	191	191	73	118	117
	4	78	207	208	77	130	129
	5	82	224	227	81	146	142

5.3.2 Cyclic Flexure

In contrast to cyclic stretch, the cyclic flexure fluid simulations showed significant contributions from all three principle components of shear rate. For reference, the coordinate system was oriented with the z-axis in the direction of flow, and the y-axis in the direction of the vertical displacement for curvature. The x-axis was normal to the curvature plane. The vector component shear rate versus time profiles for each of the flexure simulations is shown in (Figure 5.15-Figure 5.19). There were significant specimen-to-specimen variations in the time profiles, spatial distributions, and overall shear rate magnitudes. However, it is difficult to interpret the individual vector components since the vessel orientation with respect to the global coordinate system changes with time. The velocity profiles (Top of Figure 5.20-Figure 5.24) and total shear rate contours (Bottom of Figure 5.20-Figure 5.24) for each flexure simulation provide a simpler view of the flow behavior. These plots demonstrate the high specimen-to specimen variation in velocity profile, shear rate distribution, and geometry. The individual vector components of shear can be summed to determine the total shear rate versus time for the ROIs corresponding to the segments taken for biological processing from each flexure specimen (Top of Figure 5.25-Figure 5.29). In this case, the maximum and minimum shear rates tended to occur at systole and diastole, respectively. Bar charts of these values demonstrate the spatial distributions of shear rate for each flexure specimen (Bottom of Figure 5.25-Figure 5.29).

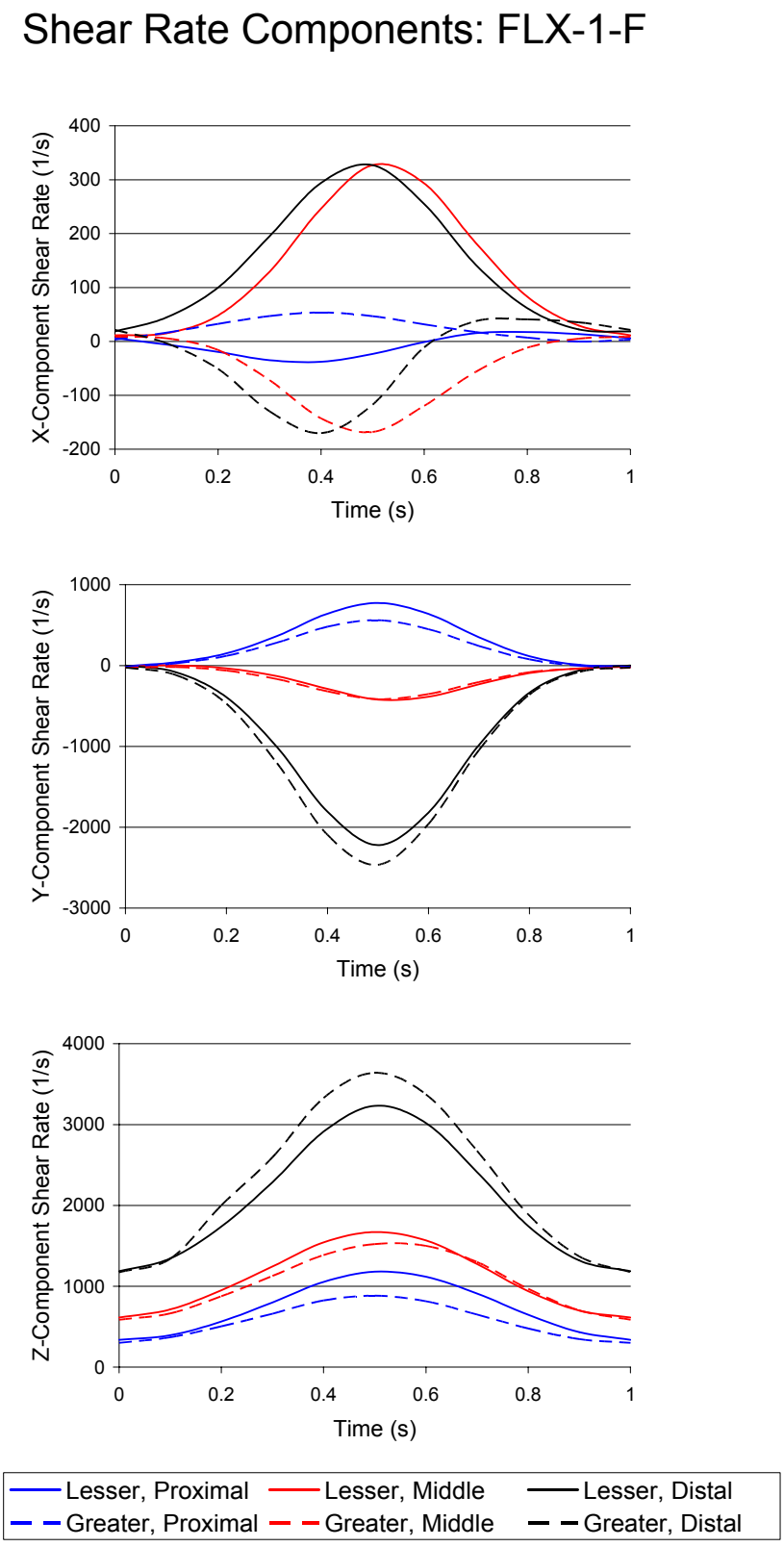

Figure 5.15 Individual vector components of shear rate versus time for the ROIs corresponding to the segments taken for biological analysis for FLX-1-F. Lesser and greater refer to curvature.

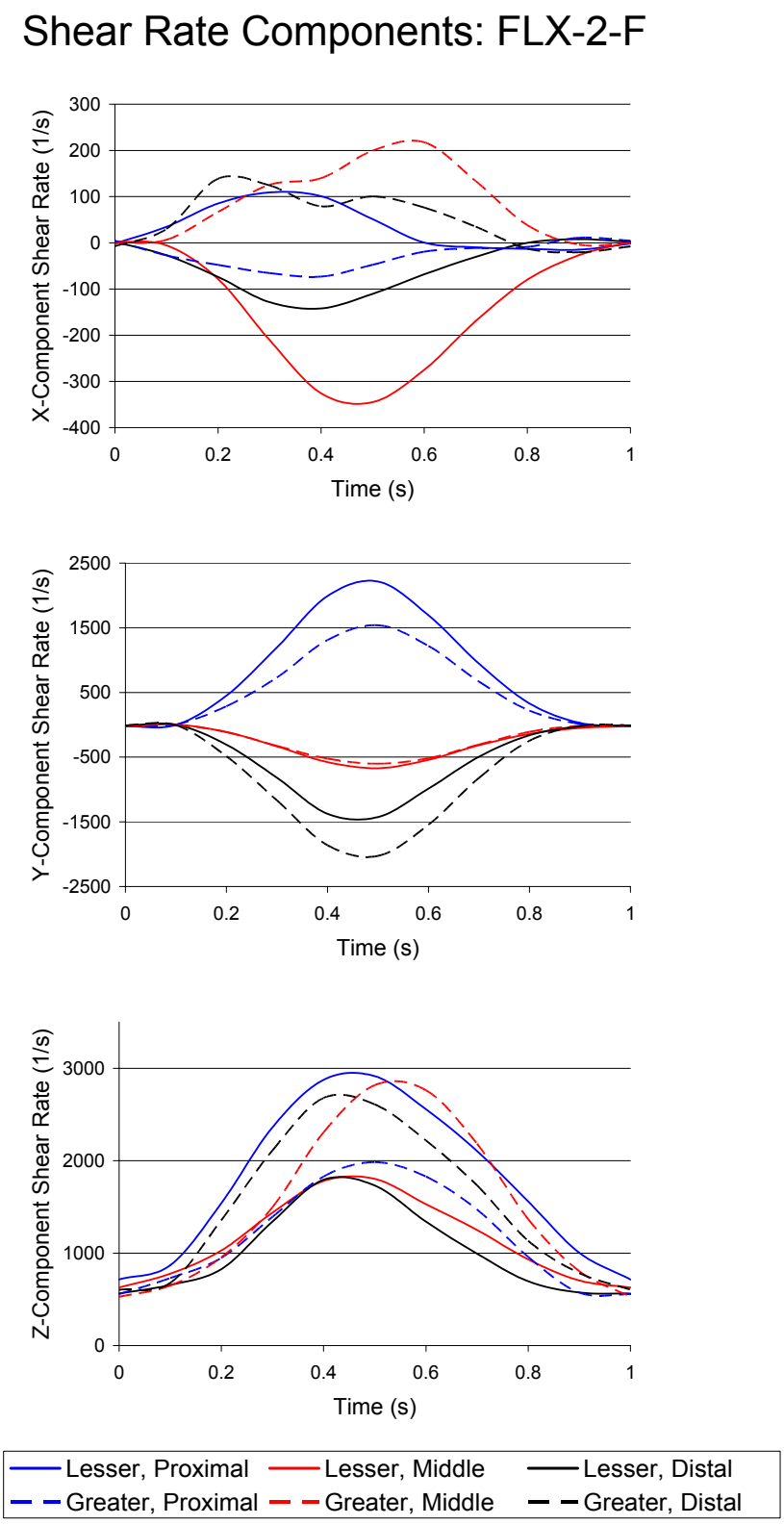

Figure 5.16 Individual vector components of shear rate versus time for the ROIs corresponding to the segments taken for biological analysis for FLX-2-F. Lesser and greater refer to curvature.

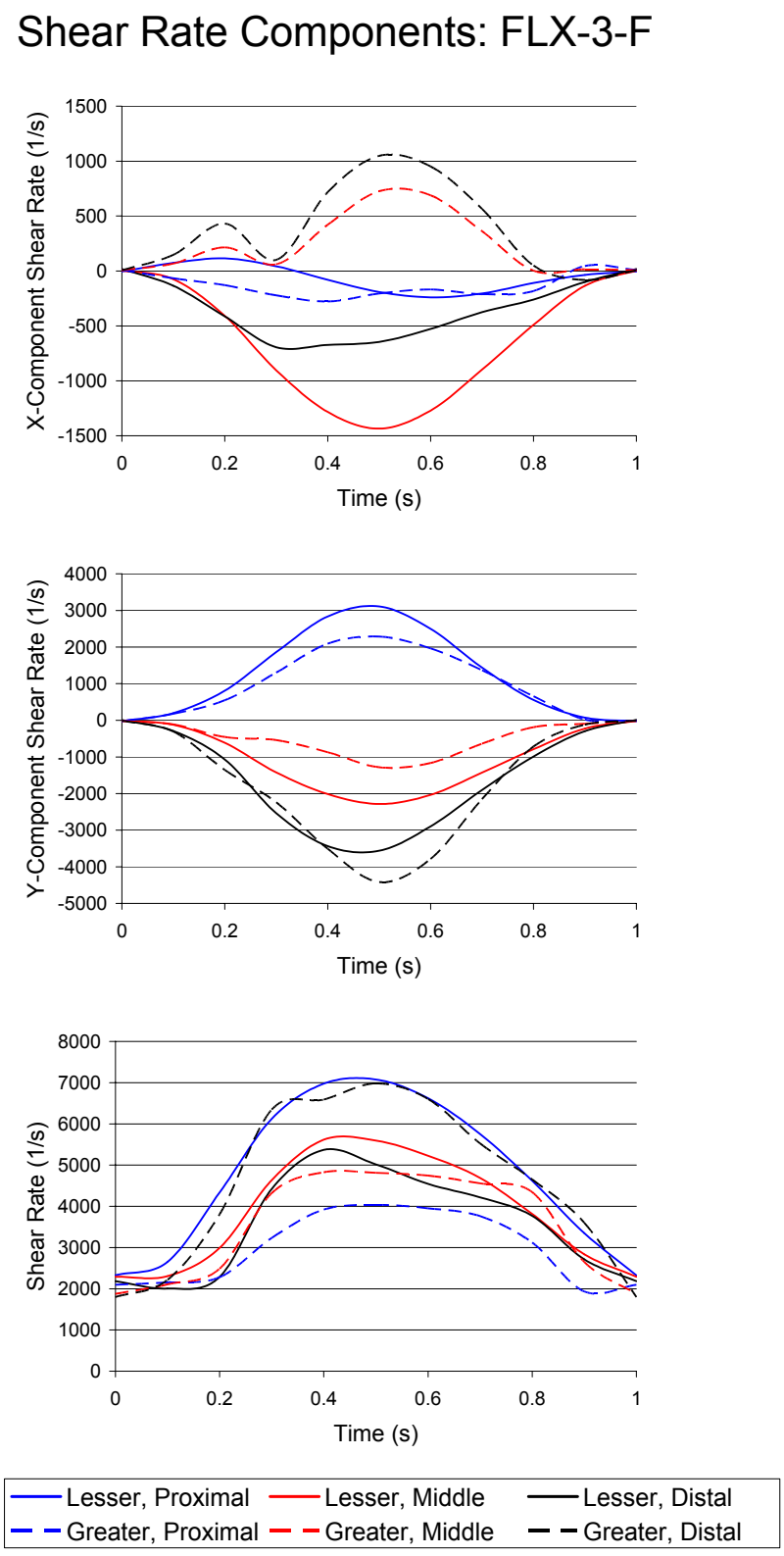

Figure 5.17 Individual vector components of shear rate versus time for the ROIs corresponding to the segments taken for biological analysis for FLX-3-F. Lesser and greater refer to curvature.

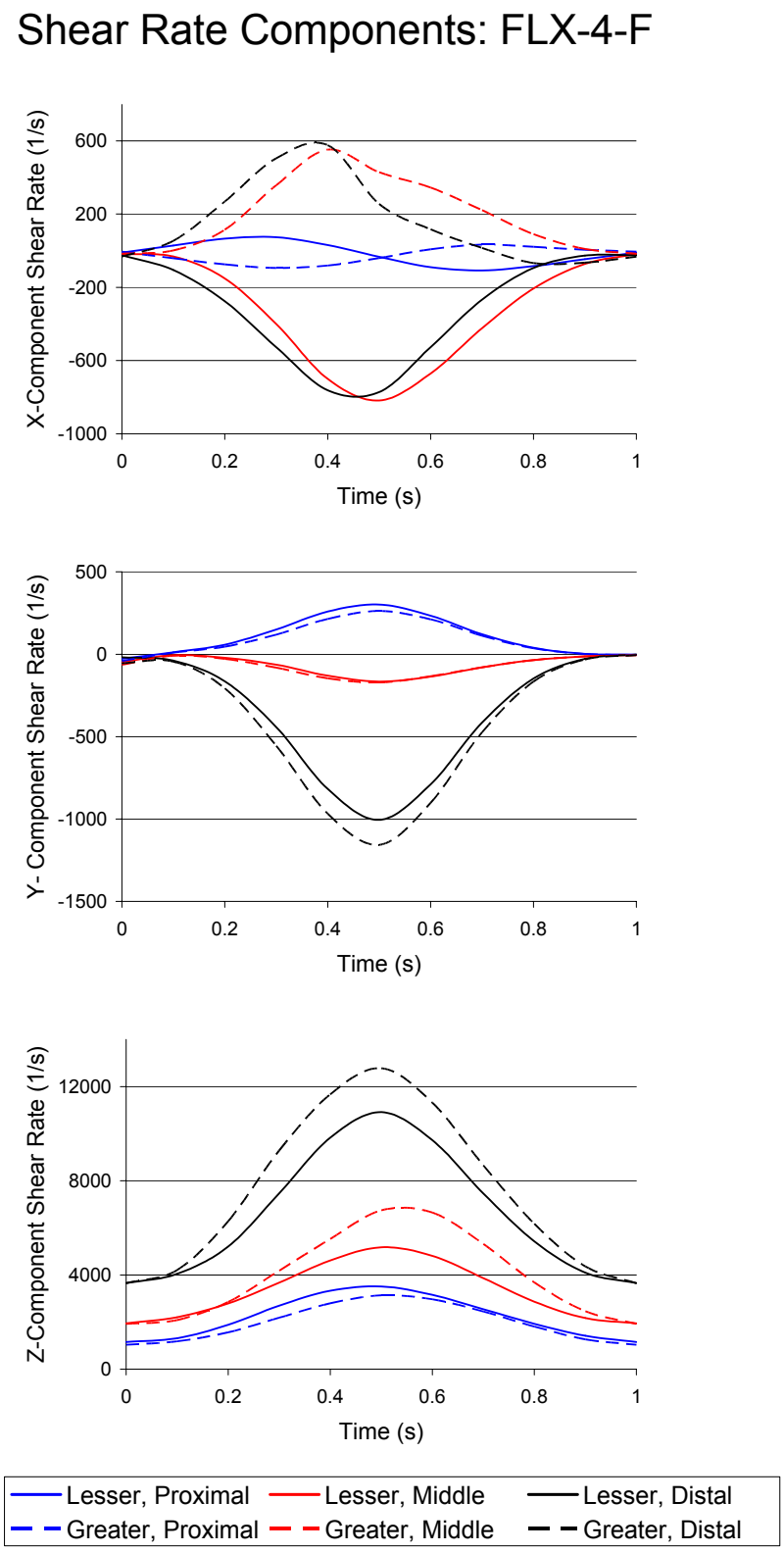

Figure 5.18 Individual vector components of shear rate versus time for the ROIs corresponding to the segments taken for biological analysis for FLX-4-F. Lesser and greater refer to curvature.

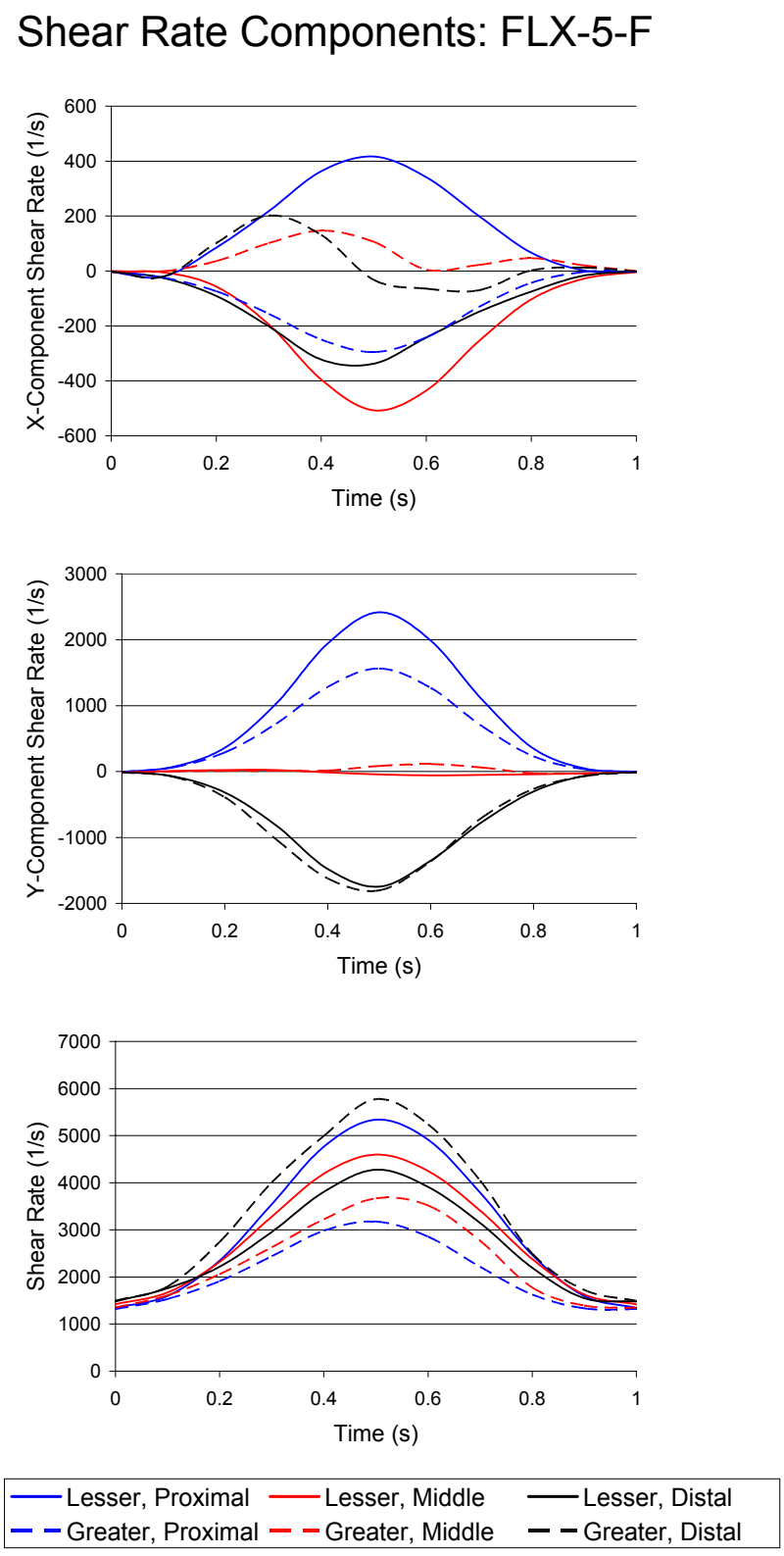

Figure 5.19 Individual vector components of shear rate versus time for the ROIs corresponding to the segments taken for biological analysis for FLX-5-F. Lesser and greater refer to curvature.

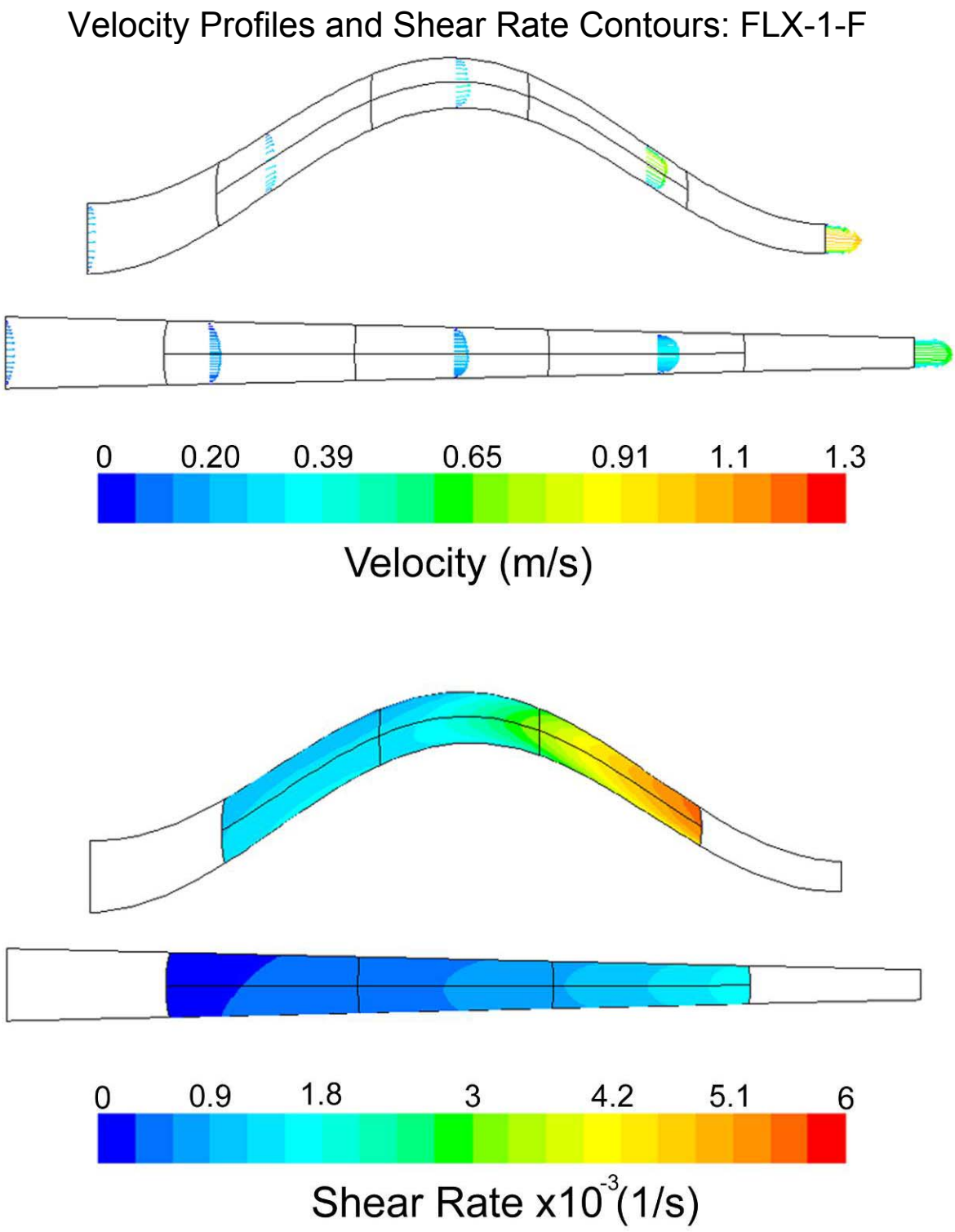

Figure 5.20 Velocity profile for FLX-1-F (Top). Velocity vectors are scaled and colored by their magnitude. Shear rate contour for FLX-1-F (Bottom). In both cases, the maximum and minimum curvatures occurring at sytole and diastole, respectively, are shown. Also, the boundaries of the biological processing ROIs are delineated. Geometries are to scale within a given specimen but not between specimens.

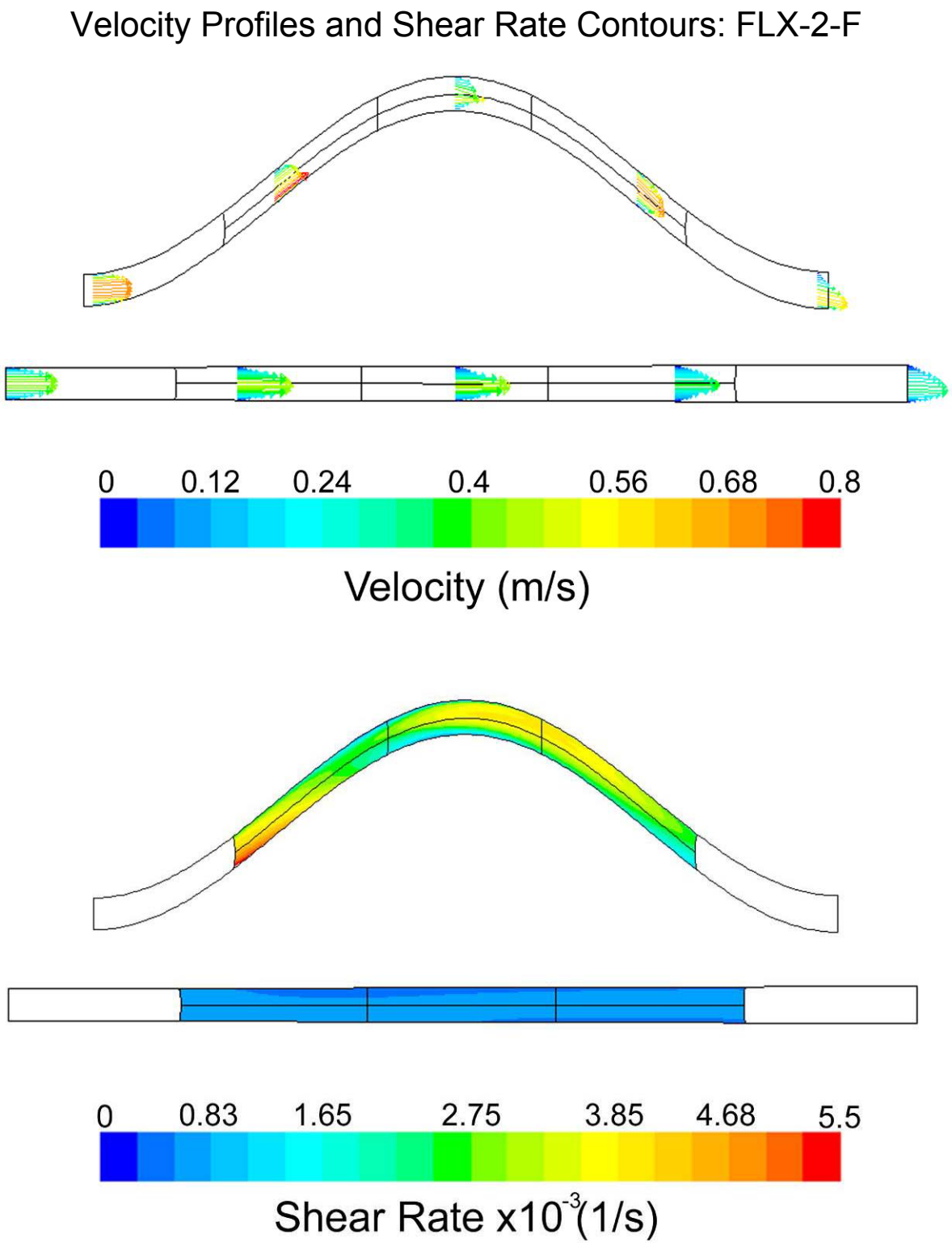

Figure 5.21 Velocity profile for FLX-2-F (Top). Velocity vectors are scaled and colored by their magnitude. Shear rate contour for FLX-2-F (Bottom). In both cases, the maximum and minimum curvatures occurring at sytole and diastole, respectively, are shown. Also, the boundaries of the biological processing ROIs are delineated. Geometries are to scale within a given specimen but not between specimens.

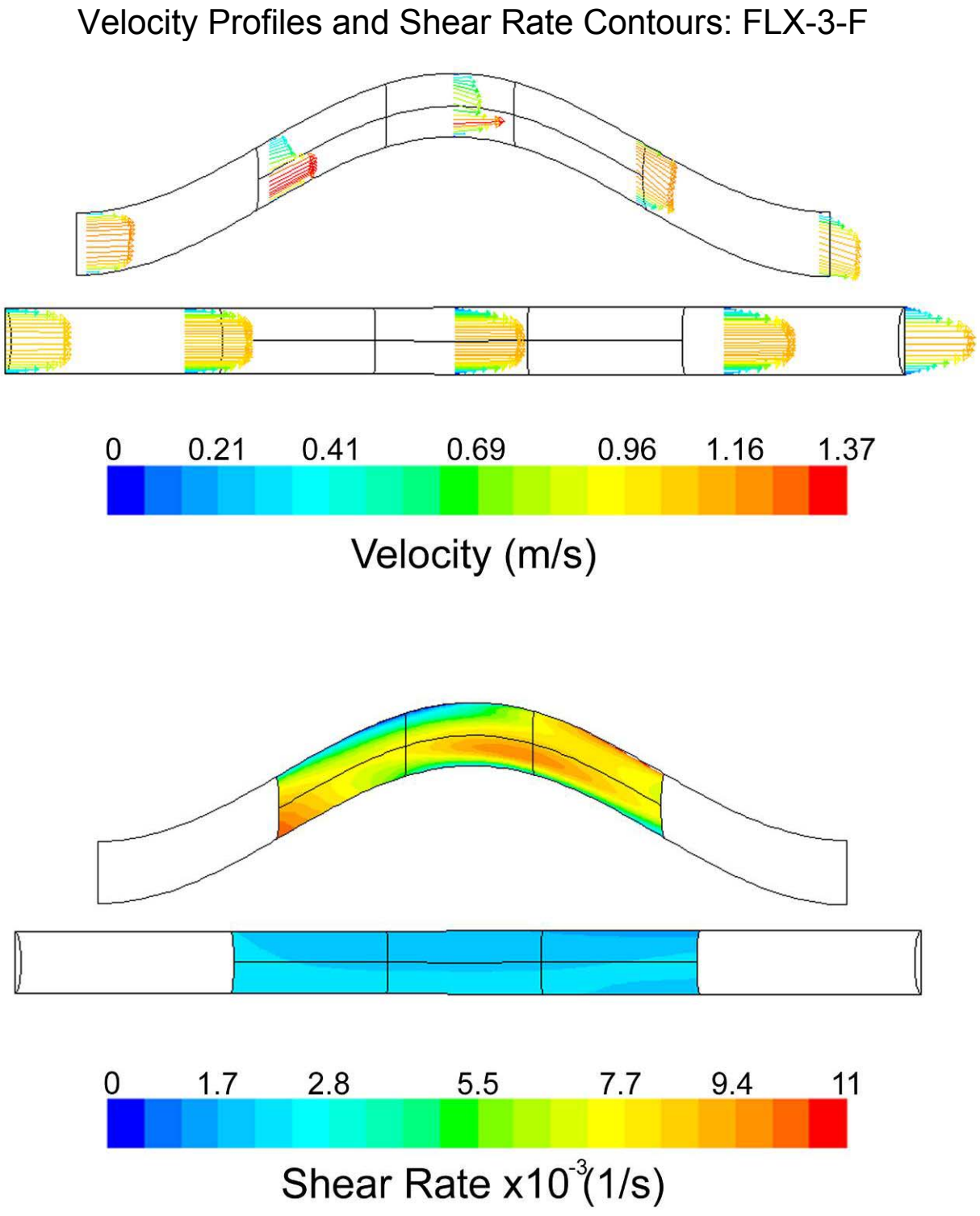

Figure 5.22 Velocity profile for FLX-3-F (Top). Velocity vectors are scaled and colored by their magnitude. Shear rate contour for FLX-3-F (Bottom). In both cases, the maximum and minimum curvatures occurring at sytole and diastole, respectively, are shown. Also, the boundaries of the biological processing ROIs are delineated. Geometries are to scale within a given specimen but not between specimens.

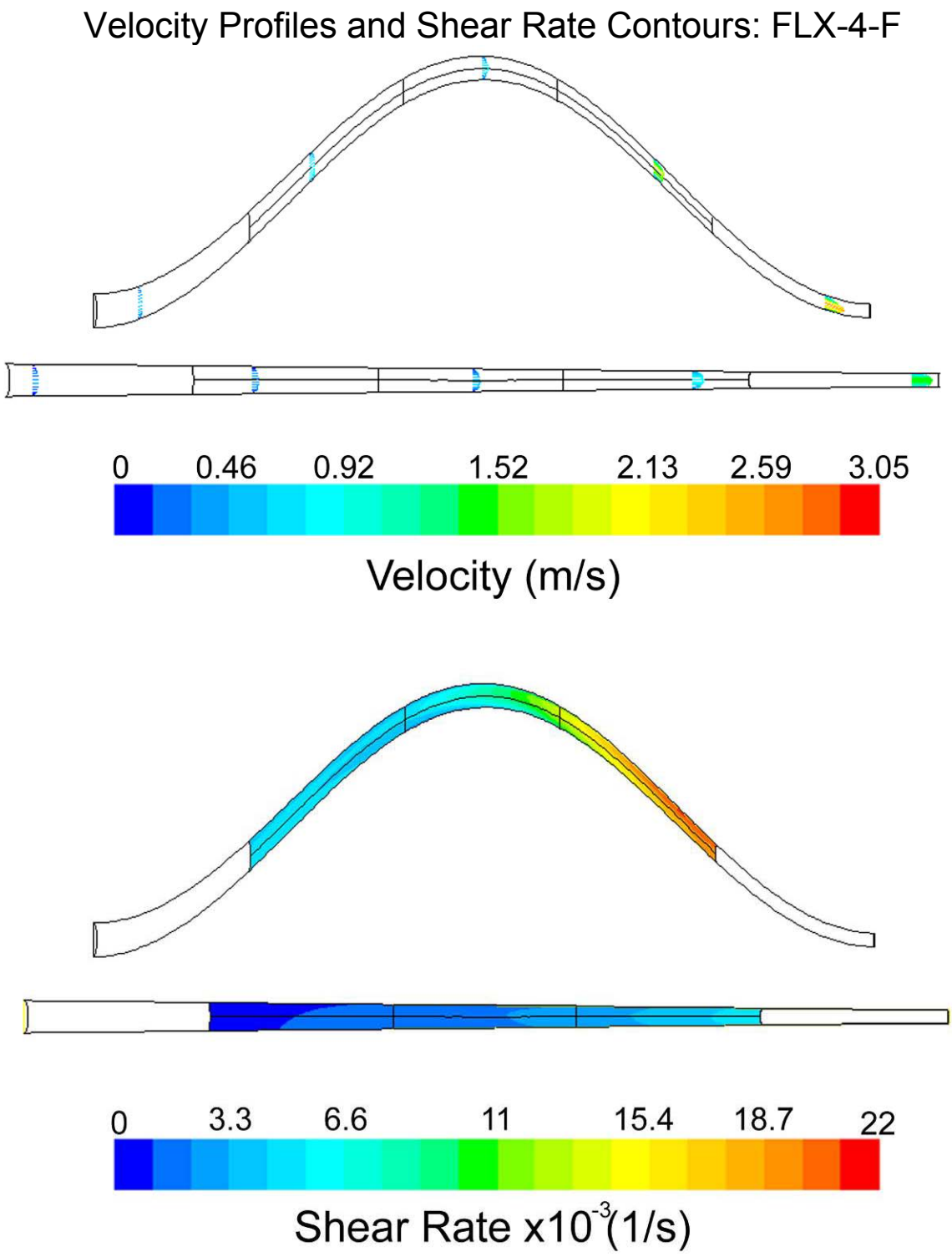

Figure 5.23 Velocity profile for FLX-4-F (Top). Velocity vectors are scaled and colored by their magnitude. Shear rate contour for FLX-4-F (Bottom). In both cases, the maximum and minimum curvatures occurring at sytole and diastole, respectively, are shown. Also, the boundaries of the biological processing ROIs are delineated. Geometries are to scale within a given specimen but not between specimens.

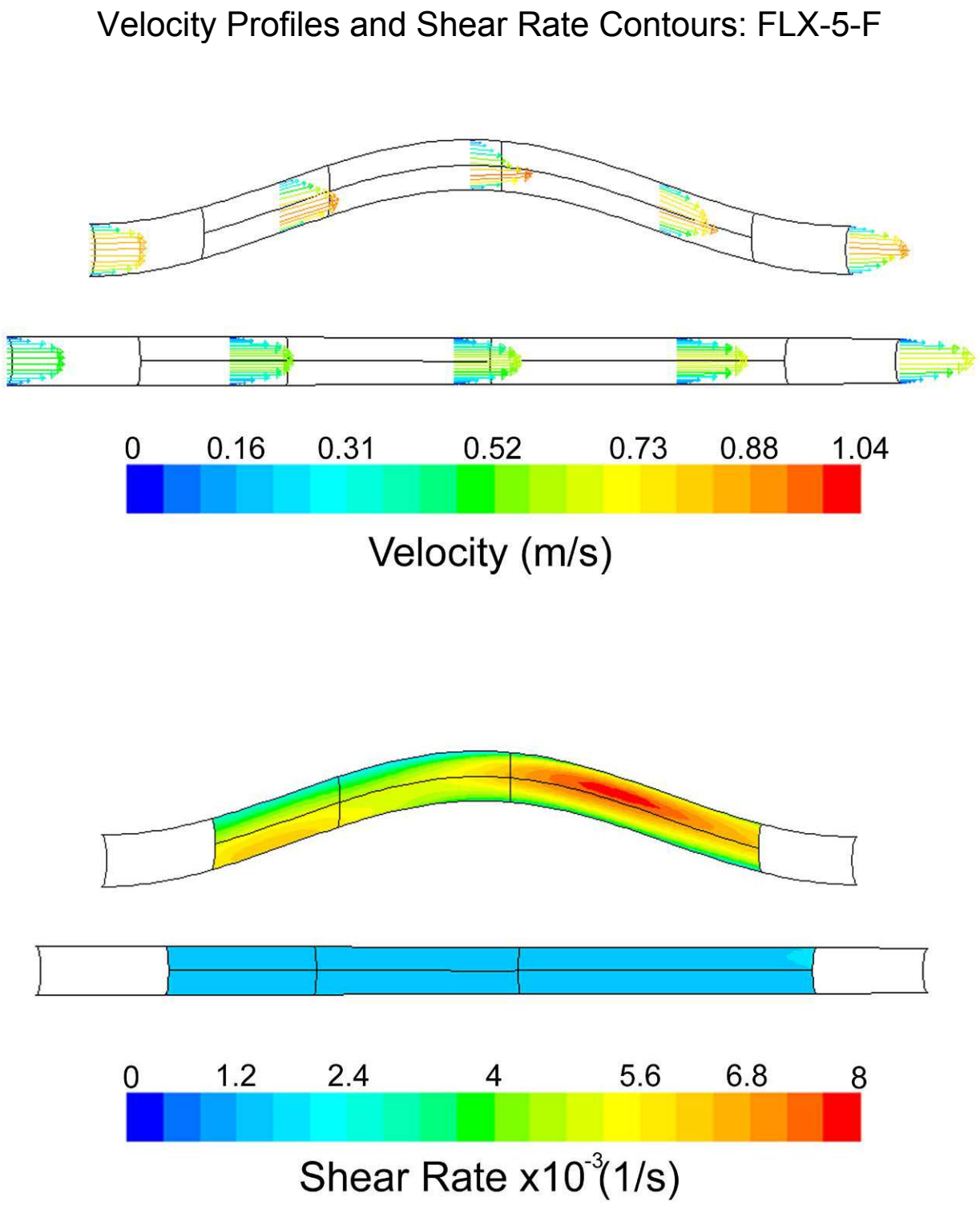

Figure 5.24 Velocity profile for FLX-5-F (Top). Velocity vectors are scaled and colored by their magnitude. Shear rate contour for FLX-5-F (Bottom). In both cases, the maximum and minimum curvatures occurring at sytole and diastole, respectively, are shown. Also, the boundaries of the biological processing ROIs are delineated. Geometries are to scale within a given specimen but not between specimens.

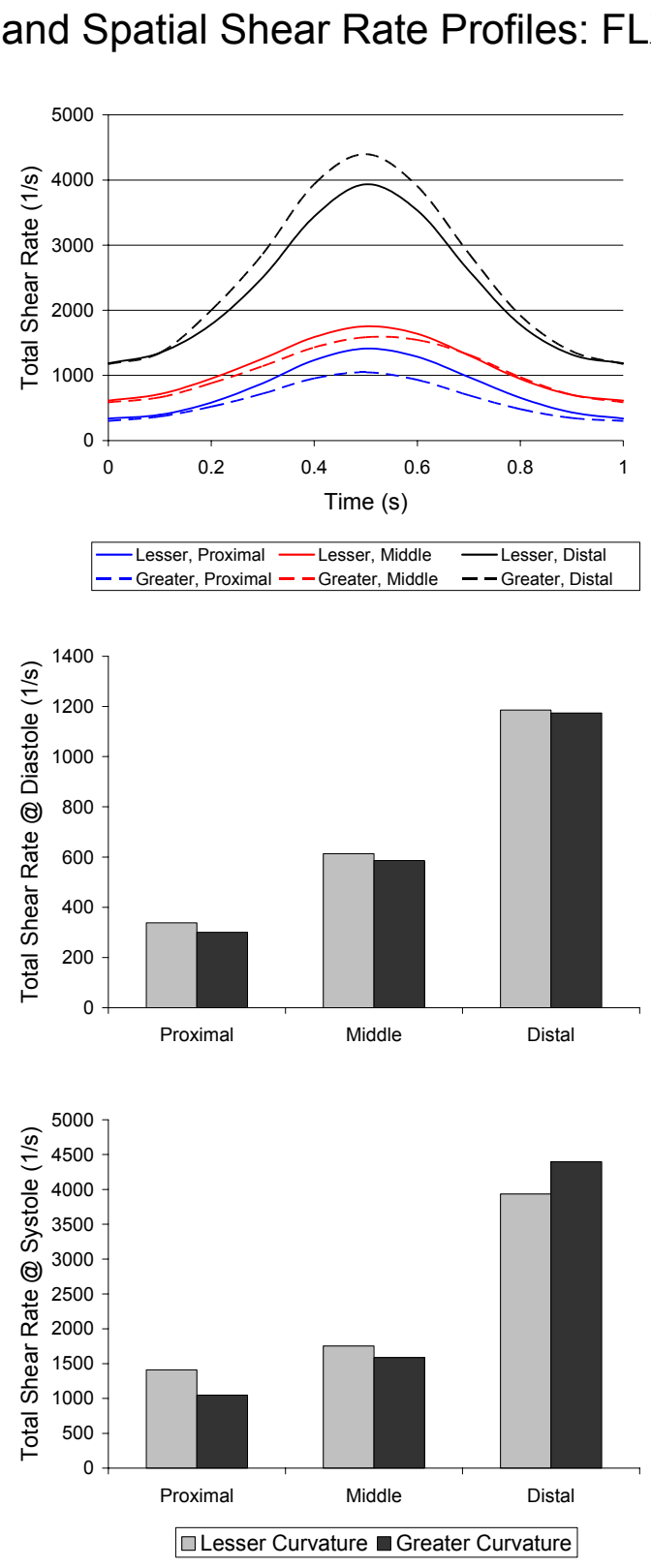

Figure 5.25 Area weighted average total shear rate versus time for the biological processing ROIs for FLX-1-F (top). The values at diastole (middle) and systole (bottom) are plotted for each ROI.

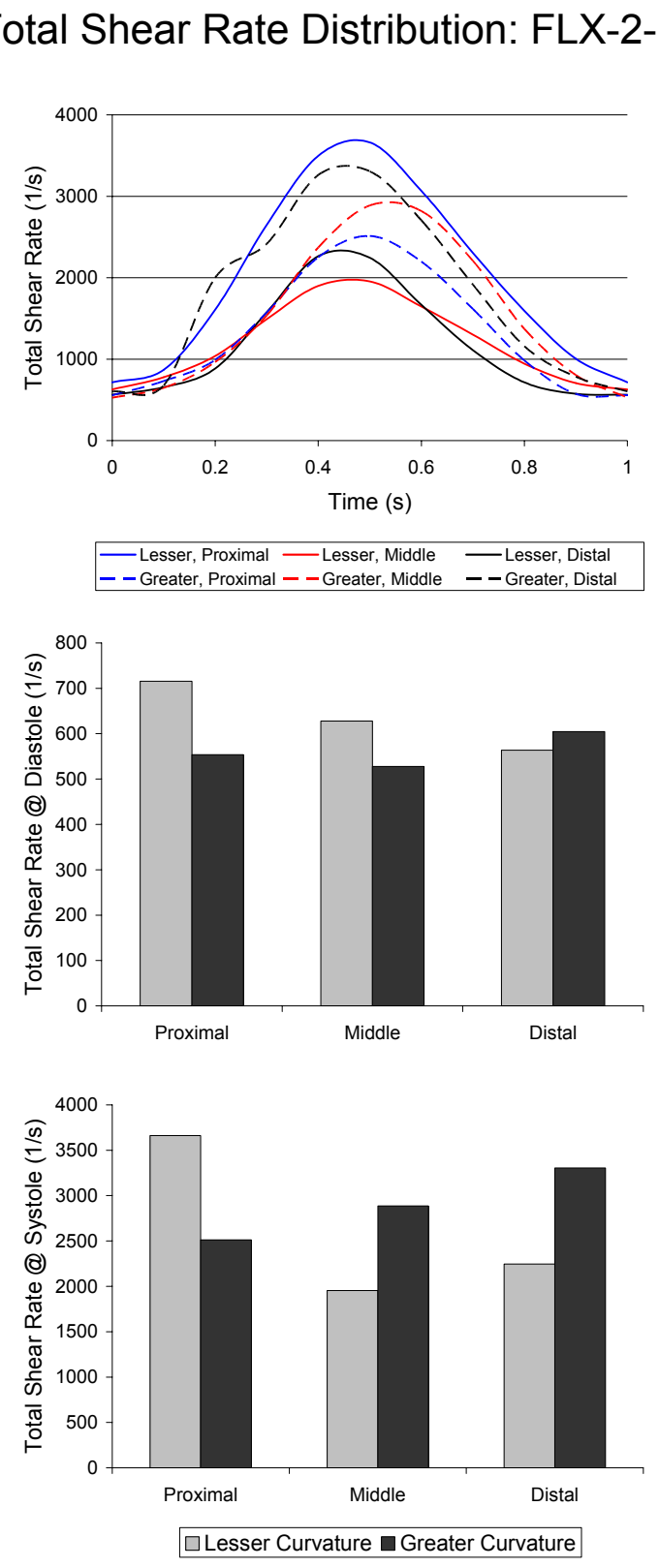

Figure 5.26 Area weighted average total shear rate versus time for the biological processing ROIs for FLX-2-F (top). The values at diastole (middle) and systole (bottom) are plotted for each ROI.

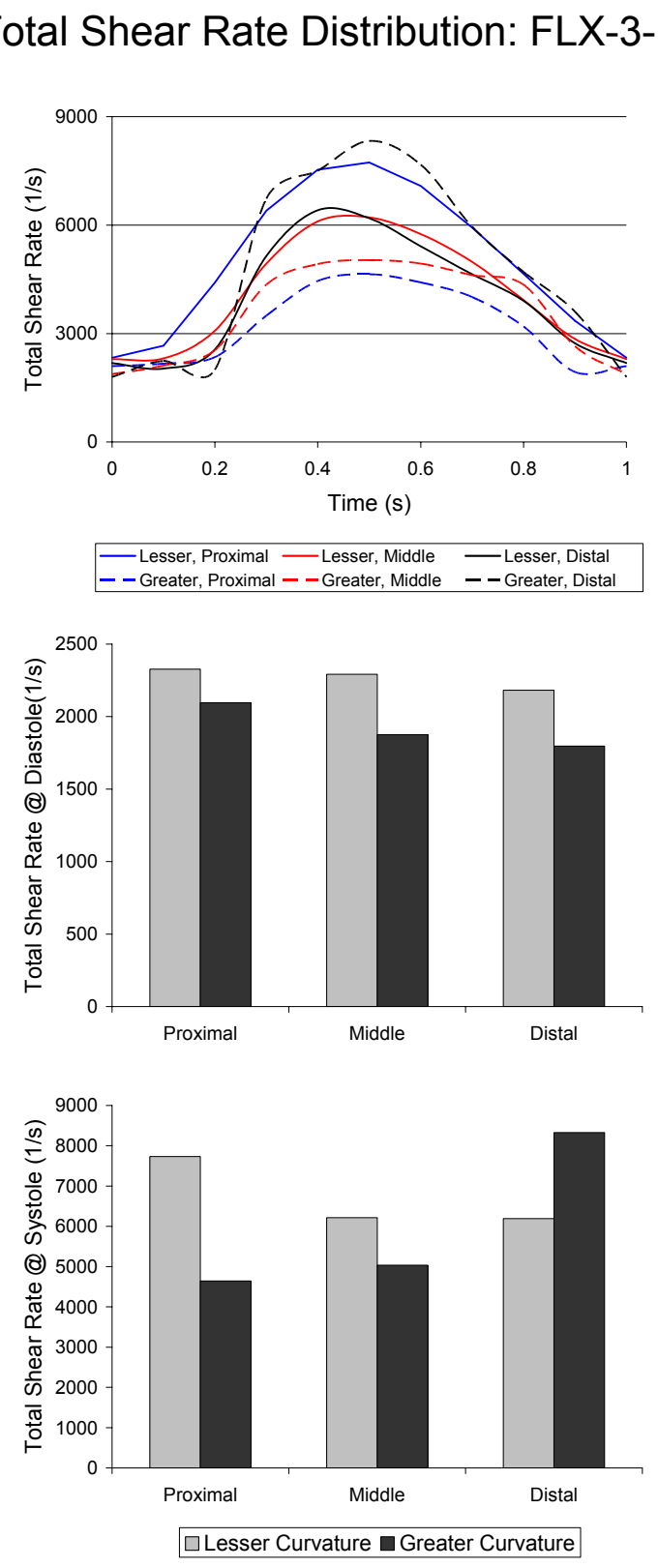

Figure 5.27 Area weighted average total shear rate versus time for the biological processing ROIs for FLX-3-F (top). The values at diastole (middle) and systole (bottom) are plotted for each ROI.

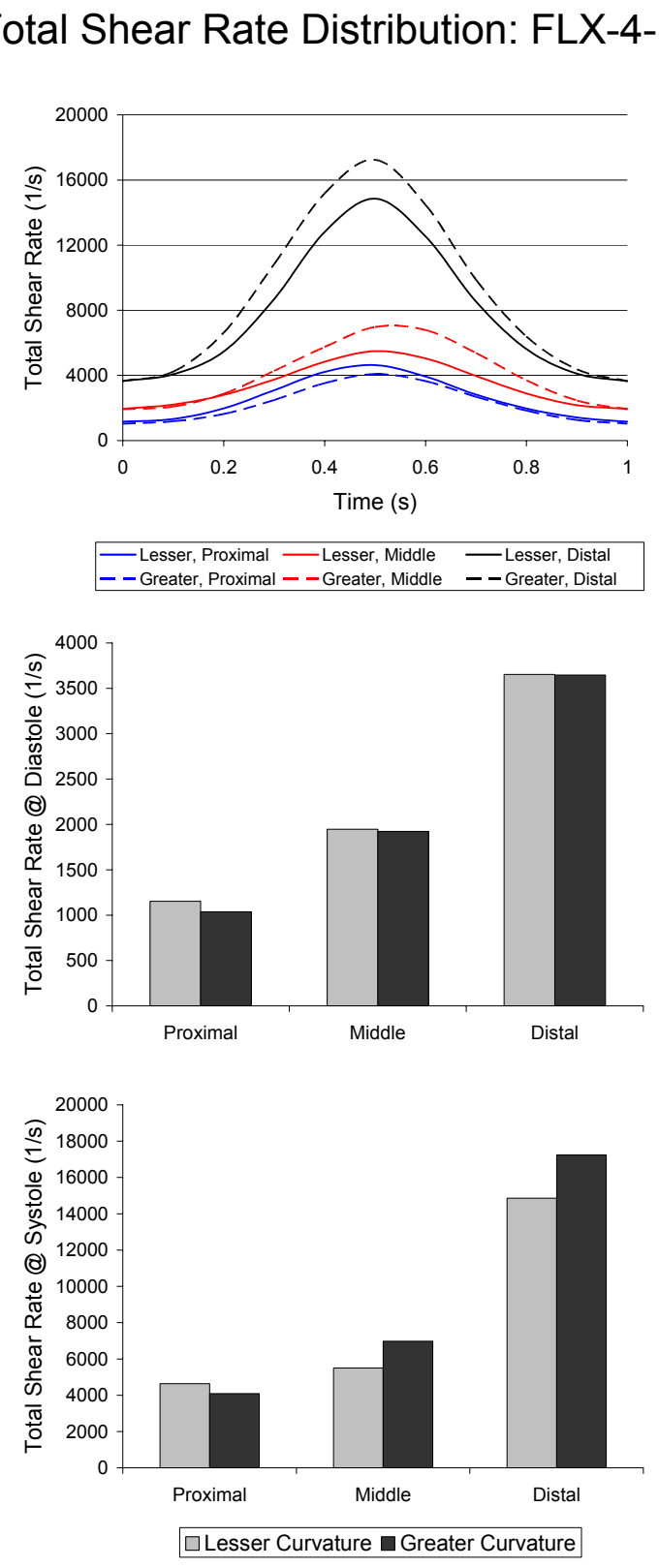

Figure 5.28 Area weighted average total shear rate versus time for the biological processing ROIs for FLX-4-F (top). The values at diastole (middle) and systole (bottom) are plotted for each ROI.

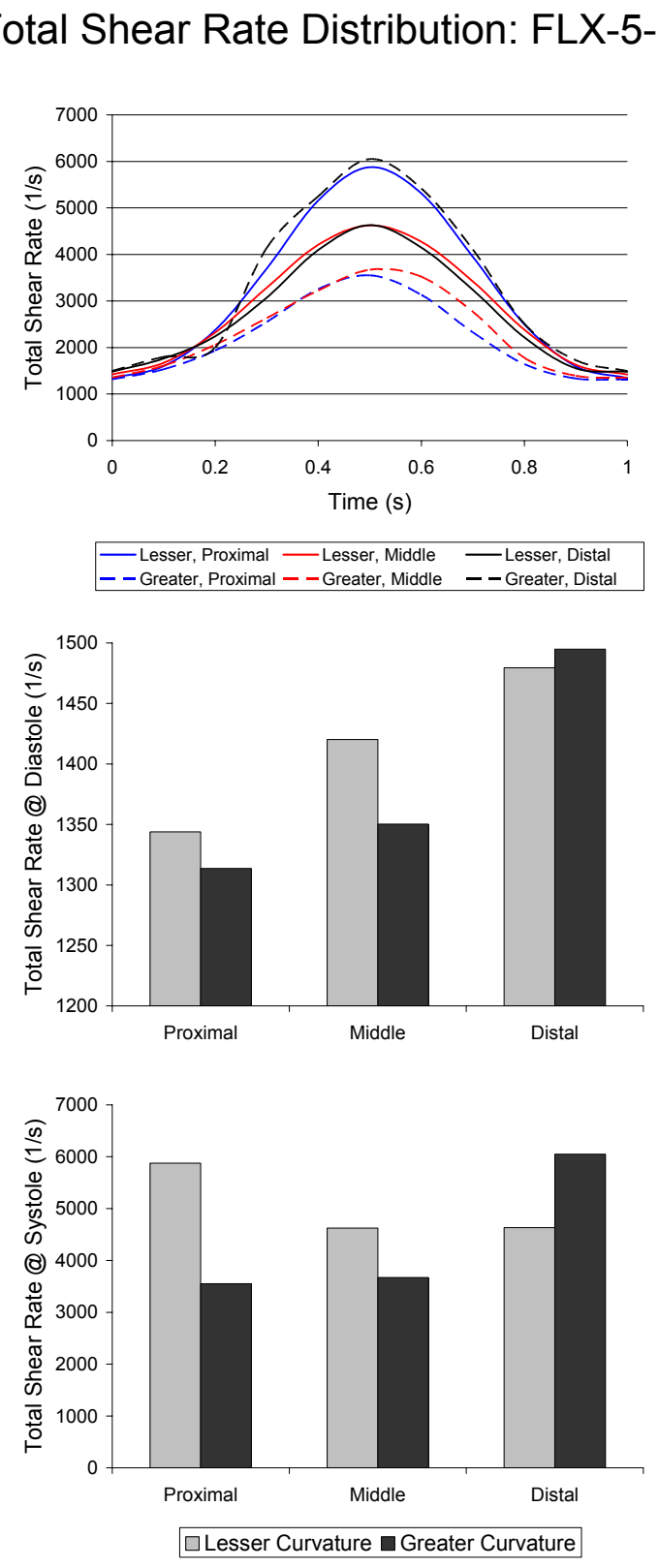

Figure 5.29 Area weighted average total shear rate versus time for the biological processing ROIs for FLX-5-F (top). The values at diastole (middle) and systole (bottom) are plotted for each ROI.

As expected from the individual vector component plots, the distributions vary widely from specimen-to-specimen. Systolic and diastolic shear rates as well as the shear rate pulse were tabulated for subsequent regression analysis in Specific Aim 4 (Table 5.6). For the flexure specimens, the maximum, minimum, and range parameters were not determined since these values tended to coincide with the values for systole, diastole, and pulse. On the other hand, the systolic and diastolic values did not coincide with the maximum and minimum values for the control specimens. Therefore, all six parameters are listed for the control specimens in the FLX experiment set in Table 5.7.

Table 5.6 Shear rate parameters for the ROIs from each flexure specimen from the FLX experiment set. ROIs are numbered from proximal to distal for the greater and lesser curvatures.

Flexure					
			Shear Rate (1/s)		
			@ Diastole	@ Systole	Pulse
FLX-1-F	Lesser	1	338	1412	1073
		2	614	1753	1140
		3	1186	3935	2749
	Greater	1	301	1047	747
		2	586	1587	1001
		3	1174	4397	3223
FLX-2-F	Lesser	1	716	3662	2946
		2	628	1955	1326
		3	564	2246	1682
	Greater	1	554	2512	1959
		2	528	2887	2359
		3	605	3306	2701
FLX-3-F	Lesser	1	2327	7734	5406
		2	2293	6213	3920
		3	2183	6189	4006
	Greater	1	2096	4643	2547
		2	1875	5033	3157
		3	1797	8328	6531
FLX-4-F	Lesser	1	1153	4631	3477
		2	1948	5495	3547
		3	3653	14859	11206
	Greater	1	1036	4086	3050
		2	1923	6971	5048
		3	3647	17238	13591
FLX-5-F	Lesser	1	1344	5876	4532
		2	1420	4626	3206
		3	1479	4632	3152
	Greater	1	1314	3552	2238
		2	1350	3671	2321
		3	1495	6051	4557

Table 5.7 Shear rate parameters for the ROIs from each control specimen from the FLX experiment set. ROIs are numbered from proximal to distal.

Control							
		Shear Rate (1/s)					
		@ Diastole	@ Systole	Maximum	Minimum	Range	Pulse
Exp #1	1	639	1332	1332	639	694	694
	2	528	1111	1111	528	583	583
	3	447	960	971	447	524	513
Exp #2	1	788	1443	1492	772	720	655
	2	693	1279	1331	672	659	586
	3	615	1148	1202	589	613	533
Exp #3	1	162	369	369	162	207	207
	2	154	355	355	153	201	201
	3	146	346	346	146	200	200
Exp #4	1	1116	1276	1367	932	436	161
	2	593	1507	1543	592	951	913
	3	354	1582	1616	351	1266	1228
Exp #5	1	793	1605	1605	793	812	812
	2	678	1358	1371	678	693	679
	3	589	1177	1201	583	618	588

5.4 DISCUSSION

5.4.1 Dynamic Geometry and Shear Rate

As described extensively in Chapter 1.0 , shear stress is an important regulator of vascular cell function and potential mediator of location specific plaque formation. It has been demonstrated that atherosclerotic lesions tend to develop in at branch points and bifurcations where flow becomes disturbed creates localized areas of low or oscillating shear stress. To understand how the dynamic motion of the coronary arteries, which includes cyclic stretching, flexing, and twisting, can influence the localization of atherosclerotic processes, it is important to understand how these motions contribute to both the mural stress and shear stress distributions. The preceding section described how the cyclic deformations of cyclic axial stretch, twist and flexure influence the mural stress distribution. In this section, dynamic deforming mesh grids were incorporated into unsteady computational fluid dynamics simulations of the *ex vivo* perfusion experiments to accurately estimate the shear rate distribution in arterial segments exposed to cyclic axial stretch and flexure.

For cyclic stretch there were notable differences in shear rate distribution between stretch and control segments. However, the differences between stretch specimens of different experiments were equally profound. This indicates that the individual vessel geometries play a considerable part in the variability of shear rate distributions. This not surprising, since the maximal wall velocity parallel to the flow direction obtained during the stretching cycle is at least an order of magnitude less than the average fluid velocity. However, as determined in the finite element analyses, cyclic stretch applied 180˚ out of phase with the pressure cycle causes dramatic difference in the diameter change in time. This type of motion is likely to have a

dramatic effect on the fluid flow characteristics. However, it remains unclear whether those effects are as important as individual static geometries.

Cyclic flexure on the other hand, had a dramatic impact on the shear rate distribution. First, the asymmetric flexure generated circumferential changes in shear stress necessitating full, three-dimensional simulations. Second, the shear rate magnitudes in the flexure specimens at maximum flexure were substantially greater than those in the control specimens. In the most extreme, there was a full order of magnitude difference. Taken together, these two observations clearly demonstrate that cyclic flexure of arterial segments in the EVPS alters the shear rate distribution in a non-uniform manner. Indeed, other researchers have found that addition of asymmetric dynamic wall motions impacts the shear stress magnitudes and distributions. Ramaswamy et al., showed that addition of realistic wall motion to unsteady simulations of blood flow in the left anterior descending coronary artery affect the time-mean wall shear stress and the oscillatory shear index [89]. Myers et al., demonstrated that the right coronary artery hemodynamics are dominated by the vessel specific geometries [84]. This indicates that a dynamic changing geometry would alter the hemodynamic environment. Weydahl et al., show specifically that dynamic changes in curvature alter the shear rate distributions at branch points and bifurcations [201].

5.4.2 Limitations

There are a few limitations of this analysis that should be noted for accurate interpretation of the results in this section. The inlet flow conditions to the actual vessel were determined by development of a uniform velocity profile over the length of an inlet flow extension. The length of the inlet (and outlet) flow extensions was 10 times the vessel diameter, which was more than

sufficient to eliminate the effects of the uniform inlet velocity profile [94, 213]. The inlet and outlet flow extensions had diameters equal to the proximal and distal inner diameter of the vessel segment, respectively. In reality the vessel was tethered to a stainless steel cannula (with sufficient length to allow for fully-developed flow) creating an initial diameter expansion at the vessel inlet. Likewise, there would be a diameter contraction at the distal end. In most cases, the vessel segment inner diameter matched the outer diameter of the cannula so that the expansion was relatively small. However, there were instances where the expansion was noticeably greater due to vessel wall distension upon pressurization. To avoid these entrance effects, ROIs for shear rate calculation and biologic processing were relative distant from the proximal and distal edges.

In Section 5.1.2.2, for the flexure simulations it was assumed that the radial distension due to the pressure pulse could be neglected, and that the vertical displacement along the lesser curvature is equal to that along the greater curvature. While the first assumption is fairly accurate (recall Figure 5.7), the second is more troublesome. In essence, the second assumption states that there is no "flattening" of the vessel segment at the point of maximal curvature. While this is probably a safe assumption for the coronary arteries *in vivo,* the finite element analysis demonstrates some decreased vertical displacement in the greater curvature causing a flattening of the vessel cross-section (recall Figure 5.7). This effect was confirmed by observation during the actual *ex vivo* perfusion experiments. Unfortunately, modeling this deformation is significantly more complicated and computational more expensive. Most of the deforming mesh algorithms used for complicated deformations of this kind are written for in-house finite volume solvers rather than commercially available software such as FLUENT [90]. Therefore, the

assumption of constant circular cross-section represents a first approximation of the fluid effects of *ex vivo* imposed cyclic flexure.

The fluid volume geometries were determined from the finite element analysis results. Given the dependence of the shear rate on the vessel geometry, the accuracy of the results for the computational fluid dynamics simulations depends on the accuracy of the material model used to predict the deformed fluid volume. In all cases, strain energy functions of the porcine coronary arteries were used to model the porcine femoral arteries. The limitations of this extrapolation are discussed in Section 4.6.2. An additional concern is the use of the Mooney-Rivlin model for the cyclic flexure simulations. Based on Figure 4.14 the Mooney-Rivlin model underestimated the the actual diameters of the cyclic flexure specimens leading to overestimation of shear rate. However, since the same model was used for all specimens this inaccuracy should be consistent across the experimental group, allowing interpretation of general stress distribution trends and regression analyses to still be valid.

A mesh independence study was not performed for these computational fluid dynamics analyses as was performed for the finite element analyses. However, two important precautions were taken to ensure accurate estimation of shear rates over time. First, a fine boundary layer mesh was applied to all of ROI surfaces. The first element of the boundary layer (i.e., the one closest to the wall) had a perpendicular dimension that was always less than 5% of the vessel radius. The growth factor for the remaining elements in the boundary layer was set at 1.4. This precaution generated a very fine mesh along the inner vessel segment wall (recall Figure 5.2 and Figure 5.4) and allowed for accurate estimation of the velocity gradient and therefore shear rate. Second, the time step size (Δt) for the dynamic solver was chosen such that

$$\Delta t = \frac{\text{typical element length}}{\text{maximum fluid veolcity}} \tag{5.8}$$

where the typical element length is in the direction of the principle component of the fluid velocity. This ensured precaution ensured solution convergence at every time step, based on the mesh density for each reconstructed segment.

Finally, time-averaged shear rates were not calculated in these simulations. Since the boundary conditions and deforming mesh functions were all trigonometric functions, the resulting shear rates were similarly symmetric. Therefore, the integrated time average of shear rate is closely approximated by the arithmetic average of the maximum and minimum shear rates during the cycle. Given this simple relationship between average shear rate and maximum and minimum shear rate, the time-averaged data would be a strong covariate of either the maximum or minimum shear rate. Therefore including it in the multivariate regression analyses would not have provided substantially more information or power to the analysis.

5.5 CONCLUSIONS

Unsteady computational fluid dynamics simulations with deforming mesh grids demonstrated specimen-specific, non-uniform shear rate distributions. The variability in shear magnitude and distribution was a function of the specimen-specific geometry and the imposed deformation (either axial stretch or flexure). The high specimen-to-specimen variability in stress distribution is similar to that shown for the biological endpoint distribution from Specific Aim 1 (see Section 3.2). To determine how these two distributions are related, multiple linear regression analyses are required. Such information has the potential to characterize how local shear stresses influence the localization of early atherogenic processes. Those regression analyses including the mural stress distributions from Specific Aim 2 (see Section 4.5) are the subject of Chapter 6.

6.0 CORRELATIONS BETWEEN BIOLOGICAL AND MECHANICAL DATA

The goal of Specific Aim 4 was to determine the correlative relationships (positive and negative) between the mural stress and shear stress distributions determined computationally (Chapters 4 and 5, respectively) and the spatial variation of atherogenic endpoints determined experimentally (Chapter 3). Multiple linear regression analyses were used to reveal which mechanical stress variables were significant predictors of endothelial permeability and apoptosis. In addition, these analyses were used to determine which mechanical stress variables contributed to the increase permeability and apoptosis caused by cyclic axial stretch and flexure.

6.1 METHODS

The statistical analysis software SPSS v15.0 was used to perform the multiple linear regression analyses. Three types of analyses were performed for each deformation experiment set. 1) Raw non-normalized biological endpoint and stress values from the deformed and paired control specimens were analyzed to examine which mechanical variables were predictive of the spatial distribution of biological variables. 2) The biological endpoints and mechanical stress variables of the deformed specimens were arithmetically normalized to the corresponding paired control values. That is, the difference between deformed and control values were used in the regression. This analysis was used to determine which mechanical stresses contributed to the observed

increases in permeability and apoptosis associated with cyclic axial stretch and flexure (see Section 3.2). 3) Geometric normalized data, where the deformed specimen biological endpoint values and mechanical stress variables were divided by the control specimen values, was used as a second means to determine which mechanical stress values played a role in the observed increased permeability and apoptosis associated with exposure to cyclic axial stretch and flexure. In addition to the individual analyses for each deformation experiment set, a single analysis pooling the non-normalized data from the STR and TWT experiments was performed. Note that since a different material model was used for the FLX experiments (see Section 4.5.1), the data from this experiment set could not be pooled with the other experiment sets. Since multiple types of experiments (i.e., stretch and twist) are included in the pooled data set, any type of normalization was no longer valid. Only raw non-normalized values were used for the pooled data. In addition, since there were no fluid shear stresses determined for the twist experiments, only mural stress parameters were considered. In this section, the individual variables used in each regression are described along with the regression protocol used.

6.1.1 Description of Variables

In all the regression analyses the Evan's blue fluorescent intensity per unit wall thickness and percent of TUNEL positives cells were the dependent biologic endpoint variables corresponding to endothelial permeability and apoptosis, respectively. For each deformation experiment set (STR, TWT, and FLX), a specific set of mechanical stress variables was considered as potential independent predictors of permeability and apoptosis.

6.1.1.1 Cyclic Axial Stretch

In the stretch deformation case, the Von Mises, circumferential, and longitudinal mural stresses were considered. In these axi-symmetric simulations, the radial stress averaged over the wall thickness is related almost entirely to the applied internal pressure. Since the pressure was the same in all experiments this variable was not considered. Values of these mural stresses at systole and diastole were included in the regression. In addition, in order to capture variation in time, the pulse (defined as the difference between the systolic and diastolic stress values) was considered for each mural stress variable.

For the shear stresses, the total shear rate was dominated by the axial component vector with little contribution from the radial component. Thus, for the regression analysis of cyclic stretch only, the total shear rate was considered. The systolic, diastolic, maximum, and minimum shear rates as well as the shear rate pulse and range (define in Section 5.3.1) were included. All mechanical variables included the regression analyses of cyclic axial stretch are summarized in Table 6.1.

6.1.1.2 Cyclic Twist

For the TWT experiment set, the mural stresses considered were the same as those for the stretch set with the addition of the torsional shear stress. Again, the radial stress was not considered since it is related almost entirely to the applied internal pressure, which was constant across all experiments. Systolic and diastolic values as well as the pulse for each mural stress variable were included in the analysis. As stated in Chapter 5 no computational fluid dynamics simulations were performed for the cyclic twist experiments. The regression analyses here were focused more specifically on the solid wall shear stress due to torsion. All mechanical variables included the regression analyses of cyclic twist are summarized in Table 6.2.

6.1.1.3 Cyclic Flexure

For cyclic flexure, the Von Mises stress and all principle components of the stress tensor (circumferential, longitudinal, and radial) were considered as potential independent predictors permeability and apoptosis. The flexure deformation provided significant contribution to the radial stress in addition to the pressure. Therefore, the radial stress component was a relevant independent variable in the regression analyses for flexure. Like in the stretch and twist experiment sets, systolic and diastolic values as well as the pulse stresses for each of these mural stress variables were included in the analysis.

While there was significant contribution from all three-dimensional components of the shear rate vector, the physical meaning of these values is difficult to interpret (see Section 5.3.2). Therefore, only the total shear rate vector was considered. Since the maximum and minimum values tended to coincide with the systolic and diastolic values, only the systolic, diastolic and pulse shear rate were included as independent variables in the regression analyses for flexure. All mechanical variables included the regression analyses of cyclic flexure are summarized in Table 6.3.

Table 6.1 Independent mechanical stresses variables used in the multiple regression analyses of the STR experiment set and their associated symbol abbreviations.

Variable	Symbol Abbreviation
Mural Stresses	
Von Mises stress @ systole	VM_{sys}
Circumferential stress @ systole	$\sigma_{\theta\ sys}$
Longitudinal stress @ systole	$\sigma_{z\ sys}$
Von Mises stress @ diastole	VM_{dia}
Circumferential stress @ diastole	$\sigma_{\theta\ dia}$
Longitudinal stress @ diastole	$\sigma_{z\ dia}$
Von Mises pulse stress	VM_{pulse}
Circumferential pulse stress	$\sigma_{\theta\ pulse}$
Longitudinal pulse stress	$\sigma_{z\ pulse}$
Shear Stresses	
Total Shear Rate @ diastole	SR_{dia}
Total Shear Rate @ systole	SR_{sys}
Maximum Shear Rate	SR_{max}
Minimum Shear Rate	SR_{min}
Shear Rate Range	SR_{range}
Shear Rate Pulse	SR_{pulse}

Table 6.2 Independent mechanical stresses variables used in the multiple regression analyses of the TWT experiment set and their associated symbol abbreviations.

Variable	Symbol Abbreviation
Von Mises stress @ systole	VM_{sys}
Circumferential stress @ systole	$\sigma_{\theta\ sys}$
Longitudinal stress @ systole	$\sigma_{z\ sys}$
Torsion shear stress @ systole	$\sigma_{\theta z\ sys}$
Von Mises stress @ diastole	VM_{dia}
Circumferential stress @ diastole	$\sigma_{\theta\ dia}$
Longitudinal stress @ diastole	$\sigma_{z\ dia}$
Torsion shear stress @ diastole	$\sigma_{\theta z\ dia}$
Von Mises pulse stress	VM_{pulse}
Circumferential pulse stress	$\sigma_{\theta\ pulse}$
Longitudinal pulse stress	$\sigma_{z\ pulse}$
Pulse torsion shear stress	$\sigma_{\theta z\ pulse}$

Table 6.3 Independent mechanical stresses variables used in the multiple regression analyses of the FLX experiment set and their associated symbol abbreviations.

Variable	Symbol Abbreviation
Mural Stresses	
Von Mises stress @ systole	VM_{sys}
Circumferential stress @ systole	$\sigma_{\theta\ sys}$
Longitudinal stress @ systole	$\sigma_{z\ sys}$
Radial stress @ systole	$\sigma_{r\ sys}$
Von Mises stress @ diastole	VM_{dia}
Circumferential stress @ diastole	$\sigma_{\theta\ dia}$
Longitudinal stress @ diastole	$\sigma_{z\ dia}$
Radial stress @ diastole	$\sigma_{r\ dia}$
Von Mises pulse stress	VM_{pulse}
Circumferential pulse stress	$\sigma_{\theta\ pulse}$
Longitudinal pulse stress	$\sigma_{z\ pulse}$
Radial pulse stress	$\sigma_{r\ pulse}$
Shear Stresses	
Total Shear Rate @ diastole	SR_{dia}
Total Shear Rate @ systole	SR_{sys}
Shear Rate Pulse	SR_{pulse}

6.1.2 Multiple Linear Regression Protocol

Multiple linear regression estimates the coefficients of the linear equation, involving multiple independent variables, that best predict the value of the dependent variable using a least squares approach [202]. The most important part of the protocol is the selection of variables to be included in the model from the entire list of potential independent variables. Included variables should have significant correlation with the dependent variable but not be collinear with any other independent variable. For the regression analyses performed here, a forward selection approach was used to select variables to be included in the regression [202]. In this approach, variables are sequentially entered into the model in a step-wise manner based on their correlation

with the dependent variable. So, the first variable considered for inclusion in the regression equation is the one with the largest correlation (positive or negative) with the dependent variable. Before being entered into the equation, the variable must meet a specific criterion for the probability of the F distribution. For these analyses, that criterion was set to a probability of 0.05. Once the first variable is entered, the remaining independent variable with the largest partial correlation is considered next. Variables are added until all remaining variables fail to meet the entry criterion.

This selection procedure only ensures that variables with significant correlation with the dependent variable are included. In order to satisfy the non-collinearity requirement, several diagnositic parameters must be examined [202]. Eigenvalues of the scaled and uncentered cross-products matrix close to zero suggest the presence collinear variables. Condition indices greater than 15 and variance inflation factors greater than 2 indicate problems with collinearity. For every regression model generated, these three diagnostics were examined to reduce collinearity in the equation.

For each experiment set and the pooled data set, Pearson correlation coefficients are reported for each combination of independent (mechanical stress variables) and dependent (permeability and apoptosis) variable. Correlations were considered significant at a t-distribution probability of 0.05. For each regression equation generated, the included independent variables, their respective standardized coefficients and p-values, and the equation fit to observed data (R^2) is reported.

6.2 RESULTS

6.2.1 Cyclic Axial Stretch

For the non-normalized data from the STR experiment set, six mechanical stress parameters had significant correlations with permeability and five had significant correlations with apoptosis (Table 6.4). Of note, only one stress variable, the Von Mises pulse stress, correlated with both permeability and apoptosis. Variable selection for permeability determined that circumferential stress and shear rate at systole were significant, independent predictors (Table 6.5).

Table 6.4 Pearson correlation coefficients (r) and their significance (p-value) for non-normalized correlations between permeability or apoptosis and the mechanical stress variables considered for the STR experiment set. Significant correlations are highlighted in green.

	Permeability		Apoptosis	
	r (Pearson)	p-value	r (Pearson)	p-value
VM_{sys}	0.425	<0.001	-0.052	0.734
$\sigma_{\theta\ sys}$	0.794	<0.001	-0.189	0.214
$\sigma_{z\ sys}$	-0.253	0.093	0.101	0.509
VM_{dia}	-0.145	0.341	0.263	0.081
$\sigma_{\theta\ dia}$	0.790	<0.001	-0.207	0.172
$\sigma_{z\ dia}$	-0.238	0.116	0.287	0.056
VM_{pulse}	-0.333	0.025	0.416	0.004
$\sigma_{\theta\ pulse}$	0.791	<0.001	-0.149	0.329
$\sigma_{z\ pulse}$	0.085	0.580	-0.315	0.035
SR_{dia}	-0.075	0.626	0.135	0.377
SR_{sys}	0.145	0.341	0.160	0.294
SR_{max}	-0.010	0.948	0.301	0.044
SR_{min}	-0.052	0.733	-0.211	0.164
SR_{range}	-0.090	0.577	0.405	0.006
SR_{pulse}	0.261	0.083	0.048	0.755

Table 6.5 Non-normalized regression results for permeability and apoptosis in the STR experiment set.

Independent Variable	Standardized Coefficient	p-value
Permeability		
$\sigma_{\theta\ sys}$	0.863	<0.001
SR_{sys}	0.327	<0.001
TUNEL		
SR_{range}	0.844	<0.001
SR_{dia}	-1.128	<0.001
$\sigma_{z\ dia}$	0.672	0.009

Both variables had positive standardized coefficients indicating that increasing systolic circumferential stress and shear rate lead to increased permeability. The resulting regression model was

$$P(\mathrm{AIU}) = 100(\mathrm{AIU}\cdot\mathrm{s})SR_{sys} + 239.5\left(\frac{\mathrm{AIU}}{\mathrm{kPa}}\right)\sigma_{\theta\,sys} - 40991(\mathrm{AIU}) \tag{6.1}$$

where permeability (P) is measured in arbitrary intensity units per unit wall thickness (AIU). This model was able to predict ~73% of the spatial variability in permeability (R^2=0.733, $p<0.001$) (Figure 6.1).

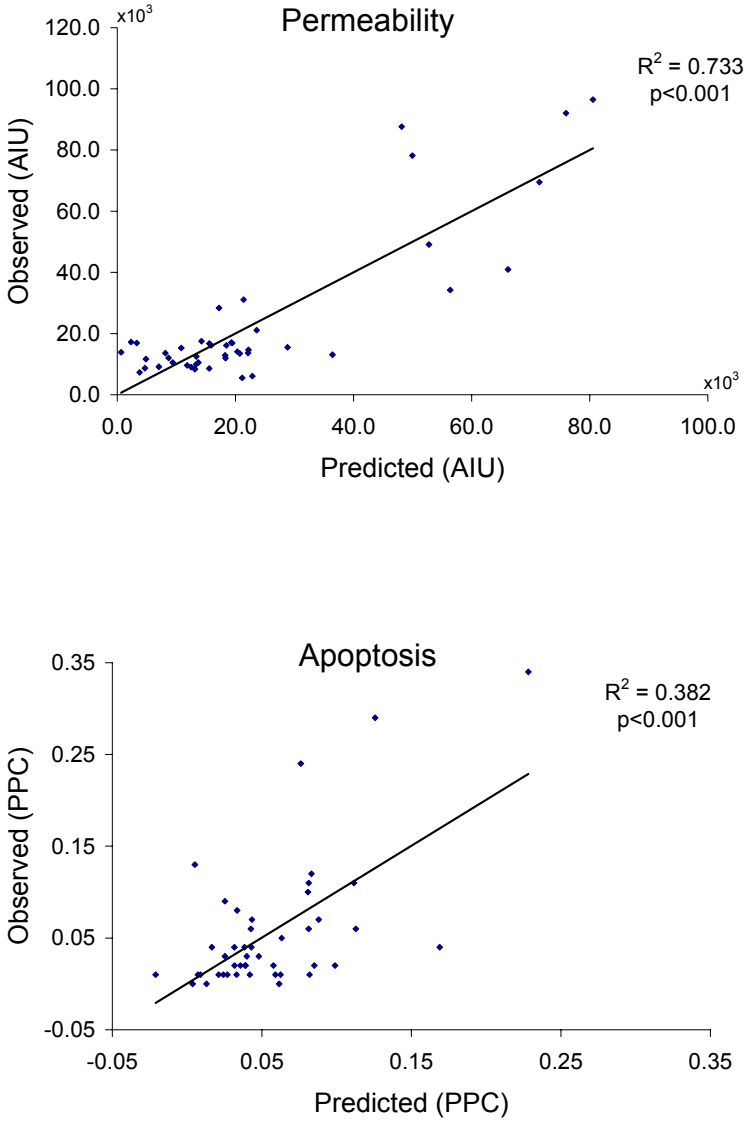

Figure 6.1 Non-normalized regression model fits for permeability (top) and apoptosis (bottom) in the STR experiment set. Observed values for permeability (arbitrary intensity units per wall thickness (AIU)) and apoptosis (percent TUNEL positive cells (PPC)) are plotted against the values predicted by the regression models given in equations (6.1) and (6.2), respectively.

For apoptosis, three variables were determined to be significant predictors (Table 6.5). Shear rate range and longitudinal stress at diastole were positively correlated with apoptosis, while shear rate at diastole was negatively correlated. The regression model including those variables was

$$A(\mathrm{PPC}) = 4.7\mathrm{x}10^{-4}\,(\mathrm{PPC}\cdot\mathrm{s})\mathrm{SR}_{\mathrm{dia}} - 1.13\mathrm{x}10^{-3}(\mathrm{PPC}\cdot\mathrm{s})\mathrm{SR}_{\mathrm{range}} + 3.5\mathrm{x}10^{-4}\left(\frac{\mathrm{PPC}}{\mathrm{kPa}}\right)\sigma_{z\,\mathrm{dia}} + 8.75\mathrm{x}10^{-3}(\mathrm{PPC}) \tag{6.2}$$

where apoptosis is measured in percent TUNEL positive cells (PPC). About 38% of the spatial variability in apoptosis is predicted by the model with these three variables (R^2=0.382, $p<0.001$) (Figure 6.1).

For the arithmetic normalized data, one mechanical stress parameter, Von Mises stress at systole, had significant correlations with differences in permeability between stretch and control. On the other hand five had significant correlations with difference in apoptosis due to stretch (Table 6.6). There were no variables that correlated with both permeability and apoptosis. Only the Von Mises stress at systole was selected as a significant positive predictor of increased permeability (Table 6.7).

Table 6.6 Pearson correlation coefficients (r) and their significance (p-value) for arithmetic normalized correlations between permeability or apoptosis and the mechanical stress variables considered for the STR experiment set. Significant correlations are highlighted in green.

	Permeability		Apoptosis	
	r (Pearson)	p-value	r (Pearson)	p-value
VM_{sys}	0.477	0.025	0.021	0.925
$\sigma_{\theta\ sys}$	0.201	0.369	-0.439	0.041
$\sigma_{z\ sys}$	0.374	0.087	0.197	0.379
VM_{dia}	0.132	0.558	0.361	0.099
$\sigma_{\theta\ dia}$	0.233	0.297	-0.434	0.044
$\sigma_{z\ dia}$	0.202	0.366	0.403	0.063
VM_{pulse}	0.217	0.332	-0.354	0.106
$\sigma_{\theta\ pulse}$	0.126	0.575	-0.437	0.042
$\sigma_{z\ pulse}$	0.183	0.415	-0.265	0.233
SR_{dia}	-0.303	0.170	0.200	0.372
SR_{sys}	-0.116	0.606	0.270	0.225
SR_{max}	-0.18	0.424	0.438	0.042
SR_{min}	-0.296	0.181	-0.539	0.010
SR_{range}	-0.291	0.189	0.408	0.060
SR_{pulse}	-0.101	0.665	0.000	1.000

Table 6.7 Arithmetic normalized regression results for permeability and apoptosis in the STR experiment set.

Independent Variable	Standardized Coefficient	p-value
Permeability		
VM_{sys}	0.477	0.025
TUNEL		
SR_{min}	-0.539	0.010

This suggests that the increases in permeability due to cyclic stretch are associated with increased Von Mises stress according to

$$P(AIU) = 36.3\left(\frac{AIU}{kPa}\right)VM_{sys} + 5313(AIU) \tag{6.3}$$

However, only about 23% of the variation in permeability changes due to stretch are predicted by this model (R^2=0.227, p=0.025) indicating the potential role of other factors (Figure 6.2).

Of the five variables significantly correlated with apoptosis changes due to stretch, only one, the minimum shear rate, was selected as an independent predictor. Changes in this stress variable with stretch were negatively correlated with changes in apoptosis (Table 6.7). This means that increases in apoptosis can be associated with decreases in shear rate due to cyclic stretch via

$$A(PPC) = -8.2x10^{-4}(PPC \cdot s)SR_{min} + 0.067(PPC) \tag{6.4}$$

Almost 30% of the changes in apoptosis due to the addition of cyclic stretch are attributable to changes in minimum shear rate (R^2=0.291, p=0.01) (Figure 6.2).

There were no significant correlations found for either permeability of apoptosis for the geometric normalized data (Table 6.8).

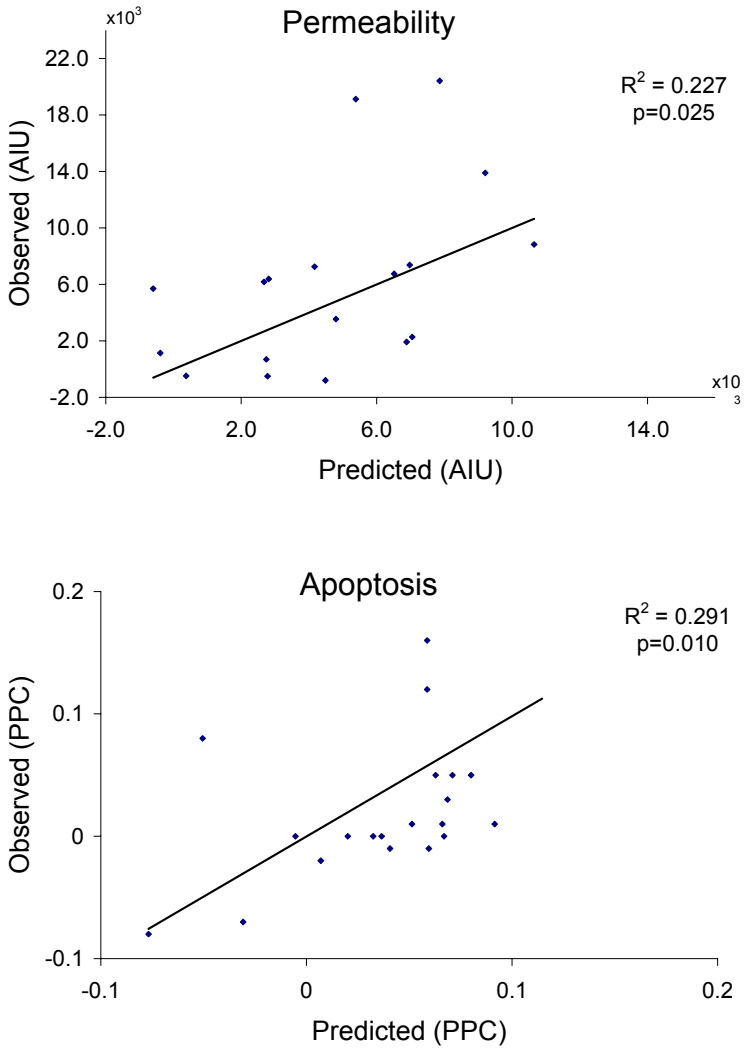

Figure 6.2 Arithmetic normalized regression model fits for permeability (top) and apoptosis (bottom) in the STR experiment set. Observed changes in permeability (arbitrary intensity units per wall thickness (AIU)) and apoptosis (percent TUNEL positive cells (PPC)) are plotted against the values predicted by the regression models given in equations (6.3) and (6.4), respectively.

Table 6.8 Pearson correlation coefficients (r) and their significance (p-value) for geometric normalized correlations between permeability or apoptosis and the mechanical stress variables considered for the STR experiment set. No significant correlations were found.

	Permeability		Apoptosis	
	r (Pearson)	p-value	r (Pearson)	p-value
VM_{sys}	0.158	0.482	-0.067	0.769
$\sigma_{\theta\ sys}$	-0.290	0.190	-0.165	0.462
$\sigma_{z\ sys}$	0.288	0.193	0.085	0.706
VM_{dia}	0.236	0.289	0.099	0.662
$\sigma_{\theta\ dia}$	-0.281	0.206	-0.189	0.400
$\sigma_{z\ dia}$	0.324	0.141	0.153	0.495
VM_{pulse}	-0.193	0.389	-0.181	0.419
$\sigma_{\theta\ pulse}$	0.181	0.421	0.243	0.275
$\sigma_{z\ pulse}$	-0.231	0.300	-0.344	0.117
SR_{dia}	-0.165	0.462	-0.075	0.742
SR_{sys}	0.054	0.811	-0.074	0.743
SR_{max}	0.081	0.721	0.084	0.709
SR_{min}	-0.358	0.101	-0.257	0.248
SR_{range}	-0.002	0.994	0.228	0.307
SR_{pulse}	-0.037	0.870	-0.205	0.361

6.2.2 Cyclic Twist

In the non-normalized data for the TWT experiment set there no were significant correlations with apoptosis. However, three mechanical stress parameters (longitudinal stress at systole and diastole and the longitudinal pulse stress) had significant correlations with permeability (Table 6.9).

Table 6.9 Pearson correlation coefficients (r) and their significance (p-value) for non-normalized correlations between permeability or apoptosis and the mechanical stress variables considered for the TWT experiment set. Significant correlations are highlighted in green.

	Permeability		Apoptosis	
	r (Pearson)	p-value	r (Pearson)	p-value
VM_{sys}	-0.119	0.491	0.09	0.601
$\sigma_{\theta\ sys}$	-0.114	0.507	0.085	0.622
$\sigma_{z\ sys}$	-0.359	0.031	-0.156	0.365
$\sigma_{\theta z\ sys}$	-0.041	0.812	-0.045	0.793
VM_{dia}	-0.122	0.478	0.099	0.564
$\sigma_{\theta\ dia}$	-0.119	0.489	0.097	0.574
$\sigma_{z\ dia}$	0.356	0.033	-0.140	0.414
$\sigma_{\theta z\ dia}$	0.083	0.629	0.185	0.280
VM_{pulse}	0.055	0.751	-0.202	0.237
$\sigma_{\theta\ pulse}$	0.081	0.640	-0.242	0.155
$\sigma_{z\ pulse}$	0.363	0.030	-0.179	0.297
$\sigma_{\theta z\ pulse}$	-0.041	0.812	-0.045	0.792

Of these, only the longitudinal pulse stress was an independent predictor of permeability (Table 6.10). The regression model with this single parameter shown here

$$P(AIU) = 59.9\left(\frac{AIU}{kPa}\right)\sigma_{z\,pulse} + 4250(AIU) \tag{6.5}$$

had an R^2 of 0.132 (p=0.03), which indicates less than 15% of the spatial variation in permeability is attributable to the longitudinal pulse stress (Figure 6.3).

Table 6.10 Non-normalized regression results for permeability and apoptosis in the TWT experiment set.

Independent Variable	Standardized Coefficient	p-value
Permeability		
$\sigma_{z\ pulse}$	0.363	0.030
TUNEL		
N/A	N/A	N/A

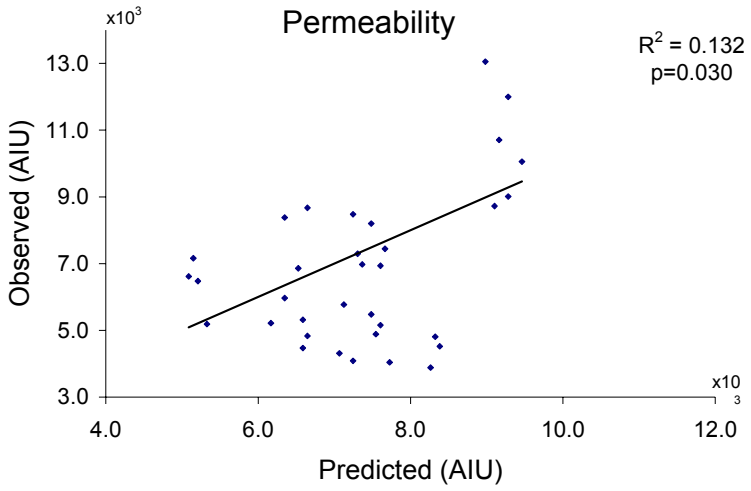

Figure 6.3 Non-normalized regression model fit for permeability in the TWT experiment set. Observed values for permeability (arbitrary intensity units per wall thickness (AIU)) are plotted against the values predicted by the regression model in (6.5).

There were no significant correlations in either the arithmetic (Table 6.11) or the geometric normalized (Table 6.12) data sets for the twist experiment set. It should be noted that the torsion shear stress was not included in the geometric normalization. This is due to the fact that there were no torsion shear stresses in the control vessel specimens. Geometric normalization would therefore, result in division by a zero. This result is expected since the addition of cyclic twist did not result in significant increases in either permeability or apoptosis.

Table 6.11 Pearson correlation coefficients (r) and their significance (p-value) for arithmetic normalized correlations between permeability or apoptosis and the mechanical stress variables considered for the TWT experiment set. No significant correlations were found.

	Permeability		Apoptosis	
	r (Pearson)	p-value	r (Pearson)	p-value
VM_{sys}	-0.078	0.759	0.259	0.299
$\sigma_{\theta\ sys}$	-0.074	0.772	0.257	0.302
$\sigma_{z\ sys}$	0.104	0.681	-0.186	0.460
$\sigma_{\theta z\ sys}$	0.050	0.844	-0.219	0.382
VM_{dia}	-0.082	0.746	0.273	0.273
$\sigma_{\theta\ dia}$	-0.080	0.752	0.272	0.275
$\sigma_{z\ dia}$	0.092	0.717	-0.164	0.515
$\sigma_{\theta z\ dia}$	0.138	0.585	0.210	0.403
VM_{pulse}	0.117	0.644	-0.383	0.117
$\sigma_{\theta\ pulse}$	0.146	0.565	-0.389	0.111
$\sigma_{z\ pulse}$	0.121	0.633	-0.215	0.392
$\sigma_{\theta z\ pulse}$	0.050	0.844	-0.219	0.382

Table 6.12 Pearson correlation coefficients (r) and their significance (p-value) for geometric normalized correlations between permeability or apoptosis and the mechanical stress variables considered for the TWT experiment set. No significant correlations were found.

	Permeability		Apoptosis	
	r (Pearson)	p-value	r (Pearson)	p-value
VM_{sys}	0.041	0.873	-0.116	0.648
$\sigma_{\theta\ sys}$	0.045	0.860	-0.133	0.600
$\sigma_{z\ sys}$	0.073	0.774	-0.280	0.261
$\sigma_{\theta z\ sys}$	N/A	N/A	N/A	N/A
VM_{dia}	0.033	0.898	-0.082	0.747
$\sigma_{\theta\ dia}$	0.029	0.908	-0.089	0.724
$\sigma_{z\ dia}$	0.060	0.813	-0.275	0.269
$\sigma_{\theta z\ dia}$	N/A	N/A	N/A	N/A
VM_{pulse}	0.297	0.232	-0.407	0.094
$\sigma_{\theta\ pulse}$	0.336	0.173	-0.444	0.065
$\sigma_{z\ pulse}$	0.090	0.721	-0.285	0.251
$\sigma_{\theta z\ pulse}$	N/A	N/A	N/A	N/A

6.2.3 Cyclic Bending

Only one mechanical stress parameter, circumferential stress at systole, had a significant correlation with permeability for the non-normalized flexure experiment data set (Table 6.13). On the other hand, three variables (longitudinal stress at diastole, Von Mises pulse stress, and longitudinal pulse stress) had significant correlations with apoptosis. In contrast to the stretch experiment set data, the circumferential stress was inversely correlated with permeability in the flexure experiment set (Table 6.14).

Table 6.13 Pearson correlation coefficients (r) and their significance (p-value) for non-normalized correlations between permeability or apoptosis and the mechanical stress variables considered for the FLX experiment set. Significant correlations are highlighted in green.

	Permeability		Apoptosis	
	r (Pearson)	p-value	r (Pearson)	p-value
VM_{sys}	0.141	0.355	-0.142	0.352
$\sigma_{\theta\ sys}$	-0.304	0.042	-0.121	0.427
$\sigma_{z\ sys}$	0.186	0.221	-0.130	0.393
$\sigma_{r\ sys}$	-0.034	0.827	-0.219	0.148
VM_{dia}	0.204	0.180	0.293	0.051
$\sigma_{\theta\ dia}$	-0.292	0.052	-0.082	0.592
$\sigma_{z\ dia}$	0.237	0.117	0.294	0.050
$\sigma_{r\ dia}$	-0.010	0.951	0.170	0.265
VM_{pulse}	-0.095	0.534	-0.612	<0.001
$\sigma_{\theta\ pulse}$	-0.111	0.468	-0.214	0.159
$\sigma_{z\ pulse}$	-0.091	0.552	-0.613	<0.001
$\sigma_{r\ pulse}$	-0.233	0.124	-0.030	0.843
SR_{dia}	0.091	0.554	0.138	0.366
SR_{sys}	0.080	0.603	0.160	0.293
SR_{pulse}	0.074	0.628	0.163	0.285

Table 6.14 Non-normalized regression results for permeability and apoptosis in the FLX experiment set.

Independent Variable	Standardized Coefficient	p-value
Permeability		
$\sigma_{\theta\ sys}$	-0.304	0.042
TUNEL		
$\sigma_{z\ pulse}$	-0.613	<0.001

However, examination of the fit plot for that regression model (shown in equation (6.6)) demonstrates that this result may be an artifact of a single aberrant experiment (Figure 6.4). Exclusion of this experiment from the data set results in a positive correlation which was not statistically significant.

$$\mathrm{P(AIU)} = -2.0\left(\frac{\mathrm{AIU}}{\mathrm{kPa}}\right)\sigma_{\theta\,\mathrm{sys}} + 14907(\mathrm{AIU}) \tag{6.6}$$

For apoptosis, the longitudinal pulse stress was selected as a significant, independent negative predictor (Table 6.14) indicating that apoptosis occurs in areas of reduced longitudinal stress. The model (shown in equation (6.7)) with this mechanical stress variable predicted ~38% of the spatial distribution of apoptosis (R^2=0.376, p<0.001) (Figure 6.4).

$$\mathrm{A(PPC)} = -7.4x10^{-6}\left(\frac{\mathrm{PPC}}{\mathrm{kPa}}\right)\sigma_{z\,\mathrm{pulse}} + 0.019(\mathrm{PPC}) \tag{6.7}$$

For the arithmetic normalized flexure data, only apoptosis had significant mechanical stress correlations (Table 6.15).

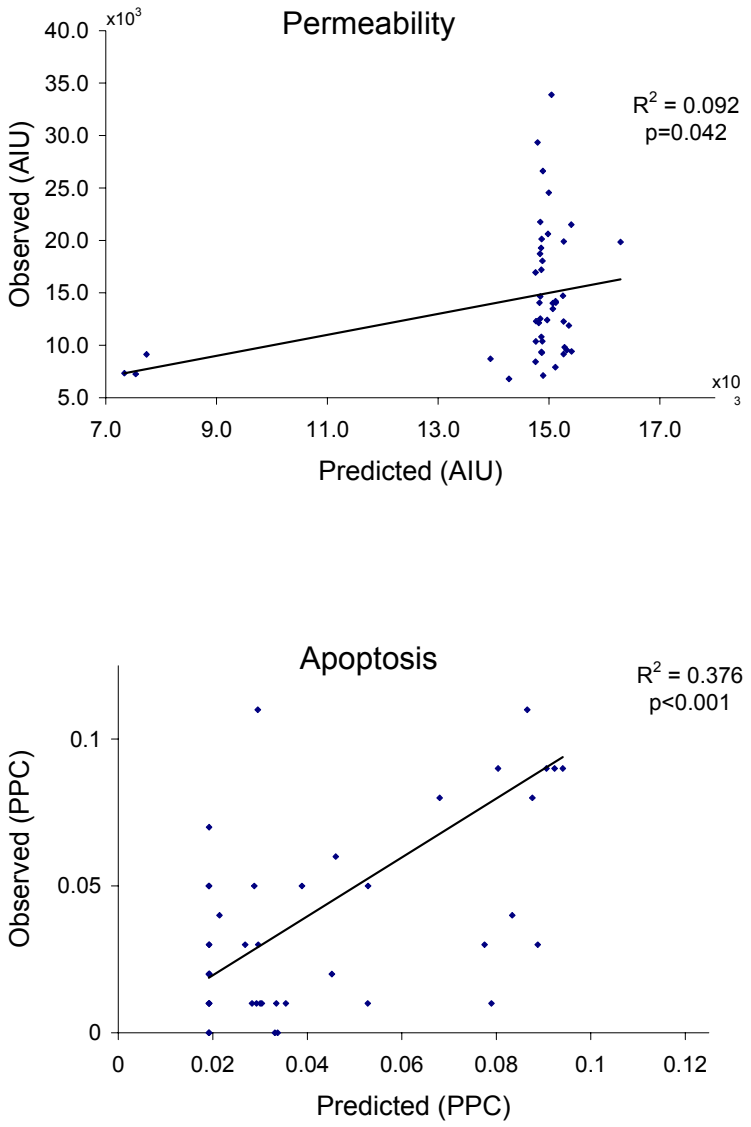

Figure 6.4 Non-normalized regression model fits for permeability (top) and apoptosis (bottom) in the FLX experiment set. Observed values for permeability (arbitrary intensity units per wall thickness (AIU)) and apoptosis (percent TUNEL positive cells (PPC)) are plotted against the values predicted by the regression models given in equations (6.6) and (6.7), respectively.

Table 6.15 Pearson correlation coefficients (r) and their significance (p-value) for arithmetic normalized correlations between permeability or apoptosis and the mechanical stress variables considered for the FLX experiment set. Significant correlations are highlighted in green.

	Permeability		Apoptosis	
	r (Pearson)	p-value	r (Pearson)	p-value
VM_{sys}	0.224	0.235	-0.125	0.511
$\sigma_{\theta\ sys}$	-0.036	0.848	-0.063	0.739
$\sigma_{z\ sys}$	0.218	0.246	-0.123	0.518
$\sigma_{r\ sys}$	-0.085	0.654	-0.263	0.161
VM_{dia}	0.219	0.244	0.038	0.841
$\sigma_{\theta\ dia}$	-0.029	0.881	-0.015	0.937
$\sigma_{z\ dia}$	0.221	0.241	0.047	0.805
$\sigma_{r\ dia}$	-0.167	0.378	0.086	0.651
VM_{pulse}	0.106	0.577	-0.407	0.026
$\sigma_{\theta\ pulse}$	-0.053	0.783	-0.320	0.084
$\sigma_{z\ pulse}$	-0.100	0.598	-0.425	0.019
$\sigma_{r\ pulse}$	-0.066	0.728	-0.272	0.145
SR_{dia}	-0.080	0.673	0.089	0.641
SR_{sys}	-0.024	0.902	0.063	0.740
SR_{pulse}	0.000	0.999	0.050	0.791

Differences in Von Mises and longitudinal pulse stresses due to the flexure deformation were negatively correlated with changes in apoptosis. However, only the longitudinal pulse stress was selected as an independent predictor (Table 6.16). The resulting regression model with this variable was

$$A(PPC) = -5.4x10^{-6}\left(\frac{PPC}{kPa}\right)\sigma_{z\ pulse} + 0.001(PPC) \tag{6.8}$$

which had an R^2 of only 0.18 (p=0.019) (Figure 6.5). This indicates that roughly 18% of the increase in apoptosis can be attributed to decreases in longitudinal pulse stress.

Table 6.16 Arithmetic normalized regression results for permeability and apoptosis in the FLX experiment set.

Independent Variable	Standardized Coefficient	p-value
Permeability		
N/A	N/A	N/A
TUNEL		
$\sigma_{z\ pulse}$	-0.425	0.019

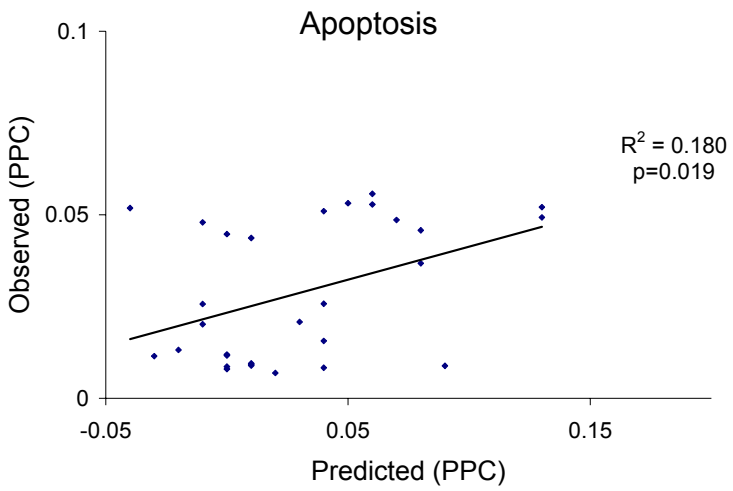

Figure 6.5 Arithmetic normalized regression model fit for apoptosis in the FLX experiment set. Observed changes in apoptosis (percent TUNEL positive cells (PPC)) associated with cyclic flexure are plotted against the values predicted by the regression model given in equation (6.8).

Only apoptosis had significant mechanical stress correlations in the geometric normalized data as well (Table 6.17).

Fold changes in radial pulse stress, radial stress at systole, and the circumferential stress at diastole were all positive correlated with fold changes in apoptosis in flexure versus control specimens. On the other hand, the circumferential stress at systole was negatively correlated and was the only significant, independent predictor (Table 6.18). The regression model for this variable was

$$A_{fold} = -1.11\,\sigma_{\theta\,sys\,fold} + 1.43 \tag{6.9}$$

where A_{fold} is the fold increase in percent TUNEL positive cells and $\sigma_{\theta\ sys\ fold}$ is the fold increase in circumferential stress due to flexure. About 63% of the fold increase in apoptosis associated with specimens exposed to cyclic flexure can be attributed to fold decreases in circumferential stress at systole (R^2=0.636, p=0.001) (Figure 6.6).

Table 6.17 Pearson correlation coefficients (r) and their significance (p-value) for geometric normalized correlations between permeability or apoptosis and the mechanical stress variables considered for the FLX experiment set. Significant correlations are highlighted in green.

	Permeability		Apoptosis	
	r (Pearson)	p-value	r (Pearson)	p-value
VM_{sys}	0.092	0.629	0.176	0.352
$\sigma_{\theta\ sys}$	-0.135	0.478	-0.565	0.001
$\sigma_{z\ sys}$	0.109	0.565	-0.005	0.980
$\sigma_{r\ sys}$	0.025	0.896	0.451	0.012
VM_{dia}	0.111	0.561	0.323	0.082
$\sigma_{\theta\ dia}$	-0.127	0.504	0.514	0.004
$\sigma_{z\ dia}$	0.112	0.556	0.005	0.981
$\sigma_{r\ dia}$	0.197	0.296	-0.327	0.078
VM_{pulse}	-0.178	0.364	0.203	0.300
$\sigma_{\theta\ pulse}$	-0.033	0.885	-0.320	0.147
$\sigma_{z\ pulse}$	-0.294	0.185	0.009	0.969
$\sigma_{r\ pulse}$	-0.068	0.763	0.514	0.014
SR_{dia}	-0.017	0.930	0.001	0.994
SR_{sys}	0.011	0.954	-0.007	0.970
SR_{pulse}	0.113	0.552	-0.031	0.869

Table 6.18 Geometric normalized regression results for permeability and apoptosis in the FLX experiment set.

Independent Variable	Standardized Coefficient	p-value
Permeability		
N/A	N/A	N/A
TUNEL		
$\sigma_{\theta\ sys}$	-0.798	<0.001

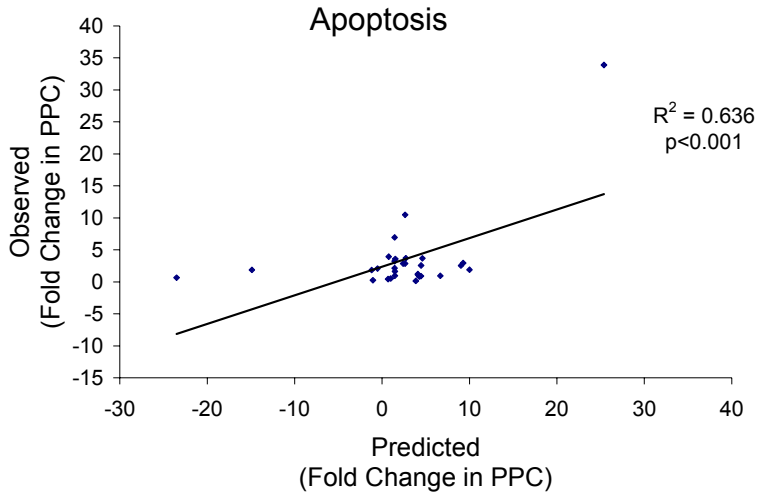

Figure 6.6 Geometric normalized regression model fit for apoptosis in the FLX experiment set. Observed fold changes in apoptosis (percent TUNEL positive cells (PPC)) associated with cyclic flexure are plotted against the values predicted by the regression model given in (6.9).

6.2.4 Pooled Data

In the pooled data, only the circumferential pulse stress had a significant correlation with permeability, while the longitudinal stress at diastole, Von Mises, and longitudinal pulse stresses all had significant correlations with apoptosis (Table 6.19). The circumferential pulse stress and the Von Mises stress at systole were selected as significant, independent predictors of permeability, while only the Von Mises pulse stress was selected for apoptosis (Table 6.20). The models for predicting permeability and apoptosis in the pooled data set are shown in equations (6.10) and (6.11).

$$P(\text{AIU}) = -6.7\left(\frac{\text{AIU}}{\text{kPa}}\right)\text{VM}_{sys} + 226.7\left(\frac{\text{AIU}}{\text{kPa}}\right)\sigma_{\theta\,\text{pulse}} - 898.7(\text{AIU}) \qquad (6.10)$$

$$A(PPC) = -2.25x10^{-4}\left(\frac{PPC}{kPa}\right)VM_{pulse} + 0.054(PPC) \quad (6.11)$$

The permeability model had an R^2=0.201 ($p<0.001$), while the apoptosis model has an R^2=0.132 ($p<0.001$) (Figure 6.7).

Table 6.19 Pearson correlation coefficients (r) and their significance (p-value) for non-normalized correlations between permeability or apoptosis and the mechanical stress variables considered for the data pooled from the STR and TWT experiment sets. Significant correlations are highlighted in green.

	Permeability		Apoptosis	
	r (Pearson)	p-value	r (Pearson)	p-value
VM_{sys}	-0.152	0.175	-0.052	0.646
$\sigma_{\theta\ sys}$	-0.134	0.234	-0.073	0.516
$\sigma_{z\ sys}$	-0.003	0.977	0.138	0.220
VM_{dia}	-0.177	0.114	-0.006	0.957
$\sigma_{\theta\ dia}$	-0.154	0.170	-0.066	0.559
$\sigma_{z\ dia}$	0.068	0.544	0.315	0.004
VM_{pulse}	0.165	0.142	-0.363	0.001
$\sigma_{\theta\ pulse}$	0.367	0.001	-0.167	0.135
$\sigma_{z\ pulse}$	-0.113	0.315	-0.351	0.001

Table 6.20 Non-normalized regression results for permeability and apoptosis in the data pooled from the STR and TWT experiment sets.

Independent Variable	Standardized Coefficient	p-value
Permeability		
$\sigma_{\theta\ pulse}$	0.435	<0.001
VM_{sys}	-0.259	0.015
TUNEL		
VM_{pulse}	-0.363	0.001

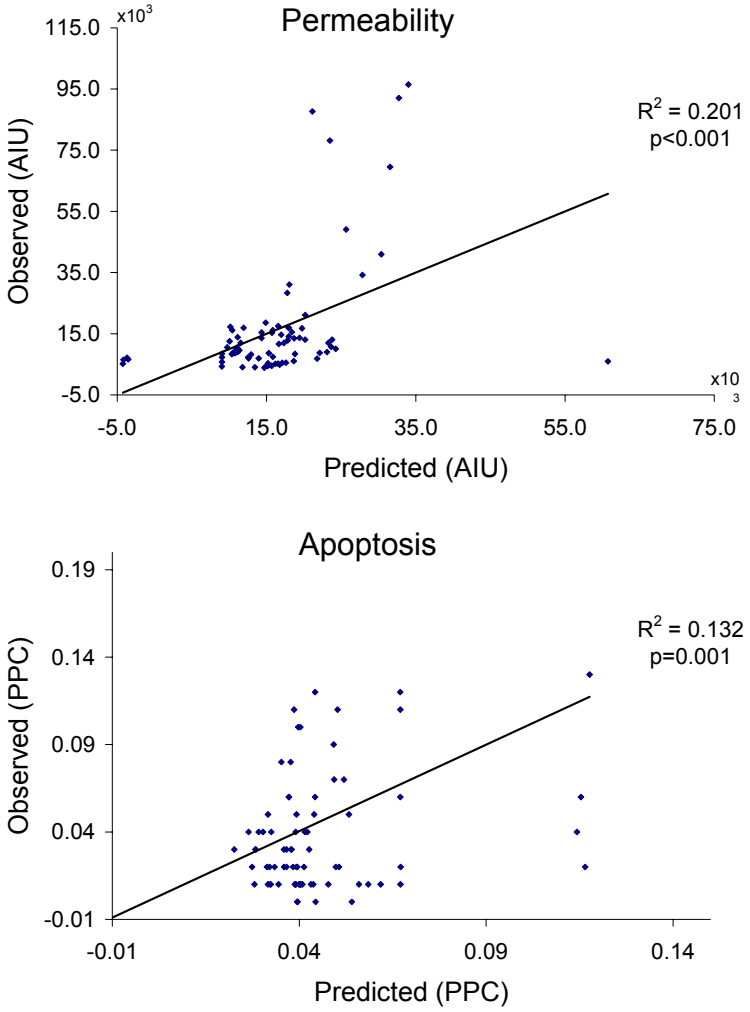

Figure 6.7 Non-normalized regression model fits for permeability (top) and apoptosis (bottom) in the data pooled from the STR and TWT experiment sets. Observed values for permeability (arbitrary intensity units per wall thickness (AIU)) and apoptosis (percent TUNEL positive cells (PPC)) are plotted against the values predicted by the regression models given in equations (6.10) and (6.11), respectively.

6.3 DISCUSSION

6.3.1 Linking the Local Mechanical and Biological Environments

Distinct coupling of *ex vivo* experiments with finite element and computational fluid dynamics analyses provided direct links between the local biomechanical milieu and certain tissue and cellular responses related to atherogenesis. Specifically, the extent and spatial distribution of permeability and apoptosis in a vessel segment exposed to coronary-like deformations of cyclic axial stretch, twist or flexure was partially predicted by a small number of mechanical stress parameters. This suggests a mechanism by which systemic risk factors such as hyperlipidemia can result in discrete, heterogeneous atherosclerotic lesion localization. The specific local biomechanical milieu provides a stimulus that either magnifies or inhibits the systemic insults known to cause vascular disease. For instance, recalling the regression model for permeability in the cyclic stretch experiments (see equation (6.1) and Table 6.5), areas of the vasculature exposed to greater circumferential wall stress may have increased permeability, allowing convection of macromolecules including cholesterol laden lipoproteins in the vessel wall. These molecules can incite a chronic inflammatory process leading to an atherosclerotic plaque. On the contrary, areas with lower circumferential stress would have decreased permeability and therefore, would be less likely to take up the cholesterol from the blood. In essence, this area would be protected from lesion formation. Indeed, the intramyocardial arteries which are surrounded by the myocardium have decreased circumferential stress due to the external compression / support applied to their outer surface [153, 155]. These arteries tend to be free of atherosclerotic lesions while the epicardial vessels that are on the outside surface of the heart are extremely susceptible [77, 78]. Similarly, the portions of the vertebral arteries that are

surrounded by bone tend to be free of lesions while the intervertebral portions are more prone to atherogenesis [155, 198, 203, 204].

Another important facet of this study is the specific focus on both mural and shear stresses in the localization of early atherogenic events. To date, the preponderance of research in the mechanopathobiology of athergenesis has been in regards to shear stress. The correlation between lesion formation and low and / or oscillatory shear stress has been confirmed several times [81, 86, 194-197, 200, 201] provide insight as to why lesions localized to branch points bifurcations [81, 83, 161-163]. The results here do not refute this well-established paradigm. Rather, they suggest a synergism between shear and mural stresses. Specifically, in the case of cyclic axial stretch both mural and shear stresses contribute in predicting the distribution in permeability and apoptosis. For cyclic flexure shear parameters were never significant independent predictors of either permeability or apoptosis despite the dramatic effect this deformation had on the shear rate distribution. This could be a function of these specific endpoints (i.e., permeability and apoptosis) or the fact that the mural stress effects are dominating over the shear effects. The results here provide an addition layer to the role of biomechanics in atherosclerotic lesion localization by focusing on the understudied mural stress distributions in addition to the shear stress distributions.

6.3.2 Limitations

An obvious limitation of these analyses linking the mechanical and biological endpoints was that while a physiologic shear rate was imposed in the EVPS, the resulting shear stress was sub-physiologic due to the low viscosity (relative to blood) of the cell culture media used as the working fluid. This may account for the predominance of mural stresses over the shear stresses

in the regression models. Most of the work correlating atherosclerosis with fluid-induced mechanical stimuli has focused specifically on shear stress, rather than shear rate (see Section 1.4.1). However, it is unclear what component of the fluid-based mechanical environment is being "sensed" by the vascular cells, in particular the endothelium. To our knowledge, only one paper has explored the differential effects of shear stress versus shear rate. Ainsle et al., demonstrated that SMC contraction was not affected by differences in shear rate with constant shear stress [205]. However, the endothelium is considered the transducer of fluid-based mechanical stimuli [206]. Therefore, without further evidence comparing shear stress and shear rate, it is difficult to separate these two interdependent stimuli factors. We hypothesize that both are important modulators of vascular cell response and atherogenic development. Deformation of cell surface receptors, specifically ion channels, by shear stress can lead to downstream cellular signaling and subsequent gene expression [207]. On the other hand, transport and diffusion of soluble factors such as metabolites [144, 208] and cell surface receptor ligands are heavily influenced by the shear rate [207]. Therefore, it is likely that fluid-induced mechanical forces act through a variety of mechanisms that include both deformation- induced stress and alterations in the solute transport environment relate to shear rate.

Another limitation is the fact that two different material models were used for the finite element analyses. This prevented the pooling of the data from the flexure experiments with the stretch and twist experiments. This combined data set would have provided the general relationship between stress distribution and biological endpoint distribution irrespective of the type of deformation applied. This type of information is necessary for developing a generalized description of the mechanopathobiology of the vasculature. Unfortunately, it was felt that in order to accurately estimate the mural stress distribution in the arterial wall exposed to cyclic

axial stretch, twist and flexure, the Fung model had to be used for the axi-symmetric loading conditions and the Mooney-Rivlin model had to be used for the asymmetric loading conditions. For more details on the rationale behind using these two models see Sections 4.2 and 4.5.1.

Finally, confidence in the regression models presented here depends on the uncertainty of the measurements used as inputs to the computational analyses. In particularly, the uncertainty in the inner and outer diameter measurements used for geometric reconstruction propagated through the finite element and computational fluid dynamic analyses. In order to better understand this uncertainty and its effects on the computational analyses a sensitivity analyis was performed and can be found in Appendix H. The results of that analysis demonstrate that the shear rate is significantly more sensitive to the uncertainty in diameter than the mural stresses. This makes sense, given the nonlinear dependence of shear rate on the vessel diameter. However, the most notable feature of this analysis is that despite the expansion of uncertainty in the computational analyses the trends over the length of the vessel segment were more significant that the errors generated by uncertainty. This indicates that while the the actual values of the regression constants may have significant uncertainty, we can be fairly confident in the presence of the trends predicted by the models.

6.4 CONCLUSIONS

Experiment specific coupling of biological analyses and computational analyses provided a means to assess how local variation in shear and mural stress influence the extent and spatial distribution of the early atherogenic markers. Several specific mechanical stress measures, both mural and shear, were shown to be associated with cellular atherogenic marker distribution. This

work demonstrates the importance of including mural stresses in the investigation of vascular mechanopathobiology and provides evidence of a mechanism by which systemic risk factors can lead to a heterogeneous disease.

7.0 STUDY SUMMARY

To summarize the work presented here, a brief description of the pertinent study findings organized by Specific Aim is first provided. Next, the technical improvements made to the experimental apparatus as well advances in computational capabilities are summarized. Finally, some recommendations for future study are made.

7.1 SUMMARY OF PERTINENT FINDINGS

7.1.1 Specific Aim 1

Paired *ex vivo* perfusion experiments utilizing a unique, well-established, and validated EVPS demonstrated that cyclic axial stretch and cyclic flexure can lead to significant increases in intimal and medial apoptosis with concomitant increases in permeability. These results indicate an increased potential for atherosclerotic lesion development associated with cyclic stretch and flexure. The spatial variations in permeability and apoptosis were non-uniform and highly vessel specimen specific, indicating local factors such as mechanical stresses influencing the individual cellular responses to the global deformation stimli.

7.1.2 Specific Aim 2

Finite element simulations of each experimentally perfused arterial segment in Specific Aim 1 demonstrated that the relatively simple mechanical deformations of axial stretch, flexure, and twist, resulted in non-uniform mural stress distributions. The stress magnitudes and distribution through the vessel volume depended heavily on the vessel specimen geometry. High specimen-to-specimen variability in mural stress distribution provided further evidence of the potential for local mechanical stress factors to influence location specific biological processes.

7.1.3 Specific Aim 3

Incorporation of deforming mesh grids into unsteady computational fluid dynamics simulations of each experimentally perfused arterial segment from Specific Aim1 provided accurate estimation experiment-specific shear rate distributions. Considerable specimen-to-specimen variability in shear magnitude and distribution echoed the results of the finite element estimations of mural stress distributions. This variability was a function of the specimen-specific geometry and the imposed deformation (either cyclic axial stretch or cyclic flexure).

7.1.4 Specific Aim 4

Experiment-specific coupling of biological data obtained experimentally in Specific Aim 1 and mechanical stress data estimated computationally in Specific Aims 2 and 3 provided data sets for multiple linear regression analyses. The analyses revealed specific mechanical stress measures, both mural and shear, that were quantitatively correlated with cellular atherogenic marker

distribution. The results demonstrated that local variation in shear and mural stress, indeed influence the extent and spatial distribution of the early atherogenic markers. In addition, the importance of including mural stresses in the investigation of vascular mechanopathobiology was highlighted. Specific example results were used to describe a potential mechanism by which systemic risk factors can lead to a heterogeneous disease.

7.2 ADVANCES IN EXPERIMENTAL AND COMPUTATIONAL CAPABILITIES

7.2.1 Improvements in *Ex Vivo* Perfusion

Two technical improvements were made to the EVPS as part of this study. First a peak-detection algorithm was use to control the phase angle between the pressure and motion waveforms. In addition to recreating the desired physiological phase angles of 0˚ and 180˚ required for this study, it was possible to generate any phase angle in between. This improvement could facilitate investigations into the potential effects of altered phase relationship between simultaneous mechanical stimuli. In addition, the dynamic motion of other arterial segments with frequency and phase relationship different from that of the coronary arteries could be studied.

Second, the EVPS was modified by the addition of a flat, flexible strip of inert polymer to provide a distributed flexure load to the vascular segment. This addition was an important improvement from previous attempts to simulate coronary arterial flexure dynamics *ex vivo*. The original design provided physiologic changes in curvature but in a non-physiologic manner. That is, the proximal and distal ends of the vessel were displaced toward each other causing it to

buckle. True flexure requires a distributed displacement load over the length of the segment as seen in the coronary arteries which are tethered to the dynamic, curved surface of the myocardium. The polymer membrane provided that distributed displacement load and generated cyclic changes in curvature in a more physiologic manner.

7.2.2 Advances in Computational Capabilities

Previous combined experimental / computational studies interested in the effect of shear distribution on biological endpoints utilized very simplified computational fluid dynamics models [168]. They employed steady flow with rigid wall boundaries. The fluid simulations described here modeled the unsteady flow regime in a dynamic deforming mesh model. Specific user-defined functions were developed to apply a user-specified deformation to the finite volume grid. Inclusion of these dynamic effects was required for accurate estimation of shear stress in arterial segments exposed to dynamic wall motion.

7.3 FUTURE DIRECTIONS

The results of this work motivate continued research along four tangentially related topics. First, a definite limitation of this work was the lack of a suitable anisotropic material model for the flexure simulations. The Mooney-Rivlin model provided a stable, converged solution in the finite element analysis, but the accuracy of the stresses is in question due to the poor circumferential distension prediction (recall Figure 4.14). Vascular tissue has been shown by several researchers to be anisotropic [199, 201, 219], however, the models developed from these

studies do not include shear strains. Future mechanical characterization of vascular tissue should focus on the including all three components of shear, so that more complex deformations (such as flexure) can be modeled accurately in finite element analyses.

Second, the overall goal of this work was to develop a model that predicts the stress field (both mural and shear) for a given deformation or mechanical stimulus and then uses that stress field to predict the spatial distribution of biological responses. In this study, some simply linear regression models were developed. The next step in model development is to test its ability to predict results on a new set of data. Future work along these lines could involve repeating the experiments performed here to test the predictve capacity of the regression models generated.

Third, a minscule subset of endpoints, indicating atherogenic potential, was considered in this study. Even if every endpoint original proposed had been experimentally feasibile this still would have only described a fraction of the complicated process of atherogenesis. Future work needs to investigate specific molecular processes in atherogenesis and the mechanism by which a mechanical stress can influence those molecular events.

Fourth, there is one particularly interesting deformation experienced by the coronary arteries that was not investigated in this study, namely cyclic radial compression. As stated in Chapter 1, the intramyocardial coronary arteries, which experience cyclic radial compression due to contraction of the surrounding myocardial muscle, have a low occurrence of atherosclerosis, indicating a protective effect of mechanical compression [77, 78]. In light of this, other evidence indicating the protective effect of circumferential wall support [78, 177], and the importance of circumferential wall stress demonstrated in regression analyses in this study, investigating the role of cyclic radial compression on arterial segments would be important step in understanding the mechanopathobiology of atherogenesis and provide a new potential treatment option.

While the combined *ex vivo* experimental / computational model described in this study was a novel and innovative approach to better understanding the mechanopathobiology of atherosclerosis, it sufferes from several limitations as outlined in the discussion sections of Chapters 3 – 6 (See Sections 3.3.2, 4.6.2, 5.4.2. 6.3.2). In light of these limitations, it is prudent to propose other experimental stategies, models, and methodologies to try and overcome these experimental concerns. We propose employing the same combined experimental / computational approach to an *in vivo* model of atherosclerosis. In particular the high cholesterol fed porcine model for atherosclerosis [178, 179]. There are a number of advantages to switching to this *in vivo* model. (1) Without the time limitation (imposed by the *ex vivo* setup), the development of mature atherosclerotic lesions can be monitored. This would allow for assessing not only very early disease markers but the progression as well. (2) There would no long be a restriction to studying the coronary arteries (See description of the rational for this restriction in Section 3.1.1). That is, the paired study design was required to remove any artifacts created by the transfer of an arterial segment from an *in vivo* to an *ex vivo* environment. In addition, the difficulting in maintaining the viability of the coronary arterial segments during harvest would no longer be an issue. Finally, the actual displacement field for each individually tested coronary artery could be specifically determined using noninvasive, cineangiographic imaging techniques [87, 88]. Therefore, the arterial bed of interest (i.e., coronary) could be studied directly, rather than extrapolating from the results of a different arterial bed (i.e., femoral). (3) Inflammatory cells play a crucial role in the development of atherosclerosis particularly macrophages [3, 8, 9, 209]. The *ex vivo* model described here cannot account for this component of the disease process. An *in vivo* model would include this component.

Of course, this new model would have a number of disadvantages to trade-off. (1) The computational modeling, both fluid and solid, would be significantly more complex. This complexity may exceed current computational capabilities and therefore require many simplifying assumptions which may limit the utility of their results. (2) The *in vivo* environment (both mechanical and neural-hormonal) is less well-controlled than the laboratory based *ex vivo* environment. Therefore, a significantly larger number of animal experiments would be required to cover the independent variable space for the regression analyses. (3) There were significant experimental obstacles in the assessment of molecular (gene and protein expression) endpoints in the porcine model as detailed in Appendix A. In order to thorough investgate the molecular pathways in detail, mouse knockout models would be required.

The exact mechanisms by which systemic risk factors lead to the heterogenous disease of atherosclerosis remain unclear. However, the work presented here provides some clarity, by demonstrating a number of potential mechanical srimuli that modulate the atherogenic processes of endothelial permeability and apoptosis. Continued research as described in this section will further clarify our understanding of the pathogenesis of atherosclerosis. Such understanding should reveal new therapeutiuc targets to slow or even halt the disease process at earlier and earlier points in its progression.

APPENDIX A

APPENDIX A: MOLECULAR ENDPOINTS

The endpoints originally proposed for Specific Aim 1 as early markers of atherogenesis included seven proteins, namely LOX-1, Choleteryl esterase, MCP-1, IL-8, P-selectin. ICAM-1, and VCAM-1. These proteins were to be assessed at the gene expression and the protein translation levels via RT-PCR and western blotting techniques, respectively. However, these assays were found to be extremely difficult.

There were two major obstacles to successful completion of these proposed endpoints. The first involved western blotting. Western blots run using protein isolated from tissue homogenates from preliminary *ex vivo* perfusion experiments ended with one of two results. Either there was absolutely no positive signal or it appeared that every band in the gel was positive. This initial problem was overcome by optimizing the protocol over the following parameters: Type of block, secondary detection system, and antibody concentration. This optimization led to a result of consistent nonspecific bands on the gel. At this point, all western blot trouble shooting was performed using a primary antibody against smooth muscle alpha actin (SMA). This was to ensure that a positive signal was present, since it was not necessarily known whether the proteins of interest would be expressed in this tissue.

Two types of protein isolation methods were considered in case any of the isolation solutions interfered with the downstream antibody reactions. A typical western blot image with protein isolated using Trizol (Invitrogen) and T-Per (Pierce) is shown in Figure A.1. Note the large amount of nonspecific staining. Also, note that staining only occurs in the gels lanes indicating that the block is adequate.

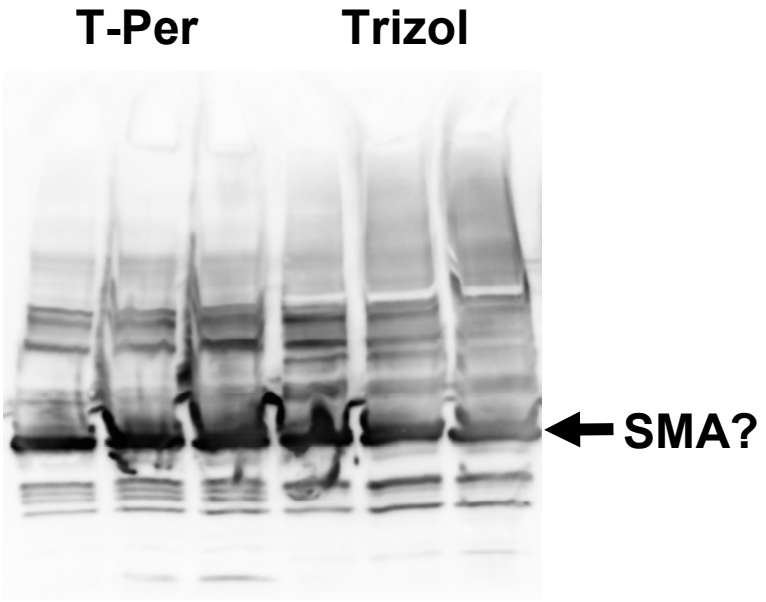

Figure A.1 Western blot for SMA of porcine arterial tissue after 12 hours of *ex vivo* perfusion. The three lanes on the left were isolated using T-Per. The three lanes on the right were isolated using Trizol.

There were minor differences in banding patterns for the two isolation techniques but nothing to indicate that the isolation technique was responsible for the problem. Immunoprecipitation (IP) was tried to reduce the potential number of proteins in the lane that could bind the antibodies non-specifically. The rationale was that the precipitate would not contain many of the nonspecific bind bands. Typical results of the IP experiments are shown in

Figure A.2. Subsequent western blotting on the IP products generated a cleaner gel but with inexplicable results (Figure A.3). That is, the alleged SMA band appeared in the first pellet lane; it was precipitated in the absence of an anti-SMA antibody.

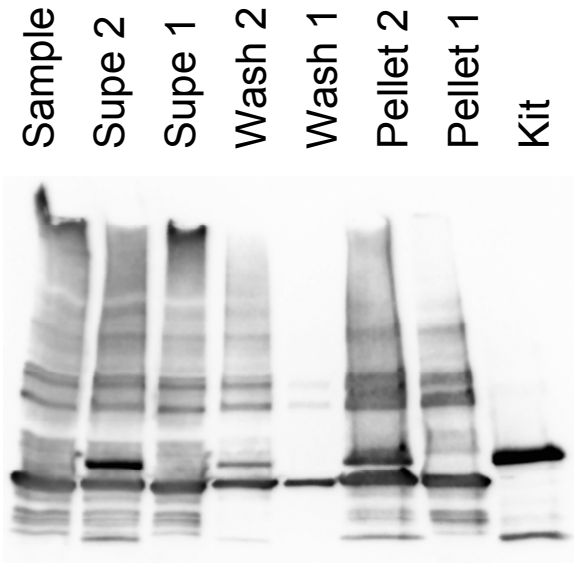

Figure A.2 Total protein stained gel of the various steps in the immunoprecipitation. From right to left: Kit is a lane loaded with only the contents of the immunopreciptation kit (BioRad). Pellet 1 is the precipitation without primary antibody. This is essentially a primary delete. Pellet 2 is the precipitant of interest. Wash 1 was used to wash pellet 1 after precipitation. Wash 2 was used to wash pellet 2 after precipitation. Supe 1 is the supernant from the first precipitation. Supe 2 is the supernant from the second precipitation. Sample is the original tissue homogenate.

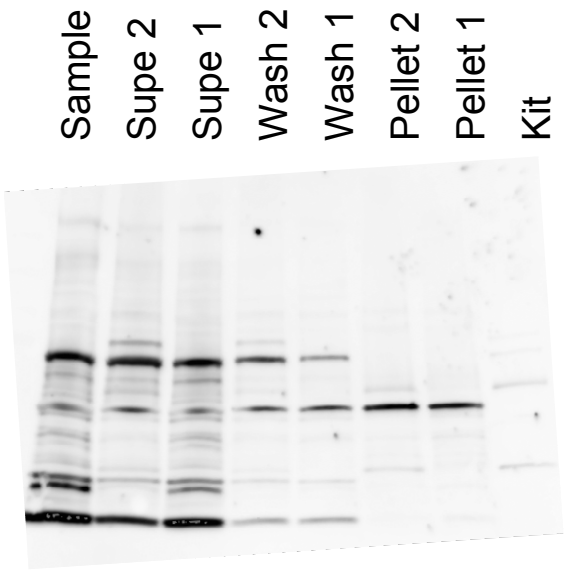

Figure A.3 Western blot of the various steps in the immunoprecipitation. From right to left: Kit is a lane loaded with only the contents of the immunopreciptation kit (BioRad). Pellet 1 is the precipitation without primary antibody. This is essentially a primary delete. Pellet 2 is the precipitant of interest. Wash 1 was used to wash pellet 1 after precipitation. Wash 2 was used to wash pellet 2 after precipitation. Supe 1 is the supernant from the first precipitation. Supe 2 is the supernant from the second precipitation. Sample is the original tissue homogenate.

Marginal improvement was obtained by switching from a secondary antibody to protein G in the western blot. The most alarming finding was that almost identical banding patterns were obtained for antibodies against complete different proteins (Figure A.4). To confirm that the western blotting protocol worked properly, total bone marrow progenitor cell lysates were blotted for SMA. These blot showed only a single band (Figure A.5).

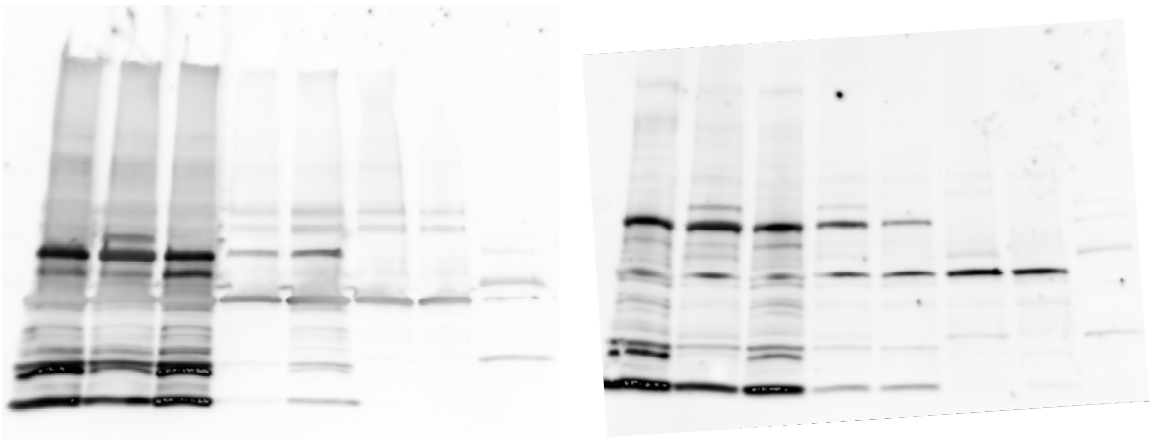

Figure A.4 Western blots of IPs performed against SMA (left) and MCP-1 (right).

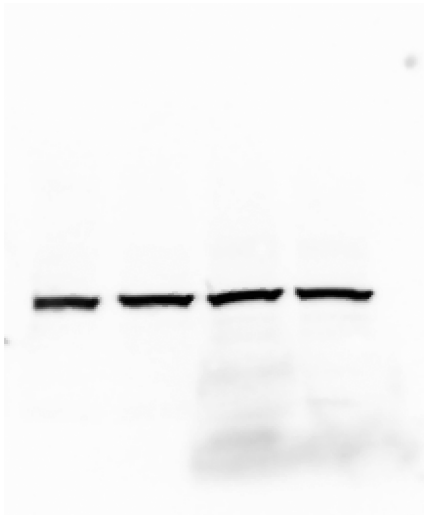

Figure A.5 Western blot for SMA on bone marrow progenitor cell lysates.

Based on these results the following hypotheses were made:

1. There is a subset of immunological active proteins in the vasculature designed to bind antibodies nonspecifically.
2. These tissues have high albumin content from the EBD-albumin supplementation for permeability studies. Because of its widely nonspecific binding capacity, albumin is interfering with the antibody binding.
3. All the antibodies used were raised in mice. Since the pigs used in this study were farm raised, it is extremely likely they have been in contact with mice and developed immuno-reactive molecules against mouse proteins.

Future recommendations for trouble shooting the western blots include:

1. Use antibodies raised in other animals if possible.
2. Increase the temperature during the antibody incubations to preferentially reduce weaker nonspecific sites.
3. Process samples through commercial available albumin extraction kits.

The second obstacle involved obtaining porcine primer-probe sets for RT-PCR. When this work was originally proposed, Applied Biosystems, Inc., suggested that they would design and manufacture custom primer-probe sets for any known gene sequence. The problem is that they do not perform all of the quality assurance checks (to ensure the primers amplify the single gene of interest) on the custom primers that they do on their inventory primers. In addition, the porcine genome is so poorly characterized that they could not be as confident in the quality of custom porcine primers as they are for other species where the genome is more fully annotated. Since we were not equipped to perform the genomics studies and quality control analyses to

ensure reliable, accurate results, we felt it was not prudent to continue with these particular endpoints. However, as a preliminary gene expression study, we were able to run all the stretch and control samples (4 each along the length) for one cyclic stretch experiment on a microarray chip of the entire porcine genome. To do this, total RNA was isolated as follows: Tissue samples were ground to a fine powder with a mortar and pestle in liquid nitrogen. The powder was transferred to 3 mls of Trizol (Invitrogen, Carlsbad, CA) isolated as directed by Invitrogen. The isolation was followed by Qiagen clean-up (Qiagen, Valencia, CA). After washing away the undesired macromolecules from the column, the RNA was eluted into water. The samples were then taken to the Genomic and Proteomics Core Laboratory at the University of Pittsburgh for hybridization and imaging of the microarry chip. The results of this preliminary study are summarized in Table A.1 and Table A.2.

Table A.1 Representative differentially expressed genes related to atherosclerosis. Fold changes in stretch with respect to control expression. Increased expression shown in red, decreased in green

Genes Grouped by Function	Fold Change
Apoptosis	
annexin A2	1.32
annexin I	1.32
apoptosis-related protein (ARP-2)	1.74
BH3 interacting domain death agonist (BID)	1.32
Immediate Early Response Genes	
cardiac ankyrin repeat protein (CARP)	12.13
c-jun protein	3.25
early growth response protein 1(EGR-1)	-1.87
Lipoprotein Modification / Lipid Metabolism	
apolipoprotein A-I (apoA-I)	-2.00
heart fatty acid-binding protein (H-FABP)	1.62
scavenger receptor class B member 1 (SCARB1)	-1.41
scavenger receptor class B member 2 (SCARB1)	-2.14
scavenger receptor for phosphatidylserine and oxidized LDL (SR-PSOX)	-1.87
superoxide dismutase (Mn type)	-5.28
Growth Factors	
connective tissue growth factor (CTGF)	6.06
epidermal growth factor (EGF)	7.46
transforming growth factor beta 1 (TGF-beta 1)	1.87
transforming growth factor beta 2 (TGF-beta 2)	2.83
transforming growth factor-beta 3 (TGF-beta 3)	-2.46
vascular endothelial growth factor 1 (VEGF 1)	1.87
vascular endothelial growth factor 2 (VEGF 2)	-2.30
Inflammatory	
alveolar macrophage-derived chemotactic factor-II (AMCF-II)	-2.30
granulocyte colony-stimulating factor (GC-SF)	-2.64
intercellular adhesion molecule-1 (ICAM-1)	-1.41
interferon (alpha, beta and omega) receptor 1	-2.64
interleukin 10 receptor, beta (IL10-beta)	-3.03
interleukin 13 receptor alpha 1(IL12-alpha)	-1.74
interleukin 1-alpha (IL1-alpha)	-6.50
interleukin-6 (IL6)	-2.46
macrophage inflammatory protein 1 alpha (MIP-1alpha)	-8.57
monocyte chemoattractant protein 1(MCP-1)	-1.74
prointerleukin-1 beta (IL1-beta)	-6.50
P-selectin (CD62P)	-2.00
vascular cell adhesion molecule (VCAM)	-10.56
Matrix-Related	
collagen I alpha-2 chain	-2.46
collagen VI alpha-1 chain	-1.52
collagen VIII	-1.74
matrix metalloproteinase 3 (MMP-3)	-6.50
tissue inhibitor of metalloproteinase-1 (TIMP-1)	-1.32
tissue inhibitor of metalloproteinase-2 (TIMP-2)	-1.32
tenascin C (TN-C)	1.32

Table A.2 Representative genes related to atherosclerosis with significant correlations to mural and/or shear stress. + refers to a positive correlation while – refers to a negative correlation.

Genes	Correlation (-/+)*
Correlated with shear stress	
apoptosis-related protein (ARP-2)	-
caspase-15	+
collagen VIII	-
C-reactive protein (CRP)	-
interleukin 21 (IL21)	+
matrix metalloproteinase 13 (MMP-13)	-
matrix metalloproteinase 9 (MMP-9)	-
matrix metalloproteinase 3 (MMP-3)	+
thrombospondin 1 (TSP-1)	+
transforming growth factor beta receptor type I	+
vascular smooth muscle alpha-actin (VSM)	+
vasopressin (AVP)	-
Correlated with mural stress	
early growth response protein 1(EGR-1)	-
caspase-3	-
soluble angiotesin-binding protein	+
smoothelin-B	+
plasminogen activator inhibitor I (PAI-1)	+
Correlated with both	
CCL19 chemokine	+ shear / - mural
FAS receptor (CD-95)	+ shear / - mural
heart fatty acid-binding protein (H-FABP)	- shear / + mural
integrin alpha v	- shear / + mural
interleukin 1 receptor antagonist (IL-1ra)	+ shear / - mural
collagen I alpha1	- shear / + mural

APPENDIX B

APPENDIX B: MOTION CONTROL / DATA ACQUISITION SYSTEM

Motion control and data acquisition for the EVPS were accomplished with a custom designed LabView VI. The block diagram for the VI described in Section 2.2.1.1 is shown on the following page.

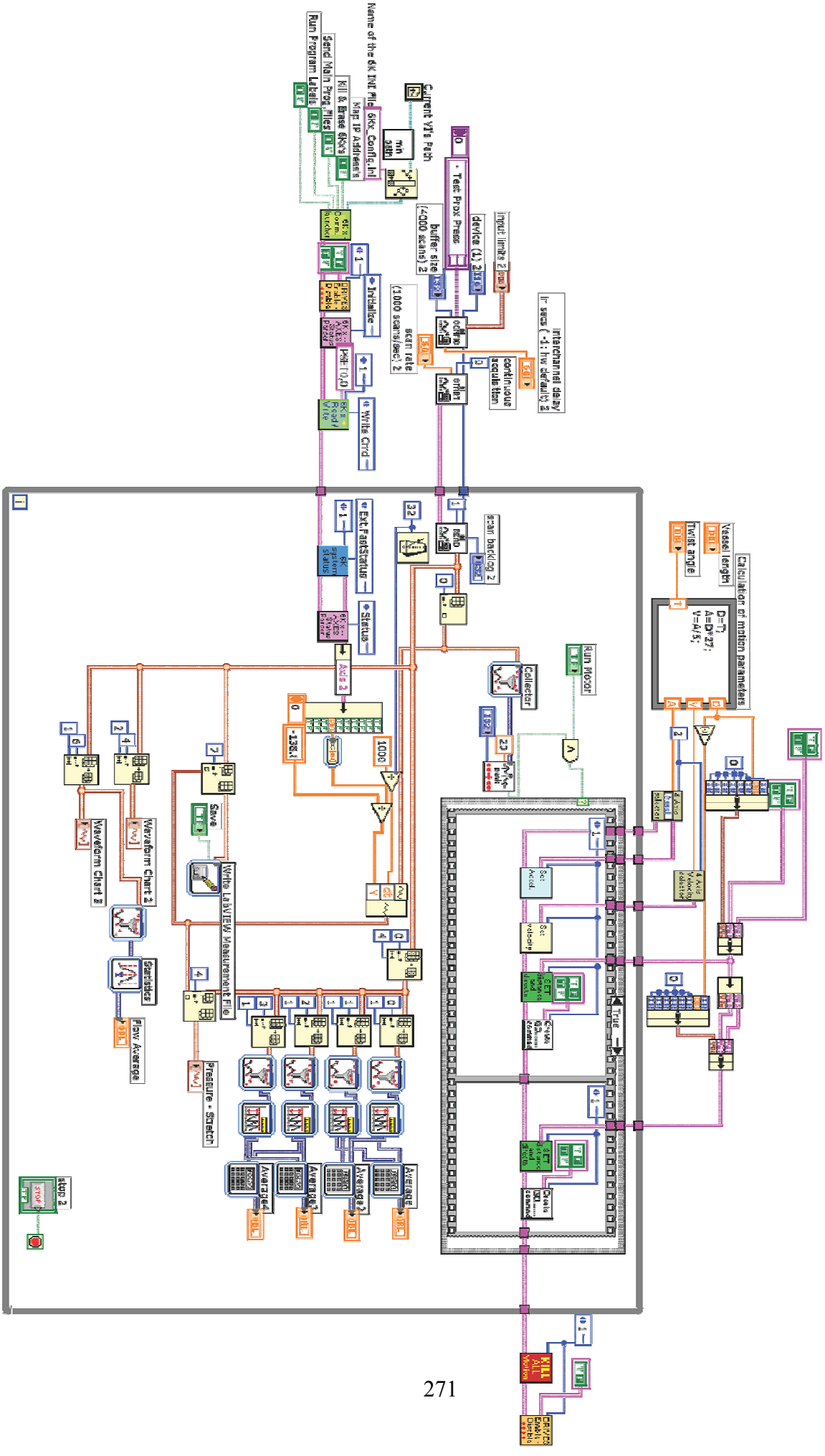
Name of the 6K INI File
6Kx_Config.ini
Current VI's Path
Run Program Labels
Send Main Prog. Files
Kill & Erase 6Kx's
Map IP Addresses
Test Prox Press
buffer size (4000 scans) 2
device (1)
Input limits 2
scan rate (1000 scans/sec) 2
continuous acquisition
interchannel delay
Initialize
Write Cmd
Ext. FastStartup
Status
scan backlog 2
Collector
Run Motor
Vessel length
Twist angle
Calculation of motion parameters
Waveform Chart 2
Save
Write LabVIEW Measurement File
Pressure - Stretch
Standdev
Flow Average
Average
Average2
Average3
Average4
Stop 2
True
KILL ALL Motion

APPENDIX C

APPENDIX C: CUSTOM IMAGE ANALYSIS SOFTWARE

C.1 EVAN'S BLUE DYE INTENSITY MATLAB CODE

Matlab script for analysis of EBD dye far red intensity in the stretch experiment set:

```
%This script reads and analyzes far red fluorescence images of cross-
%sections of arterial segments perfused ex vivo with Evan's blue dye
%labeled albumin.
%J. Scott VanEpps
%March 2007

%Experiment 091406

%This program is designed for 24-bit RGB TIF files where the far red
%fluorescence is recorded in the red channel.

%The following for loop nest is designed to read each image and sum all of
%the pixel intensities for that image.  Files names of the pictures should
%comform to the following nomenclature:
%C#_$_&.tif
%where C or S represents Control or Stretch vessel
%     # represents the segment (i.e., the vessel is divided into 5 segments
%       from proximal to distal along the length)
%     $ represents the position the picture was taken on the vessel
%       cross-section (i.e., four pictures are taken on each cross-section
%       using a clockface as a reference the pictures are taken 3,6,9,and
%       12 o'clock
%     & represents the replicate number (i.e., for each segment represented
%       by # a total of 6 sections are imaged at four positions ($)

for i=1:5 % i is the counter for #
   for j=1:4 % j is the counter for $
      for k=1:6 % k is the counter &
         read='C#_$_&.tif'; % read is the string type variable
                            % representing the image file to be read
```

```
        read=strrep(read,'#',int2str(i));
        read=strrep(read,'$',int2str(j*3));
        read=strrep(read,'&',int2str(k));
        A=imread(read); % A is the three dimensional matrix
                        % representing the RGB tif file with the name
                        % read
        C(i,j,k)=sum(sum(A(:,:,1))); % C is a three dimensional matrix
                                     % representing the sum of all
                                     % pixel intensities in the red
                                     % channel of all the images for
                                     % the control vessel
        read='S#_$_&.tif'; % the above set of commands is repeated for
                           % the stretch vessel
        read=strrep(read,'#',int2str(i));
        read=strrep(read,'$',int2str(j*3));
        read=strrep(read,'&',int2str(k));
        B=imread(read);
        S(i,j,k)=sum(sum(B(:,:,1)));
      end
    end
end

%To get a mean intensity for each section the images for the 4 clock-face
%positions are averaged

for i=1:5
    for j=1:6
        Control(i,j)=mean(C(i,:,j)); %Control(i,j) will represent the mean
                                     %intensity from cross-section j from
                                     %segment i of the control vessel
        Stretch(i,j)=mean(S(i,:,j)); %Stretch(i,j) will represent the mean
                                     %intensity from cross-section j from
                                     %segment i of the stretch vessel
    end
end

%To get a mean intensity for each segment (sampled by 6 cross sections) the
%images from the 6 replicates are averaged.  Additionally a standard
%deviation is calculated.  This is also done for the difference and
%quotients.

for i=1:5
    Controlmean(i)=mean(Control(i,:));
    Controlstd(i)=std(Control(i,:));
    Stretchmean(i)=mean(Stretch(i,:));
    Stretchstd(i)=std(Stretch(i,:));
    %For the purposes of comparison between stretch and control a
    %difference between each stretch segment and it's "paired" control
    %segment is taken.  This is valid due to the paired experimental
    %study design
    Differencemean(i)=Stretchmean(i)-Controlmean(i);
    %Similarly a quotient of stretch over control is made so that a
    %fold increase or decrease comparison can be made
    Foldmean(i)=Stretchmean(i)/Controlmean(i);
end

%The analysis results are written to an excel spreadsheet.
```

```
Headers={'Segment','Str','Str STD','Ctl','Ctl STD','Diff','Fold'};
Segments=[1;2;3;4;5];
xlswrite('091406_Perm_Results.xls',Headers,'Sheet1','A1');
xlswrite('091406_Perm_Results.xls',Segments,'Sheet1','A2');
xlswrite('091406_Perm_Results.xls',Stretchmean','Sheet1','B2');
xlswrite('091406_Perm_Results.xls',Stretchstd','Sheet1','C2');
xlswrite('091406_Perm_Results.xls',Controlmean','Sheet1','D2');
xlswrite('091406_Perm_Results.xls',Controlstd','Sheet1','E2');
xlswrite('091406_Perm_Results.xls',Differencemean','Sheet1','F2');
xlswrite('091406_Perm_Results.xls',Foldmean','Sheet1','G2');
```

Matlab script for analysis of EBD dye far red intensity in the twist experiment set:

```
%This script reads and analyzes far red fluorescence images of cross-
%sections of arterial segments perfused ex vivo with Evan's blue dye
%labeled albumin.
%J. Scott VanEpps
%March 2007

%Experiment 031507

%This program is designed for 24-bit RGB TIF files where the far red
%fluorescence is recorded in the red channel.

%The following for loop nest is designed to read each image and sum all of
%the pixel intensities for that image.  Files names of the pictures should
%comform to the following nomenclature:
%C#_$_&.tif T#_$_&.tif
%where C or T represents Control or Twist vessel
%     # represents the segment (i.e., the vessel is divided into 4 segments
%       from proximal to distal along the length)
%     $ represents the position the picture was taken on the vessel
%       cross-section (i.e., four pictures are taken on each cross-section
%       using a clockface as a reference the pictures are taken 3,6,9,and
%       12 o'clock
%     & represents the replicate number (i.e., for each segment represented
%       by # a total of 6 sections are imaged at four positions ($)

for i=1:4 % i is the counter for #
   for j=1:4 % j is the counter for $
      for k=1:6 % k is the counter &
         read='C#_$_&.tif'; % read is the string type variable
                    % representing the image file to be read
         read=strrep(read,'#',int2str(i));
         read=strrep(read,'$',int2str(j*3));
         read=strrep(read,'&',int2str(k));
         A=imread(read); % A is the three dimensional matrix
                  % representing the RGB tif file with the name
                  % read
         C(i,j,k)=sum(sum(A(:,:,1))); % C is a three dimensional matrix
                           % representing the sum of all
                           % pixel intensities in the red
                           % channel of all the images for
                           % the control vessel
         read='T#_$_&.tif'; % the above set of commands is repeated for
```

```
                    % the twist vessel
        read=strrep(read,'#',int2str(i));
        read=strrep(read,'$',int2str(j*3));
        read=strrep(read,'&',int2str(k));
        B=imread(read);
        T(i,j,k)=sum(sum(B(:,:,1)));
      end
   end
end

%To get a mean intensity for each section the images for the 4 clock-face
%positions are averaged

for i=1:4
   for j=1:6
      Control(i,j)=mean(C(i,:,j)); %Control(i,j) will represent the mean
                          %intensity from cross-section j from
                          %segment i of the control vessel
      Twist(i,j)=mean(T(i,:,j)); %Stretch(i,j) will represent the mean
                          %intensity from cross-section j from
                          %segment i of the stretch vessel
   end
end

%To get a mean intensity for each segment (sampled by 6 cross sections) the
%images from the 6 replicates are averaged.  Additionally a standard
%deviation is calculated.  This is also done for the difference and
%quotients.

for i=1:4
   Controlmean(i)=mean(Control(i,:));
   Controlstd(i)=std(Control(i,:));
   Twistmean(i)=mean(Twist(i,:));
   Twiststd(i)=std(Twist(i,:));
   %For the purposes of comparison between stretch and control a
   %difference between each twist segment and it's "paired" control
   %segment is taken.  This is valid due to the paired experimental
   %study design
   Differencemean(i)=Twistmean(i)-Controlmean(i);
   %Similarly a quotient of twist over control is made so that a
   %fold increase or decrease comparison can be made
   Foldmean(i)=Twistmean(i)/Controlmean(i);
end

%The analysis results are written to an excel spreadsheet.

Headers={'Segment','Twist','Twist STD','Ctl','Ctl STD','Diff','Fold'};
Segments=[1;2;3;4];
xlswrite('031507_Perm_Results.xls',Headers,'Sheet1','A1');
xlswrite('031507_Perm_Results.xls',Segments,'Sheet1','A2');
xlswrite('031507_Perm_Results.xls',Twistmean','Sheet1','B2');
xlswrite('031507_Perm_Results.xls',Twiststd','Sheet1','C2');
xlswrite('031507_Perm_Results.xls',Controlmean','Sheet1','D2');
xlswrite('031507_Perm_Results.xls',Controlstd','Sheet1','E2');
xlswrite('031507_Perm_Results.xls',Differencemean','Sheet1','F2');
xlswrite('031507_Perm_Results.xls',Foldmean','Sheet1','G2');
```

Matlab script for analysis of EBD dye far red intensity in the flexure experiment set:

```
%This script reads and analyzes far red fluorescence images of cross-
%sections of arterial segments perfused ex vivo with Evan's blue dye
%labeled albumin.
%J. Scott VanEpps
%March 2007

%Experiment 010407

%This program is designed for 24-bit RGB TIF files where the far red
%fluorescence is recorded in the red channel.

%The following for loop nest is designed to read each image and sum all of
%the pixel intensities for that image.  Files names of the pictures should
%comform to the following nomenclature: C#_$_&.tif for control vessel
%segments, B#B_$_&.tif for the bottom segments of the bend vessel, and
%B#T_$_&.tif for the top segments of the bend vessel
%
%     # represents the segment (i.e., the vessel is divided into 3 segments
%       from proximal to distal along the length)
%     $ represents the position the picture was taken on the vessel
%       cross-section (i.e., four pictures are taken on each cross-section
%       using a clockface as a reference the pictures are taken 3,6,9,and
%       12 o'clock
%     & represents the replicate number (i.e., for each segment represented
%       by # a total of 6 sections are imaged at four positions ($)

for i=1:3 % i is the counter for #
   for j=1:4 % j is the counter for $
      for k=1:6 % k is the counter &
         read='C#_$_&.tif'; % read is the string type variable
                     % representing the image file to be read
         read=strrep(read,'#',int2str(i));
         read=strrep(read,'$',int2str(j*3));
         read=strrep(read,'&',int2str(k));
         A=imread(read); % A is the three dimensional matrix
                     % representing the RGB tif file with the name
                     % read
         CC(i,j,k)=sum(sum(A(:,:,1))); % C is a three dimensional matrix
                              % representing the sum of all
                              % pixel intensities in the red
                              % channel of all the images for
                              % the control vessel
         read='B#B_$_&.tif'; % the above set of commands is repeated for
                     % the bottom of the bend vessel
         read=strrep(read,'#',int2str(i));
         read=strrep(read,'$',int2str(j*3));
         read=strrep(read,'&',int2str(k));
         R=imread(read);
         BB(i,j,k)=sum(sum(R(:,:,1))); % B is a three dimensional matrix
                              % representing the sum of all
                              % pixel intensities in the red
                              % channel of all the images for
                              % the bottom of the bend vessel
         read='B#T_$_&.tif'; % the above set of commands is repeated for
```

```
                    % the top of the bend vessel
        read=strrep(read,'#',int2str(i));
        read=strrep(read,'$',int2str(j*3));
        read=strrep(read,'&',int2str(k));
        D=imread(read);
        TT(i,j,k)=sum(sum(D(:,:,1))); % T is a three dimensional matrix
                                % representing the sum of all
                                % pixel intensities in the red
                                % channel of all the images for
                                % the top of the bend vessel
    end
  end
end

%To get a mean intensity for each section the images for the 4 clock-face
%positions are averaged

for i=1:3
  for j=1:6
    Control(i,j)=mean(CC(i,:,j)); %Control(i,j) will represent the mean
                                %intensity from cross-section j from
                                %segment i of the control vessel
    Bottom(i,j)=mean(BB(i,:,j));  %Bottom(i,j) will represent the mean
                                %intensity from cross-section j from
                                %segment i of the bottom of the bend
                                %vessel
    Top(i,j)=mean(TT(i,:,j));     %Top(i,j) will represent the mean
                                %intensity from cross-section j from
                                %segment i of the bottom of the bend
                                %vessel
  end
end

%To get a mean intensity for each segment (sampled by 6 cross sections) the
%images from the 6 replicates are averaged.  Additionally a standard
%deviation is calculated.  This is also done for the difference and
%quotients.

for i=1:3
  Controlmean(i)=mean(Control(i,:));
  Controlstd(i)=std(Control(i,:));
  Bottommean(i)=mean(Bottom(i,:));
  Bottomstd(i)=std(Bottom(i,:));
  Topmean(i)=mean(Top(i,:));
  Topstd(i)=std(Top(i,:));
  %For the purposes of comparison between bend (top and bottom)and
  %control a difference between each bend segment and it's "paired"
  %control segment is taken. This is valid due to the paired experimental
  %study design
  Bottomdiffmean(i)=Bottommean(i)-Controlmean(i);
  Topdiffmean(i)=Topmean(i)-Controlmean(i);
  %Similarly a quotient of bend (top and bottom) over control is made so
  %that a fold increase or decrease comparison can be made
  Bottomfoldmean(i)=Bottommean(i)/Controlmean(i);
  Topfoldmean(i)=Topmean(i)/Controlmean(i);
end
```

```
%The analysis results are written to an excel spreadsheet.

Headers={'Segment','Top','Top STD','Bottom','Bottom STD','Ctl','Ctl STD'};
Segments=[1;2;3];
xlswrite('010407_Perm_Results.xls',Headers,'Sheet1','A1');
xlswrite('010407_Perm_Results.xls',Segments,'Sheet1','A2');
xlswrite('010407_Perm_Results.xls',Topmean,'Sheet1','B2');
xlswrite('010407_Perm_Results.xls',Topstd,'Sheet1','C2');
xlswrite('010407_Perm_Results.xls',Bottommean,'Sheet1','D2');
xlswrite('010407_Perm_Results.xls',Bottomstd,'Sheet1','E2');
xlswrite('010407_Perm_Results.xls',Controlmean,'Sheet1','F2');
xlswrite('010407_Perm_Results.xls',Controlstd,'Sheet1','G2');
```

C.2 CELL COUNTING MATLAB CODE

Cell counting Matlab function:

```
function percentPositive=countcells(f)
% This function counts the total number of cells (blue) and the number of
% positive cells (red) and returns the percent of positive cells.

%J. Scott VanEpps
%February 13, 2006

%Read the image and separate the blue and the red channels
raw=imread(f);
red=raw(:,:,1);
blue=raw(:,:,3);

%Then both images (red and blue) must be thresholded and converted from
%gray scale to black and white
bluelevel=graythresh(blue);
bluethresh=im2bw(blue,bluelevel);
redlevel=graythresh(red);
redthresh=im2bw(red,0.3);

%Objects less than 50 pixels (too small to be nuclei) are removed
bluethreshminus=bwareaopen(bluethresh,50);
redthreshminus=bwareaopen(redthresh,10);

%Blue and red objects are counted
[Lcells,Ncells]=bwlabeln(bluethreshminus,8);
[Lpos,Npos]=bwlabeln(redthreshminus,8);
Percent=Npos/Ncells;

%Red objects that do not overlap blue objects are subtracted from the red
%count
sub=imsubtract(redthreshminus,bluethreshminus);
subbw=bwareaopen(im2bw(sub,graythresh(sub)),15);
[Lsub,Nsub]=bwlabeln(subbw,8);
NewNpos=Npos-Nsub;
```

```
if ((NewNpos/Ncells)<0)
   percentPositive=0;
else
   percentPositive=NewNpos/Ncells;
end
```

Matlab script for analysis of TUNEL images for the stretch experiment set:

```
%This script reads and analyzes images of cross-sections of arterial
%segments perfused ex vivo and processed for TUNEL assay.
%J. Scott VanEpps
%February 2006

%This program is designed for 24-bit RGB TIF files

%The following for loop nest is designed to read each image and return the
%percent of cells that are positive for TUNEL.  Files names of the pictures
%should comform to the following nomenclature:
%C#_$_&.tif or D#_$_&.tif
%where C or D represents Control or Deformed vessel
%     # represents the segment (i.e., the vessel is divided into 5 segments
%       from proximal to distal along the length)
%     $ represents the position the picture was taken on the vessel
%       cross-section (i.e., four pictures are taken on each cross-section
%       using a clockface as a reference the pictures are taken 3,6,9,and
%       12 o'clock
%     & represents the replicate number (i.e., for each segment represented
%       by # a total of 6 sections are imaged at four positions ($))

for i=1:5 % i is the counter for #
   for j=1:4 % j is the counter for $
      for k=1:3 % k is the counter &
         read='C#_$_&.tif'; % read is the string type variable represent
                  % ing the image file to be read
         read=strrep(read,'#',int2str(i));
         read=strrep(read,'$',int2str(j*3));
         read=strrep(read,'&',int2str(k));
         C(i,j,k)=countcells(read); % C is a three dimensional matrix
                        % representing the percent positive
                        % cells of all the images for the
                        % control vessel
         read='S#_$_&.tif'; % the above set of commands is repeated for
                  % the deformed vessel
         read=strrep(read,'#',int2str(i));
         read=strrep(read,'$',int2str(j*3));
         read=strrep(read,'&',int2str(k));
         D(i,j,k)=countcells(read);
      end
   end
end

%To get a mean percent positive cells for each section the images for the
%4 clock-face positions are averaged

for i=1:5
   for j=1:3
```

```
        Control(i,j)=mean(C(i,:,j)); %Control(i,j) will represent the mean
                                     %percent positive cells from cross-
                                     %section j from segment i of the
                                     %control vessel
        Deformed(i,j)=mean(D(i,:,j)); %Deformed(i,j) will represent the
                                      %mean percent positive cells from
                                      %cross-section j from segment i of
                                      %the stretch vessel
        %For the purposes of comparison between deformed and control a
        %difference between each deformed image and it's "paired" control
        %image is taken.  This is valid due to the paired experimental
        %study design
        Difference(i,j)=Deformed(i,j)-Control(i,j);
        %Similarly a quotient of deformed over control is made so that a
        %fold increase or decrease comparison can be made
        Fold(i,j)=Deformed(i,j)./Control(i,j);
    end
end

%To get a mean percent positive cells for each segment (sampled by 6 cross
%sections) the images from the 6 replicates are averaged.  Additionally a
%standard deviation is calculated.  This is also done for the difference
%and quotients.

for i=1:5
    Controlmean(i)=mean(Control(i,:));
    Controlstd(i)=std(Control(i,:));
    Deformedmean(i)=mean(Deformed(i,:));
    Deformedstd(i)=std(Deformed(i,:));
    Differencemean(i)=mean(Difference(i,:));
    Differencestd(i)=std(Difference(i,:));
    Foldmean(i)=mean(Fold(i,:));
    Foldstd(i)=std(Fold(i,:));
end

%The analysis results are written to an excel spreadsheet.

Headers={'Segment','Str','Str STD','Ctl','Ctl STD','Diff','Fold'};
Segments=[1;2;3;4;5];
xlswrite('091406_TUNEL_Results.xls',Headers,'Sheet1','A1');
xlswrite('091406_TUNEL_Results.xls',Segments,'Sheet1','A2');
xlswrite('091406_TUNEL_Results.xls',Deformedmean','Sheet1','B2');
xlswrite('091406_TUNEL_Results.xls',Deformedstd','Sheet1','C2');
xlswrite('091406_TUNEL_Results.xls',Controlmean','Sheet1','D2');
xlswrite('091406_TUNEL_Results.xls',Controlstd','Sheet1','E2');
xlswrite('091406_TUNEL_Results.xls',Differencemean','Sheet1','F2');
xlswrite('091406_TUNEL_Results.xls',Foldmean','Sheet1','G2');
```

Matlab script for analysis of TUNEL images for the twist experiment set:

```
%This script reads and analyzes images of cross-sections of arterial
%segments perfused ex vivo and processed for TUNEL assay.
%J. Scott VanEpps
%February 2006

%This program is designed for 24-bit RGB TIF files
```

```
%The following for loop nest is designed to read each image and return the
%percent of cells that are positive for TUNEL.  Files names of the pictures
%should comform to the following nomenclature:
%C#_$_&.tif or T#_$_&.tif
%where C or T represents Control or Twist vessel
%     # represents the segment (i.e., the vessel is divided into 5 segments
%       from proximal to distal along the length)
%     $ represents the position the picture was taken on the vessel
%       cross-section (i.e., four pictures are taken on each cross-section
%       using a clockface as a reference the pictures are taken 3,6,9,and
%       12 o'clock
%     & represents the replicate number (i.e., for each segment represented
%       by # a total of 6 sections are imaged at four positions ($))

for i=1:4 % i is the counter for #
   for j=1:4 % j is the counter for $
      for k=1:3 % k is the counter &
         read='C#_$_&.tif'; % read is the string type variable represent
                    % ing the image file to be read
         read=strrep(read,'#',int2str(i));
         read=strrep(read,'$',int2str(j*3));
         read=strrep(read,'&',int2str(k));
         C(i,j,k)=countcells(read); % C is a three dimensional matrix
                          % representing the percent positive
                          % cells of all the images for the
                          % control vessel
         read='T#_$_&.tif'; % the above set of commands is repeated for
                    % the twist vessel
         read=strrep(read,'#',int2str(i));
         read=strrep(read,'$',int2str(j*3));
         read=strrep(read,'&',int2str(k));
         D(i,j,k)=countcells(read);
      end
   end
end

%To get a mean percent positive cells for each section the images for the
%4 clock-face positions are averaged

for i=1:4
   for j=1:3
      Control(i,j)=mean(C(i,:,j)); %Control(i,j) will represent the mean
                          %percent positive cells from cross-
                          %section j from segment i of the
                          %control vessel
      Deformed(i,j)=mean(D(i,:,j)); %Deformed(i,j) will represent the
                          %mean percent positive cells from
                          %cross-section j from segment i of
                          %the twist vessel
      %For the purposes of comparison between deformed and control a
      %difference between each deformed image and it's "paired" control
      %image is taken.  This is valid due to the paired experimental
      %study design
      Difference(i,j)=Deformed(i,j)-Control(i,j);
      %Similarly a quotient of deformed over control is made so that a
      %fold increase or decrease comparison can be made
```

```
      Fold(i,j)=Deformed(i,j)./Control(i,j);
   end
end

%To get a mean percent positive cells for each segment (sampled by 6 cross
%sections) the images from the 6 replicates are averaged.  Additionally a
%standard deviation is calculated.  This is also done for the difference
%and quotients.

for i=1:4
   Controlmean(i)=mean(Control(i,:));
   Controlstd(i)=std(Control(i,:));
   Deformedmean(i)=mean(Deformed(i,:));
   Deformedstd(i)=std(Deformed(i,:));
   Differencemean(i)=mean(Difference(i,:));
   Differencestd(i)=std(Difference(i,:));
   Foldmean(i)=mean(Fold(i,:));
   Foldstd(i)=std(Fold(i,:));
end

%The analysis results are written to an excel spreadsheet.

Headers={'Segment','Twist','Twist STD','Ctl','Ctl STD','Diff','Fold'};
Segments=[1;2;3;4];
xlswrite('031507_TUNEL_Results.xls',Headers,'Sheet1','A1');
xlswrite('031507_TUNEL_Results.xls',Segments,'Sheet1','A2');
xlswrite('031507_TUNEL_Results.xls',Deformedmean','Sheet1','B2');
xlswrite('031507_TUNEL_Results.xls',Deformedstd','Sheet1','C2');
xlswrite('031507_TUNEL_Results.xls',Controlmean','Sheet1','D2');
xlswrite('031507_TUNEL_Results.xls',Controlstd','Sheet1','E2');
xlswrite('031507_TUNEL_Results.xls',Differencemean','Sheet1','F2');
xlswrite('031507_TUNEL_Results.xls',Foldmean','Sheet1','G2');
```

Matlab script for analysis of TUNEL images for the twist experiment set:

```
%This script reads and analyzes far red fluorescence images of cross-
%sections of arterial segments perfused ex vivo with Evan's blue dye
%labeled albumin.
%J. Scott VanEpps
%March 2007

%Experiment 030707

%This program is designed for 24-bit RGB TIF files where the far red
%fluorescence is recorded in the red channel.

%The following for loop nest is designed to read each image and sum all of
%the pixel intensities for that image.  Files names of the pictures should
%comform to the following nomenclature: C#_$_&.tif for control vessel
%segments, B#B_$_&.tif for the bottom segments of the bend vessel, and
%B#T_$_&.tif for the top segments of the bend vessel
%
%     # represents the segment (i.e., the vessel is divided into 3 segments
%       from proximal to distal along the length)
%     $ represents the position the picture was taken on the vessel
```

```
%       cross-section (i.e., four pictures are taken on each cross-section
%       using a clockface as a reference the pictures are taken 3,6,9,and
%       12 o'clock
%     & represents the replicate number (i.e., for each segment represented
%       by # a total of 6 sections are imaged at four positions ($)

for i=1:3 % i is the counter for #
   for j=1:4 % j is the counter for $
      for k=1:3 % k is the counter &
         read='C#_$_&.tif'; % read is the string type variable
                  % representing the image file to be read
         read=strrep(read,'#',int2str(i));
         read=strrep(read,'$',int2str(j*3));
         read=strrep(read,'&',int2str(k));
         CC(i,j,k)=countcells(read); % C is a three dimensional matrix
                           % representing the sum of all
                           % pixel intensities in the red
                           % channel of all the images for
                           % the control vessel
         read='B#B_$_&.tif'; % the above set of commands is repeated for
                  % the bottom of the bend vessel
         read=strrep(read,'#',int2str(i));
         read=strrep(read,'$',int2str(j*3));
         read=strrep(read,'&',int2str(k));
         BB(i,j,k)=countcells(read); % B is a three dimensional matrix
                           % representing the sum of all
                           % pixel intensities in the red
                           % channel of all the images for
                           % the bottom of the bend vessel
         read='B#T_$_&.tif'; % the above set of commands is repeated for
                  % the top of the bend vessel
         read=strrep(read,'#',int2str(i));
         read=strrep(read,'$',int2str(j*3));
         read=strrep(read,'&',int2str(k));
         TT(i,j,k)=countcells(read); % T is a three dimensional matrix
                           % representing the sum of all
                           % pixel intensities in the red
                           % channel of all the images for
                           % the top of the bend vessel
      end
   end
end

%To get a mean intensity for each section the images for the 4 clock-face
%positions are averaged

for i=1:3
   for j=1:3
      Control(i,j)=mean(CC(i,:,j)); %Control(i,j) will represent the mean
                           %intensity from cross-section j from
                           %segment i of the control vessel
      Bottom(i,j)=mean(BB(i,:,j));  %Bottom(i,j) will represent the mean
                           %intensity from cross-section j from
                           %segment i of the bottom of the bend
                           %vessel
      Top(i,j)=mean(TT(i,:,j));     %Top(i,j) will represent the mean
                           %intensity from cross-section j from
```

```
                        %segment i of the bottom of the bend
                        %vessel
    end
end

%To get a mean intensity for each segment (sampled by 6 cross sections) the
%images from the 6 replicates are averaged.  Additionally a standard
%deviation is calculated.  This is also done for the difference and
%quotients.

for i=1:3
    Controlmean(i)=mean(Control(i,:));
    Controlstd(i)=std(Control(i,:));
    Bottommean(i)=mean(Bottom(i,:));
    Bottomstd(i)=std(Bottom(i,:));
    Topmean(i)=mean(Top(i,:));
    Topstd(i)=std(Top(i,:));
    %For the purposes of comparison between bend (top and bottom)and
    %control a difference between each bend segment and it's "paired"
    %control segment is taken. This is valid due to the paired experimental
    %study design
    Bottomdiffmean(i)=Bottommean(i)-Controlmean(i);
    Topdiffmean(i)=Topmean(i)-Controlmean(i);
    %Similarly a quotient of bend (top and bottom) over control is made so
    %that a fold increase or decrease comparison can be made
    Bottomfoldmean(i)=Bottommean(i)/Controlmean(i);
    Topfoldmean(i)=Topmean(i)/Controlmean(i);
end

%The analysis results are written to an excel spreadsheet.

Headers={'Segment','Top','Top STD','Bottom','Bottom STD','Ctl','Ctl STD'};
Segments=[1;2;3];
xlswrite('030707_Perm_Results.xls',Headers,'Sheet1','A1');
xlswrite('030707_Perm_Results.xls',Segments,'Sheet1','A2');
xlswrite('030707_Perm_Results.xls',Topmean','Sheet1','B2');
xlswrite('030707_Perm_Results.xls',Topstd','Sheet1','C2');
xlswrite('030707_Perm_Results.xls',Bottommean','Sheet1','D2');
xlswrite('030707_Perm_Results.xls',Bottomstd','Sheet1','E2');
xlswrite('030707_Perm_Results.xls',Controlmean','Sheet1','F2');
xlswrite('030707_Perm_Results.xls',Controlstd','Sheet1','G2');
```

APPENDIX D

APPENDIX D: DEVELOPMENT OF UMAT FILE FOR ABAQUS

Mathematica v5 was used to determine functions for the individual Cauchy stress tensor components from the deformation gradient components and the strain energy function as well as the Jacobian matrix for the UMAT files. An example of one of those worksheets is shown below. Input commands are given in normal or bold text, output responses from the Mathematica kernel are shown with a green highlight.

```
F = {{F11, 0, 0}, {0, F22, F23}, {0, 0, F33}};
DW = {{DWrr, DWrθ, DWrz}, {0, DWθθ, DWθz}, {0, DWθz, DWzz}};
MatrixForm[Transpose[F].F]
```

$$\begin{pmatrix} F11^2 & 0 & 0 \\ 0 & F22^2 & F22\ F23 \\ 0 & F22\ F23 & F23^2 + F33^2 \end{pmatrix}$$

```
σ=MatrixForm[F.DW.Transpose[F]]
```

$$\begin{pmatrix} DWrr\ F11^2 & DWr\theta\ F11\ F22 + DWrz\ F11\ F23 & DWrz\ F11\ F33 \\ 0 & F23\ (DW\theta z\ F22 + DWzz\ F23) + F22\ (DW\theta\theta\ F22 + DW\theta z\ F23) & (DW\theta z\ F22 + DWzz\ F23)\ F33 \\ 0 & DW\theta z\ F22\ F33 + DWzz\ F23\ F33 & DWzz\ F33^2 \end{pmatrix}$$

```
Q = e^(c1*Er^2+c2*Eq^2+c3*Ez^2+2*(c4*Eq*Er+c5*Eq*Ez+c6*Ez*Er
      +c7*Erz^2+c8*Eqz^2+c9*Eqr^2));
σr=c0*(1+2*Er)*(c1*Er+c6*Ez+c4*Eq)*Q;
```

$$\partial_{Er}\,\sigma r\ //.\ \left\{e^{c2\,Eq^2+c1\,Er^2+c3\,Ez^2+2\,(c9\,Eqr^2+c8\,Eqz^2+c4\,Eq\,Er+c7\,Erz^2+c5\,Eq\,Ez+c6\,Er\,Ez)}\to M,\right.$$
$$(c4*Er+C5*Ez+C2*Eq)\to DWq,\ (c6*Er+C3*Ez+C5*Eq)\to DWz,$$
$$(2\,c1\,Er+2\,(c4\,Eq+c6\,Ez))\to 2*DWr,\ (2\,c2\,Eq+2\,(c4\,Er+c5\,Ez))\to 2*DWq,$$
$$\left.(2\,(c5\,Eq+c6\,Er)+2\,c3\,Ez)\to 2*DWz,\ (c4\,Eq+c1\,Er+c6\,Ez)\to DWr\right\}$$

$$2\,c0\,DWr\,M+c0\,c1\,(1+2\,Er)\,M+2\,c0\,DWr^2\,(1+2\,Er)\,M$$

$$\partial_{Eq}\,\sigma r\ //.\ \left\{e^{c2\,Eq^2+c1\,Er^2+c3\,Ez^2+2\,(c9\,Eqr^2+c8\,Eqz^2+c4\,Eq\,Er+c7\,Erz^2+c5\,Eq\,Ez+c6\,Er\,Ez)}\to M,\right.$$
$$(c4*Er+C5*Ez+C2*Eq)\to DWq,\ (c6*Er+C3*Ez+C5*Eq)\to DWz,$$
$$(2\,c1\,Er+2\,(c4\,Eq+c6\,Ez))\to 2*DWr,\ (2\,c2\,Eq+2\,(c4\,Er+c5\,Ez))\to 2*DWq,$$
$$\left.(2\,(c5\,Eq+c6\,Er)+2\,c3\,Ez)\to 2*DWz,\ (c4\,Eq+c1\,Er+c6\,Ez)\to DWr\right\}$$

$$c0\ c4\ (1+2\ Er)\ M+2\ c0\ DWq\ DWr\ (1+2\ Er)\ M$$

$$\partial_{Ez}\,\sigma r\ //.\ \left\{e^{c2\,Eq^2+c1\,Er^2+c3\,Ez^2+2\,(c9\,Eqr^2+c8\,Eqz^2+c4\,Eq\,Er+c7\,Erz^2+c5\,Eq\,Ez+c6\,Er\,Ez)}\to M,\right.$$
$$(c4*Er+C5*Ez+C2*Eq)\to DWq,\ (c6*Er+C3*Ez+C5*Eq)\to DWz,$$
$$(2\,c1\,Er+2\,(c4\,Eq+c6\,Ez))\to 2*DWr,\ (2\,c2\,Eq+2\,(c4\,Er+c5\,Ez))\to 2*DWq,$$
$$\left.(2\,(c5\,Eq+c6\,Er)+2\,c3\,Ez)\to 2*DWz,\ (c4\,Eq+c1\,Er+c6\,Ez)\to DWr\right\}$$

$$c0\ c6\ (1+2\ Er)\ M+2\ c0\ DWr\ DWz\ (1+2\ Er)\ M$$

$$\partial_{Eqz}\,\sigma r\ //.\ \left\{e^{c2\,Eq^2+c1\,Er^2+c3\,Ez^2+2\,(c9\,Eqr^2+c8\,Eqz^2+c4\,Eq\,Er+c7\,Erz^2+c5\,Eq\,Ez+c6\,Er\,Ez)}\to M,\right.$$
$$(c4*Er+C5*Ez+C2*Eq)\to DWq,\ (c6*Er+C3*Ez+C5*Eq)\to DWz,$$
$$(2\,c1\,Er+2\,(c4\,Eq+c6\,Ez))\to 2*DWr,\ (2\,c2\,Eq+2\,(c4\,Er+c5\,Ez))\to 2*DWq,$$
$$\left.(2\,(c5\,Eq+c6\,Er)+2\,c3\,Ez)\to 2*DWz,\ (c4\,Eq+c1\,Er+c6\,Ez)\to DWr\right\}$$

$$4\ c0\ c8\ DWr\ Eqz\ (1+2\ Er)\ M$$

$$\sigma\theta = c0*(1+2*Eq)*(c4*Er+c5*Ez+c2*Eq)*Q+8*Eqz*c0*c8*Eqz*Q+\left(\frac{4*Eqz^2}{1+2*Eq}\right)*c0*(c6*Er+c3*Ez+c5*Eq)*Q;$$

$$\sigma\theta\ //.\ \left\{e^{c2\,Eq^2+c1\,Er^2+c3\,Ez^2+2\,(c9\,Eqr^2+c8\,Eqz^2+c4\,Eq\,Er+c7\,Erz^2+c5\,Eq\,Ez+c6\,Er\,Ez)}\to M,\right.$$
$$(c4*Er+c5*Ez+c2*Eq)\to DWq,\ (c6*Er+c3*Ez+c5*Eq)\to DWz,$$
$$\left.(2\,c1\,Er+2\,(c4\,Eq+c6\,Ez))\to 2\,DWr,\ \left(\frac{4*Eqz^2}{1+2*Eq}\right)\to F23^2\right\}$$

$$c0\,DWq\,(1+2\,Eq)\,M+8\,c0\,c8\,Eqz^2\,M+c0\,DWz\,F23^2\,M$$

$$\partial_{Er}\,\sigma\theta\ //.\ \left\{e^{c2\,Eq^2+c1\,Er^2+c3\,Ez^2+2\,(c9\,Eqr^2+c8\,Eqz^2+c4\,Eq\,Er+c7\,Erz^2+c5\,Eq\,Ez+c6\,Er\,Ez)}\to M,\right.$$
$$(c4*Er+c5*Ez+c2*Eq)\to DWq,\ (c6*Er+c3*Ez+c5*Eq)\to DWz,$$
$$\left.(2\,c1\,Er+2\,(c4\,Eq+c6\,Ez))\to 2\,DWr\right\}$$

$$c0\,c4\,(1+2\,Eq)\,M+2\,c0\,DWq\,DWr\,(1+2\,Eq)\,M+16\,c0\,c8\,DWr\,Eqz^2\,M+\frac{4\,c0\,c6\,Eqz^2\,M}{1+2\,Eq}+\frac{8\,c0\,DWr\,DWz\,Eqz^2\,M}{1+2\,Eq}$$

$$\partial_{Eq}\,\sigma\theta\ //.\ \left\{e^{c2\,Eq^2+c1\,Er^2+c3\,Ez^2+2\,(c9\,Eqr^2+c8\,Eqz^2+c4\,Eq\,Er+c7\,Erz^2+c5\,Eq\,Ez+c6\,Er\,Ez)}\to M,\right.$$
$$(c4*Er+c5*Ez+c2*Eq)\to DWq,\ (c6*Er+c3*Ez+c5*Eq)\to DWz,$$
$$\left.(2\,c1\,Er+2\,(c4\,Eq+c6\,Ez))\to 2*DWr,\ (2\,c2\,Eq+2\,(c4\,Er+c5\,Ez))\to 2*DWq\right\}$$

$$2\,c0\,DWq\,M+c0\,c2\,(1+2\,Eq)\,M+2\,c0\,DWq^2\,(1+2\,Eq)\,M+8\,c0\,c8\,DWq\,Eqz^2\,M-\frac{8\,c0\,DWz\,Eqz^2\,M}{(1+2\,Eq)^2}+\frac{4\,c0\,c5\,Eqz^2\,M}{1+2\,Eq}+\frac{8\,c0\,DWq\,DWz\,Eqz^2\,M}{1+2\,Eq}$$

$$\partial_{Ez}\ \sigma\theta\ //.\ \left\{e^{c2\,Eq^2+c1\,Er^2+c3\,Ez^2+2\,(c9\,Eqr^2+c8\,Eqz^2+c4\,Eq\,Er+c7\,Erz^2+c5\,Eq\,Ez+c6\,Er\,Ez)}\to M,\right.$$
$$(c4*Er+c5*Ez+c2*Eq)\to DWq,\ (c6*Er+c3*Ez+c5*Eq)\to DWz,$$
$$(2\,c1\,Er+2\,(c4\,Eq+c6\,Ez))\to 2*DWr,\ (2\,c2\,Eq+2\,(c4\,Er+c5\,Ez))\to 2*DWq,$$
$$\left.(2\,(c5\,Eq+c6\,Er)+2\,c3\,Ez)\to 2*DWz\right\}$$

$$c0\ c5\ (1+2\,Eq)\ M+2\,c0\ DWq\ DWz\ (1+2\,Eq)\ M+$$
$$8\,c0\ c8\ DWz\ Eqz^2\ M+\frac{4\,c0\ c3\ Eqz^2\ M}{1+2\,Eq}+\frac{8\,c0\ DWz^2\ Eqz^2\ M}{1+2\,Eq}$$

$$\partial_{Eqz}\ \sigma\theta\ //.\ \left\{e^{c2\,Eq^2+c1\,Er^2+c3\,Ez^2+2\,(c9\,Eqr^2+c8\,Eqz^2+c4\,Eq\,Er+c7\,Erz^2+c5\,Eq\,Ez+c6\,Er\,Ez)}\to M,\right.$$
$$(c4*Er+c5*Ez+c2*Eq)\to DWq,\ (c6*Er+c3*Ez+c5*Eq)\to DWz,$$
$$(2\,c1\,Er+2\,(c4\,Eq+c6\,Ez))\to 2*DWr,\ (2\,c2\,Eq+2\,(c4\,Er+c5\,Ez))\to 2*DWq,$$
$$\left.(2\,(c5\,Eq+c6\,Er)+2\,c3\,Ez)\to 2*DWz\right\}$$

$$8\,c0\,c8\,Eqz\ M+\frac{8\,c0\,DWz\,Eqz\,M}{1+2\,Eq}+$$
$$4\,c0\,c8\,DWq\ (1+2\,Eq)\,Eqz\ M+16\,c0\,c8^2\,Eqz^3\,M+\frac{16\,c0\,c8\,DWz\,Eqz^3\,M}{1+2\,Eq}$$

$$\sigma z=c0*(1+2*Ez)*(c6*Er+c3*Ez+c5*Eq)*Q;$$

$$\partial_{Er}\ \sigma z\ //.\ \left\{e^{c2\,Eq^2+c1\,Er^2+c3\,Ez^2+2\,(c9\,Eqr^2+c8\,Eqz^2+c4\,Eq\,Er+c7\,Erz^2+c5\,Eq\,Ez+c6\,Er\,Ez)}\to M,\right.$$
$$(c4*Er+C5*Ez+C2*Eq)\to DWq,\ (c6*Er+C3*Ez+C5*Eq)\to DWz,$$
$$(2\,c1\,Er+2\,(c4\,Eq+c6\,Ez))\to 2*DWr,\ (2\,c2\,Eq+2\,(c4\,Er+c5\,Ez))\to 2*DWq,$$
$$(2\,(c5\,Eq+c6\,Er)+2\,c3\,Ez)\to 2*DWz,\ (c4\,Eq+c1\,Er+c6\,Ez)\to DWr,$$
$$\left.(c5\,Eq+c6\,Er+c3\,Ez)\to DWz\right\}$$

$$c0\ c6\ (1+2\ Ez)\ M+2\ c0\ DWr\ DWz\ (1+2\ Ez)\ M$$

$$\partial_{Eq}\ \sigma z\ //.\ \left\{e^{c2\,Eq^2+c1\,Er^2+c3\,Ez^2+2\,(c9\,Eqr^2+c8\,Eqz^2+c4\,Eq\,Er+c7\,Erz^2+c5\,Eq\,Ez+c6\,Er\,Ez)}\to M,\right.$$
$$(c4*Er+C5*Ez+C2*Eq)\to DWq,\ (c6*Er+C3*Ez+C5*Eq)\to DWz,$$
$$(2\,c1\,Er+2\,(c4\,Eq+c6\,Ez))\to 2*DWr,\ (2\,c2\,Eq+2\,(c4\,Er+c5\,Ez))\to 2*DWq,$$
$$(2\,(c5\,Eq+c6\,Er)+2\,c3\,Ez)\to 2*DWz,\ (c4\,Eq+c1\,Er+c6\,Ez)\to DWr,$$
$$\left.(c5\,Eq+c6\,Er+c3\,Ez)\to DWz\right\}$$

$$c0\ c5\ (1+2\ Ez)\ M+2\ c0\ DWq\ DWz\ (1+2\ Ez)\ M$$

$$\partial_{Ez}\ \sigma z\ //.\ \left\{e^{c2\,Eq^2+c1\,Er^2+c3\,Ez^2+2\,(c9\,Eqr^2+c8\,Eqz^2+c4\,Eq\,Er+c7\,Erz^2+c5\,Eq\,Ez+c6\,Er\,Ez)}\to M,\right.$$
$$(c4*Er+C5*Ez+C2*Eq)\to DWq,\ (c6*Er+C3*Ez+C5*Eq)\to DWz,$$
$$(2\,c1\,Er+2\,(c4\,Eq+c6\,Ez))\to 2*DWr,\ (2\,c2\,Eq+2\,(c4\,Er+c5\,Ez))\to 2*DWq,$$
$$(2\,(c5\,Eq+c6\,Er)+2\,c3\,Ez)\to 2*DWz,\ (c4\,Eq+c1\,Er+c6\,Ez)\to DWr,$$
$$\left.(c5\,Eq+c6\,Er+c3\,Ez)\to DWz\right\}$$

$$2\,c0\,DWz\ M+c0\,c3\ (1+2\,Ez)\ M+2\,c0\,DWz^2\ (1+2\,Ez)\ M$$

$$\partial_{Eqz}\ \sigma z\ //.\ \left\{e^{c2\,Eq^2+c1\,Er^2+c3\,Ez^2+2\,(c9\,Eqr^2+c8\,Eqz^2+c4\,Eq\,Er+c7\,Erz^2+c5\,Eq\,Ez+c6\,Er\,Ez)}\to M,\right.$$
$$(c4*Er+C5*Ez+C2*Eq)\to DWq,\ (c6*Er+C3*Ez+C5*Eq)\to DWz,$$
$$(2\,c1\,Er+2\,(c4\,Eq+c6\,Ez))\to 2*DWr,\ (2\,c2\,Eq+2\,(c4\,Er+c5\,Ez))\to 2*DWq,$$
$$(2\,(c5\,Eq+c6\,Er)+2\,c3\,Ez)\to 2*DWz,\ (c4\,Eq+c1\,Er+c6\,Ez)\to DWr,$$
$$\left.(c5\,Eq+c6\,Er+c3\,Ez)\to DWz\right\}$$

$$4\ c0\ c8\ DWz\ Eqz\ (1+2\ Ez)\ M$$

$$\sigma rz=2*c0*c7*\sqrt{(1+2*Er)}\ \sqrt{(1+2*Ez)-\left(\frac{4*Eqz^2}{1+2*Eq}\right)}\ Erz*Q;$$

```
σrz //. {e^(c2 Eq^2+c1 Er^2+c3 Ez^2+2 (c9 Eqr^2+c8 Eqz^2+c4 Eq Er+c7 Erz^2+c5 Eq Ez+c6 Er Ez)) → M,
   (c4 * Er + C5 * Ez + C2 * Eq) → DWq, (c6 * Er + C3 * Ez + C5 * Eq) → DWz,
   (2 c1 Er + 2 (c4 Eq + c6 Ez)) → 2 * DWr, (2 c2 Eq + 2 (c4 Er + c5 Ez)) → 2 * DWq,
   (2 (c5 Eq + c6 Er) + 2 c3 Ez) → 2 * DWz, (c4 Eq + c1 Er + c6 Ez) → DWr,
   (c5 Eq + c6 Er + c3 Ez) → DWz, √(1 + 2 * Er) → F11, √((1 + 2 * Ez) - (4 * Eqz^2)/(1 + 2 * Eq)) → F33}
```

```
2 c0 c7 Erz F11 F33 M
```

```
∂Erz σrz //. {e^(c2 Eq^2+c1 Er^2+c3 Ez^2+2 (c9 Eqr^2+c8 Eqz^2+c4 Eq Er+c7 Erz^2+c5 Eq Ez+c6 Er Ez)) → M,
   (c4 * Er + C5 * Ez + C2 * Eq) → DWq, (c6 * Er + C3 * Ez + C5 * Eq) → DWz,
   (2 c1 Er + 2 (c4 Eq + c6 Ez)) → 2 * DWr, (2 c2 Eq + 2 (c4 Er + c5 Ez)) → 2 * DWq,
   (2 (c5 Eq + c6 Er) + 2 c3 Ez) → 2 * DWz, (c4 Eq + c1 Er + c6 Ez) → DWr,
   (c5 Eq + c6 Er + c3 Ez) → DWz, √(1 + 2 * Er) → F11, √((1 + 2 * Ez) - (4 * Eqz^2)/(1 + 2 * Eq)) → F33}
```

```
2 c0 c7 F11 F33 M + 8 c0 c7^2 Erz^2 F11 F33 M
```

```
σqr = 2 * c0 * c9 * √((1 + 2 * Eq) * (1 + 2 * Er)) Eqr * Q +
   2 * c0 * c7 √(1 + 2 * Er) (2 Eqz)/√(1 + 2 * Eq) Erz * Q;
```

```
σqr //. {e^(c2 Eq^2+c1 Er^2+c3 Ez^2+2 (c9 Eqr^2+c8 Eqz^2+c4 Eq Er+c7 Erz^2+c5 Eq Ez+c6 Er Ez)) → M,
   (c4 * Er + C5 * Ez + C2 * Eq) → DWq, (c6 * Er + C3 * Ez + C5 * Eq) → DWz,
   (2 c1 Er + 2 (c4 Eq + c6 Ez)) → 2 * DWr, (2 c2 Eq + 2 (c4 Er + c5 Ez)) → 2 * DWq,
   (2 (c5 Eq + c6 Er) + 2 c3 Ez) → 2 * DWz, (c4 Eq + c1 Er + c6 Ez) → DWr,
   (c5 Eq + c6 Er + c3 Ez) → DWz, √(1 + 2 Er)/√(1 + 2 Eq) → F11/F22, √((1 + 2 Eq) (1 + 2 Er)) → F11 * F22}
```

```
(4 c0 c7 Eqz Erz F11 M)/F22 + 2 c0 c9 Eqr F11 F22 M
```

```
∂Eqr σqr //. {e^(c2 Eq^2+c1 Er^2+c3 Ez^2+2 (c9 Eqr^2+c8 Eqz^2+c4 Eq Er+c7 Erz^2+c5 Eq Ez+c6 Er Ez)) → M,
   (c4 * Er + C5 * Ez + C2 * Eq) → DWq, (c6 * Er + C3 * Ez + C5 * Eq) → DWz,
   (2 c1 Er + 2 (c4 Eq + c6 Ez)) → 2 * DWr, (2 c2 Eq + 2 (c4 Er + c5 Ez)) → 2 * DWq,
   (2 (c5 Eq + c6 Er) + 2 c3 Ez) → 2 * DWz, (c4 Eq + c1 Er + c6 Ez) → DWr,
   (c5 Eq + c6 Er + c3 Ez) → DWz, √(1 + 2 Er)/√(1 + 2 Eq) → F11/F22, √((1 + 2 Eq) (1 + 2 Er)) → F11 * F22}
```

```
(16 c0 c7 c9 Eqr Eqz Erz F11 M)/F22 + 2 c0 c9 F11 F22 M + 8 c0 c9^2 Eqr^2 F11 F22 M
```

```
σqz = 2 * c0 * c8 √(1 + 2 * Eq) √((1 + 2 * Ez) - (4 * Eqz^2)/(1 + 2 * Eq)) Eqz * Q +
   c0 * (2 * Eqz)/√(1 + 2 * Eq) √((1 + 2 * Ez) - (4 * Eqz^2)/(1 + 2 * Eq)) * (c6 * Er + c3 * Ez + c5 * Eq) * Q;
```

$$\sigma qz \;//.\; \left\{ e^{c2\,Eq^2+c1\,Er^2+c3\,Ez^2+2\,(c9\,Eqr^2+c8\,Eqz^2+c4\,Eq\,Er+c7\,Erz^2+c5\,Eq\,Ez+c6\,Er\,Ez)} \to M,\right.$$
$$(c4*Er+C5*Ez+C2*Eq)\to DWq,\ (c6*Er+C3*Ez+C5*Eq)\to DWz,$$
$$(2\,c1\,Er+2\,(c4\,Eq+c6\,Ez))\to 2*DWr,\ (2\,c2\,Eq+2\,(c4\,Er+c5\,Ez))\to 2*DWq,$$
$$(2\,(c5\,Eq+c6\,Er)+2\,c3\,Ez)\to 2*DWz,\ (c4\,Eq+c1\,Er+c6\,Ez)\to DWr,$$
$$(c5\,Eq+c6\,Er+c3\,Ez)\to DWz,\ \sqrt{1-\frac{4\,Eqz^2}{1+2\,Eq}+2\,Ez}\to F33,\ \sqrt{1+2\,Eq}\to F22,$$
$$\left.\frac{1}{\sqrt{1+2\,Eq}}\to\frac{1}{F22},\ \frac{1}{\sqrt{1-\frac{4\,Eqz^2}{1+2\,Eq}+2\,Ez}}\to\frac{1}{F33},\ \frac{1}{(1+2\,Eq)^{3/2}}\to\frac{1}{F22^3}\right\}$$

$$\frac{2\,c0\,DWz\,Eqz\,F33\,M}{F22}+2\,c0\,c8\,Eqz\,F22\,F33\,M$$

$$\partial_{Er}\,\sigma qz \;//.\; \left\{ e^{c2\,Eq^2+c1\,Er^2+c3\,Ez^2+2\,(c9\,Eqr^2+c8\,Eqz^2+c4\,Eq\,Er+c7\,Erz^2+c5\,Eq\,Ez+c6\,Er\,Ez)} \to M,\right.$$
$$(c4*Er+C5*Ez+C2*Eq)\to DWq,\ (c6*Er+C3*Ez+C5*Eq)\to DWz,$$
$$(2\,c1\,Er+2\,(c4\,Eq+c6\,Ez))\to 2*DWr,\ (2\,c2\,Eq+2\,(c4\,Er+c5\,Ez))\to 2*DWq,$$
$$(2\,(c5\,Eq+c6\,Er)+2\,c3\,Ez)\to 2*DWz,\ (c4\,Eq+c1\,Er+c6\,Ez)\to DWr,$$
$$(c5\,Eq+c6\,Er+c3\,Ez)\to DWz,\ \sqrt{1-\frac{4\,Eqz^2}{1+2\,Eq}+2\,Ez}\to F33,\ \sqrt{1+2\,Eq}\to F22,$$
$$\left.\frac{1}{\sqrt{1+2\,Eq}}\to\frac{1}{F22},\ \frac{1}{\sqrt{1-\frac{4\,Eqz^2}{1+2\,Eq}+2\,Ez}}\to\frac{1}{F33},\ \frac{1}{(1+2\,Eq)^{3/2}}\to\frac{1}{F22^3}\right\}$$

$$\frac{2\,c0\,c6\,Eqz\,F33\,M}{F22}+\frac{4\,c0\,DWr\,DWz\,Eqz\,F33\,M}{F22}+4\,c0\,c8\,DWr\,Eqz\,F22\,F33\,M$$

$$\partial_{Eq}\,\sigma qz \;//.\; \left\{ e^{c2\,Eq^2+c1\,Er^2+c3\,Ez^2+2\,(c9\,Eqr^2+c8\,Eqz^2+c4\,Eq\,Er+c7\,Erz^2+c5\,Eq\,Ez+c6\,Er\,Ez)} \to M,\right.$$
$$(c4*Er+C5*Ez+C2*Eq)\to DWq,\ (c6*Er+C3*Ez+C5*Eq)\to DWz,$$
$$(2\,c1\,Er+2\,(c4\,Eq+c6\,Ez))\to 2*DWr,\ (2\,c2\,Eq+2\,(c4\,Er+c5\,Ez))\to 2*DWq,$$
$$(2\,(c5\,Eq+c6\,Er)+2\,c3\,Ez)\to 2*DWz,\ (c4\,Eq+c1\,Er+c6\,Ez)\to DWr,$$
$$(c5\,Eq+c6\,Er+c3\,Ez)\to DWz,\ \sqrt{1-\frac{4\,Eqz^2}{1+2\,Eq}+2\,Ez}\to F33,\ \sqrt{1+2\,Eq}\to F22,$$
$$\frac{1}{\sqrt{1+2\,Eq}}\to\frac{1}{F22},\ \frac{1}{\sqrt{1-\frac{4\,Eqz^2}{1+2\,Eq}+2\,Ez}}\to\frac{1}{F33},\ \frac{1}{(1+2\,Eq)^{3/2}}\to\frac{1}{F22^3},$$
$$\left.\frac{1}{(1+2\,Eq)^{5/2}}\to\frac{1}{F22^5}\right\}$$

$$\frac{8\,c0\,DWz\,Eqz^3\,M}{F22^5\,F33}+\frac{8\,c0\,c8\,Eqz^3\,M}{F22^3\,F33}-\frac{2\,c0\,DWz\,Eqz\,F33\,M}{F22^3}+\frac{2\,c0\,c5\,Eqz\,F33\,M}{F22}+$$
$$\frac{2\,c0\,c8\,Eqz\,F33\,M}{F22}+\frac{4\,c0\,DWq\,DWz\,Eqz\,F33\,M}{F22}+4\,c0\,c8\,DWq\,Eqz\,F22\,F33\,M$$

$$\partial_{Ez}\,\sigma qz\ //.\ \left\{e^{c2\,Eq^2+c1\,Er^2+c3\,Ez^2+2\,(c9\,Eqr^2+c8\,Eqz^2+c4\,Eq\,Er+c7\,Erz^2+c5\,Eq\,Ez+c6\,Er\,Ez)}\to M,\right.$$
$$(c4*Er+C5*Ez+C2*Eq)\to DWq,\ (c6*Er+C3*Ez+C5*Eq)\to DWz,$$
$$(2\,c1\,Er+2\,(c4\,Eq+c6\,Ez))\to 2*DWr,\ (2\,c2\,Eq+2\,(c4\,Er+c5\,Ez))\to 2*DWq,$$
$$(2\,(c5\,Eq+c6\,Er)+2\,c3\,Ez)\to 2*DWz,\ (c4\,Eq+c1\,Er+c6\,Ez)\to DWr,$$
$$(c5\,Eq+c6\,Er+c3\,Ez)\to DWz,\ \sqrt{1-\frac{4\,Eqz^2}{1+2\,Eq}+2\,Ez}\to F33,\ \sqrt{1+2\,Eq}\to F22,$$
$$\left.\frac{1}{\sqrt{1+2\,Eq}}\to\frac{1}{F22},\ \frac{1}{\sqrt{1-\frac{4\,Eqz^2}{1+2\,Eq}+2\,Ez}}\to\frac{1}{F33},\ \frac{1}{(1+2\,Eq)^{3/2}}\to\frac{1}{F22^3}\right\}$$

$$\frac{2\,c0\,DWz\,Eqz\,M}{F22\,F33}+\frac{2\,c0\,c8\,Eqz\,F22\,M}{F33}+$$
$$\frac{2\,c0\,c3\,Eqz\,F33\,M}{F22}+\frac{4\,c0\,DWz^2\,Eqz\,F33\,M}{F22}+4\,c0\,c8\,DWz\,Eqz\,F22\,F33\,M$$

$$\partial_{Eqz}\,\sigma qz\ //.\ \left\{e^{c2\,Eq^2+c1\,Er^2+c3\,Ez^2+2\,(c9\,Eqr^2+c8\,Eqz^2+c4\,Eq\,Er+c7\,Erz^2+c5\,Eq\,Ez+c6\,Er\,Ez)}\to M,\right.$$
$$(c4*Er+C5*Ez+C2*Eq)\to DWq,\ (c6*Er+C3*Ez+C5*Eq)\to DWz,$$
$$(2\,c1\,Er+2\,(c4\,Eq+c6\,Ez))\to 2*DWr,\ (2\,c2\,Eq+2\,(c4\,Er+c5\,Ez))\to 2*DWq,$$
$$(2\,(c5\,Eq+c6\,Er)+2\,c3\,Ez)\to 2*DWz,\ (c4\,Eq+c1\,Er+c6\,Ez)\to DWr,$$
$$(c5\,Eq+c6\,Er+c3\,Ez)\to DWz,\ \sqrt{1-\frac{4\,Eqz^2}{1+2\,Eq}+2\,Ez}\to F33,\ \sqrt{1+2\,Eq}\to F22,$$
$$\left.\frac{1}{\sqrt{1+2\,Eq}}\to\frac{1}{F22},\ \frac{1}{\sqrt{1-\frac{4\,Eqz^2}{1+2\,Eq}+2\,Ez}}\to\frac{1}{F33},\ \frac{1}{(1+2\,Eq)^{3/2}}\to\frac{1}{F22^3}\right\}$$

$$-\frac{8\,c0\,DWz\,Eqz^2\,M}{F22^3\,F33}-\frac{8\,c0\,c8\,Eqz^2\,M}{F22\,F33}+\frac{2\,c0\,DWz\,F33\,M}{F22}+$$
$$\frac{8\,c0\,c8\,DWz\,Eqz^2\,F33\,M}{F22}+2\,c0\,c8\,F22\,F33\,M+8\,c0\,c8^2\,Eqz^2\,F22\,F33\,M$$

UMAT for axi-symmetric cyclic stretch simulations:

```
C-------------------------------------------------------------
C-------------------------------------------------------------
      SUBROUTINE UMAT(STRESS,STATEV,DDSDDE,SSE,SPD,SCD,
     1 RPL,DDSDDT,DRPLDE,DRPLDT,STRAN,DSTRAN,
     2 TIME,DTIME,TEMP,DTEMP,PREDEF,DPRED,MATERL,NDI,NSHR,NTENS,
     3 NSTATV,PROPS,NPROPS,COORDS,DROT,PNEWDT,CELENT,
     4 DFGRD0,DFGRD1,NOEL,NPT,KSLAY,KSPT,KSTEP,KINC)
C
      INCLUDE 'ABA_PARAM.INC'
C
      CHARACTER*8 MATERL
      DIMENSION STRESS(NTENS),STATEV(NSTATV),
     1 DDSDDE(NTENS,NTENS),DDSDDT(NTENS),DRPLDE(NTENS),
     2 STRAN(NTENS),DSTRAN(NTENS),DFGRD0(3,3),DFGRD1(3,3),
     3 TIME(2),PREDEF(1),DPRED(1),PROPS(NPROPS),COORDS(3),DROT(3,3)
C
C -----------------------------------------------------------------
C    UMAT FOR FUNG 7-PARAMETER ORTHOTROPIC MODEL OF HYPERELASTICITY
C    FOR AN AXISYMMETRIC MODEL
C
C     WRITTEN BY:
C     J. SCOTT VANEPPS
C     PH.D CANDIDATE
C     ADVISOR: DR. DAVID VORP
C     VASCULAR BIOENGINEER LABORATORY
C     DEPT OF SURGERY AND BIOENGINEERING
C     MCGOWAN INSTITUTE FOR REGENERATIVE MEDICINE
C     UNIVERSITY OF PITTSBURGH
C     DATE: AUGUST 2006
C -----------------------------------------------------------------
C     VARIABLE DEFINITIONS
C -----------------------------------------------------------------
      real*8 c0, c1, c2, c3, c4, c5, c6, c7, c8
C     These are the parameters for the Fung material model
C
      real*8 Er, Eq, Ez, Erz, Eqz, W, Q, J, N, Kappa
C     E - Green strains in the r, theta (q), and z directions as well as
C         Greens shear strains in the rz and theta-z (qz) planes
C     W - strain energy density
C     Q - exponent on the strain energy density function
C     J - determinant of the deformation gradient
C     N - penalty parameter in cauchy stress
C     Kappa - penalty term in stiffness matrix
C
      real*8 F11, F12, F13, F21, F22, F23, F31, F32, F33
C     F - deformation gradient tensor
C
      real*8 Drr, Drq, Drz, Dqr, Dqq, Dqz, Dzr, Dzq, Dzz
C     Dij - derivative of cauchy stress with respect to Ej.
C
      real*8 DWr, DWq, DWz, DWrz, DWqz
C     DWr, DWq, DWz - derivative of Q with respect to Er, Eq,
C                     and Ez respectively
C -----------------------------------------------------------------
```

```
C     RETRIEVE MODEL PARAMETERS FROM ABAQUS
C -------------------------------------------------------------
      c0=PROPS(1)
      c1=PROPS(2)
      c2=PROPS(3)
      c3=PROPS(4)
      c4=PROPS(5)
      c5=PROPS(6)
      c6=PROPS(7)
      c7=PROPS(8)
      c8=PROPS(9)
C -------------------------------------------------------------
C     DEFORMATION GRADIENT AND IT'S DETERMINANT
C -------------------------------------------------------------
      F11=DFGRD1(1, 1)
      F12=DFGRD1(1, 2)
      F13=DFGRD1(1, 3)
      F21=DFGRD1(2, 1)
      F22=DFGRD1(2, 2)
      F23=DFGRD1(2, 3)
      F31=DFGRD1(3, 1)
      F32=DFGRD1(3, 2)
      F33=DFGRD1(3, 3)
C
      J=F11*F22*F33+F12*F23*F31+F13*F21*F32-F13*F22*F31-F11*F23*F32-
     1  F12*F21*F33
C -------------------------------------------------------------
C     GREEN'S STRAIN
C -------------------------------------------------------------
      Er=0.5*(F11*F11+F21*F21+F31*F31-1)
      Ez=0.5*(F22*F22+F12*F12+F32*F32-1)
      Eq=0.5*(F33*F33+F13*F13+F23*F23-1)
      Erz=0.5*(F11*F12+F31*F32+F21*F22)
      Eqz=0.5*(F12*F13+F22*F23+F32*F33)
C -------------------------------------------------------------
C     STRAIN ENERGY FUNCTION
C -------------------------------------------------------------
      Q=EXP(c1*Er*Er)*EXP(c2*Eq*Eq)*EXP(c3*Ez*Ez)*EXP(2*c4*Er*Eq)*
     1 EXP(2*c5*Eq*Ez)*EXP(2*c6*Ez*Er)*EXP(2*c7*Erz**2)*EXP(2*c8*Eqz**2)
      W=0.5*c0*(Q-1)
      SSE=W
C -------------------------------------------------------------
C     CAUCHY STRESS
C -------------------------------------------------------------
      N=10**6
      DWr=(c1*Er+c6*Ez+c4*Eq)
      DWq=(c4*Er+c5*Ez+c2*Eq)
      DWz=(c6*Er+c3*Ez+c5*Eq)
      STRESS(1)=c0*(1+2*Er)*DWr*Q+N*2*(J-1)*J
      STRESS(3)=c0*(1+2*Eq)*DWq*Q+N*2*(J-1)*J
      STRESS(2)=c0*(1+2*Ez)*DWz*Q+N*2*(J-1)*J
      STRESS(4)=c0*c7*(((1+2*Er)*(1+2*Ez))**0.5)*Erz*Q
      STRESS(6)=c0*c8*(((1+2*Eq)*(1+2*Ez))**0.5)*Eqz*Q
      STATEV(4)=J
C -------------------------------------------------------------
C     STIFFNESS MATRIX
C -------------------------------------------------------------
```

```
      Kappa = 2*N*(2*J*J-J)
      Drr=2*c0*DWr*Q+c0*c1*Q*(1+2*Er)+2*c0*DWr*DWr*Q*(1+2*Er)
      Drq=c0*c4*(1+2*Er)*Q+2*c0*DWr*DWq*Q*(1+2*Er)
      Drz=c0*c6*(1+2*Er)*Q+2*c0*DWr*DWz*Q*(1+2*Er)
      Dqr=c0*c4*(1+2*Eq)*Q+2*c0*DWq*DWr*Q*(1+2*Eq)
      Dqq=2*c0*DWq*Q+c0*c2*Q*(1+2*Eq)+2*c0*DWq*DWq*Q*(1+2*Eq)
      Dqz=c0*c5*(1+2*Eq)*Q+2*c0*DWz*DWq*Q*(1+2*Eq)
      Dzr=c0*c6*(1+2*Ez)*Q+2*c0*DWr*DWz*Q*(1+2*Ez)
      Dzq=c0*c5*(1+2*Ez)*Q+2*c0*DWz*DWq*Q*(1+2*Ez)
      Dzz=2*c0*DWz*Q+c0*c3*Q*(1+2*Ez)+2*c0*DWz*DWz*Q*(1+2*Ez)
C
      DDSDDE(1, 1)=(1+2*Er)*Drr+Kappa
      DDSDDE(1, 3)=(1+2*Eq)*Drq+Kappa
      DDSDDE(1, 2)=(1+2*Ez)*Drz+Kappa
      DDSDDE(3, 1)=(1+2*Er)*Dqr+Kappa
      DDSDDE(3, 3)=(1+2*Eq)*Dqq+Kappa
      DDSDDE(3, 2)=(1+2*Ez)*Dqz+Kappa
      DDSDDE(2, 1)=(1+2*Er)*Dzr+Kappa
      DDSDDE(2, 3)=(1+2*Eq)*Dzq+Kappa
      DDSDDE(2, 2)=(1+2*Ez)*Dzz+Kappa
      DDSDDE(4, 4)=c0*c7*(((1+2*Er)*(1+2*Ez))**0.5)*Q
      DDSDDE(6, 6)=c0*c8*(((1+2*Eq)*(1+2*Ez))**0.5)*Q
C
      RETURN
      END
```

UMAT for axi-symmetric cyclic twist simulations:

```
C-----------------------------------------------------------------
C-----------------------------------------------------------------
      SUBROUTINE UMAT(STRESS,STATEV,DDSDDE,SSE,SPD,SCD,
     1 RPL,DDSDDT,DRPLDE,DRPLDT,STRAN,DSTRAN,
     2 TIME,DTIME,TEMP,DTEMP,PREDEF,DPRED,MATERL,NDI,NSHR,NTENS,
     3 NSTATV,PROPS,NPROPS,COORDS,DROT,PNEWDT,CELENT,
     4 DFGRD0,DFGRD1,NOEL,NPT,KSLAY,KSPT,KSTEP,KINC)
C
      INCLUDE 'ABA_PARAM.INC'
C
      CHARACTER*8 MATERL
      DIMENSION STRESS(NTENS),STATEV(NSTATV),
     1 DDSDDE(NTENS,NTENS),DDSDDT(NTENS),DRPLDE(NTENS),
     2 STRAN(NTENS),DSTRAN(NTENS),DFGRD0(3,3),DFGRD1(3,3),
     3 TIME(2),PREDEF(1),DPRED(1),PROPS(NPROPS),COORDS(3),DROT(3,3)
C
C -----------------------------------------------------------------
C    UMAT FOR FUNG 7-PARAMETER ORTHOTROPIC MODEL OF HYPERELASTICITY
C    FOR AN AXISYMMETRIC MODEL
C
C     WRITTEN BY:
C     J. SCOTT VANEPPS
C     PH.D CANDIDATE
C     ADVISOR: DR. DAVID VORP
C     VASCULAR BIOENGINEER LABORATORY
C     DEPT OF SURGERY AND BIOENGINEERING
C     MCGOWAN INSTITUTE FOR REGENERATIVE MEDICINE
```

```
C     UNIVERSITY OF PITTSBURGH
C     DATE: AUGUST 2006
C -------------------------------------------------------------
C     VARIABLE DEFINITIONS
C -------------------------------------------------------------
      real*8 c0, c1, c2, c3, c4, c5, c6, c7, c8
C     These are the parameters for the Fung material model
C
      real*8 Er, Eq, Ez, Erz, Eqz, Eqr, W, Q, J, N, Kappa
C     E - Green strains in the r, theta (q), and z directions as well as
C         Greens shear strains in the rz, theta-r (qr) and theta-z (qz)
C         planes
C     W - strain energy density
C     Q - exponent on the strain energy density function
C     J - determinant of the deformation gradient
C     N - penalty parameter in cauchy stress
C     Kappa - penalty term in stiffness matrix
C
      real*8 F11, F12, F13, F21, F22, F23, F31, F32, F33
C     F - deformation gradient tensor
C
      real*8 Drr, Drq, Drz, Drqz, Dqr, Dqq, Dqz, Dqqz, Dzr, Dzq, Dzz, Dzqz,
     1 Drzrz, Drqrq, Dqzr, Dqzq, Dqzz, Dqzqz
C     Dij - derivative of cauchy stress with respect to Ej.
C
      real*8 DWr, DWq, DWz, DWrz, DWqz
C     DWr, DWq, DWz - derivative of Q with respect to Er, Eq,
C                     and Ez respectively
C -------------------------------------------------------------
C     RETRIEVE MODEL PARAMETERS FROM ABAQUS
C -------------------------------------------------------------
      c0=PROPS(1)
      c1=PROPS(2)
      c2=PROPS(3)
      c3=PROPS(4)
      c4=PROPS(5)
      c5=PROPS(6)
      c6=PROPS(7)
      c7=PROPS(8)
      c8=PROPS(9)
      c9=PROPS(10)
C -------------------------------------------------------------
C     DEFORMATION GRADIENT AND IT'S DETERMINANT
C -------------------------------------------------------------
C      F11=DFGRD1(1, 1)*STATEV(1)
      F11=DFGRD1(1, 1)
      F12=DFGRD1(1, 3)
      F13=DFGRD1(1, 2)
      F21=DFGRD1(3, 1)
C      F22=DFGRD1(3, 3)*STATEV(3)
      F22=DFGRD1(3, 3)
C      F23=DFGRD1(3, 2)*STATEV(2)
      F23=DFGRD1(3, 2)
      F31=DFGRD1(2, 1)
      F32=DFGRD1(2, 3)
C      F33=DFGRD1(2, 2)*STATEV(2)
      F33=DFGRD1(2, 2)
```

```
C
      J=F11*F22*F33+F13*F32*F21+F12*F31*F23-F12*F33*F21-F11*F32*F23-
     1  F13*F31*F22
C
C -------------------------------------------------------------------
C     GREEN'S STRAIN
C -------------------------------------------------------------------
      Er=0.5*(F11*F11-1)
      Eq=0.5*(F22*F22-1)
      Ez=0.5*(F33*F33+F23*F23-1)
      Erz=0.5*(F11*F13+F21*F23+F31*F33)
      Eqz=0.5*(F22*F23)
      Eqr=0.5*(F11*F12+F31*F32+F21*F22)
C -------------------------------------------------------------------
C     STRAIN ENERGY FUNCTION
C -------------------------------------------------------------------
      Q=EXP(c1*Er*Er)*EXP(c2*Eq*Eq)*EXP(c3*Ez*Ez)*EXP(2*c4*Er*Eq)*
     1 EXP(2*c5*Eq*Ez)*EXP(2*c6*Ez*Er)*EXP(2*c7*Erz**2)*
     2 EXP(2*c8*Eqz**2)*EXP(2*c9*Eqr**2)
      W=0.5*c0*(Q-1)
      SSE=W
C -------------------------------------------------------------------
C     CAUCHY STRESS
C -------------------------------------------------------------------
      N=10**6
      DWr=(c1*Er+c6*Ez+c4*Eq)
      DWq=(c4*Er+c5*Ez+c2*Eq)
      DWz=(c6*Er+c3*Ez+c5*Eq)
      STRESS(1)=c0*(1+2*Er)*DWr*Q+N*2*(J-1)*J
      STRESS(3)=c0*(1+2*Eq)*DWq*Q+8*(Eqz**2)*c0*c8*Q+c0*(F23**2)*DWz*Q+
     1 N*2*(J-1)*J
      STRESS(2)=c0*(1+2*Ez)*DWz*Q+N*2*(J-1)*J
      STRESS(4)=2*c0*c7*Erz*F11*F33*Q
      STRESS(5)=((4*c0*c7*Eqz*Erz*F11*Q)/(F22))+2*c0*c9*Eqr*F11*F22*Q
      STRESS(6)=((2*c0*DWz*Eqz*F33*Q)/(F22))+2*c0*c8*Eqz*F22*F33*Q
      STATEV(4)=J
C -------------------------------------------------------------------
C     STIFFNESS MATRIX
C -------------------------------------------------------------------
      Kappa = 2*N*(2*J*J-J)
C
C - DERIVATIVES OF RADIAL STRESS
C
      Drr=2*c0*DWr*Q+c0*c1*Q*(1+2*Er)+2*c0*DWr*DWr*Q*(1+2*Er)
      Drq=c0*c4*(1+2*Er)*Q+2*c0*DWr*DWq*Q*(1+2*Er)
      Drz=c0*c6*(1+2*Er)*Q+2*c0*DWr*DWz*Q*(1+2*Er)
      Drqz=4*c0*c8*Dwr*Eqz*(1+2*Er)*Q
C
C - DERIVATIVES OF CIRCUMFERENTIAL STRESS
C
      Dqr=c0*c4*(1+2*Eq)*Q+2*c0*DWq*DWr*Q*(1+2*Eq)+
     1 (4*c0*c6*(Eqz**2)*Q)/(1+2*Eq)+(8*c0*Dwr*Dwz*(Eqz**2)*Q)/(1+2*Eq)+
     2 16*c0*c8*DWr*(Eqz**2)*Q
C
      Dqq=2*c0*DWq*Q+c0*c2*Q*(1+2*Eq)+2*c0*(DWq**2)*Q*(1+2*Eq)-
     1 (8*c0*DWz*(Eqz**2)*Q)/((1+2*Eq)**2)+(4*c0*c5*(Eqz**2)*Q)/(1+2*Eq)+
     2 (8*c0*DWq*DWz*(Eqz**2)*Q)/(1+2*Eq)+16*c0*c8*DWq*(Eqz**2)*Q
```

```
C
      Dqz=c0*c5*(1+2*Eq)*Q+2*c0*DWz*DWq*Q*(1+2*Eq)+
     1 (4*c0*c3*(Eqz**2)*Q)/(1+2*Eq)+(8*c0*(Dwz**2)*(Eqz**2)*Q)/(1+2*Eq)+
     2 16*c0*c8*DWz*(Eqz**2)*Q
C

Dqqz=16*c0*c8*Eqz*Q+(8*c0*DWz*Eqz*Q)/(1+2*Eq)+4*c0*c8*DWq*(1+2*Eq)*Eqz*Q+
     1 32*c0*(c8**2)*(Eqz**3)*Q+(16*c0*c8*DWz*(Eqz**3)*Q)/(1+2*Eq)
C
C - DERIVATIVES OF LONGITUDINAL STRESS
C
      Dzr=c0*c6*(1+2*Ez)*Q+2*c0*DWr*DWz*Q*(1+2*Ez)
      Dzq=c0*c5*(1+2*Ez)*Q+2*c0*DWz*DWq*Q*(1+2*Ez)
      Dzz=2*c0*DWz*Q+c0*c3*Q*(1+2*Ez)+2*c0*DWz*DWz*Q*(1+2*Ez)
      Dzqz=4*c0*c8*DWz*Eqz*(1+2*Ez)*Q
C
C - DERIVATIVES OF RZ STRESS
C
      Drzrz=2*c0*c7*F11*F33*Q+8*c0*(c7**2)*(Erz**2)*F11*F33*Q
C
C - DERIVATIVES OF RQ STRESS
C
      Drqrq=(16*c0*c7*c9*Eqr*Eqz*Erz*F11*Q)/(F22)+2*c0*c9*F11*F22*Q+
     1 8*c0*(c9**2)*(Eqr**2)*F11*F22*Q
C
C - DERIVATIVES OF QZ STRESS
C
      Dqzr=(2*c0*c6*Eqz*F33*Q)/(F22)+(4*c0*DWr*DWz*Eqz*F33*Q)/(F22)+
     1 4*c0*c8*DWr*Eqz*F22*F33*Q
C
      Dqzq=(8*c0*DWz*(Eqz**3)*Q)/((F22**5)*F33)+
     1 (8*c0*c8*(Eqz**3)*Q)/((F22**3)*F33)-(2*c0*DWz*Eqz*F33*Q)/(F22**3)+
     2 (2*c0*c5*Eqz*F33*Q)/(F22)+(2*c0*c8*Eqz*F33*Q)/(F22)+
     3 (4*c0*DWq*DWz*Eqz*F33*Q)/(F22)+4*c0*c8*DWq*Eqz*F22*F33*Q
C
      Dqzz=(2*c0*DWz*(Eqz**2)*Q)/(F22*F33)+(2*c0*c8*Eqz*F22*Q)/(F33)+
     1 (2*c0*c3*Eqz*F33*Q)/(F22)+(4*c0*(DWz**2)*Eqz*F33*Q)/(F22)+
     2 4*c0*c8*DWz*Eqz*F22*F33*Q
C
      Dqzqz=(-8*c0*DWz*(Eqz**2)*Q)/((F22**3)*F33)-
     1 (8*c0*c8*(Eqz**2)*Q)/(F22*F33)+(2*c0*DWz*F33*Q)/(F22)+
     2 (8*c0*c8*DWz*(Eqz**2)*F33*Q)/(F22)+2*c0*c8*F22*F33*Q+
     3 8*c0*(c8**2)*(Eqz**2)*F22*F33*Q
C
C - DERIVATIVES WITH RESPECT TO LOG STRAIN (STIFFNESS MATRIX FOR ABAQUS)
C
      DDSDDE(1, 1)=(1+2*Er)*Drr+Kappa
      DDSDDE(1, 3)=(1+2*Eq)*Drq+Kappa
      DDSDDE(1, 2)=(1+2*Ez)*Drz+Kappa
      DDSDDE(1, 6)=Drqz
      DDSDDE(3, 1)=(1+2*Er)*Dqr+Kappa
      DDSDDE(3, 3)=(1+2*Eq)*Dqq+Kappa
      DDSDDE(3, 2)=(1+2*Ez)*Dqz+Kappa
      DDSDDE(3, 6)=Dqqz
      DDSDDE(2, 1)=(1+2*Er)*Dzr+Kappa
      DDSDDE(2, 3)=(1+2*Eq)*Dzq+Kappa
      DDSDDE(2, 2)=(1+2*Ez)*Dzz+Kappa
```

```
      DDSDDE(2, 6)=2*Eqz*Dzqz
      DDSDDE(4, 4)=Drzrz
      DDSDDE(5, 5)=Drqrq
      DDSDDE(6, 1)=(1+2*Er)*Dqzr
      DDSDDE(6, 3)=(1+2*Eq)*Dqzq
      DDSDDE(6, 2)=(1+2*Ez)*Dqzz
      DDSDDE(6, 6)=2*Dqzqz
C      u=6
C      write(unit=u,fmt="(I,E,F)")NOEL,DDSDDE(1,1),J
C
      RETURN
      END
```

UMAT for 3D cyclic flexure simulations:

```
C-----------------------------------------------------------------
C-----------------------------------------------------------------
      SUBROUTINE UMAT(STRESS,STATEV,DDSDDE,SSE,SPD,SCD,
     1 RPL,DDSDDT,DRPLDE,DRPLDT,STRAN,DSTRAN,
     2 TIME,DTIME,TEMP,DTEMP,PREDEF,DPRED,MATERL,NDI,NSHR,NTENS,
     3 NSTATV,PROPS,NPROPS,COORDS,DROT,PNEWDT,CELENT,
     4 DFGRD0,DFGRD1,NOEL,NPT,KSLAY,KSPT,KSTEP,KINC)
C
      INCLUDE 'ABA_PARAM.INC'
C
      CHARACTER*8 MATERL
      DIMENSION STRESS(NTENS),STATEV(NSTATV),
     1 DDSDDE(NTENS,NTENS),DDSDDT(NTENS),DRPLDE(NTENS),
     2 STRAN(NTENS),DSTRAN(NTENS),DFGRD0(3,3),DFGRD1(3,3),
     3 TIME(2),PREDEF(1),DPRED(1),PROPS(NPROPS),COORDS(3),DROT(3,3)
C
C -----------------------------------------------------------------
C    UMAT FOR FUNG 7-PARAMETER ORTHOTROPIC MODEL OF HYPERELASTICITY
C    FOR AN AXISYMMETRIC MODEL
C
C     WRITTEN BY:
C     J. SCOTT VANEPPS
C     PH.D CANDIDATE
C     ADVISOR: DR. DAVID VORP
C     VASCULAR BIOENGINEER LABORATORY
C     DEPT OF SURGERY AND BIOENGINEERING
C     MCGOWAN INSTITUTE FOR REGENERATIVE MEDICINE
C     UNIVERSITY OF PITTSBURGH
C     DATE: AUGUST 2006
C -----------------------------------------------------------------
C     To run the program:
C     NEED TO FILL THIS IN LATER!!!!!!!!!!!!!!!!!!!!!!!!!!!!!!!!
C -----------------------------------------------------------------
C     VARIABLE DEFINITIONS
C -----------------------------------------------------------------
      real*8 c0, c1, c2, c3, c4, c5, c6, c7, c8
C     These are the parameters for the Fung material model
C
      real*8 Er, Eq, Ez, Erz, Eqz, Eqr, W, Q, J, N, Kappa
C     E - Green strains in the r, theta (q), and z directions as well as
```

```
C         Greens shear strains in the rz, theta-r (qr) and theta-z (qz)
C         planes
C     W - strain energy density
C     Q - exponent on the strain energy density function
C     J - determinant of the deformation gradient
C     N - penalty parameter in cauchy stress
C     Kappa - penalty term in stiffness matrix
C
      real*8 F11, F12, F13, F21, F22, F23, F31, F32, F33
C     F - deformation gradient tensor
C
      real*8 Drr, Drq, Drz, Drqz, Dqr, Dqq, Dqz, Dqqz, Dzr, Dzq, Dzz, Dzqz,
     1 Drzrz, Drqrq, Dqzr, Dqzq, Dqzz, Dqzqz
C     Dij - derivative of cauchy stress with respect to Ej.
C
      real*8 DWr, DWq, DWz, DWrz, DWqz
C     DWr, DWq, DWz - derivative of Q with respect to Er, Eq,
C                     and Ez respectively
C -------------------------------------------------------------------
C     RETRIEVE MODEL PARAMETERS FROM ABAQUS
C -------------------------------------------------------------------
      c0=PROPS(1)
      c1=PROPS(2)
      c2=PROPS(3)
      c3=PROPS(4)
      c4=PROPS(5)
      c5=PROPS(6)
      c6=PROPS(7)
      c7=PROPS(8)
      c8=PROPS(9)
      c9=PROPS(10)
C -------------------------------------------------------------------
C     DEFORMATION GRADIENT AND IT'S DETERMINANT
C -------------------------------------------------------------------
      F11=DFGRD1(1, 1)
      F12=DFGRD1(1, 2)
      F13=DFGRD1(1, 3)
      F21=DFGRD1(2, 1)
      F22=DFGRD1(2, 2)
      F23=DFGRD1(2, 2)
      F31=DFGRD1(3, 1)
      F32=DFGRD1(3, 2)
      F33=DFGRD1(3, 3)
C
      J=F11*F22*F33+F13*F32*F21+F12*F31*F23-F12*F33*F21-F11*F32*F23-
     1  F13*F31*F22
C
C -------------------------------------------------------------------
C     GREEN'S STRAIN
C -------------------------------------------------------------------
      Er=0.5*(F11*F11-1)
      Eq=0.5*(F22*F22-1)
      Ez=0.5*(F33*F33+F23*F23-1)
      Erz=0.5*(F11*F13+F21*F23+F31*F33)
      Eqz=0.5*(F22*F23)
      Eqr=0.5*(F11*F12+F31*F32+F21*F22)
C -------------------------------------------------------------------
```

```
C     STRAIN ENERGY FUNCTION
C -------------------------------------------------------------------
      Q=EXP(c1*Er*Er)*EXP(c2*Eq*Eq)*EXP(c3*Ez*Ez)*EXP(2*c4*Er*Eq)*
     1 EXP(2*c5*Eq*Ez)*EXP(2*c6*Ez*Er)*EXP(2*c7*Erz**2)*
     2 EXP(2*c8*Eqz**2)*EXP(2*c9*Eqr**2)
      W=0.5*c0*(Q-1)
      SSE=W
C -------------------------------------------------------------------
C     CAUCHY STRESS
C -------------------------------------------------------------------
      N=10**6
      DWr=(c1*Er+c6*Ez+c4*Eq)
      DWq=(c4*Er+c5*Ez+c2*Eq)
      DWz=(c6*Er+c3*Ez+c5*Eq)
      STRESS(1)=c0*(1+2*Er)*DWr*Q+N*2*(J-1)*J
      STRESS(2)=c0*(1+2*Eq)*DWq*Q+8*(Eqz**2)*c0*c8*Q+c0*(F23**2)*DWz*Q+
     1 N*2*(J-1)*J
      STRESS(3)=c0*(1+2*Ez)*DWz*Q+N*2*(J-1)*J
      STRESS(5)=2*c0*c7*Erz*F11*F33*Q
      STRESS(4)=((4*c0*c7*Eqz*Erz*F11*Q)/(F22))+2*c0*c9*Eqr*F11*F22*Q
      STRESS(6)=((2*c0*DWz*Eqz*F33*Q)/(F22))+2*c0*c8*Eqz*F22*F33*Q
      STATEV(4)=Q
C -------------------------------------------------------------------
C     STIFFNESS MATRIX
C -------------------------------------------------------------------
      Kappa = 2*N*(2*J*J-J)
C
C - DERIVATIVES OF RADIAL STRESS
C
      Drr=2*c0*DWr*Q+c0*c1*Q*(1+2*Er)+2*c0*DWr*DWr*Q*(1+2*Er)
      Drq=c0*c4*(1+2*Er)*Q+2*c0*DWr*DWq*Q*(1+2*Er)
      Drz=c0*c6*(1+2*Er)*Q+2*c0*DWr*DWz*Q*(1+2*Er)
      Drqz=4*c0*c8*Dwr*Eqz*(1+2*Er)*Q
C
C - DERIVATIVES OF CIRCUMFERENTIAL STRESS
C
      Dqr=c0*c4*(1+2*Eq)*Q+2*c0*DWq*DWr*Q*(1+2*Eq)+
     1 (4*c0*c6*(Eqz**2)*Q)/(1+2*Eq)+(8*c0*Dwr*Dwz*(Eqz**2)*Q)/(1+2*Eq)+
     2 16*c0*c8*DWr*(Eqz**2)*Q
C
      Dqq=2*c0*DWq*Q+c0*c2*Q*(1+2*Eq)+2*c0*(DWq**2)*Q*(1+2*Eq)-
     1 (8*c0*DWz*(Eqz**2)*Q)/((1+2*Eq)**2)+(4*c0*c5*(Eqz**2)*Q)/(1+2*Eq)+
     2 (8*c0*DWq*DWz*(Eqz**2)*Q)/(1+2*Eq)+16*c0*c8*DWq*(Eqz**2)*Q
C
      Dqz=c0*c5*(1+2*Eq)*Q+2*c0*DWz*DWq*Q*(1+2*Eq)+
     1 (4*c0*c3*(Eqz**2)*Q)/(1+2*Eq)+(8*c0*(Dwz**2)*(Eqz**2)*Q)/(1+2*Eq)+
     2 16*c0*c8*DWz*(Eqz**2)*Q
C

Dqqz=16*c0*c8*Eqz*Q+(8*c0*DWz*Eqz*Q)/(1+2*Eq)+4*c0*c8*DWq*(1+2*Eq)*Eqz*Q+
     1 32*c0*(c8**2)*(Eqz**3)*Q+(16*c0*c8*DWz*(Eqz**3)*Q)/(1+2*Eq)
C
C - DERIVATIVES OF LONGITUDINAL STRESS
C
      Dzr=c0*c6*(1+2*Ez)*Q+2*c0*DWr*DWz*Q*(1+2*Ez)
      Dzq=c0*c5*(1+2*Ez)*Q+2*c0*DWz*DWq*Q*(1+2*Ez)
      Dzz=2*c0*DWz*Q+c0*c3*Q*(1+2*Ez)+2*c0*DWz*DWz*Q*(1+2*Ez)
```

```
      Dzqz=4*c0*c8*DWz*Eqz*(1+2*Ez)*Q
C
C - DERIVATIVES OF RZ STRESS
C
      Drzrz=2*c0*c7*F11*F33*Q+8*c0*(c7**2)*(Erz**2)*F11*F33*Q
C
C - DERIVATIVES OF RQ STRESS
C
      Drqrq=(16*c0*c7*c9*Eqr*Eqz*Erz*F11*Q)/(F22)+2*c0*c9*F11*F22*Q+
     1 8*c0*(c9**2)*(Eqr**2)*F11*F22*Q
C
C - DERIVATIVES OF QZ STRESS
C
      Dqzr=(2*c0*c6*Eqz*F33*Q)/(F22)+(4*c0*DWr*DWz*Eqz*F33*Q)/(F22)+
     1 4*c0*c8*DWr*Eqz*F22*F33*Q
C
      Dqzq=(8*c0*DWz*(Eqz**3)*Q)/((F22**5)*F33)+
     1 (8*c0*c8*(Eqz**3)*Q)/((F22**3)*F33)-(2*c0*DWz*Eqz*F33*Q)/(F22**3)+
     2 (2*c0*c5*Eqz*F33*Q)/(F22)+(2*c0*c8*Eqz*F33*Q)/(F22)+
     3 (4*c0*DWq*DWz*Eqz*F33*Q)/(F22)+4*c0*c8*DWq*Eqz*F22*F33*Q
C
      Dqzz=(2*c0*DWz*(Eqz**2)*Q)/(F22*F33)+(2*c0*c8*Eqz*F22*Q)/(F33)+
     1 (2*c0*c3*Eqz*F33*Q)/(F22)+(4*c0*(DWz**2)*Eqz*F33*Q)/(F22)+
     2 4*c0*c8*DWz*Eqz*F22*F33*Q
C
      Dqzqz=(-8*c0*DWz*(Eqz**2)*Q)/((F22**3)*F33)-
     1 (8*c0*c8*(Eqz**2)*Q)/(F22*F33)+(2*c0*DWz*F33*Q)/(F22)+
     2 (8*c0*c8*DWz*(Eqz**2)*F33*Q)/(F22)+2*c0*c8*F22*F33*Q+
     3 8*c0*(c8**2)*(Eqz**2)*F22*F33*Q
C
C - DERIVATIVES WITH RESPECT TO LOG STRAIN (STIFFNESS MATRIX FOR ABAQUS)
C
      DDSDDE(1, 1)=(1+2*Er)*Drr+Kappa
      DDSDDE(1, 2)=(1+2*Eq)*Drq+Kappa
      DDSDDE(1, 3)=(1+2*Ez)*Drz+Kappa
      DDSDDE(1, 6)=Drqz
      DDSDDE(2, 1)=(1+2*Er)*Dqr+Kappa
      DDSDDE(2, 2)=(1+2*Eq)*Dqq+Kappa
      DDSDDE(2, 3)=(1+2*Ez)*Dqz+Kappa
      DDSDDE(2, 6)=Dqqz
      DDSDDE(3, 1)=(1+2*Er)*Dzr+Kappa
      DDSDDE(3, 2)=(1+2*Eq)*Dzq+Kappa
      DDSDDE(3, 3)=(1+2*Ez)*Dzz+Kappa
      DDSDDE(3, 6)=2*Eqz*Dzqz
      DDSDDE(5, 5)=Drzrz
      DDSDDE(4, 4)=Drqrq
      DDSDDE(6, 1)=(1+2*Er)*Dqzr
      DDSDDE(6, 2)=(1+2*Eq)*Dqzq
      DDSDDE(6, 3)=(1+2*Ez)*Dqzz
      DDSDDE(6, 6)=2*Dqzqz
C      u=6
C      write(unit=u,fmt="(I,E,F)")NOEL,DDSDDE(1,1),J
C
      RETURN
      END
```

APPENDIX E

APPENDIX E: ABAQUS USER DEFINED FUNCTIONS FOR INITIAL STRESS STRAIN STATE DUE TO OPENING ANGLE

SDVINI File for initial strain state due to residual stresses characterized by the opening angle. This function was used for the development of the Fung model that includes torsion shear stress.

```
C-----------------------------------------------------------------
SUBROUTINE SDVINI(STATEV,COORDS,NSTATV,NCRDS,NOEL,NPT,
     1 LAYER,KSPT)
C
      INCLUDE 'ABA_PARAM.INC'
C
      DIMENSION STATEV(NSTATV),COORDS(NCRDS)
C
C-----------------------------------------------------------------
C     SDVINI TO WRITE STATE VARIABLES REPRESENTING THE INITIAL
C     STRAIN STATE OF THE VESSEL SEGMENT DUE TO RESIDUAL
C     STRESSES CHARACTERIZED BY THE OPENING ANGLE IN AN AXISYMMETRIC
C     MODEL
C
C     WRITTEN BY:
C     J. SCOTT VANEPPS
C     PH.D CANDIDATE
C     ADVISOR: DR. DAVID VORP
C     VASCULAR BIOENGINEERING LABORATORY
C     DEPT OF SURGERY AND BIOENGINEERING
C     MCGOWAN INSTITUTE FOR REGENERATIVE MEDICINE
C     UNIVERSITY OF PITTSBURGH
C     DATE: AUGUST 2006
C -----------------------------------------------------------------
C     VARIABLE DEFINITIONS
C -----------------------------------------------------------------
      real*8 Noloadri, Zerostressri, Noloadrad, Zerostressrad,
     1 Phi
C     Noloadri - inner radius in the no load state
C     Zerostressri - inner radius in the zero stress state
```

```
C     Noloadrad - radial coordinate in the no load state
C     Zerostressrad - radial coordinate in the zero stress state
C     Phi - opening angle (radians)
C
      real*8 ProxID, DistID, ProxOD, DistOD, ProxZR, DistZR,
     1 ProxPhi, DistPhi, L
C     ProxID - proximal inside diameter (no load state)
C     DistID - distal inside diameter (no load state)
C     ProxOD - proximal outside diameter (no load state)
C     DistOD - distal outside diameter (no load state)
C     ProxZR - proximal inside radius (zero stress state)
C     DistZR - distal inside radius (zero stress state)
C     ProxPhi - proximal opening angle (radians)
C     DistPhi - distal opening angle (radians)
C     L - length of the vessel segment
C
      real*8 Slopenlri, Internlri, Slopezsri, Interzsri,
     1 Slopephi, Interphi
C     Based on proximal and distal measurements the geometry of the
C           entire vessel segment is modeled via linear interpolation.
C     The inner radii (in the no load and zero stress states) and
C     the opening angles are then determined as linear functions
C     of the longitudinal coordinate.
C
C     Slopenlri - slope for no load inner radius
C     Internlri - intercept for the no load inner radius
C     Slopezsri - slope for the zero stress inner radius
C     Interzsri - intercept for the zero stress inner radius
C     Slopephi - slope for the opening angle
C     Interphi - intercept for the opening angle
C
      real*8 pi, F11, F22, F33
C     pi - ratio of the circumference a circle to the radius
C     F - diagonal components of the deformation gradient
C           tensor for the zero stress to no load deformation
C-----------------------------------------------------------------
C     GEOMETRY AND OPENING ANGLE MEASURED QUANTITIES
C     To be filled in by user: These are the experiment specific
C     measured quantites.
C-----------------------------------------------------------------
      ProxID=2.55
      DistID=2.95
      ProxOD=4.4
      DistOD=4.35
      ProxZR=19.7625
      DistZR=22.8625
      ProxPhi=0.192
      DistPhi=0.192
      L=36
C-----------------------------------------------------------------
C     LINEAR INTERPOLATION OF RADII AND OPENING ANGLE
C-----------------------------------------------------------------
      Slopenlri=(DistID-ProxID)/(2*L)
      Internlri=(DistID/2)-(Slopenlri*L/2)
      Slopezsri=(DistZR-ProxZR)/L
      Interzsri=DistZR-(Slopezsri*L/2)
      Slopephi=(DistPhi-ProxPhi)/L
```

```
      Interphi=DistPhi-(Slopephi*L/2)
C-----------------------------------------------------------------
C     MAPPING OF NO LOAD RADIAL COORD. TO ZERO STRESS RADIAL COORD.
C-----------------------------------------------------------------
      pi=3.14159
      Noloadri=Slopenlri*COORDS(2)+Internlri
      Zerostressri=Slopezsri*COORDS(2)+Interzsri
      Phi=Slopephi*COORDS(2)+Interphi
C
      Noloadrad=COORDS(1)
      Zerostressrad=((pi/Phi)*(Noloadrad**2-Noloadri**2)+
     1 Zerostressri**2)**0.5
C-----------------------------------------------------------------
C     DEFORMATION GRADIENT TENSOR
C-----------------------------------------------------------------
      F22=1.017695
      F11=(Phi*Zerostressrad)/(pi*Noloadrad*F22)
      F33=(pi*Noloadrad)/(Phi*Zerostressrad)
C-----------------------------------------------------------------
C     ASSIGNMENT OF ABAQUS STATE VARIABLES
C-----------------------------------------------------------------
      STATEV(1)=F11
      STATEV(2)=F22
      STATEV(3)=F33
C
      RETURN
      END
```

SIGINI File for initial stress state due to residual stresses characterized by the opening angle.

This function was used for the development of the Fung model that includes torsion shear stress.

```
C-----------------------------------------------------------------
C     SIGINI FOR INITIAL STRESS STATE OF THE VESSEL SEGMENT DUE TO
C     RESIDUAL STRESSES CHARACTERIZED BY THE OPENING ANGLE IN AN
C     AXISYMMETRIC MODEL
C
C     WRITTEN BY:
C     J. SCOTT VANEPPS
C     PH.D CANDIDATE
C     ADVISOR: DR. DAVID VORP
C     VASCULAR BIOENGINEERING LABORATORY
C     DEPT OF SURGERY AND BIOENGINEERING
C     MCGOWAN INSTITUTE FOR REGENERATIVE MEDICINE
C     UNIVERSITY OF PITTSBURGH
C     DATE: AUGUST 2006
C -----------------------------------------------------------------
C     VARIABLE DEFINITIONS
C -----------------------------------------------------------------
      real*8 Noloadri, Zerostressri, Zerostressrad, Phi
C     Noloadri - inner radius in the no load state
C     Zerostressri - inner radius in the zero stress state
C     Zerostressrad - radial coordinate in the zero stress state
C     Phi - opening angle (radians)
```

```
C
      real*8 ProxID, DistID, ProxOD, DistOD, ProxZR, DistZR,
     1 ProxPhi, DistPhi, L
C     ProxID - proximal inside diameter (no load state)
C     DistID - distal inside diameter (no load state)
C     ProxOD - proximal outside diameter (no load state)
C     DistOD - distal outside diameter (no load state)
C     ProxZR - proximal inside radius (zero stress state)
C     DistZR - distal inside radius (zero stress state)
C     ProxPhi - proximal opening angle (radians)
C     DistPhi - distal opening angle (radians)
C     L - length of the vessel segment
C
      real*8 Slopenlri, Internlri, Slopezsri, Interzsri,
     1 Slopephi, Interphi
C     Based on proximal and distal measurements the entire vessel
C       segment is modeled via linear interpolation.  The inner
C       radii (no load and zero stress states) and the opening
C       angles are then determined as linear functions
C       of the longitudinal coordinate.
C
C     Slopenlri - slope for no load inner radius
C     Internlri - intercept for the no load inner radius
C     Slopezsri - slope for the zero stress inner radius
C     Interzsri - intercept for the zero stress inner radius
C     Slopephi - slope for the opening angle
C     Interphi - intercept for the opening angle
C
      real*8 pi, Er, Eq, Ez, Erz, Eqz, Eqr, intu, intl, lagrange, F11,
     1 F22, F33, F11i, F33i
C     pi - ratio of the circumference a circle to the radius
C     E - Green strains in r, theta (q), and z directions, as well as
C         Greens shear strains in the rz, theta-r (qr)  and theta-z
C         (qz) planes
C     int - evaluation of the integral portion of the lagrange
C           multiplier formula at the upper (u) and lower (l) limits
C     lagrange - lagrange multiplier
C     F11,F22,F33 - diagonal components of the deformation gradient
C     F11i,F33i - deformation gradient components at the inner radius
C
      real*8 c0, c1, c2, c3, c4, c5, c6, c7, c8, W, Q, Dr, Dq, Dz
C     c - parameters for the Fung material model
C     W - strain energy density
C     Q - exponent on the strain energy density function
C     DWr, DWq, DWz - derivative of Q with respect to Er, Eq, and Ez
C                  respectively
C-----------------------------------------------------------------
C     FUNG MODEL PARAMETERS AND MEASURED QUANTITIES
C     To be filled in by user:  These are the experiment specific
C     measured quantites.
C-----------------------------------------------------------------
      c0=8.92
      c1=0.55
      c2=1.25
      c3=2.46
      c4=0.08
      c5=0.36
```

```
      c6=0.06
      c7=10
      c8=0.075
      c9=10
      ProxID=2.55
      DistID=2.95
      ProxOD=4.4
      DistOD=4.35
      ProxZR=19.7625
      DistZR=22.8625
      ProxPhi=0.192
      DistPhi=0.192
      L=36
C-----------------------------------------------------------------
C     LINEAR INTERPOLATION OF RADII AND OPENING ANGLE
C-----------------------------------------------------------------
      Slopenlri=(DistID-ProxID)/(2*L)
      Internlri=(DistID/2)-(Slopenlri*L/2)
      Slopezsri=(DistZR-ProxZR)/L
      Interzsri=DistZR-(Slopezsri*L/2)
      Slopephi=(DistPhi-ProxPhi)/L
      Interphi=DistPhi-(Slopephi*L/2)
C-----------------------------------------------------------------
C     MAPPING OF NO LOAD RADIAL COORD. TO ZERO STRESS RADIAL COORD.
C-----------------------------------------------------------------
      pi=3.14159
      Noloadri=Slopenlri*COORDS(2)+Internlri
      Zerostressri=Slopezsri*COORDS(2)+Interzsri
      Phi=Slopephi*COORDS(2)+Interphi
C
      Zerostressrad=((pi/Phi)*(COORDS(1)**2-Noloadri**2)+
     1 Zerostressri**2)**0.5
C-----------------------------------------------------------------
C     DEFORMATION GRADIENT TENSOR
C-----------------------------------------------------------------
      F22=1.017695
      F11=(Phi*Zerostressrad)/(pi*COORDS(1)*F22)
      F11i=(Phi*Zerostressri)/(pi*Noloadri*F22)
      F33=(pi*COORDS(1))/(Phi*Zerostressrad)
      F33i=(pi*Noloadri)/(Phi*Zerostressri)
C-----------------------------------------------------------------
C     LAGRANGE MULTIPLIER
C-----------------------------------------------------------------
      pi=3.14159
      intu=0.5*c0*(exp((c1/4)+(c3/4)+c6+((c3/4)*F33**4)-((c3/2)*F33**2)-
     1 ((c6/2)*F33**2)-((c1/2)*F11**2)-((c6/2)*F11**2)+((c1/4)*F11**4)))
C
      intl=0.5*c0*(exp((c1/4)+(c3/4)+c6+((c3/4)*F33i**4)-((c3/2)*F33i**2)-
     1 ((c6/2)*F33i**2)-((c1/2)*F11i**2)-((c6/2)*F11i**2)+((c1/4)*F11i**4)))
C-----------------------------------------------------------------
C     STRESS / STRAIN
C-----------------------------------------------------------------
      Er=0.5*(F11**2-1)
      Eq=0.5*(F33**2-1)
      Ez=0.5*(F22**2-1)
      Erz=0
      Eqz=0
```

```
      Eqr=0
C
      Q=(c1*Er*Er+c2*Eq*Eq+c3*Ez*Ez+2*(c4*Er*Eq+c5*Eq*Ez+c6*Ez*Er+
     1 c7*Erz**2+c8*Eqz**2))
      W=0.5*c0*(EXP(Q)-1)
C
      DWr=(c1*Er+c6*Ez+c4*Eq)
      DWq=(c4*Er+c5*Ez+c2*Eq)
      DWz=(c6*Er+c3*Ez+c5*Eq)
C
      lagrange=c0*(1+2*Er)*DWr*EXP(Q)-(intu-intl)
C
      SIGMA(1)=-lagrange+c0*(1+2*Er)*DWr*EXP(Q)
      SIGMA(3)=-lagrange+c0*(1+2*Eq)*DWq*EXP(Q)
      SIGMA(2)=-lagrange+c0*(1+2*Ez)*DWz*EXP(Q)
C
      RETURN
      END
```

APPENDIX F

APPENDIX F: ABAQUS USER DEFINED FUNCTIONS FOR CUSTOM FIELD DISPLACEMENT

DISP file for user define flexure displacement

```
SUBROUTINE DISP(U,KSTEP,KINC,TIME,NODE,NOEL,JDOF,COORDS)
C
      INCLUDE 'ABA_PARAM.INC'
C
      DIMENSION U(3),TIME(2),COORDS(3)
C
      PI=ATAN(1.)*4.
      TFREQ=2.4*COS(2.*PI*TIME(1))-2.4+27.5
      TVAMP=2.4*COS(PI*(COORDS(2)/TFREQ))+2.4
      TSLOPE=0.00948*COS(2.*PI*TIME(1))-0.11678
      THAMP=TSLOPE*COORDS(2)
C
      IF(JDOF.EQ.3) THEN
          U(1)=-TVAMP*COS(2.*PI*TIME(1))+TVAMP
      ELSE IF(JDOF.EQ.2) THEN
          U(1)=-THAMP*COS(2.*PI*TIME(1))+THAMP
      ELSE
          U(1)=0
      END IF
        RETURN
      END
```

APPENDIX G

APPENDIX G: FLUENT USER DEFINED FUNCTIONS FOR PERIODIC BOUNDARY FUNCTIONS AND CUSTOM FIELD DISPLACEMENT

```
/************************************************************/
/*                                                          */
/* User-Defined Function for unsteady pressure and flow     */
/* in ex vivo perfused arterial segments                    */
/*                                                          */
/* Fluent 6                                                 */
/*                                                          */
/* Author: J. Scott VanEpps                          */
/*   Date: 011607                                           */
/*                                                          */
/* This function prescribes an oscillating velocity at the  */
/* vessel inlet and oscillating pressure with mass flow rate */
/* at the vessel outlet                                     */
/*                                                          */
/************************************************************/

#include "udf.h"

DEFINE_PROFILE(unsteady_inlet, thread, position)
{

  float t, velocity;
  face_t f;

  t = RP_Get_Real("flow-time");

  velocity = -0.05224*cos(6.28*t)+0.17414;

  begin_f_loop(f, thread)
  {
   F_PROFILE(f, thread, position) = velocity;
  }
  end_f_loop(f, thread)
}
```

```
DEFINE_PROFILE(unsteady_oulet, thread, position)
{

  float t, pressure;
  face_t f;

  t = RP_Get_Real("flow-time");

  pressure = -2667*cos(6.28*t)+13332;

  begin_f_loop(f, thread)
  {
   F_PROFILE(f, thread, position) = pressure;
  }
  end_f_loop(f, thread)
}

DEFINE_PROFILE(unsteady_mass, thread, position)
{

  float t, mass;
  face_t f;

  t = RP_Get_Real("flow-time");

  mass = -0.0005*cos(6.28*t)+0.0016667;

  begin_f_loop(f, thread)
  {
   F_PROFILE(f, thread, position) = mass;
  }
  end_f_loop(f, thread)
}

DEFINE_GRID_MOTION(prox_tee,domain,dt,time,dtime)
{
  Thread *tf = DT_THREAD(dt);
  face_t f;
  Node *v;
  real velx, vely, sine, ratio;
  int n;

  sine = 6.2832 * sin (6.2832*time);

  begin_f_loop(f,tf)
    {
      f_node_loop(f,tf,n)
      {
        v = F_NODE(f,tf,n);
        ratio = NODE_Y(v)/0.00226;
        velx = 0.01605*0.25*sin(6.28*time);
        vely = 0;/*-0.000258965*0.5*sine;*/
        NODE_X(v) = NODE_X(v) + (velx * dtime);
        if(NODE_Y(v) <= 0.0017)
          {
            NODE_Y(v) = NODE_Y(v) + (vely * ratio * dtime);
```

```
          }
        else
          {
            NODE_Y(v) = NODE_Y(v) + (vely * dtime);
          }
      }
    }
  end_f_loop(f,tf)
}

DEFINE_GRID_MOTION(dist_tee,domain,dt,time,dtime)
{
  Thread *tf = DT_THREAD(dt);
  face_t f;
  Node *v;
  real velx, vely, sine, ratio;
  int n;

  sine = 6.2832 * sin (6.2832*time);

  begin_f_loop(f,tf)
    {
      f_node_loop(f,tf,n)
      {
        v = F_NODE(f,tf,n);
          ratio = NODE_Y(v)/0.00206;
        velx = -0.01605*0.25*sin(6.28*time);
        vely = 0;/*-0.000235065*0.5*sine;*/
        NODE_X(v) = NODE_X(v) + (velx * dtime);
               if(NODE_Y(v) <= 0.0015)
          {
            NODE_Y(v) = NODE_Y(v) + (vely * ratio * dtime);
          }
        else
          {
            NODE_Y(v) = NODE_Y(v) + (vely * dtime);
          }
      }
    }
  end_f_loop(f,tf)
}

DEFINE_GRID_MOTION(vessel,domain,dt,time,dtime)
{
  Thread *tf = DT_THREAD(dt);
  face_t f;
  Node *v;
  real sine, cosine, deltaRx, velx, epsilon, m, b, yamp, vely, rxto;
  real slope, intercept, ryto;
  int n;

  sine = 6.2832 * sin (6.2832*time);
  cosine = cos (6.2832*time);
  epsilon = -0.035;
  m = -0.000000327;
  b = 0.000247;
  slope = -0.000002793;
```

```
  intercept = 0.00216138;

  begin_f_loop(f,tf)
    {
      f_node_loop(f,tf,n)
      {
        v = F_NODE(f,tf,n);
        rxto = - NODE_X(v) / (epsilon * cosine - epsilon - 1);
        ryto = (NODE_X(v) * slope) + intercept;
          yamp = (((m * rxto) + b)/2);
        velx = epsilon * rxto * 0.5 * sine;
        if (NODE_Y(v) <= 0.001)
          {
            vely = 0;
          }
        else
          {
            vely = yamp * sine;
          }
        NODE_X(v) = NODE_X(v) + (velx * dtime);
              NODE_Y(v) = NODE_Y(v) + (vely * dtime);
      }
    }
  end_f_loop(f,tf)
  printf("%f %f %f %f/n", rxto, NODE_X(v), dtime, velx);
}
```

APPENDIX H

APPENDIX H: SENSITIVITY ANALYSIS

To determine the uncertainty in the measurement of inner and outer diameter (protocol described in Section 4.1.1), a ring of L/S 16 Tygon tubing (Cole Parmer, Vernon Hills, Illinois) was placed in small culture dish filled with saline at 37° C. Five, high resolution digital images were taken of the ring. Inner and outer diameter measurements were made for each individual image using Scion Image as described in Section 4.1.1. The uncertainty in these measurements was assumed to be equal to the 95% confidence interval (σ) given by [210]:

$$\sigma = (2)\ (1.96)\left(\frac{S}{\sqrt{n}}\right) \tag{H.1}$$

where S is the standard deviation and n is the number of measurements made (in this case 5). The uncertainty in the inner and outer diameter measurements was calculated and then converted to the uncertainty for the inner and outer radii according to:

$$\sigma_{radius} = \frac{\sigma_{diameter}}{2} \tag{H.2}$$

In addition to the uncertainty, the percent error for the inner and outer radii was determined via:

$$\varepsilon\% = 100\frac{\sigma}{\bar{x}} \tag{H.3}$$

where $\bar{x}$ is the computed average radius for the 5 images. The uncertainties and percent error for inner and outer diameter measurements can be found in Table H.1.

Table H.1 Uncertainty and percent error for the inner and outer radii calculated from equations H.1 – H.3.

	σ (mm)	ε%
Inner Radii	0.04	2.2%
Outer Radii	0.05	1.4%

To determine the sensitivity of the stress estimations in the finite element and computational fluid dynamics analyses these uncertainties were applied to a representative stretch experiment specimen. A total of three finite element and three computational fluid dynamics simulations were run for this specimen. The first simulation utilized radii measurements at the low end of the certainty interval (MIN); the second simulation utilized actual measured radii (MEAN); and the third simulation utilized the radii at the high end of the uncertainty interval (MAX). For the finite element analyses the Von Mises stress at systole, which is a composite measurement of all components of the stress tensor, was used to determine the sensitivity. For the computational fluid dynamics analyses the shear rate at systole was used. Plots of mid-wall Von Mises stress and shear rate over the normalized length of the vessel segment are shown in Figure H.1 and Figure H.2, respectively. The percent error in stress at each point along the length was calculated as

$$\%\text{Error} = \frac{\text{MAX} - \text{MIN}}{\text{MEAN}} \tag{H.4}$$

The maximum percent error for the finite element and computational fluid dynamic analyses are given in Table H.2.

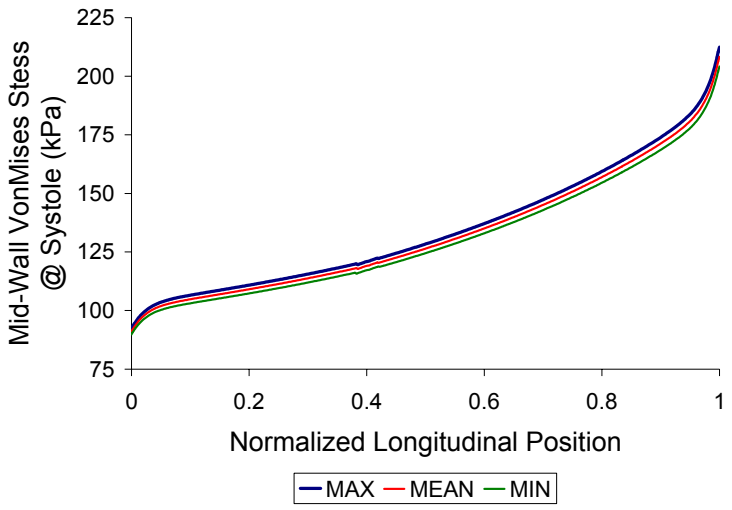

Figure H.1 Sensitivity of finite element analysis to the uncertainty in diameter measurement. MAX – vessel geometry at the maximum of the uncertainty interval. MEAN – actual measured vessel geometry. MIN – vessel geometry at the minimum of the uncertainty interval.

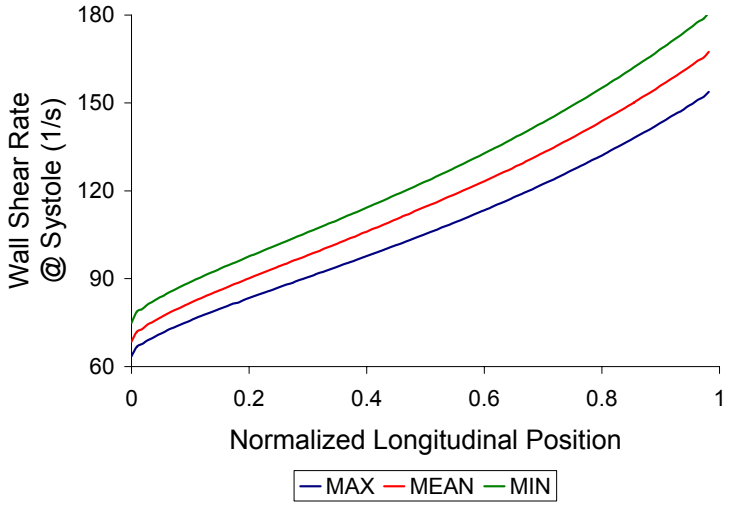

Figure H.2 Sensitivity of computational fluid dynamic analysis to the uncertainty in diameter measurement. MAX – vessel geometry at the maximum of the uncertainty interval. MEAN – actual measured vessel geometry. MIN – vessel geometry at the minimum of the uncertainty interval.

Table H.2 Maximum percent error due to uncertainty in the diameter measurements for the mural stress (estimated from the Von Mises Stress at systole) and the shear rate (estimated from the shear rate at systole).

	%Error
Mural Stress	4%
Shear Rate	16%

BIBLIOGRAPHY

1. *Heart Disease and Stroke Statistics - 2005 Update*. 2005, American Heart Association: Dallas, Texas.

2. *Preventing Heart Disease and Stroke: Addressing the Nation's Leading Killers*. Revised August 2005, The Department of Heath And Human Services, Centers For Disease Control And Prevention, Coordinating Center For Health Promotion.

3. Ross, R., *Atherosclerosis--an inflammatory disease.* N Engl J Med, 1999. **340**(2): p. 115-26.

4. Schoen, F. and R. Cotran, *Blood Vessels*, in *Robbins Pathological Basis of Disease*, R.S. Cotran, V. Kumar, and T. Collins, Editors. 1999, W. B. Saunders Company: Philadelphia. p. 493-542.

5. McGovern, P.G., et al., *Recent trends in acute coronary heart disease--mortality, morbidity, medical care, and risk factors. The Minnesota Heart Survey Investigators.* N Engl J Med, 1996. **334**(14): p. 884-90.

6. Cooper, R., et al., *Trends and disparities in coronary heart disease, stroke, and other cardiovascular diseases in the United States: findings of the national conference on cardiovascular disease prevention.* Circulation, 2000. **102**(25): p. 3137-47.

7. Wentzel, J.J., et al., *Extension of increased atherosclerotic wall thickness into high shear stress regions is associated with loss of compensatory remodeling.* Circulation, 2003. **108**(1): p. 17-23.

8. Ross, R., *The pathogenesis of atherosclerosis--an update.* N Engl J Med, 1986. **314**(8): p. 488-500.

9. Ross, R., *The pathogenesis of atherosclerosis: a perspective for the 1990s.* Nature, 1993. **362**(6423): p. 801-9.

10. Mora, R., F. Lupu, and N. Simionescu, *Prelesional events in atherogenesis. Colocalization of apolipoprotein B, unesterified cholesterol and extracellular phospholipid liposomes in the aorta of hyperlipidemic rabbit.* Atherosclerosis, 1987. **67**(2-3): p. 143-54.

11. Gimbrone, M.A., *Culture of vascular endothelium.* Prog Hemost Thromb, 1976. **3**: p. 1-28.

12. Stoneman, V.E. and M.R. Bennett, *Role of apoptosis in atherosclerosis and its therapeutic implications.* Clin Sci, 2004. **107**(4): p. 343-54.

13. Minamino, T., et al., *Endothelial cell senescence in human atherosclerosis: role of telomere in endothelial dysfunction.* Circulation, 2002. **105**(13): p. 1541-4.

14. Penn, M.S., et al., *Macromolecular transport in the arterial intima: comparison of chronic and acute injuries.* Am J Physiol, 1997. **272**(4 Pt 2): p. H1560-70.

15. Guretzki, H.J., et al., *Atherogenic levels of low density lipoprotein alter the permeability and composition of the endothelial barrier.* Atherosclerosis, 1994. **107**(1): p. 15-24.

16. Rong, J.X., et al., *Arterial injury by cholesterol oxidation products causes endothelial dysfunction and arterial wall cholesterol accumulation.* Arterioscler Thromb Vasc Biol, 1998. **18**(12): p. 1885-94.

17. Lin, S.J., et al., *Increased aortic endothelial death and enhanced transendothelial macromolecular transport in streptozotocin-diabetic rats.* Diabetologia, 1993. **36**(10): p. 926-30.

18. Lin, S.J., et al., *Long-term nicotine exposure increases aortic endothelial cell death and enhances transendothelial macromolecular transport in rats.* Arterioscler Thromb Vasc Biol, 1992. **12**(11): p. 1305-12.

19. Mehta, J.L., et al., *Lectin-like, oxidized low-density lipoprotein receptor-1 (LOX-1): a critical player in the development of atherosclerosis and related disorders.* Cardiovasc Res, 2006. **69**(1): p. 36-45.

20. Sawamura, T., et al., *An endothelial receptor for oxidized low-density lipoprotein.* Nature, 1997. **386**(6620): p. 73-7.

21. Holvoet, P., *Endothelial dysfunction, oxidation of low-density lipoprotein, and cardiovascular disease.* Ther Apher, 1999. **3**(4): p. 287-93.

22. Li, D. and J.L. Mehta, *Antisense to LOX-1 inhibits oxidized LDL-mediated upregulation of monocyte chemoattractant protein-1 and monocyte adhesion to human coronary artery endothelial cells.* Circulation, 2000. **101**(25): p. 2889-95.

23. Li, D., et al., *Proapoptotic effects of ANG II in human coronary artery endothelial cells: role of AT1 receptor and PKC activation.* Am J Physiol, 1999. **276**(3 Pt 2): p. H786-92.

24. Aoyama, T., et al., *Induction of lectin-like oxidized LDL receptor by oxidized LDL and lysophosphatidylcholine in cultured endothelial cells.* J Mol Cell Cardiol, 1999. **31**(12): p. 2101-14.

25. Mehta, J.L. and D.Y. Li, *Identification and autoregulation of receptor for OX-LDL in cultured human coronary artery endothelial cells.* Biochem Biophys Res Commun, 1998. **248**(3): p. 511-4.

26. Kikuta, K., et al., *High-affinity arginine transport of bovine aortic endothelial cells is impaired by lysophosphatidylcholine.* Circ Res, 1998. **83**(11): p. 1088-96.

27. Kugiyama, K., et al., *Impairment of endothelium-dependent arterial relaxation by lysolecithin in modified low-density lipoproteins.* Nature, 1990. **344**(6262): p. 160-2.

28. Kume, N., M.I. Cybulsky, and M.A. Gimbrone, *Lysophosphatidylcholine, a component of atherogenic lipoproteins, induces mononuclear leukocyte adhesion molecules in cultured human and rabbit arterial endothelial cells.* J Clin Invest, 1992. **90**(3): p. 1138-44.

29. Barath, P., et al., *Tumor necrosis factor gene expression in human vascular intimal smooth muscle cells detected by in situ hybridization.* Am J Pathol, 1990. **137**(3): p. 503-9.

30. Tipping, P.G. and W.W. Hancock, *Production of tumor necrosis factor and interleukin-1 by macrophages from human atheromatous plaques.* Am J Pathol, 1993. **142**(6): p. 1721-8.

31. Kume, N., et al., *Inducible expression of lectin-like oxidized LDL receptor-1 in vascular endothelial cells.* Circ Res, 1998. **83**(3): p. 322-7.

32. Li, D., et al., *Oxidized LDL upregulates angiotensin II type 1 receptor expression in cultured human coronary artery endothelial cells: the potential role of transcription factor NF-kappaB.* Circulation, 2000. **102**(16): p. 1970-6.

33. Draude, G., N. Hrboticky, and R.L. Lorenz, *The expression of the lectin-like oxidized low-density lipoprotein receptor (LOX-1) on human vascular smooth muscle cells and monocytes and its down-regulation by lovastatin.* Biochem Pharmacol, 1999. **57**(4): p. 383-6.

34. Hinagata, J., et al., *Oxidized LDL receptor LOX-1 is involved in neointimal hyperplasia after balloon arterial injury in a rat model.* Cardiovasc Res, 2006. **69**(1): p. 263-71.

35. Ge, J., et al., *Upregulation of lectinlike oxidized low-density lipoprotein receptor-1 expression contributes to the vein graft atherosclerosis: modulation by losartan.* Atherosclerosis, 2004. **177**(2): p. 263-8.

36. Mehta, J.L. and D. Li, *Identification, regulation and function of a novel lectin-like oxidized low-density lipoprotein receptor.* J Am Coll Cardiol, 2002. **39**(9): p. 1429-35.

37. Leake, D.S. and S.M. Rankin, *The oxidative modification of low-density lipoproteins by macrophages.* Biochem J, 1990. **270**(3): p. 741-8.

38. Steinberg, D., *Lipoprotein modification and atherogenesis.* Atheroscler Rev, 1991. **23**: p. 115.

39. Faggiotto, A., R. Ross, and L. Harker, *Studies of hypercholesterolemia in the nonhuman primate. I. Changes that lead to fatty streak formation.* Arteriosclerosis, 1984. **4**(4): p. 323-40.

40. Goldstein, J.L., et al., *Binding site on macrophages that mediates uptake and degradation of acetylated low density lipoprotein, producing massive cholesterol deposition.* Proc Natl Acad Sci U S A, 1979. **76**(1): p. 333-7.

41. Okamoto, E., et al., *Diversity of the synthetic-state smooth-muscle cells proliferating in mechanically and hemodynamically injured rabbit arteries.* Lab Invest, 1996. **74**(1): p. 120-8.

42. Thyberg, J., *Phenotypic modulation of smooth muscle cells during formation of neointimal thickenings following vascular injury.* Histol Histopathol, 1998. **13**(3): p. 871-91.

43. Campbell, J.H., et al., *Lipid accumulation in arterial smooth muscle cells. Influence of phenotype.* Atherosclerosis, 1983. **47**(3): p. 279-95.

44. Gown, A.M., T. Tsukada, and R. Ross, *Human atherosclerosis. II. Immunocytochemical analysis of the cellular composition of human atherosclerotic lesions.* Am J Pathol, 1986. **125**(1): p. 191-207.

45. Jonasson, L., et al., *Regional accumulations of T cells, macrophages, and smooth muscle cells in the human atherosclerotic plaque.* Arteriosclerosis, 1986. **6**(2): p. 131-8.

46. Davies, M.J., et al., *Morphology of the endothelium over atherosclerotic plaques in human coronary arteries.* British Heart Journal, 1988. **60**(6): p. 459-64.

47. Reape, T.J. and P.H. Groot, *Chemokines and atherosclerosis.* Atherosclerosis, 1999. **147**(2): p. 213-25.

48. Huo, Y. and K. Ley, *Adhesion molecules and atherogenesis.* Acta Physiol Scand, 2001. **173**(1): p. 35-43.

49. Proost, P., A. Wuyts, and J. van_Damme, *The role of chemokines in inflammation.* Int J Clin Lab Res, 1996. **26**(4): p. 211-23.

50. Springer, T.A., *Traffic signals for lymphocyte recirculation and leukocyte emigration: the multistep paradigm.* Cell, 1994. **76**(2): p. 301-14.

51. Cinamon, G., et al., *Novel chemokine functions in lymphocyte migration through vascular endothelium under shear flow.* J Leukoc Biol, 2001. **69**(6): p. 860-6.

52. Cinamon, G., V. Shinder, and R. Alon, *Shear forces promote lymphocyte migration across vascular endothelium bearing apical chemokines.* Nat Immunol, 2001. **2**(6): p. 515-22.

53. Takeya, M., et al., *Detection of monocyte chemoattractant protein-1 in human atherosclerotic lesions by an anti-monocyte chemoattractant protein-1 monoclonal antibody.* Hum Pathol, 1993. **24**(5): p. 534-9.

54. Nelken, N.A., et al., *Monocyte chemoattractant protein-1 in human atheromatous plaques.* J Clin Invest, 1991. **88**(4): p. 1121-7.

55. Yla-Herttuala, S., et al., *Expression of monocyte chemoattractant protein 1 in macrophage-rich areas of human and rabbit atherosclerotic lesions.* Proc Natl Acad Sci U S A, 1991. **88**(12): p. 5252-6.

56. Yu, X., et al., *Elevated expression of monocyte chemoattractant protein 1 by vascular smooth muscle cells in hypercholesterolemic primates.* Proc Natl Acad Sci U S A, 1992. **89**(15): p. 6953-7.

57. Cushing, S.D., et al., *Minimally modified low density lipoprotein induces monocyte chemotactic protein 1 in human endothelial cells and smooth muscle cells.* Proc Natl Acad Sci U S A, 1990. **87**(13): p. 5134-8.

58. Takahara, N., et al., *Lysophosphatidylcholine stimulates the expression and production of MCP-1 by human vascular endothelial cells.* Metabolism, 1996. **45**(5): p. 559-64.

59. Shin, W.S., A. Szuba, and S.G. Rockson, *The role of chemokines in human cardiovascular pathology: enhanced biological insights.* Atherosclerosis, 2002. **160**(1): p. 91-102.

60. Gerszten, R.E., et al., *MCP-1 and IL-8 trigger firm adhesion of monocytes to vascular endothelium under flow conditions.* Nature, 1999. **398**(6729): p. 718-23.

61. Lum, A.F., et al., *Dynamic regulation of LFA-1 activation and neutrophil arrest on intercellular adhesion molecule 1 (ICAM-1) in shear flow.* J Biol Chem, 2002. **277**(23): p. 20660-70.

62. Kansas, G.S., *Selectins and their ligands: current concepts and controversies.* Blood, 1996. **88**(9): p. 3259-87.

63. Johnson Tidey, R.R., et al., *Increase in the adhesion molecule P-selectin in endothelium overlying atherosclerotic plaques. Coexpression with intercellular adhesion molecule-1.* Am J Pathol, 1994. **144**(5): p. 952-61.

64. Manka, D.R., et al., *Arterial injury increases expression of inflammatory adhesion molecules in the carotid arteries of apolipoprotein-E-deficient mice.* J Vasc Res, 1999. **36**(5): p. 372-8.

65. O'Brien, K.D., et al., *Vascular cell adhesion molecule-1 is expressed in human coronary atherosclerotic plaques. Implications for the mode of progression of advanced coronary atherosclerosis.* J Clin Invest, 1993. **92**(2): p. 945-51.

66. Li, H., et al., *An atherogenic diet rapidly induces VCAM-1, a cytokine-regulatable mononuclear leukocyte adhesion molecule, in rabbit aortic endothelium.* Arterioscler Thromb Vasc Biol, 1993. **13**(2): p. 197-204.

67. Saijo, Y., C.S. Jorgensen, and E. Falk, *Ultrasonic tissue characterization of collagen in lipid-rich plaques in apoE-deficient mice.* Atherosclerosis, 2001. **158**(2): p. 289-95.

68. Allen, S., et al., *Native low density lipoprotein-induced calcium transients trigger VCAM-1 and E-selectin expression in cultured human vascular endothelial cells.* J Clin Invest, 1998. **101**(5): p. 1064-75.

69. Erl, W., P.C. Weber, and C. Weber, *Monocytic cell adhesion to endothelial cells stimulated by oxidized low density lipoprotein is mediated by distinct endothelial ligands.* Atherosclerosis, 1998. **136**(2): p. 297-303.

70. Khan, B.V., et al., *Modified low density lipoprotein and its constituents augment cytokine-activated vascular cell adhesion molecule-1 gene expression in human vascular endothelial cells.* J Clin Invest, 1995. **95**(3): p. 1262-70.

71. Hope, S.A. and I.T. Meredith, *Cellular adhesion molecules and cardiovascular disease. Part I. Their expression and role in atherogenesis.* Intern Med J, 2003. **33**(8): p. 380-6.

72. Caro, C.G., J.M. Fitz_Gerald, and R.C. Schroter, *Arterial wall shear and distribution of early atheroma in man.* Nature, 1969. **223**(211): p. 1159-60.

73. Ding, Z., et al., *Influence of the geometry of the left main coronary artery bifurcation on the distribution of sudanophilia in the daughter vessels.* Arterioscler Thromb Vasc Biol, 1997. **17**(7): p. 1356-60.

74. Fox, B. and W.A. Seed, *Location of early atheroma in the human coronary arteries.* J Biomech Eng, 1981. **103**(3): p. 208-12.

75. Friedman, M.H., et al., *Arterial geometry affects hemodynamics. A potential risk factor for athersoclerosis.* Atherosclerosis, 1983. **46**(2): p. 225-31.

76. Liu, X.M., et al., *Physiologic cyclic stretch inhibits apoptosis in vascular endothelium.* FEBS Lett, 2003. **541**(1-3): p. 52-6.

77. Draney, M.T., C.K. Zarins, and C.A. Taylor, *Three-dimensional analysis of renal artery bending motion during respiration.* J Endovasc Ther, 2005. **12**(3): p. 380-6.

78. Grigioni, M., et al., *A mathematical description of blood spiral flow in vessels: application to a numerical study of flow in arterial bending.* J Biomech, 2005. **38**(7): p. 1375-86.

79. Asakura, T. and T. Karino, *Flow patterns and spatial distribution of atherosclerotic lesions in human coronary arteries.* Circ Res, 1990. **66**(4): p. 1045-66.

80. Bell, D.R., H.N. Sabbah, and P.D. Stein, *Profiles of velocity in coronary arteries of dogs indicate lower shear rate along inner arterial curvature.* Arteriosclerosis, 1989. **9**(2): p. 167-75.

81. Friedman, M.H., et al., *Relationship between the geometry and quantitative morphology of the left anterior descending coronary artery.* Atherosclerosis, 1996. **125**(2): p. 183-92.

82. Kirpalani, A., et al., *Velocity and wall shear stress patterns in the human right coronary artery.* J Biomech Eng, 1999. **121**(4): p. 370-5.

83. Tsutsui, H., et al., *Intravascular ultrasound evaluation of plaque distribution at curved coronary segments.* Am J Cardiol, 1998. **81**(8): p. 977-81.

84. Myers, J.G., et al., *Factors influencing blood flow patterns in the human right coronary artery.* Ann Biomed Eng, 2001. **29**(2): p. 109-20.

85. Gross, M.F. and M.H. Friedman, *Dynamics of coronary artery curvature obtained from biplane cineangiograms.* J Biomech, 1998. **31**(5): p. 479-84.

86. Pao, Y.C., J.T. Lu, and E.L. Ritman, *Bending and twisting of an in vivo coronary artery at a bifurcation.* J Biomech, 1992. **25**(3): p. 287-95.

87. Ding, Z. and M.H. Friedman, *Dynamics of human coronary arterial motion and its potential role in coronary atherogenesis.* J Biomech Eng, 2000. **122**(5): p. 488-92.

88. Ding, Z., H. Zhu, and M.H. Friedman, *Coronary artery dynamics in vivo.* Ann Biomed Eng, 2002. **30**(4): p. 419-29.

89. Ramaswamy, S.D., et al., *Fluid dynamic analysis in a human left anterior descending coronary artery with arterial motion.* Ann Biomed Eng, 2004. **32**(12): p. 1628-41.

90. Zeng, D., et al., *Effects of cardiac motion on right coronary artery hemodynamics.* Ann Biomed Eng, 2003. **31**(4): p. 420-9.

91. VanEpps, J.S. and D.A. Vorp, *Mechanopathobiology of Atherogenesis: A Review.* J Surg Res, 2006. **In Press**.

92. Milovanova, T., et al., *Endothelial cell proliferation associated with abrupt reduction in shear stress is dependent on reactive oxygen species.* Antioxid Redox Signal, 2004. **6**(2): p. 245-58.

93. Arisaka, T., et al., *Effects of shear stress on glycosaminoglycan synthesis in vascular endothelial cells.* Annals of the New York Academy of Sciences, 1995. **748**: p. 543-54.

94. Davies, P.F., et al., *Turbulent fluid shear stress induces vascular endothelial cell turnover in vitro.* Proc Natl Acad Sci U S A, 1986. **83**(7): p. 2114-7.

95. White, C.R., et al., *Temporal gradients in shear, but not spatial gradients, stimulate endothelial cell proliferation.* Circulation, 2001. **103**(20): p. 2508-13.

96. Lin, K., et al., *Molecular mechanism of endothelial growth arrest by laminar shear stress.* Proc Natl Acad Sci U S A, 2000. **97**(17): p. 9385-9.

97. Li, G., Mills, I., and Sumpio, B. E., Endothelium : Journal of Endothelial Cell Research, 1994. **2**: p. 177-184.

98. Rosales, O.R. and B.E. Sumpio, *Protein kinase C is a mediator of the adaptation of vascular endothelial cells to cyclic strain in vitro.* Surgery, 1992. **112**(2): p. 459-66.

99. Dimmeler, S., et al., *Fluid shear stress stimulates phosphorylation of Akt in human endothelial cells: involvement in suppression of apoptosis.* Circ Res, 1998. **83**(3): p. 334-41.

100. Dimmeler, S., et al., *Shear stress inhibits apoptosis of human endothelial cells.* Febs Lett, 1996. **399**(1-2): p. 71-4.

101. Haga, M., et al., *Shear stress and cyclic strain may suppress apoptosis in endothelial cells by different pathways.* Endothelium, 2003. **10**(3): p. 149-57.

102. Hermann, C., A.M. Zeiher, and S. Dimmeler, *Shear stress inhibits H2O2-induced apoptosis of human endothelial cells by modulation of the glutathione redox cycle and nitric oxide synthase.* Arterioscler Thromb Vasc Biol, 1997. **17**(12): p. 3588-92.

103. Pi, X., C. Yan, and B.C. Berk, *Big mitogen-activated protein kinase (BMK1)/ERK5 protects endothelial cells from apoptosis.* Circ Res, 2004. **94**(3): p. 362-9.

104. Yoshizumi, M., et al., *Stress and vascular responses: atheroprotective effect of laminar fluid shear stress in endothelial cells: possible role of mitogen-activated protein kinases.* J Pharmacol Sci, 2003. **91**(3): p. 172-6.

105. Sho, E., et al., *Blood flow decrease induces apoptosis of endothelial cells in previously dilated arteries resulting from chronic high blood flow.* Arterioscler Thromb Vasc Biol, 2001. **21**(7): p. 1139-45.

106. Birukov, K.G., et al., *Magnitude-dependent regulation of pulmonary endothelial cell barrier function by cyclic stretch.* Am J Physiol, 2003. **285**(4): p. L785-97.

107. Himburg, H.A., et al., *Spatial comparison between wall shear stress measures and porcine arterial endothelial permeability.* Am J Physiol, 2004. **286**(5): p. H1916-22.

108. Phelps, J.E. and N. DePaola, *Spatial variations in endothelial barrier function in disturbed flows in vitro.* Am J Physiol, 2000. **278**(2): p. H469-76.

109. Friedman, M.H., et al., *Effect of periodic alterations in shear on vascular macromolecular uptake.* Biorheology, 2000. **37**(4): p. 265-77.

110. Caro, C.G. and M.J. Lever, *Factors influencing arterial wall mass transport.* Biorheology, 1984. **21**(1-2): p. 197-205.

111. Caro, C.G. and M.J. Lever, *The mass transport of the arterial wall: effect of mechanical stresses and vasoactive agents, including nitrates.* Zeitschrift Fur Kardiologie, 1983. **72 Suppl 3**: p. 178-81.

112. Nielsen, L.B., *Transfer of low density lipoprotein into the arterial wall and risk of atherosclerosis.* Atherosclerosis, 1996. **123**(1-2): p. 1-15.

113. Herman, I.M., et al., *Hemodynamics and the vascular endothelial cytoskeleton.* J Cell Biol, 1987. **105**(1): p. 291-302.

114. Murase, T., et al., *Fluid shear stress transcriptionally induces lectin-like oxidized LDL receptor-1 in vascular endothelial cells.* Circ Res, 1998. **83**(3): p. 328-33.

115. Birukov, K.G., et al., *Stretch affects phenotype and proliferation of vascular smooth muscle cells.* Mol Cell Biochem, 1995. **144**(2): p. 131-9.

116. Dufourcq, P., et al., *Phenotypic modification of arterial smooth muscle cells in response to medial dissection.* Coron Artery Dis, 1997. **8**(3-4): p. 163-70.

117. Goldman, J., L. Zhong, and S.Q. Liu, *Degradation of alpha-actin filaments in venous smooth muscle cells in response to mechanical stretch.* Am J Physiol, 2003. **284**(5): p. H1839-47.

118. Zeidan, A., et al., *Stretch-dependent modulation of contractility and growth in smooth muscle of rat portal vein.* Circ Res, 2000. **87**(3): p. 228-34.

119. Zhang, W.D., et al., *Association of smooth muscle cell phenotypic modulation with extracellular matrix alterations during neointima formation in rabbit vein grafts.* J Vasc Surg, 1999. **30**(1): p. 169-83.

120. Bao, X., C. Lu, and J.A. Frangos, *Temporal gradient in shear but not steady shear stress induces PDGF-A and MCP-1 expression in endothelial cells: role of NO, NF kappa B, and egr-1.* Arterioscler Thromb Vasc Biol, 1999. **19**(4): p. 996-1003.

121. Wang, D.L., et al., *Mechanical strain induces monocyte chemotactic protein-1 gene expression in endothelial cells. Effects of mechanical strain on monocyte adhesion to endothelial cells.* Circ Res, 1995. **77**(2): p. 294-302.

122. Wung, B.S., et al., *Cyclical strain increases monocyte chemotactic protein-1 secretion in human endothelial cells.* Am J Physiol, 1996. **270**(4 Pt 2): p. H1462-8.

123. Wung, B.S., et al., *Cyclic strain-induced monocyte chemotactic protein-1 gene expression in endothelial cells involves reactive oxygen species activation of activator protein 1.* Circ Res, 1997. **81**(1): p. 1-7.

124. Chen, H., et al., *Effects of laminar shear stress on IL-8 mRNA expression in endothelial cells.* Biorheology, 2003. **40**(1-3): p. 53-8.

125. Kato, H., et al., *Fluid shear stress suppresses interleukin 8 production by vascular endothelial cells.* Biorheology, 2001. **38**(4): p. 347-53.

126. Yoshisue, H., et al., *Large scale isolation of non-uniform shear stress-responsive genes from cultured human endothelial cells through the preparation of a subtracted cDNA library.* Atherosclerosis, 2002. **162**(2): p. 323-34.

127. Lawrence, M.B., et al., *Threshold levels of fluid shear promote leukocyte adhesion through selectins (CD62L,P,E).* J Cell Biol, 1997. **136**(3): p. 717-27.

128. Yoshida, Y., et al., *Hemodynamic-force-induced difference of interendothelial junctional complexes.* Ann N Y Acad Sci, 1995. **748**: p. 104-20; discussion 120-1.

129. Okano, M. and Y. Yoshida, *Junction complexes of endothelial cells in atherosclerosis-prone and atherosclerosis-resistant regions on flow dividers of brachiocephalic bifurcations in the rabbit aorta.* Biorheology, 1994. **31**(2): p. 155-61.

130. Albuquerque, M.L., et al., *Shear stress enhances human endothelial cell wound closure in vitro.* Am J Physiol, 2000. **279**(1): p. H293-302.

131. Ando, J., H. Nomura, and A. Kamiya, *The effect of fluid shear stress on the migration and proliferation of cultured endothelial cells.* Microvasc Res, 1987. **33**(1): p. 62-70.

132. Levesque, M.J., R.M. Nerem, and E.A. Sprague, *Vascular endothelial cell proliferation in culture and the influence of flow.* Biomaterials, 1990. **11**(9): p. 702-7.

133. Imberti, B., et al., *The response of endothelial cells to fluid shear stress using a co-culture model of the arterial wall.* Endothelium, 2002. **9**(1): p. 11-23.

134. Williams, C. and T.M. Wick, *Endothelial cell-smooth muscle cell co-culture in a perfusion bioreactor system.* Ann Biomed Eng, 2005. **33**(7): p. 920-8.

135. Bareille, R., et al., *Caution regarding the combined effects of extracellular matrices and nutrient media on cultured endothelial cells.* Cell Biol Int, 2003. **27**(5): p. 439-43.

136. Waybill, P.N. and L.J. Hopkins, *Arterial and venous smooth muscle cell proliferation in response to co-culture with arterial and venous endothelial cells.* J Vasc Interv Radiol, 1999. **10**(8): p. 1051-7.

137. Severyn, D.A., S.C. Muluk, and D.A. Vorp, *The influence of hemodynamics and wall biomechanics on the thrombogenicity of vein segments perfused in vitro.* J Surg Res, 2004. **121**(1): p. 31-7.

138. Vorp, D.A., D.G. Peters, and M.W. Webster, *Gene expression is altered in perfused arterial segments exposed to cyclic flexure ex vivo.* Ann Biomed Eng, 1999. **27**(3): p. 366-71.

139. Traub, O. and B.C. Berk, *Laminar shear stress: mechanisms by which endothelial cells transduce an atheroprotective force.* Arterioscler Thromb Vasc Biol, 1998. **18**(5): p. 677-85.

140. Shin, H.Y., M.E. Gerritsen, and R. Bizios, *Regulation of endothelial cell proliferation and apoptosis by cyclic pressure.* Ann Biomed Eng, 2002. **30**(3): p. 297-304.

141. Cheng, J.J., et al., *Cyclic strain-induced plasminogen activator inhibitor-1 (PAI-1) release from endothelial cells involves reactive oxygen species.* Biochem Biophys Res Commun, 1996. **225**(1): p. 100-5.

142. Howard, A.B., et al., *Cyclic strain induces an oxidative stress in endothelial cells.* Am J Physiol, 1997. **272**(2 Pt 1): p. C421-7.

143. Deng, X., et al., *Luminal surface concentration of lipoprotein (LDL) and its effect on the wall uptake of cholesterol by canine carotid arteries.* J Vasc Surg, 1995. **21**(1): p. 135-45.

144. Berceli, S.A., et al., *Mechanisms of vein graft atherosclerosis: LDL metabolism and endothelial actin reorganization.* J Vasc Surg, 1991. **13**(2): p. 336-47.

145. Okada, M., et al., *Cyclic stretch upregulates production of interleukin-8 and monocyte chemotactic and activating factor/monocyte chemoattractant protein-1 in human endothelial cells.* Arterioscler Thromb Vasc Biol, 1998. **18**(6): p. 894-901.

146. Shyy, Y.J., et al., *Fluid shear stress induces a biphasic response of human monocyte chemotactic protein 1 gene expression in vascular endothelium.* Proc Natl Acad Sci U S A, 1994. **91**(11): p. 4678-82.

147. Morigi, M., et al., *Fluid shear stress modulates surface expression of adhesion molecules by endothelial cells.* Blood, 1995. **85**(7): p. 1696-703.

148. Nagel, T., et al., *Shear stress selectively upregulates intercellular adhesion molecule-1 expression in cultured human vascular endothelial cells.* J Clin Invest, 1994. **94**(2): p. 885-91.

149. Tsuboi, H., et al., *Flow stimulates ICAM-1 expression time and shear stress dependently in cultured human endothelial cells.* Biochem Biophys Res Commun, 1995. **206**(3): p. 988-96.

150. Golledge, J., et al., *Circumferential deformation and shear stress induce differential responses in saphenous vein endothelium exposed to arterial flow.* J Clin Invest, 1997. **99**(11): p. 2719-26.

151. Golledge, J., et al., *Arterial flow induces changes in saphenous vein endothelium proteins transduced by cation channels.* Eur J Vasc Endovasc Surg, 2000. **19**(5): p. 545-50.

152. Hamid, M.S., T. P. Davis, and P. D. Stein., *Cyclic flexion of the coronary arteries is a possible contributing factor to coronary atherosclerosis.* Adv Bioeng, 1992. **22**: p. 329-331.

153. Robicsek, F. and M.J. Thubrikar, *The freedom from atherosclerosis of intramyocardial coronary arteries: reduction of mural stress--a key factor.* Eur J Cardiothorac Surg, 1994. **8**(5): p. 228-35.

154. Stein, P.D., et al., *Effects of cyclic flexion of coronary arteries on progression of atherosclerosis.* Am J Cardiol, 1994. **73**(7): p. 431-7.

155. Thubrikar, M.J. and F. Robicsek, *Pressure-induced arterial wall stress and atherosclerosis.* Ann Thorac Surg, 1995. **59**(6): p. 1594-603.

156. Vorp, D.A., et al., *A device for the application of cyclic twist and extension on perfused vascular segments.* Am J Physiol, 1996. **270**(2 Pt 2): p. H787-95.

157. Haruguchi, H. and S. Teraoka, *Intimal hyperplasia and hemodynamic factors in arterial bypass and arteriovenous grafts: a review.* J Artif Organs, 2003. **6**(4): p. 227-35.

158. Kute, S.M. and D.A. Vorp, *The effect of proximal artery flow on the hemodynamics at the distal anastomosis of a vascular bypass graft: computational study.* J Biomech Eng, 2001. **123**(3): p. 277-83.

159. Kornet, L., et al., *Differences in near-wall shear rate in the carotid artery within subjects are associated with different intima-media thicknesses.* Arterioscler Thromb Vasc Biol, 1998. **18**(12): p. 1877-84.

160. Pedersen, E.M., A.P. Yoganathan, and X.P. Lefebvre, *Pulsatile flow visualization in a model of the human abdominal aorta and aortic bifurcation.* J Biomech, 1992. **25**(8): p. 935-44.

161. He, X. and D.N. Ku, *Pulsatile flow in the human left coronary artery bifurcation: average conditions.* J Biomech Eng, 1996. **118**(1): p. 74-82.

162. Iwami, T., et al., *Importance of left anterior descending coronary artery curvature in determining cross-sectional plaque distribution assessed by intravascular ultrasound.* Am J Cardiol, 1998. **82**(3): p. 381-4.

163. Jeremias, A., et al., *Spatial orientation of atherosclerotic plaque in non-branching coronary artery segments.* Atherosclerosis, 2000. **152**(1): p. 209-15.

164. Gibson, C.M., et al., *Relation of vessel wall shear stress to atherosclerosis progression in human coronary arteries.* Arterioscler Thromb Vasc Biol, 1993. **13**(2): p. 310-5.

165. Aikawa, M., et al., *Human smooth muscle myosin heavy chain isoforms as molecular markers for vascular development and atherosclerosis.* Circ Res, 1993. **73**(6): p. 1000-12.

166. Thubrikar, M.J., J.W. Baker, and S.P. Nolan, *Inhibition of atherosclerosis associated with reduction of arterial intramural stress in rabbits.* Arteriosclerosis, 1988. **8**(4): p. 410-20.

167. Humphrey, J.D., *Cardiovascular Solid Mechanics Cells, Tissues, and Organs*. 2002, New York: Springer.

168. Kute, S.M., *A Combined Experimental and Computational Approach to Study the Biological Effect of Hemodynamics In End-To-Side Vascular Bypass Grafts*, in *School of Engineering*. 2002, University of Pittsburgh: Pittsburgh.

169. Labadie, R.F., et al., *Pulsatile perfusion system for ex vivo investigation of biochemical pathways in intact vascular tissue.* The American Journal of Physiology, 1996. **270**(2 Pt 2): p. H760-8.

170. Labadie, R.F., *Design and construction of a computer-controlled, pulsatile, ex-vivo, vascular perfusion system and its use in investigating stimulation of the nitric oxide pathway in human saphenous vein grafts.*, in *Bioengineering Department*. 1995, University of Pittsburgh: Pittsburgh.

171. Ligush, J., et al., *Evaluation of endothelium-derived nitric oxide mediated vasodilation utilizing ex vivo perfusion of an intact vessel.* The Journal of Surgical Research, 1992. **52**(5): p. 416-21.

172. Muluk, S.C., et al., *Enhancement of tissue factor expression by vein segments exposed to coronary arterial hemodynamics.* Journal of Vascular Surgery : Official Publication, the Society For Vascular Surgery [and] International Society For Cardiovascular Surgery, North American Chapter, 1998. **27**(3): p. 521-7.

173. *LabView 7.1 Help*. 2004, National Instruments: Austin, TX.

174. Strang, G., *Calculus*. 1991, Wellesley: Wellesley-Cambridge Press.

175. Balcells, M., et al., *Cells in fluidic environments are sensitive to flow frequency.* J Cell Physiol, 2005. **204**(1): p. 329-35.

176. Prosi, M., et al., *Influence of curvature dynamics on pulsatile coronary artery flow in a realistic bifurcation model.* J Biomech, 2004. **37**(11): p. 1767-75.

177. Moghadasian, M.H., J.J. Frohlich, and B.M. McManus, *Advances in experimental dyslipidemia and atherosclerosis.* Laboratory Investigation; a Journal of Technical Methods and Pathology, 2001. **81**(9): p. 1173-83.

178. Holvoet, P., et al., *LDL hypercholesterolemia is associated with accumulation of oxidized LDL, atherosclerotic plaque growth, and compensatory vessel enlargement in coronary arteries of miniature pigs.* Arteriosclerosis, Thrombosis, and Vascular Biology (Online), 1998. **18**(3): p. 415-22.

179. Griggs, T.R., et al., *Development of coronary atherosclerosis in swine with severe hypercholesterolemia. Lack of influence of von Willebrand factor or acute intimal injury.* Arteriosclerosis (Dallas, Tex.), 1986. **6**(2): p. 155-65.

180. Prescott, M.F., et al., *Development of complex atherosclerotic lesions in pigs with inherited hyper-LDL cholesterolemia bearing mutant alleles for apolipoprotein B.* Am J Pathol, 1991. **139**(1): p. 139-47.

181. Rapacz, J., et al., *Lipoprotein mutations in pigs are associated with elevated plasma cholesterol and atherosclerosis.* Science, 1986. **234**(4783): p. 1573-7.

182. Kroger, K., et al., *Atherosclerotic lesions are more frequent in femoral arteries than in carotid arteries independent of increasing number of risk factors.* Angiology, 1999. **50**(8): p. 649-54.

183. Choi, G., et al. *Methods for quantifying vessel deformation due to pulsatile and non-pulsatile forces*. in *Summer Bioegineering Conference*. 2007. Keystone Resort & Conference Center, Keystone, Colorado, USA: ASME.

184. Lin, S.J., K.M. Jan, and S. Chien, *Temporal and spatial changes in macromolecular uptake in rat thoracic aorta and relation to [3H]thymidine uptake.* Atherosclerosis, 1990. **85**(2-3): p. 229-38.

185. Murphy, C.L. and M.J. Lever, *A ratiometric method of autofluorescence correction used for the quantification of Evans blue dye fluorescence in rabbit arterial tissues.* Exp Physiol, 2002. **87**(2): p. 163-70.

186. Conour, J.E., et al., *Acidomucin goblet cell expansion induced by parenteral nutrition in the small intestine of piglets.* Am J Physiol Gastrointest Liver Physiol, 2002. **283**(5): p. G1185-96.

187. Lally, C., A.J. Reid, and P.J. Prendergast, *Elastic behavior of porcine coronary artery tissue under uniaxial and equibiaxial tension.* Ann Biomed Eng, 2004. **32**(10): p. 1355-64.

188. Mooney, M., *A theory of large elastic deformation.* J Appl Phys, 1940. **11**: p. 582-592.

189. Wang, C., et al., *Three-dimensional mechanical properties of porcine coronary arteries: a validated two-layer model.* Am J Physiol Heart Circ Physiol, 2006. **291**(3): p. H1200-9.

190. Chuong, C.J. and Y.C. Fung, *Three-dimensional stress distribution in arteries.* J Biomech Eng, 1983. **105**(3): p. 268-74.

191. Lu, X., et al., *Shear modulus of porcine coronary artery: contributions of media and adventitia.* Am J Physiol Heart Circ Physiol, 2003. **285**(5): p. H1966-75.

192. *What principle governs the stress distribution in living organisms*, in *Biomechanics in China, Japan, and USA*, Y.C. Fung, E. Fakada, and J. Wang, Editors. 1983, Science Press: Beijing. p. 1-13.

193. Vaishnav, R.N. and J. Vossoughi, *Estimation of residual strains in aortic segments*, in *Biomechanical Engineering II, Recent Developments*, C.W. Hall, Editor. 1983, Pergamon: New York. p. 330-333.

194. Frobert, O., et al., *Relation between zero-stress state and branching order of porcine left coronary arterial tree.* Am J Physiol, 1998. **275**(6 Pt 2): p. H2283-90.

195. Deng, S.X., et al., *New experiments on shear modulus of elasticity of arteries.* Am J Physiol, 1994. **266**(1 Pt 2): p. H1-10.

196. Guo, X. and G.S. Kassab, *Distribution of stress and strain along the porcine aorta and coronary arterial tree.* Am J Physiol Heart Circ Physiol, 2004. **286**(6): p. H2361-8.

197. *ABAQUS 6.5 Documentation*. 2004, ABAQUS, Inc.: Beachwood, OH.

198. Zhang, W., et al., *Effect of surrounding tissue on vessel fluid and solid mechanics.* J Biomech Eng, 2004. **126**(6): p. 760-9.

199. Vorp, D.A., M.L. Raghavan, and M.W. Webster, *Mechanical wall stress in abdominal aortic aneurysm: influence of diameter and asymmetry.* Journal of Vascular Surgery : Official Publication, the Society For Vascular Surgery [and] International Society For Cardiovascular Surgery, North American Chapter, 1998. **27**(4): p. 632-9.

200. Bunce, D.F.M., *Atlas of arterial histology*. 1974, St. Louis: W. H. Green. xi, 269.

201. Weydahl, E.S. and J.E. Moore, *Dynamic curvature strongly affects wall shear rates in a coronary artery bifurcation model.* J Biomech, 2001. **34**(9): p. 1189-96.

202. *SPSS v15.0 Help Topics*. 2006, SPSS, Inc.: Chicago, IL.

203. Friedman, M.H., et al., *Correlation between intimal thickness and fluid shear in human arteries.* Atherosclerosis, 1981. **39**(3): p. 425-36.

204. Moore, J.E., et al., *Fluid wall shear stress measurements in a model of the human abdominal aorta: oscillatory behavior and relationship to atherosclerosis.* Atherosclerosis, 1994. **110**(2): p. 225-40.

205. Ainslie, K.M., et al., *Vascular smooth muscle cell glycocalyx influences shear stress-mediated contractile response.* J Appl Physiol, 2005. **98**(1): p. 242-9.

206. Chen, K.D., et al., *Mechanotransduction in response to shear stress. Roles of receptor tyrosine kinases, integrins, and Shc.* The Journal of Biological Chemistry, 1999. **274**(26): p. 18393-400.

207. Gautam, M., A. Gojova, and A.I. Barakat, *Flow-activated ion channels in vascular endothelium.* Cell Biochem Biophys, 2006. **46**(3): p. 277-84.

208. Berceli, S.A., et al., *Hemodynamics and low density lipoprotein metabolism. Rates of low density lipoprotein incorporation and degradation along medial and lateral walls of the rabbit aorto-iliac bifurcation.* Arteriosclerosis, 1990. **10**(5): p. 686-94.

209. Ross, R. and L. Agius, *The process of atherogenesis--cellular and molecular interaction: from experimental animal models to humans.* Diabetologia, 1992. **35 Suppl 2**: p. S34-40.

210. Rosner, B., *Fundamentals of Biostatistics 5th edition*. 2000, Pacific Grove, CA: Duxbury.